

University of Warwick institutional repository: <http://go.warwick.ac.uk/wrap>

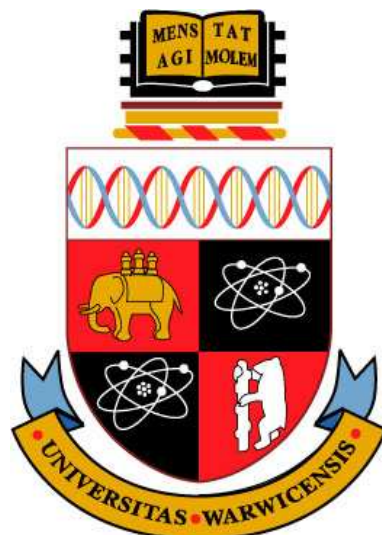
**A Thesis Submitted for the Degree of PhD at the University of Warwick**

<http://go.warwick.ac.uk/wrap/59702>

This thesis is made available online and is protected by original copyright.

Please scroll down to view the document itself.

Please refer to the repository record for this item for information to help you to cite it. Our policy information is available from the repository home page.



# **Thermal Differential EXAFS**

by

**Matthew Paul Ruffoni**

**Thesis**

Submitted to the University of Warwick

for the degree of

**Doctor of Philosophy**

**Physics**

November 2006

THE UNIVERSITY OF  
**WARWICK**

# Contents

<b>List of Tables</b>	<b>vi</b>
<b>List of Figures</b>	<b>viii</b>
<b>Acknowledgments</b>	<b>xviii</b>
<b>Declarations</b>	<b>xx</b>
<b>Abstract</b>	<b>xxi</b>
<b>Chapter 1 Plan of Thesis</b>	<b>1</b>
1.1 Introduction . . . . .	1
<b>Chapter 2 X-ray Absorption Spectroscopy and EXAFS</b>	<b>3</b>
2.1 Introduction . . . . .	3
2.2 Background to XAS and EXAFS . . . . .	4
2.3 Basic Theory of EXAFS . . . . .	6
2.4 Differential EXAFS: A Probe to Small Atomic Displacements . . . . .	11
2.5 Thermal Differential EXAFS . . . . .	12
<b>Chapter 3 Apparatus for Thermal Differential EXAFS</b>	<b>16</b>
3.1 Introduction . . . . .	16
3.2 Beamline Requirements for Detection and Measurement of Differential EXAFS . . . . .	17
3.3 X-ray Absorption Spectroscopy Beamline BM29 of the ESRF . . . . .	21

3.4	Dispersive EXAFS Beamline ID24 of the ESRF . . . . .	23
3.4.1	Extracting DiffEXAFS signals from measurements on ID24 . . . .	30
3.5	Requirements for the Thermal Modulation Apparatus . . . . .	32
3.6	Design and Manufacture of the Thermal Modulation Apparatus . . . .	34
3.7	Temperature Measurement and Sample Mounting Systems . . . . .	40
3.7.1	Initial designs . . . . .	40
3.7.2	The revised design . . . . .	42
3.7.3	'X-ray Temperature' Measurement . . . . .	49
<b>Chapter 4</b>	<b>Development of Data Analysis Techniques</b>	<b>51</b>
4.1	Introduction . . . . .	51
4.2	Calibration of spectra from ID24 . . . . .	52
4.2.1	Coordinate transformation . . . . .	52
4.2.2	Compensating for background effects . . . . .	53
4.2.3	Handling beamline specific spectral artifacts . . . . .	53
4.2.4	The General Non-Linear Levenberg-Marquardt algorithm . . . .	55
4.3	Fitting EXAFS spectra to theory . . . . .	58
4.3.1	<i>ab initio</i> EXAFS spectra using the FEFF code . . . . .	58
4.3.2	Extraction and normalisation of experimental XAFS signals . . .	60
4.3.3	Fitting conventional EXAFS spectra to theory . . . . .	62
4.4	Fitting Differential EXAFS spectra to theory . . . . .	64
4.4.1	Fitting paradigm and considerations for fit conditioning . . . .	64
4.4.2	Analysis of fitting errors . . . . .	67
<b>Chapter 5</b>	<b>Differential EXAFS to Measure Thermal Expansion</b>	<b>69</b>
5.1	Introduction . . . . .	69
5.2	Selection of samples for Thermal Expansion measurements . . . . .	70
5.3	Strontium Fluoride and Alpha-Iron . . . . .	71
5.4	Ensuring Observed Structure is Thermal in Origin . . . . .	73
5.4.1	Checking the DiffEXAFS Baseline . . . . .	73
5.4.2	Checking the Phase-Reversed Signal . . . . .	76

5.5	Experimental Results . . . . .	76
5.6	Extraction of the Thermal Expansion Coefficients . . . . .	81
5.6.1	Generation of Theory Phase and Amplitude Information . . . . .	81
5.6.2	Establishing a Perturbation Reference Point . . . . .	81
5.6.3	Fitting the Differential Fine-Structure . . . . .	84
5.7	Discussion of Thermal Expansion Measurements . . . . .	84
<b>Chapter 6</b>	<b>Differential XRD to complement DiffEXAFS</b>	<b>88</b>
6.1	Introduction . . . . .	88
6.2	Experiment . . . . .	90
6.3	Discussion . . . . .	93
<b>Chapter 7</b>	<b>Differential EXAFS to Study Phase Transitions</b>	<b>95</b>
7.1	Introduction . . . . .	95
7.2	Ni <sub>2</sub> MnGa and its Martensitic Phase Transition . . . . .	97
7.3	Experimental Results . . . . .	100
7.4	Analysis of the Low Temperature Martensite Phase . . . . .	106
7.4.1	Conventional EXAFS . . . . .	106
7.4.2	Differential EXAFS . . . . .	111
7.5	Discussion of Phase Transition Studies . . . . .	116
<b>Chapter 8</b>	<b>General Discussion and Future Outlook</b>	<b>119</b>
8.1	DiffEXAFS vs. Conventional EXAFS . . . . .	119
8.2	Future work . . . . .	121
8.3	Extension to Studies of Non-Thermal Phenomena . . . . .	123
<b>Appendix A</b>	<b>Gas Jet Blueprints</b>	<b>124</b>
<b>Appendix B</b>	<b>The Ni<sub>2</sub>MnGa Crystal Structure</b>	<b>147</b>
<b>Appendix C</b>	<b>Further details on DiffEXAFS analysis</b>	<b>151</b>
C.1	Fe and SrF <sub>2</sub> Thermal Expansion Analysis . . . . .	152
C.1.1	FEFF Input Configuration Files . . . . .	152

C.1.2	Scattering Paths Retained After Filtering . . . . .	154
C.1.3	FitChi2 Input for Conventional EXAFS Fits . . . . .	156
C.1.4	FitChi2 Input for DiffEXAFS Fits . . . . .	156
C.1.5	FitChi2 Output . . . . .	158
C.2	Ni <sub>2</sub> MnGa Phase Transition Analysis . . . . .	161
C.2.1	FEFF Input Configuration Files . . . . .	161
C.2.2	Scattering Paths Retained After Filtering . . . . .	161
C.2.3	FitChi2 for Conventional EXAFS Fits . . . . .	162
C.2.4	FitChi2 for DiffEXAFS Fits . . . . .	164
<b>Appendix D Papers submitted from work in this thesis</b>		<b>167</b>
	"Calibration of spectra from dispersive XAS beamlines" . . . . .	168
	"An Introduction to Differential EXAFS" . . . . .	173
	"Verifying DiffEXAFS measurements with Differential X-ray Diffraction" . . .	176
<b>Bibliography</b>		<b>187</b>

# List of Tables

3.1	Information pertaining to the undulator source mounted on ID24. These data have been compiled from references [27] and [55]. . . . .	27
3.2	Information pertaining to the first coupling mirror mounted on ID24. These data have been compiled from references [27] and [55]. . . . .	29
3.3	Information pertaining to the second coupling mirror mounted on ID24. These data have been compiled from references [27] and [55]. . . . .	29
3.4	Information pertaining to the CCD detector on ID24. These data have been compiled from references [31] and [100]. . . . .	31
5.1	Crystal structure with lattice parameter, $a$ ; thermal expansion coefficient, $\alpha$ ; and Debye temperature, $\Theta_D$ ; of $\text{SrF}_2$ and $\alpha\text{-Fe}$ . References are shown in brackets. . . . .	73
5.2	The primary parameters found when fitting the Fe and $\text{SrF}_2$ conventional EXAFS. The $\sigma_j^2$ shown are for the first three single-scattering paths, where $j = 1, 2, 3$ respectively. . . . .	83
5.3	The DiffEXAFS parameters for $\alpha\text{-Fe}$ and $\text{SrF}_2$ . $\alpha$ is in units of $10^{-6}K^{-1}$ and $\partial\sigma_j^2/\partial T$ in $10^{-5}\text{\AA}^2K^{-1}$ . Note that errors for $\alpha$ and the $\partial\sigma_j^2$ are based on the fit errors only and do not include possible errors from $\Delta T$ . . . . .	86

6.1	Fitted parameters for the diffraction peak shown in Figure 6.2 and for the corresponding DiffXRD feature shown in Figure 6.3. The thermal expansion coefficient has been derived using equation (6.2). Energies shown are not absolute energies, but based on a calibration with respect to another spectrum of known calibration. The errors shown are for the Gaussian and DiffXRD fits only and do not incorporate errors in calibration.	93
7.1	Fitted parameter values for Ni <sub>2</sub> MnGa EXAFS at the Ni-K edge for a range of temperatures away from the transition in the Martensite phase. In each fit, $S_0^2$ was fixed at 0.8. It is important to note that given the first two Debye-Waller factors correspond to Ni-Mn and Ni-Ga, which have equivalent radii, and also that there is little phase contrast between these two paths, FitChi2 is unable to accurately distinguish one from the other. Therefore, it is only the average of these two parameters that is meaningful; hence $\langle \sigma_1^2, \sigma_2^2 \rangle$ . Errors are based on the fit only, and do not include other sources such as T or E <sub>0</sub> drift.	107
7.2	Fitted parameter values for Ni <sub>2</sub> MnGa EXAFS at the Ni-K edge for a range of temperatures close to the transition in the Martensite phase. In each fit, $S_0^2$ was fixed at 0.8. Again, errors come from the fit only.	108
7.3	Fitted parameter values for Ni <sub>2</sub> MnGa DiffEXAFS at the Ni-K edge approaching the transition in the Martensite phase. The lack of contrast between the Ni-Mn and Ni-Ga paths again requires their results to be averaged. Errors quoted arise from the fits only.	113



# List of Figures

2.1	DiffEXAFS signals at the Fe-K edge for magnetisation modulation of FeCo (provided by R.F. Pettifer) and thermal modulation of Fe foil. EXAFS for the pure Fe sample is shown, which is virtually identical to the FeCo structure. As can be seen, the modulation of different sample properties results in very different signals. The magnetisation signal only contains one component through magnetostrictive strain, whereas the thermal signal contains components from expansion of the crystal lattice and changes to atomic vibrational amplitudes. . . . .	14
3.1	A schematic representation of a twin crystal, Bragg reflecting monochromator, arranged in the parallel configuration. . . . .	23
3.2	A schematic representation of the optical components of ID24. Reproduced from [55] with modifications. . . . .	25
3.3	A bent crystal polychromator diffracts x-rays of a continuous range of wavelengths as the angle of incidence of impinging radiation changes along its length. The result is polychromatic illumination at the focal point rather than monochromatic as would be obtained from a flat crystal.	25
3.4	A schematic representation of an undulator/wiggler insertion device. Electrons perform small amplitude oscillations, causing the emission of radiation along the axial direction. . . . .	26

3.5	The Gas jet thermal modulation apparatus. a) A schematic of the apparatus showing the two-way valve, heatsinks with gas flow channels, and the gas output needles. b) The gas jet <i>in situ</i> on ID24 A: X-rays in, B: Thermopile, C: Heaters and temperature sensors, D: Heatsink, E: Valve behind heatsink. . . . .	35
3.6	A horizontal cross-section through the gas jet apparatus along the line of the beam. The contour plot shows the velocity of gas flowing through the channels of the upper heatsink based on an input flow rate of 2 lpm.	38
3.7	A close-up of the channels in the heatsinks in the region where gas flow is split into three. A problem with the design shows that the central channel has a significantly greater flow rate than the outer two channels.	39
3.8	FEA of gas temperature whilst traversing the upper heatsink. The heatsink is heated to 323K, and gas injected at 2lpm. Poor flow through the outer heatsink channels results in insufficient heating, with gas being expelled at about 319K before reaching equilibrium with the heatsink. .	40
3.9	A schematic representation of the completed copper-constantan thermopile. The copper coloured lines indicate deposited copper, and the grey lines, constantan. The two concentric rings towards the outside of the device show where the thermally massive aluminium rings should be attached. The sample is attached at the centre. . . . .	42
3.10	An exploded view of the upgraded sample mount. Components 1a and 1b form the sample sheath, 2 is the sample holder, and 3 is the collar for the sample holder. . . . .	44
3.11	An assembled view of the upgraded sample mount with one of the two gas jets shown. 1: gas jet, 2: sample position, 3: gas exit channel. . . .	44
3.12	A close-up of the velocity of gas flow around the revised sample mount. Gas ejected from the needle forms a jet, hitting the sample before passing out between the needles or around the rear of the sample mount. . . .	47
3.13	A close-up of the temperature of the gas jets around the revised sample mount. . . . .	48

3.14	Normalised Thermal response profiles. The black line shows the fraction of $\Delta T$ attained by an Fe foil in the beam as a function of elapsed time after gas jet switching, and is derived from its XRT. The blue line is the corresponding temperature measurement for a thermocouple spot welded to an Fe foil, and the orange line, the temperature measurement for a thermopile attached to the rear of an Fe foil with a thermally conductive compound. Whilst the response times of the sample and thermocouple are roughly comparable, the thermopile responds extremely slowly to a change in gas temperature. . . . .	50
4.1	A typical X-ray absorption spectrum, taken on BM29 of the ESRF, with splines fitted to the pre- and post-edge regions to enable extraction of the observed fine-structure. . . . .	61
5.1	Anticipated DiffEXAFS signals, calculated using <i>ab initio</i> theory for a 1K change in $\alpha$ -Fe (top) and SrF <sub>2</sub> (bottom). In each graph, the blue line is the thermal expansion component of the differential fine-structure function, the red line the disorder component, and the black line the sum of the two. . . . .	72
5.2	A spurious DiffEXAFS spectrum taken through Fe foil for $\Delta T = 0$ K. The structure seen is Fe EXAFS leaking into the DiffEXAFS as a result of a change in gas pressure in ID24's third mirror upon switching the gas jets. This pressure change is about 10mbar, resulting in a change in beam attenuation of about 0.2% along the length of the mirror. . . . .	74
5.3	A spurious DiffEXAFS spectrum taken through Fe foil for $\Delta T = 0$ K. Once the problem shown in Figure 5.2 was eliminated the resulting DiffEXAFS baseline was still not flat. This was due to changes in gas pressure across the spatially dispersed beam inside the sample mount. . . . .	75

5.4	Two DiffEXAFS signals, in this case taken at the Fe-K edge in $\alpha$ -Fe, showing the effect of gas jet phase inversion. The black plot was produced based upon $T^+ - T^-$ , and the red upon $T^- - T^+$ . The structure in the latter is thus inverted about $\Delta\chi = 0$ , producing this distinctive eye-pattern. . . . .	77
5.5	Taking the data from Figure 5.4 and inverting the phase-reversed signal shows the structure in two spectra is identical. It can therefore be stated that this structure is entirely thermal in origin, with no corruption from non-thermal sources. . . . .	77
5.6	Experimental EXAFS and DiffEXAFS for the K-edges of $\alpha$ -Fe (top graph) and $\text{SrF}_2$ (bottom graph) at room temperature. The EXAFS plots have been scaled to 0.3% of their original amplitude so as to be of comparable size to the difference signals. Temperature modulation in the difference spectra is accurate to $\pm 0.2\text{K}$ . The gray plots are the inverted gas jet phase-reversed signals, which are essentially identical to the black plots, proving the thermal origin of the signal. The dashed vertical lines, which are centred on peaks in the EXAFS plots, highlight the phase shift of the difference signals with respect to the EXAFS. . . . .	79
5.7	A comparison between Difference EXAFS data taken, under similar conditions, through Fe foil during experiment MI-740 (top) and MI-803 (bottom). The upgraded sample mount used in MI-803, which allowed the time between measurements to be reduced to about 1.5s, yielded significantly better data. . . . .	80
5.8	Theory fit to experimental EXAFS, taken on BM29, at the Fe-K edge in $\alpha$ -Fe (top) and the Sr-K edge in $\text{SrF}_2$ (bottom). The theory spectra, shown in red, were calculated as described in section 5.6.2. The experimental spectra are shown in black. . . . .	82

5.9	Fourier filtered experimental Difference EXAFS spectra (black lines) for $\alpha$ -Fe (top graph) and $\text{SrF}_2$ (bottom graph), which have been fitted to the DiffEXAFS fine-structure function (2.14) (red lines). $\Delta T$ for each spectrum is given to the right. The associated fit parameters are shown in table 5.3. . . . .	85
6.1	The Sr-K edge measured in transmission on ID24 through a single crystal of $\text{SrF}_2$ (top plot with left scale). The amplitude has been normalised to unit edge jump. Diffraction glitches are clearly present on the absorption fine-structure. As the temperature of the specimen is changed by 1K at room temperature, these glitches shift in energy due to thermal expansion in the crystal, producing the DiffXRD signal shown below (right scale). . . . .	90
6.2	The diffraction glitch (dashed line) at about 16.35keV is extracted from the x-ray <i>transmission</i> spectrum, and the background subtracted. A Gaussian is fitted to the glitch (solid line) to determine its centroid energy, width at half maximum, and relative height. . . . .	91
6.3	The DiffXRD transmission signal obtained for $\Delta T = 6K$ in the energy region of the glitch shown in Fig 6.2 (dashed line). The difference between a pair of Gaussians of width and height determined by the fit in Fig 6.2, and offset in energy relative to one another, are fitted to the feature (solid line); the energy offset being related to the fractional change in lattice spacing. . . . .	92
7.1	A schematic representation of shape changes observed in specimens containing Martensites. The top diagram shows the effect of surface upheaval in the region of a Martensite, and the bottom, surface skewing, which bends any fiducial lines. Both the upheaval and skewing are regular and without distortion. . . . .	98

- 7.2 A microscopic schematic representation of lattice invariant shears that must occur as part of a Martensitic phase transformation. On the left are slip shear planes, and on the right twinned shear planes. Habit planes can be imagined to run roughly vertically along each side of these units, appearing homogeneous on a macroscopic scale. In  $\text{Ni}_2\text{MnGa}$ , the primary mechanism for lattice-invariant shear is twinning [12]. . . . . 100
- 7.3 Differential EXAFS spectra (i.e. normalised to a 1K modulation) taken at the Ni-K edge and heating through the Martensitic phase transition in  $\text{Ni}_2\text{MnGa}$ . The six spectra below the horizontal grey line were taken in the Martensitic phase, and the top four in the Austenite phase. The lowermost and uppermost spectra are the conventional EXAFS for the corresponding phases, scaled to 5% of their actual amplitude. . . . . 102
- 7.4 Differential EXAFS spectra (i.e. normalised to a 1K modulation) taken at the Ga-K edge and through the Martensitic phase transition in  $\text{Ni}_2\text{MnGa}$ . The spectra below the horizontal grey line were taken in the Martensitic phase, and those above in the Austenite phase. The lowermost and uppermost spectra are the conventional EXAFS for the corresponding phases, scaled to 5% of their actual amplitude. . . . . 103
- 7.5  $\text{Ni}_2\text{MnGa}$  Ni-K edge DiffEXAFS taken at 326K in the Austenite phase. The red signal was obtained with the gas jet phase reversed with respect to the black signal. The blue line is the inverted phase reversed signal, which reveals good agreement between the spectra taken with each gas phase. The two differ slightly, particular at high energies, but are sufficiently similar to state that the structure is thermal in origin. . . . 104
- 7.6 BM29 Conventional EXAFS spectra of  $\text{Ni}_2\text{MnGa}$  at the Ni-K edge for various temperatures away from the transition temperature in the Martensite phase (black lines). Each has been Fourier filtered to the first four single-scattering paths only. Overlaid in red are theory spectra, generated for the same scattering paths, fitted to experiment between  $70 \leq E' \leq 550\text{eV}$ . 107

- 7.7 ID24 Conventional EXAFS spectra of  $\text{Ni}_2\text{MnGa}$  at the Ni-K edge for various temperatures close to the transition temperature in the Martensite phase (black lines). Each has been Fourier filtered to the first four single-scattering paths only. Overlaid in red are theory spectra, generated for the same scattering paths, fitted to experiment between  $70 \leq E' \leq 550\text{eV}$ . The apparently poor fit at high energies is due to larger experimental noise on ID24 (from a lower x-ray flux) in this region. 108
- 7.8 A schematic representation of the photoelectron scattering paths considered during Ni-K edge EXAFS and DiffEXAFS analysis of the Martensite phase of  $\text{Ni}_2\text{MnGa}$ . The Ni-Mn and Ni-Ga paths are of the same length and are closest to the emitter atom, Ni-Ni 1 is next in length, and Ni-Ni 2 the longest. The precise crystal structure is given in Appendix B. . . . 109
- 7.9 Fourier transform of experimental Ni-K edge EXAFS in  $\text{Ni}_2\text{MnGa}$  taken away from (top) and close to (bottom)  $T_p$ . The transform was performed with a Hann window to reduce termination effects. It must be noted that the abscissa is the apparent atomic radial distribution function (RDF) rather than the real RDF. The two differ by an offset of approximately  $0.3\text{\AA}$  due to phase shifts experienced by the photoelectron. . . . . 110
- 7.10 DiffEXAFS spectra from  $\text{Ni}_2\text{MnGa}$  at the Ni-K edge approaching  $T_p$  in the Martensite phase (black lines). Each has been Fourier filtered to the first four single-scattering paths only. Overlaid in red are theory spectra, generated for the same scattering paths and fitted to experiment. . . . 112
- 7.11 Absolute  $\sigma_j^2$  for each of the first four single-scattering paths in  $\text{Ni}_2\text{MnGa}$ , determined by DiffEXAFS (solid lines) and conventional EXAFS (dashed lines) in the region of the phase-transition. DiffEXAFS results were obtained by integrating  $\partial\sigma_j^2/\partial T(T)$  and offsetting to  $\sigma_j^2(303\text{K})$  found from conventional EXAFS. All paths show the correct, descending trend, but values for Ni-Ni 1 and Ni-Ni 2 are clearly unphysical for  $T$  greater than about  $308\text{K}$ . This suggests a breakdown of the present theory close to  $T_p$ . Errors in  $T$  are smaller than the point size. . . . . 115

7.12	Absolute $s_j$ for each of the first four single-scattering paths in $\text{Ni}_2\text{MnGa}$ relative to their values at $293K$ . These are $2.5039\text{\AA}$ for Ni-Mn and Ni-Ga, $2.7700\text{\AA}$ for Ni-Ni 1, and $2.9500\text{\AA}$ for Ni-Ni 2. These reveal that each scattering path shortens at $T$ increases. The last three points for both Ni-Ni paths should not be considered meaningful given unphysical values were obtained for $\sigma_j^2$ from the same fits. Errors in $T$ are smaller than the point size. . . . .	116
A.1	Sputter Masks for deposition of an eight element copper-constantan thermopile. These masks should be laser etched from sheet aluminium of no more than $200\mu\text{m}$ thick. Constantan should be deposited first, and then copper over the top. . . . .	125
A.2	A base plate onto which the gas jet and sample holder components are mounted. It is carved from a single piece of aluminium and may be attached directly to any of the beamline apparatus tables. . . . .	126
A.3	Some of the parts that construct a thermally insulating case around the aluminium heatsinks. Two of each must be produced - one for each heatsink. . . . .	127
A.4	Some of the parts that construct a thermally insulating case around the aluminium heatsinks. Two of each must be produced - one for each heatsink. . . . .	128
A.5	The remaining parts that construct a thermally insulating case around the aluminium heatsinks. These parts make a base for the heatsinks. Only one of each is needed. . . . .	129
A.6	Rear projection of the aluminium heatsink. It is produced from a single piece of aluminium with channels cut into it for gas flow. . . . .	130
A.7	Front projection of the aluminium heatsink. It is produced from a single piece of aluminium with channels cut into it for gas flow. The gas hose attachment nipples and gas jet needle are also shown. . . . .	131
A.8	A cross-section through the heatsink showing the Nitrogen gas flow channels that are used to form the gas jets. . . . .	132



A.9	A cross-section through the heatsink showing the cooling fluid channels.	133
A.10	The completed pair of heatsinks with brass nipples attached. Any hole shown drilled through the heatsink in Figures A.8 and A.9 that does not have a nipple attached is blocked with an aluminium plug. . . . .	134
A.11	The completed pair of heatsinks with perspex case, ready to mount on the base plate shown in Figure A.2. . . . .	135
A.12	The sample sheath for the revised sample mount described in Section 3.7.2. . . . .	136
A.13	Upright onto which the sample sheath is attached. The sample support is pushed through the hole shown and into the sheath. . . . .	137
A.14	The sample support for the revised sample mount described in Section 3.7.2. . . . .	138
A.15	The sample support buffer ring described in Section 3.7.2. . . . .	139
A.16	Cross-section through the revised sample mount described in Section 3.7.2, showing how all the pieces are assembled. . . . .	140
A.17	Base section of the sample holder. This plate has a slot cut into it so that it may be attached to the aluminium base plate shown in Figure A.2.	141
A.18	Lateral support struts attached between the sample holder base plate in Figure A.17, and the front plate in Figure A.13 . . . . .	142
A.19	The complete sample mount, ready to be attached to the aluminium base plate shown in Figure A.2. . . . .	143
A.20	The complete gas jet apparatus. . . . .	144
A.21	Circuit schematics for the temperature measurement amplifiers. Designed by A. Lovejoy of the Warwick Physics Dept. Electronics Workshop.	145
A.22	Circuit schematics for the Proportional Integral Derivative (PID) Controller for the Gas Jet heatsinks. Designed by A. Lovejoy of the Warwick Physics Dept. Electronics Workshop. . . . .	146

B.1	Crystal structure of the Body-Centred Tetragonal (BCT) Martensite in $\text{Ni}_2\text{MnGa}$ . The structure is of space group $I4/mmm$ with lattice parameters $a = b = 5.90\text{\AA}$ and $c = 5.54\text{\AA}$ . Ni atoms are shown in light blue and have crystallographic coordinates of 0.25, 0.25, 0.25; Mn atoms are red, positioned at 0.5, 0.0, 0.0; and Ga atoms are Green, positioned at 0.0, 0.0, 0.0. . . . .	148
B.2	Crystal structure of the $L2_1$ Face-centred Cubic (FCC) Austenite in $\text{Ni}_2\text{MnGa}$ . The structure is of space group $Fm3m$ with lattice parameters $a = b = c = 5.825\text{\AA}$ . Ni atoms are shown in light blue and have crystallographic coordinates of 0.25, 0.25, 0.25; Mn atoms are red, positioned at 0.5, 0.0, 0.0; and Ga atoms are Green, positioned at 0.0, 0.0, 0.0. . .	149
B.3	A 3D view of the BCT Martensite in $\text{Ni}_2\text{MnGa}$ . Ni atoms are shown in light blue, Mn atoms in red, and Ga atoms in Green. A similar view of the $L2_1$ FCC Austenite could also be included here, but the differences in structure are too small to be visible by eye. . . . .	150

# Acknowledgments

Over the course of my PhD, numerous people have kindly provided me with help and assistance. Whilst their contributions have varied widely in nature, all have been vital to the success of this thesis. I would therefore like to extend my thanks to them.

**S. Pascarelli, O. Mathon, A. Trapananti**, and the other staff of beamlines ID24 and BM29 at the ESRF for their continuous help and support over the past three years.

**D. Sutherland, A. Sheffield** and the other staff of Warwick Physics Department's Mechanical workshop, primarily for manufacturing the apparatus for Thermal DiffEXAFS experiments, but also for other help and support over the years.

**A. Lovejoy** of the Department's Electronic workshop for designing and manufacturing the electronic control systems to accompany the DiffEXAFS apparatus.

**M. Pasquale** of the IEN in Torino, Italy for kindly providing Ni<sub>2</sub>MnGa samples for the phase transition studies in this thesis.

**M. Lees** and the other staff of Warwick's Superconductivity and Magnetism group for use of their apparatus and for help taking magnetic susceptibility and heat capacity measurements with it.

**R. Johnston** for help with the department's sputter deposition apparatus (and for fixing it on each of the three occasions that I blew it up!)

**J. Rehr** of the University of Washington, Seattle, USA for helpful discussions regarding Debye-Waller factors and the use of the FEFF code.

My friends, family, and housemates for their support, and for listening to me when I enthusiastically bored them with the wonders of DiffEXAFS.

The biggest thanks of all, however, is reserved for my supervisor **Robert Pettifer**. Without his help and support, and advice and guidance over the past three years, this thesis would never have even come close to fruition.

# Declarations

I hereby declare that the work in this thesis is my own, and present it in accordance with the regulations for the degree of Doctor of Philosophy. It has not previously been submitted to this or any other institution for any degree, diploma or other qualification.

Work concerning the development of the 'DXAS Calibration' code, described in Section 4.2, has been published in the Journal of Synchrotron Radiation [75]; work on 'Differential XRD' described in Chapter 6 has been submitted for publication, also to the Journal of Synchrotron Radiation [77]; and a paper providing a general introduction to Differential EXAFS has been accepted for publication in the 'Conference Proceedings of XAFS13' [79]. These papers are provided for reference in Appendix D.

The gas jet apparatus described in Section 3.6 and shown in Appendix A was designed by myself in its entirety, but manufactured by D. Sutherland and A. Sheffield of the Warwick Physics Department's Mechanical Workshop. The associated electronics, also shown in Appendix A, were designed and manufactured by A. Lovejoy of the Warwick Physics Department's Electronic Workshop.

# Abstract

Differential EXAFS (DiffEXAFS) is a new and novel technique for the study of small atomic strains. It relies on examining tiny differences in x-ray absorption spectra - taken under high-stability, low-noise conditions - generated by unit modulation of some sample bulk parameter.

Initial experiments conducted by Pettifer et al. [64] to measure the magnetostriction of FeCo, revealed a sensitivity to atomic displacements of the order of one femtometre ( $10^{-15}\text{m}$ ). This was two orders of magnitude more sensitive than thought possible, based on conventional EXAFS techniques [16] [2].

The mandate for this thesis was to extend DiffEXAFS to the case of samples undergoing temperature modulation - to develop Thermal Differential EXAFS - and in doing so, demonstrate that DiffEXAFS is a generally applicable technique for studying small atomic strains.

Topics covered here include the nature of Thermal DiffEXAFS signals, the design, manufacture, and characterisation of apparatus for Thermal DiffEXAFS experiments, and new analysis techniques developed to extract information from DiffEXAFS data.

Thermal expansion coefficients have been determined for Fe and  $\text{SrF}_2$ , for temperature modulation of the order of one Kelvin, proving the viability of the technique. Numerically, these were  $\alpha_{\text{Fe}} = (11.6 \pm 0.4) \times 10^{-6} \text{K}^{-1}$  and  $\alpha_{\text{SrF}_2} = (19 \pm 2) \times 10^{-6} \text{K}^{-1}$  respectively, which agreed with published values [52] [74]. In these measurements sensitivity to mean atomic displacements of about 0.3 femtometres was achieved.

The more interesting case of thermally induced phase transitions has also been studied, with DiffEXAFS measurements taken through the Martensitic phase transition of the Heusler alloy  $\text{Ni}_2\text{MnGa}$ . These revealed a hardening of the lattice as the transition was approached in the Martensite phase, agreeing with published trends [93][56], and an accompanying lattice contraction not seen previously.



# Chapter 1

## Plan of Thesis

### 1.1 Introduction

This thesis is intended to be a definitive guide to Thermal Differential EXAFS, containing all the information required to allow the reader to perform their own Thermal DiffEXAFS experiments. Each chapter is written as a self-contained package that may be read in isolation if so desired, but at the same time, each one builds on information provided in the previous.

Chapter 2 starts, naturally, with the theory of Differential EXAFS, and looks in detail at the Thermal Differential Fine-structure Function.

Chapter 3 gives a full account of the experimental apparatus for Thermal DiffEXAFS experiments, both in terms of thermal modulation equipment, and of beamline requirements in order to detect DiffEXAFS signals.

Chapter 4 studies data processing techniques for Thermal DiffEXAFS, whilst chapter 5 introduces Differential XRD - a complementary technique that enables DiffEXAFS measurements to be independently verified via a common experimental arrangement.

Chapters 6 and 7 then look in detail at the DiffEXAFS experiments performed as part of this thesis, on ID24 of the ESRF. Chapter 6 gives an account of thermal expansion measurements that were taken to prove Thermal DiffEXAFS is a viable technique, and chapter 7 an account of measurements taken through the thermally induced Martensitic phase transition of the Heusler alloy  $\text{Ni}_2\text{MnGa}$ .



Finally, chapter 8 examines the impact of this work, and looks to possible future developments in DiffEXAFS.

Three appendices are given at the end of the thesis. The first contains the blueprints for apparatus designed for Thermal DiffEXAFS experiments, the second, some key information that was used during the process of analysing DiffEXAFS data described in chapters 6 and 7, and the third, a compilation of all the research papers written in relation to the work presented in this thesis.

## Chapter 2

# X-ray Absorption Spectroscopy and EXAFS

### 2.1 Introduction

The presence of fine-structure in x-ray absorption spectra was first noted by Stenstrom in 1918 [87], with theories for its generation put forward by Kronig in 1931 and 32 [17][18][19]. However, it wasn't until the advent of synchrotron sources in the 1970's that extensive studies of x-ray fine-structure became viable. This period then saw a rapid development in the theoretical understanding of x-ray fine-structure, transforming such studies into a viable tool for structural analyses.

With the development of 2<sup>nd</sup>-generation sources in the 1980's and 3<sup>rd</sup>-generation sources in the 90's, X-ray Absorption Spectroscopy (XAS) went mainstream. Since then it has become a key tool across a broad range of disciplines, from Engineering to Chemistry and Biology, and, of course, including Physics.

Today, work still continues in developing a complete theoretical understanding of x-ray fine-structure, with novel experiments still pushing the boundaries of sensitivity and resolution in structural analyses.

This chapter introduces the concept of XAS and provides the basic theory behind x-ray fine-structure in the extended regime (EXAFS). Discussion then focuses on Differential EXAFS, a novel tool for measuring atomic perturbations [64], with a detailed examina-

tion of Thermal Differential EXAFS - the primary subject of this thesis.

## 2.2 Background to XAS and EXAFS

When x-rays pass through matter, they are subjected to both absorption and scattering processes, which remove flux from a given incident beam. Both can be significant when passing through light elements, but in heavier elements, absorption dominates; the resulting reduction in incident x-ray flux being described by the standard absorption relation

$$I = I_0 e^{-\mu_m \rho z} \quad (2.1)$$

$\mu_m$  is the mass absorption coefficient (typically given in  $\text{cm}^2 \text{g}^{-1}$ ),  $\rho$  the density of the material through which the beam is passing (in  $\text{g cm}^{-3}$ ), and  $z$  the thickness of sample material (in cm). The linear absorption coefficient for a material, which is more often quoted, is given by  $\mu = \mu_m \rho$ .

For a monoatomic material, the mass absorption coefficient may be expressed in terms of the mean atomic absorption cross-section,  $\sigma_a$  (in  $\text{cm}^2$  per atom)

$$\mu_m = \frac{N_A}{A} \sigma_a \quad (2.2)$$

where  $N_A$  is Avogadro's number, and  $A$  the atomic weight of the material. For other materials,  $\mu_m$  is given based on the atomic cross-sections of all its constituent elements

$$\mu_m = \frac{N_A}{\sum_i n_i A_i} \sum_i n_i \sigma_{ai} \quad (2.3)$$

where  $n_i$  is the number of atoms of type  $i$  in the material.

In the x-ray regime, absorption is predominantly due to the photoelectric effect, caused by the excitation of electrons in atomic core states. The observed absorption is therefore dependent on the arrangement of these states, making the process chemically selective, and on which are excited by photons of a given energy.

As a result, for most x-ray energies, the absorption profile is a smoothly varying function, which decreases as x-ray energy increases. However, if x-ray photons become sufficiently

energetic to promote previously untouched core electrons to an allowed excited state, a sudden increase in absorption is observed.

These discontinuities, first seen by M. de Broglie in 1913 [10], are referred to as absorption edges, and each is named according to which core electron was excited to generate it. At the highest x-ray energies, the deepest 1s electrons are excited, generating the *K*-edge. As x-ray energies decrease, the  $L_1$ ,  $L_2$ , and  $L_3$  edges are observed, which describe excitations of 2s,  $2p^{1/2}$ , and  $2p^{3/2}$  electrons respectively.  $M_1$  to  $M_5$  are then seen for d-shell electrons, and so on. Degeneracy of these latter edges is broken mainly due to relativistic spin-orbit effects.

The exact energy required to promote an electron is equivalent to the photon energy to within some  $\Delta E$ , described by the Uncertainty Principle

$$\Delta E \Delta t \geq \hbar/2\pi \quad (2.4)$$

where  $\Delta t$  is the lifetime of the excited states. For 1Å radiation, this is dictated by radiative de-excitation of the core hole, which, according to the classical treatment of Hedin [28], gives  $\Delta E$  as

$$\Delta E \simeq 0.952 \times 10^{-8} E^2 \quad (2.5)$$

For x-rays of 12keV, this is equivalent to 1eV.

Closer examination of x-ray absorption spectra reveals still more structure. As far back as 1918, Stenstrom [87] noted that on the high energy side of absorption edges - and up to, typically, 1000eV beyond - a series of small oscillations are observed in the x-ray absorption coefficient.

This is the structure that we now refer to as X-Ray Absorption Fine Structure (XAFS), which, with today's understanding of the processes involved, is split into two regions, the X-ray Absorption Near Edge Structure (XANES) within about 40eV of the edge, and the Extended X-ray Absorption Fine Structure (EXAFS) beyond that.

The physics of EXAFS, was originally explained by the short range order theory of Kronig in 1932 [18][19], and confirmed experimentally by Sayers, Lytle, and Stern in 1971 [81]. In this region photo-electrons have sufficient energy to effectively propagate through the sample as free particles. Some of these electrons are captured by atoms surrounding

the source atom, others near surfaces are ejected from the sample altogether, and some simply scatter off surrounding atoms and return to the atom from which they came. In this latter case the wave-function of an electron returning to the source atom interferes with its outgoing wave-function, affecting the transition probability for absorption through a changing overlap between the atom's final state wave-function and its perturbed initial state [59]. This results in modulation of the x-ray absorption cross-section, producing the observed oscillations in a sample's absorption coefficient. Critically, the interference pattern generated by scattered electrons is dependent upon what atoms they have scattered from, and where those atoms are located in relation to the source atom. EXAFS is therefore sensitive to the local structure surrounding the source atom, and may be studied to reveal that information. Furthermore, since the absorption process involved in EXAFS is chemically selective - each absorption edge energy being different depending on the absorbing element - the structure may be studied from the point of view of different atomic species simply by tuning x-ray energies to the appropriate absorption edge.

## 2.3 Basic Theory of EXAFS

The first task in developing a theory of EXAFS is to define some quantity which represents the x-ray fine-structure in terms of experimental observables. This quantity is obtained from the normalised oscillatory part of the x-ray absorption coefficient above a given edge,  $\chi(k)$ . For a monoatomic sample, and assuming electron excitation from just a single level, this is given by

$$\chi(k) = \frac{\mu(k) - \mu_0(k)}{\mu_0(k)} \quad (2.6)$$

where  $k$ , the photo-electron wave-vector, is related to the energy of the incident x-ray photon,  $E$ , above the edge energy,  $E_0$ , by

$$(E - E_0)\text{eV} = \frac{\hbar^2 k^2}{2m} \text{\AA}^{-1} \simeq 3.81 k^2 \text{\AA}^{-1} \quad (2.7)$$

Here,  $\mu(k)$  is the observed, linear x-ray absorption coefficient, and  $\mu_0(k)$  is the equivalent absorption when the atom under study is considered in isolation; that is, outside its local

environment. In the first instance, photo-electron scattering occurs off surrounding atoms, generating fine-structure, and in the latter, there is nothing from which the electrons may scatter, resulting in structure-less absorption.

Taking the difference between these two quantities thus isolates the oscillatory part of the x-ray absorption coefficient: the XAFS. The subsequent division of this structure by  $\mu_0(k)$  normalises its amplitude, eliminating effects from the thickness of the sample. Typically, within the assumptions stated, the amplitude of  $\chi(k)$  is about 10% the amplitude of the edge jump.

Unfortunately though, it is rarely the case that a measured spectrum contains absorption from only a single level of excitation. Indeed, most work in XAFS is conducted at K-edges where every possible electron energy level is excited. Thus (2.8) must be modified to subtract absorption from each of those  $n$  levels, and ensure correct normalisation.

$$\chi(k) = \frac{\mu(k) - \mu_0(k)}{\mu_0(k) - \sum_n \mu_{en}(k)} \quad (2.8)$$

$\mu_{en}(k)$  is the *in situ* absorption for the  $n^{th}$  edge of energy less than that of the edge under study. For instance, when working at K-edges,  $\mu_{en}(k)$  would cover all L-edges, M-edges, and so on.

Further complications arise in that it is often the case that samples contain more than one atomic species. In these instances, the *in situ* x-ray absorption coefficient,  $\mu(k)$ , will contain edges from more than one of those species. These edges won't be present in  $\mu_0(k)$ , when the studied atom is considered in isolation. Thus in order to extract the oscillatory part of the absorption coefficient, it is necessary to subtract the isolated atom absorption of each atomic species,  $i$

$$\chi(k) = \frac{\mu(k) - \sum_i \mu_{0i}(k)}{\mu_0(k) - \sum_n \mu_{en}(k)} \quad (2.9)$$

where  $\mu_0(k)$  remains the isolated atom absorption of the species under study, and  $\mu_{en}(k)$  covers all edges of lower energy irrespective of which atomic species they originated from. With the experimental fine-structure obtained, it is necessary to construct a theoretical description of  $\chi(k)$ . This should, in principle, contain all the physical processes from

which fine-structure originates, allowing it to be fitted to experimental spectra to extract important parameters.

In the broadest terms, this theory is based upon the generation of photo-electrons, their subsequent scattering within some atomic structure - be it crystalline, molecular, amorphous, or so on - the generation of a photo-electron wave interference pattern, and the effect of this interference upon the transition probability of the electron excitation via the Fermi Golden Rule. Therefore, such calculations are not trivial.

Indeed, a complete appraisal and/or derivation of EXAFS theory is beyond the scope of this thesis. However, what follows is a discussion of some of the physical concepts enshrined in the theory, with the inclusion of key equations and results required for Differential EXAFS. For a more in-depth discussion on the theory of EXAFS, the reader is directed to, for instance, [72][37][40][89][44].

The first standard method for EXAFS data analysis was introduced by Sayers et al. in 1971 [81]. Working within the assumptions that photo-electrons propagate as plane waves between source and scatterer atoms, and that only single backscattering events are significant in generating the fine-structure, they proposed Fourier transforming EXAFS data to obtain a radial distribution function of the environment surrounding the source atom. The peaks in this function then lie close to the atomic positions. However, they do not coincide exactly with the true atomic positions. They occur at lower radii, typically about 0.3 to 0.4 Å lower, due to phase-shifts experienced by the photo-electron both on scattering, and on climbing out of, and returning to, the emitter potential.

Rather than calculating such shifts from *ab initio* theory, Sayers et al. proposed to infer them by transforming EXAFS spectra from similar compounds of known structure. This approach is generally acceptable when extracting information regarding the first coordination shell around the source atom, but fails at larger radii, due, primarily, to the presence of multiple-scattering phenomena.

Nonetheless, they produced an expression for  $\chi(k)$  that contains many of the physical attributes of the modern fine-structure function, although it is worth re-emphasising

that this equation describes single-scattering only.

$$\chi(k) = -\frac{1}{k} \sum_j \frac{N_j}{R_j^2} S_j(k) \sin(2kR_j + 2\delta'_1(k) + \eta_j(k)) e^{-2\sigma_j^2 k^2} e^{-\gamma R_j} \quad (2.10)$$

$N_j$  is the number of atoms in coordination shell  $j$  of radius  $R_j$  surrounding the source atom,  $S_j(k)$  is the backscattering amplitude from each atom, and the factor  $\exp(-\gamma R_j)$  describes the decay of the photo-electron.  $\delta'_1$  describes the  $l=1$  phase-shift experienced by the photo-electron due to the potential of the source atom (when considering dipole transitions only). This phase shift dictates the  $\sin$  dependency of the photo-electron phase, such that the shift is zero in the absence of a potential.  $\eta_j(k)$  is the scattering phase function.

The factor  $\exp(-2\sigma_j^2 k^2)$  is a Debye-Waller factor that describes the loss of scattering coherence generated by structural disorder - be it either static, as in glassy materials, or dynamic, from thermal vibrations - where  $\sigma_j$ , is the variance in relative atomic emitter-scatterer distance. Such loss of coherence reduces the strength of any photo-electron interference pattern, washing out the fine-structure. The effects of disorder become more pronounced the shorter the De Broglie wavelength of the the photo-electron; hence the  $k$  dependence of the Debye-Waller factor, where  $k \sim 1/\lambda$ . Modelling disorder according to a Gaussian assumes a symmetric atomic pair potential function, such that disorder itself may be considered symmetric about some mean atomic position.

This factor is extremely important from the point of view of Thermal Differential EXAFS, since - because dynamic disorder is generally thermal in origin - it will vary as the temperature of the sample is changed, and so manifest itself in the differential fine-structure.

Work in describing Debye-Waller factors was conducted by Shmidt as far back as 1961 [84][85]. More recently, much work has been done to develop an *ab initio* description of the effects of structural disorder, which, significantly, must include multiple-scattering [65][66][11]. Unfortunately, a complete and entirely *ab initio* theory of the effects of structural disorder is still to be developed.

Progress has also been made in other areas. The plane-wave approximation of Sayers et al. was lifted by Schaich in 1973 for the single-scattering case [82], and developed to



include multiple-scattering in 1975 by both Lee & Pendry [41] and Ashley & Doniach [8]. These latter two papers did, however, rely on the assumption that multiple-scattering is weak enough to permit its description by only low order paths. It was Durham et al. [21] that provided a similar theory that included all orders of multiple-scattering; a theory that was later simplified by Pettifer et al. [62], Gurman et al. [25][24], and Rehr et al. [73], with the latter authors also removing the small atom approximation used by Sayers et al.

Indeed, work conducted by Rehr et al. led to the development of the FEFF code for XAFS calculations [71], a code that forms an important part of DiffEXAFS analysis. With these improvements to the theory of EXAFS, the modern fine-structure function may be written down as

$$\chi(k) = \sum_j A_j(k) e^{-2k^2 \sigma_j^2} \sin(s_j k + \phi_j(k)) \quad (2.11)$$

where  $A_j(k)$  is an amplitude function that contains, for instance, backscattering amplitudes; photo-electron decay effects, similar to  $\exp(-\gamma R_j)$  above; and  $S_0^2$ , which describes many-body effects due to relaxation in response to the creation of a core hole.  $\phi_j(k)$  is a phase function that describes a number of phase-shifts experienced by the photo-electron. These include the  $\delta_1'$  phase-shifts above and the phase-function incurred at each scattering event.

Since multiple-scattering is now considered, the coordination shell radius,  $R_j$ , is replaced with  $s_j$ , the total photo-electron scattering path length. For single-scattering,  $s_j$  is equivalent to  $2R_j$ . Likewise,  $\sigma_j^2$  is redefined as the variance of the half-path length.

Despite constant progress in the development of a fully-quantitative, *ab initio* theory of XAFS, numerous deficiencies still exist in the theory. One of the most notable of these is the muffin-tin approximation that has been adopted since the 1970s. Foulis et al. took the first steps to eliminating this approximation in 1990 by successfully performing a full-potential, non-muffin-tin calculation for the fine-structure of the hydrogen ion. They extended this result in 1995 [23] with a similar calculation for molecular chlorine. However, such calculations are still yet to be demonstrated for the general case in any of the XAFS analysis codes available today.

## 2.4 Differential EXAFS: A Probe to Small Atomic Displacements

Differential EXAFS (DiffEXAFS) is a novel technique for the study of small atomic strains, which was developed by Pettifer et al. over a period of years leading up to publication in May 2005 [64]. Taking a sample where the fundamental structure is known, the technique employs the subtle changes in EXAFS signals induced by the modulation of a given sample property to measure changes in photo-electron scattering path length, and thus deduce any atomic perturbations in the local area of the absorbing atom [79].

A DiffEXAFS spectrum is the difference between two conventional EXAFS spectra (designated + and -), taken with all sample properties kept constant, except for the *unit* modulation of some property of interest<sup>1</sup>. For thermal studies unit modulation would typically be 1K. This is very similar in principle to XMCD, except that instead of only studying magnetic effects in the near-edge region, DiffEXAFS examines the extended x-ray absorption structure for perturbations of the sample. Given that strains contributing to these signals are small, it is possible to express them in terms of a first order Taylor expansion of the x-ray fine-structure function (2.11) with respect to the modulated parameter.

$$\Delta\chi = \sum_j A_j(k) k e^{-2k^2\sigma_j^2} \cos(ks_j + \phi_j(k)) \Delta s_j \quad (2.12)$$

Strictly speaking,  $A_j(k)$  and  $\phi_j(k)$  are also path length,  $s_j$ , dependent, but changes in these parameters are negligible compared to  $\Delta s_j$ .

Given the fundamental structure of the sample is known beforehand, fitting this function to experimental data deals with a strictly limited number of parameters; positions of atoms are fixed, and thus shell radii and coordination numbers. Consequently,  $A_j(k)$  and  $\phi_j(k)$  may be determined from first principles, and  $\sigma_j^2$  from a conventional EXAFS fit, leaving only the perturbation  $\Delta s_j$  to be determined from the DiffEXAFS. The whole analysis procedure, which is described in Chapter 4, can therefore be thought of as

---

<sup>1</sup>If non-unit modulation is employed, the spectrum is referred to as a Difference EXAFS spectrum, which must be normalised to unit modulation in order to extract information on structural changes.

*pseudo-ab initio*.

In principle, a DiffEXAFS spectrum may be constructed from the modulation of any chosen bulk property of a given sample, the difference between the two XAS spectra then revealing any structural changes in the sample material induced as a result of the change in bulk property. Since the structure present in a DiffEXAFS spectrum is intimately linked to atomic strains, a different signal can be expected from the same absorption edge depending on which property is modulated, and how that affects the sample structure.

In this thesis, temperature is the chosen property, and the effects of thermal expansion and thermally induced phase transitions are studied by cycling a sample's temperature by a few Kelvin between two otherwise identical absorption measurements.

It is important to emphasise at this stage a subtle distinction in DiffEXAFS nomenclature. A *Difference* EXAFS measurement is concerned simply with the difference between two given EXAFS spectra, whereas a *Differential* EXAFS measurement goes further, implying *unit modulation* of the chosen sample property. In this sense, a differential spectrum is a normalised difference spectrum. Although the abbreviation DiffEXAFS will be used throughout this thesis, the terms *Difference* and *Differential* will be used explicitly in any discussion where confusion may arise.

## 2.5 Thermal Differential EXAFS

Thermal Differential EXAFS describes those DiffEXAFS measurements taken with modulation of a sample's temperature. In this particular situation, the physics of DiffEXAFS is more complicated than that described by equation (2.12) since it is not just the mean scattering path length  $s_j$  that is dependent on sample temperature, but also the variance in scattering path length  $\sigma_j^2$ .

It is also important, therefore, to consider the form of the atomic pair-correlation function. In order for thermal expansion, or any other such thermally induced strain, to exist within a material, the pair-correlation function must be asymmetric. This in turn requires anharmonicity to be considered, and thus the (harmonic) Gaussian Debye-Waller

factor must be replaced. Commonly, this results in the fine-structure function being manipulated in terms of a cumulant expansion [72]. However, for DiffEXAFS, temperature changes are very small, and so anharmonic contributions to the fine-structure from any source other than thermal expansion are negligible. In this case it is possible to adopt the quasi-harmonic approximation of Leibfried & Ludwig [42], whereby the Gaussian form of the pair-correlation function is retained, but the centroid of that Gaussian displaced to model thermal expansion.

Under these conditions, the Taylor expansion of (2.11) becomes

$$\Delta\chi = \sum_j A_j(k) e^{-2k^2\sigma_j^2} \left( k \cos(k s_j + \phi_j(k)) \Delta s_j - 2k^2 \sin(k s_j + \phi_j(k)) \Delta\sigma_j^2 \right) \quad (2.13)$$

The Thermal Differential Fine-structure Function therefore contains two signals superimposed upon one another. The first, as in (2.12) is characterised by  $\Delta s_j$ . In the absence of any non-linear phenomena such as phase-transitions, this just arises from thermal expansion in the sample. The second, new term is characterised by  $\Delta\sigma_j^2$ , and so describes changes to thermal disorder.

The difference between this function and that of (2.12) can be seen in Figure 2.1, where a typical Joule magnetostriction DiffEXAFS signal is plotted for a 90° rotation in sample magnetisation, and a typical Thermal DiffEXAFS signal plotted for a 1K change in sample temperature; both at the Fe-K edge.

Examining (2.13), it is clear first and foremost that the disorder term retains the  $\sin$  phase dependency of the original fine-structure function (2.11), whereas the expansion term has changed to a  $\cos$  dependency. Contributions from thermal disorder are therefore in phase with the conventional EXAFS, whilst contributions from thermal expansion are in quadrature. This difference is key in providing the ability to resolve one term from the other in an experimental DiffEXAFS spectrum.

It can also be seen that both terms scale with photoelectron wavevector; expansion by  $k^1$  and disorder by  $k^2$ . This indicates that both terms are amplified relative to the conventional EXAFS as x-ray energy increases, resulting in more high-k oscillations being present in the DiffEXAFS compared to the conventional fine-structure. This in

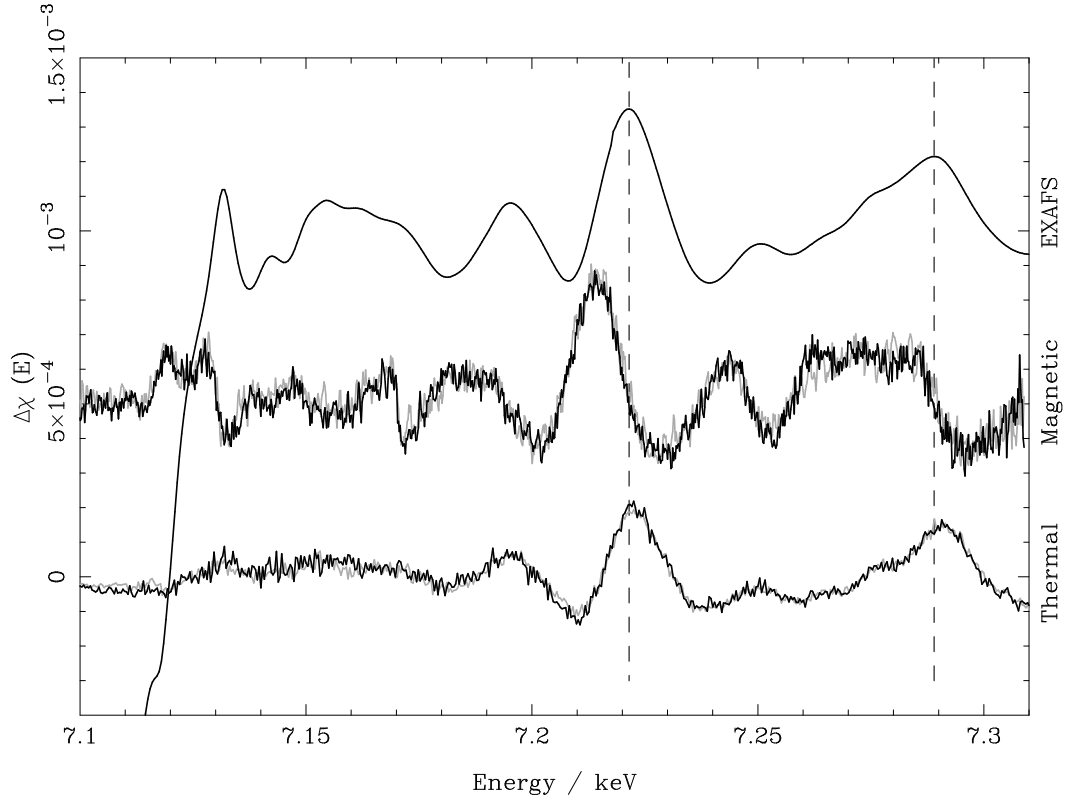


Figure 2.1: DiffEXAFS signals at the Fe-K edge for magnetisation modulation of FeCo (provided by R.F. Pettifer) and thermal modulation of Fe foil. EXAFS for the pure Fe sample is shown, which is virtually identical to the FeCo structure. As can be seen, the modulation of different sample properties results in very different signals. The magnetisation signal only contains one component through magnetostrictive strain, whereas the thermal signal contains components from expansion of the crystal lattice and changes to atomic vibrational amplitudes.

turn allows DiffEXAFS data to be acquired further from the edge, with the structure not being washed-out till  $k$  is typically around  $15$  to  $20 \text{ \AA}^{-1}$ .

Now, inserting the thermal expansion coefficient for each path  $\alpha_j$ , and considering the possibility of non-unit temperature modulation, (2.13) becomes

$$\begin{aligned} \frac{\Delta\chi}{\Delta T} = \sum_j A_j(k) & \left( ks_j \cos(ks_j + \phi_j(k)) \alpha_j \right. \\ & \left. - 2k^2 \sin(ks_j + \phi_j(k)) \frac{\Delta\sigma_j^2}{\Delta T} \right) \end{aligned} \quad (2.14)$$

Each coefficient is assumed to be a constant, independent of temperature. This is not

true for large changes in temperature, but is acceptable when working with DiffEXAFS, since temperature modulation is only of the order of few Kelvin<sup>2</sup>. This expression will also hold when other strains, not related to thermal expansion, must be considered, so long as the components of  $\alpha_j$  include the contributions from all source of thermal strain. Each  $\alpha_j$  may be analysed in the context of the geometry of path  $j$  in order to obtain the second-rank thermal expansion tensor  $\alpha_{mn}$ . Depending on the type of crystal under study,  $\alpha_{mn}$  may contain up to nine independent parameters, describing atomic strains along different crystallographic directions. Each coefficient must be determined by the analysis of a scattering path with geometry sensitive to strains along the same direction described by the coefficient. Some paths, particularly multiple scattering paths, may be sensitive to strains described by two or more coefficients.

However, the point group crystal symmetry of a chosen sample material can be exploited through von Neumann's Principle to reduce the number of independent coefficients [53]. For instance, with crystals of cubic symmetry, the tensor is isotropic; all off-diagonal elements are zero, and all diagonal elements equal. This reduces the number of independent coefficients to one and  $\alpha_{mn}$  to  $\alpha$ .

Note also, that in inserting  $\alpha_j$  into (2.13) an additional coefficient,  $s_j$ , is needed. This reveals the last key property of the differential fine-structure function: larger scattering paths are relatively amplified compared to shorter ones. High-order paths therefore hold relatively greater significance than they would do in conventional EXAFS. Critically, the thermal disorder term does not scale with  $s_j$ . As a result, when  $s_j$  is large, the thermal expansion component of the differential fine-structure becomes a greater fraction of the total observed signal than when it is small. This allows expansion to be more easily detected in high-order scattering paths.

---

<sup>2</sup>Even so, it is still reasonable to expect a different values to be obtained when the absolute temperature, about which the DiffEXAFS measurements are made, is significantly altered.

## Chapter 3

# Apparatus for Thermal Differential EXAFS

### 3.1 Introduction

Since DiffEXAFS is an entirely new experimental technique, no standard apparatus may be purchased commercially to allow such data to be taken. Pettifer et al. identified ID24 of the ESRF as a suitable candidate beamline for DiffEXAFS experiments, but had to design and construct their own magnetisation modulation apparatus prior to making their magnetostriction measurements. In addition, the beamline had to be optimised for DiffEXAFS applications, and control code written for DiffEXAFS data acquisition.

The approach to Thermal DiffEXAFS has been no different. To thermally modulate a given sample material, novel apparatus had to be designed and constructed. Indeed, the requirements for such apparatus had to be examined in detail prior to its design phase, and after construction, tests performed to verify the finished product met these requirements. Further modifications and upgrades were also needed to ID24 to allow integration of this apparatus into the beamline control systems.

This chapter presents each step of that process in detail - from experimental requirements to evaluation of the final product. In addition, ID24, and its complementary beamline BM29, are described in detail to justify their selection for DiffEXAFS, and associated experiments.

## 3.2 Beamline Requirements for Detection and Measurement of Differential EXAFS

Given that DiffEXAFS signals from structurally perturbative phenomena, such as thermal expansion, are generated by atomic strains of the order of  $10^{-5}$  per unit parameter modulation (1K for thermal studies), several demanding requirements must be met in order to successfully detect them. These can be split into beamline requirements, covering the actual measurement needs, and sample environment requirements, detailing what must be provided by the modulation apparatus.

In terms of beamline requirements, the first problem is that of statistical noise. In order to detect strains of the order of  $10^{-5}$ , the fractional statistical noise present in a measured absorption spectrum must be of the order of  $10^{-5}$  or less. This demands the use of a high intensity 3rd generation source, where fluxes can be as much as  $10^{13}$  photons per second per eV. Under optimal conditions, such a source should be capable of reducing fractional statistical noise in absorption to the order of  $10^{-6}$  in a few hours. In addition, the chosen source must be coupled to a beamline armed with a sensitive detector, capable of accepting and measuring the incoming flux.

The next problem is that of beam energy stability. If the energy of photons passing through the sample changes between the + and - state measurements, spurious signals can be generated from the resulting shift in fine-structure. A simple calculation shows that an edge energy shift of as little as 1meV between measurements at the Fe-K edge can generate a nominal difference of about  $2 \times 10^{-5}$  across the spectrum, peaking to around  $10^{-4}$  at the edge. Such a signal would be of comparable amplitude to the true DiffEXAFS signal from an atomic displacement of around 2 fm, and thus would corrupt it. Assuming the noise limit on a DiffEXAFS measurement is  $10^{-5}$ , limiting displacement resolution to no less than 1 fm, the edge energy would need to be stable to at least 0.1meV for any drift signal be indistinguishable from the noise.

Unfortunately, unless both measurements are taken simultaneously, or at least in a tiny amount of time, temporal changes in the properties of various beamline components could easily generate energy drifts of the order of several meV. For example, given



the thermal expansion coefficient of silicon at room temperature is  $2.6 \times 10^{-6} \text{K}^{-1}$ , a temperature drift of just 0.4K in a Si(111) polychromator crystal would generate a shift in diffracted energy of 5.2meV when working at 10 keV; more than enough to destroy a DiffEXAFS signal.

Since it is not possible to measure the same part of the same sample in two different thermal states at the same time, the best approach is to heat and cool the sample as quickly as possible, allowing two measurements to be made under different conditions in as short a space of time as possible. Empirically, it has been found that the best DiffEXAFS data is obtained when the delay between measurements is less than a second, but acceptable data can be acquired with up to a three or four second delay depending on the circumstances. Experiments with delays in excess of five seconds produce poor results.

The third and final major problem is that of spatial beam stability. Unless the sample material under study is perfectly homogeneous, subtle changes in thickness could generate a difference in x-ray absorption if the beam were to move between + and - measurements. Taking the standard absorption relation  $I = I_0 e^{-\mu z}$  and the definition of  $\chi$  in (2.6), it can be shown that, for point illumination of the sample

$$\frac{\Delta\mu}{\mu} = -\frac{\Delta z}{z} \quad \frac{\Delta\chi}{\chi} = \frac{\mu}{\mu - \mu_0} \frac{\Delta\mu}{\mu} \quad (3.1)$$

thus the following condition must hold

$$\frac{\Delta\chi}{\chi} = \frac{\mu}{\mu - \mu_0} \frac{\Delta z_p}{z_p} \leq 10^{-5} \quad (3.2)$$

where  $\Delta z_p$  describes the variation in sample homogeneity. If  $\Delta z_p$  is assumed to be a well-behaved, integrable function, it is possible perform a Taylor series expansion and evaluate the partial derivatives of sample thickness with respect to beam movements. Given  $\mu/(\mu - \mu_0)$  is about 10 for a monoatomic sample, a fractional change in sample thickness of more than  $10^{-6}$ , caused by some movement of the point of illumination, would generate a signal detectable in a DiffEXAFS measurement. Since typical sample thicknesses are of the order of ten to several tens of microns, this would make the signal sensitive to changes in thickness of the order of  $0.1\text{\AA}$ , or effectively a single atomic layer!

Fortunately, the finite size of a real beam focal spot helps, since the larger the spot, the smaller the fractional change in illumination of the sample as the beam moves. Only the small parts at the edge of the spot will contribute to any apparent change in sample thickness. A rigorous theoretical analysis of such a problem is not trivial and is beyond the scope of this thesis. However, it is clear that one of three criteria must be met for DiffEXAFS measurements. Either the sample homogeneity must be extremely high, allowing the beam to drift somewhat between measurements, or the beam stability be extremely high to compensate for a certain degree of sample inhomogeneity; alternatively, the beam spot size must be sufficiently large that any drift in position represents only a tiny fractional change in the part of the sample illuminated. Empirical experience has revealed that both powder specimens and polycrystalline foils with grain sizes of less than about  $3\mu\text{m}$  yield good DiffEXAFS data, providing the beam is no less than about  $10\mu\text{m} \times 10\mu\text{m}$  in size and drifts by no more than about 10nm in either dimension between measurements.

Perversely enough though, a tiny spot size can actually be better than a larger one despite the problems shown with point illumination in (3.2). So long as the spatial stability condition is not violated, reducing the spot size, and so reducing the area of sample material illuminated, allows tiny samples to be used for DiffEXAFS measurements. In the case of Thermal DiffEXAFS, such tiny samples have a low thermal mass, and so change temperature more quickly for a given heat input. Thus a suitable trade-off should be established between the two effects.

Indeed, this desire to minimise the time between measurements should be examined in more detail since it goes against the idea of increasing the exposure time of an acquisition to minimise statistical noise, suggesting the best approach for minimisation of such noise is not to expose each spectrum for a long time, but to average signals over many measurements. In the case of DiffEXAFS, this means averaging the signal over many pairs of  $+/-$  measurements as will be explained in section 3.4.1.

However, a more fundamental issue must first be resolved. When we talk of 'taking a spectrum', we are referring to the acquisition of an *entire* EXAFS spectrum, typically covering an energy range of several hundred eV. On a standard step-scanning XAS

beamline, integrating for 100ms, say, at each energy point, such an acquisition will take about a minute plus the time needed to physically move the monochromator crystal from one energy to the next; so several minutes in total. Even if the integration time is reduced to 1ms at the expense of statistical noise, the time required to scan from one energy to another imposes a lower limit on the total acquisition time of the order of a minute or more. So evidently, it is not possible to perform DiffEXAFS measurements by step-scanning an entire spectrum, changing the state of the sample, and step-scanning another whole spectrum.

The obvious solution would be to measure both states of the sample material at one energy to obtain the difference with minimal beam drift, and then scan to the next energy, taking two more measurements, and so on. This approach was tried by Pettifer et al. on BM29 of the ESRF prior to their published magnetostrictive DiffEXAFS measurements [64], but failed to work. Whilst taking the difference at single energies minimises beam drift for each given data point, the spectrum as a whole is still time-dependent. Thus, whilst each single point contains the correct DiffEXAFS based on the beam and sample properties at the time of measurement, the spectrum from one point to the next is a composite of DiffEXAFS signals from slightly different beam conditions; the structure at one point may be either translated with respect to the adjacent points due to an energy drift, or of the incorrect amplitude, due to differing sample thicknesses resulting from spatial drift.

The solution therefore, is to illuminate the sample material with polychromatic radiation, allowing the whole spectrum to be acquired in a single snapshot. This can be achieved by using a Dispersive XAS (D-XAS) geometry. With polychromatic illumination, the spectrum becomes time-independent from one energy to the next, so two complete EXAFS spectra can be taken under differing sample conditions in less than a second or so, as required. This does however come at the expense of beam intensity. Whereas on a step-scanning beamline the entire beam flux is effectively from a single x-ray energy, on a D-XAS beamline, the available flux is split over several hundred eV, making each wavelength component relatively dimmer. Thus, to be of any use, the D-XAS beamline must be mounted on a high-intensity 3rd generation synchrotron source, such as a

wiggler, which offers an intensity increase of a couple of orders of magnitude over a standard bending magnet source, or an undulator, which offers a further couple of orders of magnitude increase in intensity. At present, there is only one D-XAS beamline in the world that utilises a 3rd generation undulator source: ID24 of the ESRF. Therefore, this was the beamline selected for DiffEXAFS measurements.

### 3.3 X-ray Absorption Spectroscopy Beamline BM29 of the ESRF

Before examining ID24, it is helpful to consider the operation of a conventional step-scanning XAS beamline mounted on a bending magnet source, such as BM29 of the ESRF. This beamline is also important since it provides conventional EXAFS spectra that are used to calibrate those from ID24, and hence is used to put DiffEXAFS spectra on a known energy scale [75]. This calibration process is discussed in section 4.2.

Bending magnet sources generate synchrotron radiation by accelerating electrons, travelling at relativistic speeds, in a circular arc. At such speeds, the electromagnetic emission predicted by classical electrodynamics is subject to a Lorentz transformation. When the bending magnet is viewed in the plane of the storage ring, the familiar sinusoidal characteristic of electron dipole radiation is severely deformed, with the emitted intensity being collimated into a narrow cone along the instantaneous direction of electron motion [36]; the angular divergence of which is inversely proportional to the electron energy [39]. This radiation is also strongly Doppler shifted - from the shortwave region at non-relativistic speeds, to hard x-rays as  $v$  tends to the speed of light. The energy of an electron at speed  $v$  is given by [5]

$$E_e = \frac{mc^2}{\sqrt{1 - \left(\frac{v}{c}\right)^2}} \quad (3.3)$$

At relativistic speeds, it is useful to express this in terms of the electron rest mass energy  $\gamma \equiv E_e/mc^2$ , and the electron velocity in units of the velocity of light  $\beta_e = v/c$  so that (3.3) becomes

$$\gamma \equiv \frac{1}{\sqrt{1 - \beta_e^2}} \quad (3.4)$$

Also in these units, the characteristic opening angle for synchrotron radiation, that is the root mean square angle of emission, is [39]

$$\langle \psi^2 \rangle^{1/2} = \frac{1}{\gamma} \quad (3.5)$$

At the ESRF, the energy of electrons in the storage ring is  $E_e = 6.03$  GeV, so the opening angle of radiation is 0.08 mrad.

The radius of curvature of the electron path through a bending magnet is determined by its magnetic field strength - 0.8 T for ESRF bending magnets, including BM29 - and the Lorentz force, such that, given  $v \simeq c$

$$R = \frac{eB}{\gamma mc} = 25m \text{ on BM29} \quad (3.6)$$

One final, important parameter to consider is the beam flux. This is derived from the power radiated over the area of the beamline aperture, by dividing by the photon energy at a given wavelength,  $E = hc/\lambda$ . At BM29's characteristic energy,  $E = 3hc\gamma^3/4\pi R = 19.2\text{keV}$ , the peak flux is  $3.5 \times 10^{11}$  photons  $\text{s}^{-1}(0.1\% \text{ BW})^{-1}$  in a bandwidth of 0.1% by convention. However, it is more useful to obtain the flux per eV. On BM29, this corresponds to a bandwidth of 0.005%, giving a peak flux at 19.2keV of  $1.75 \times 10^{10}$  photons  $\text{s}^{-1}\text{eV}^{-1}$ . A more rigorous analysis of beam characteristics is given for instance in [39] or [5].

Beyond the front-end aperture, the optical components of BM29 are very simple. An ESRF standard primary slits package is used to define the white beam profile, typically to 10 to 20mm horizontally and 0.2 to 1.0mm vertically [99] before the beam enters the monochromator. The vertical gap of these slits is important in that it largely defines the energy resolution of the beamline for a given set of monochromator crystals.

The monochromator itself works on the Bragg diffraction of two single crystals of silicon, typically Si(111) or Si(311), arranged in the parallel configuration as shown in Figure 3.1. These crystals are cooled to about 125 K, where the thermal expansion coefficient of silicon is approximately zero, to minimise beam energy drifts due to changes in specific heat load in the monochromator. The use of a double crystal design such as this allows beam harmonics to be rejected by changing the relative angle between the two crystals,

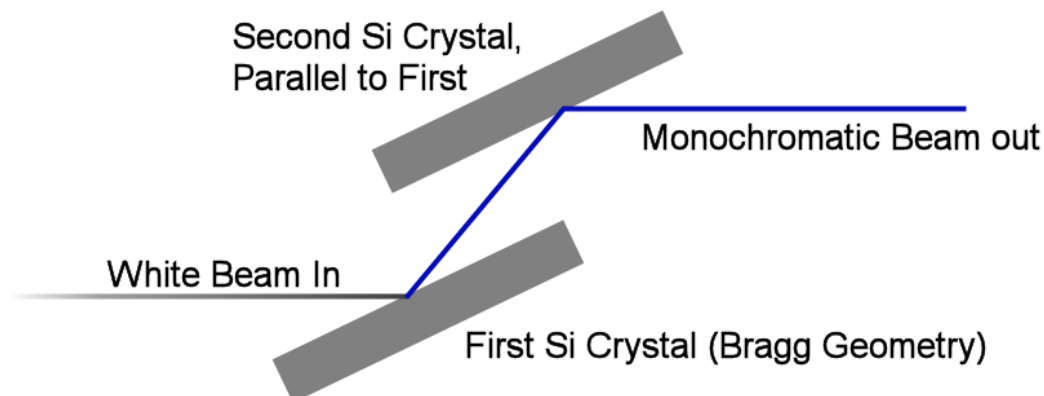


Figure 3.1: A schematic representation of a twin crystal, Bragg reflecting monochromator, arranged in the parallel configuration.

reducing the degree of parallelism between them [20]. On BM29, this detuning is performed in units of the FWHM of the diffraction rocking curve, measured by scanning the beam intensity as a function of the crystal parallelism [99]. Beyond the exit port of the monochromator, a secondary set of slits define the profile of the monochromatic beam.

BM29 offers several types of detector, but those most commonly used - and which are used when acquiring spectra to calibrate DiffEXAFS data - are ionisation chambers [60].

### 3.4 Dispersive EXAFS Beamline ID24 of the ESRF

All DiffEXAFS experiments conducted to date have been carried out on ID24, the D-XAS beamline of the ESRF [27] [55], which is shown schematically in figure 3.2.

Unlike a standard step-scanning XAS beamline, a dispersive beamline produces polychromatic illumination at the sample, which in turn allows an entire spectrum covering several hundred electron-volts to be acquired simultaneously. This feat is achieved by replacing common, flat monochromator crystals with a single bent crystal: the polychromator. When this is illuminated by a spatially dispersed x-ray beam, Bragg's Law dictates that it produces a continuous range of diffracted wavelengths, as the angle of incidence of impinging photons changes in relation to the diffracting plane's local normal.

This result, shown in figure 3.3, means that the equivalent energy of diffracted photons changes continuously along the length of the polychromator, and holds regardless of whether the polychromator is used in Bragg or Laue diffraction geometries.

The curvature of the crystal also causes each component of the diffracted beam to be focused to a point, at which the sample is placed. Beyond the focal point, the beam diverges and the intensity of each component measured with a position sensitive detector (PSD) - commonly a CCD array. Each pixel in the array only detects a small range of x-ray wavelengths, and so the array as a whole effectively makes  $n$  simultaneous measurements at different x-ray energies, where  $n$  is the number of pixels.

ID24 uses two types of polychromator, both made from a single crystal of silicon. The first is cut and polished with Si(111) or Si(311) planes parallel to the surface and is used for Bragg diffraction at low energies - up to 15 keV. This limit is imposed since higher energy photons penetrate deeply into the crystal, causing significant degradation in energy resolution. The crystal is elliptically bent by a four point bender, with spherical aberrations in the focal spot minimised by cutting the crystal into a specially designed profile that naturally deforms elliptically when bent at its ends. The second type of crystal is cut and polished with Si(111) planes perpendicular to the surface, and is used for Laue diffraction beyond 12 keV and up to about 28 keV. This crystal is bent so as to have a cylindrical profile.

In both cases, the degree of bending is controlled dynamically. This allows both the range of diffracted x-ray wavelengths and the distance to the focused image to be altered. The focal point may lie between 0.8 and 2.0 m from the crystal.

Commonly, D-XAS beamlines are mounted on bending magnet sources, which naturally offer the large spatial divergence (in the horizontal plane) required to generate a wavelength dispersive beam. ID24 however, is unique in that it is mounted on an undulator source.

Unlike bending magnets, undulators and wigglers are installed on straight sections of a storage ring and consist of an array of magnets with alternating field polarity along the axial direction, as shown in Figure 3.4. These magnets cause passing electrons to execute oscillations in a series of circular arcs in the horizontal plane. Assuming these

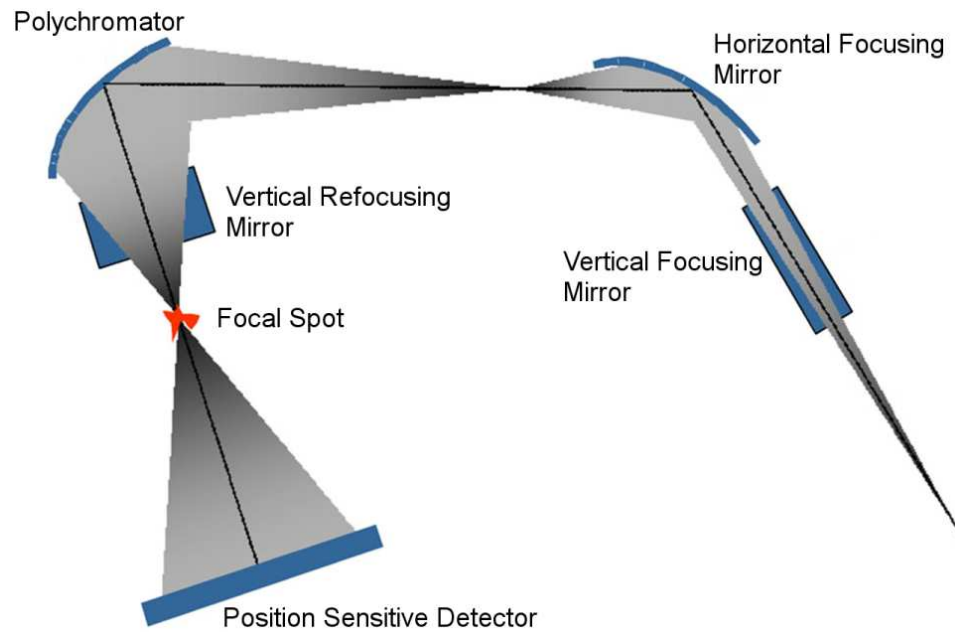


Figure 3.2: A schematic representation of the optical components of ID24. Reproduced from [55] with modifications.

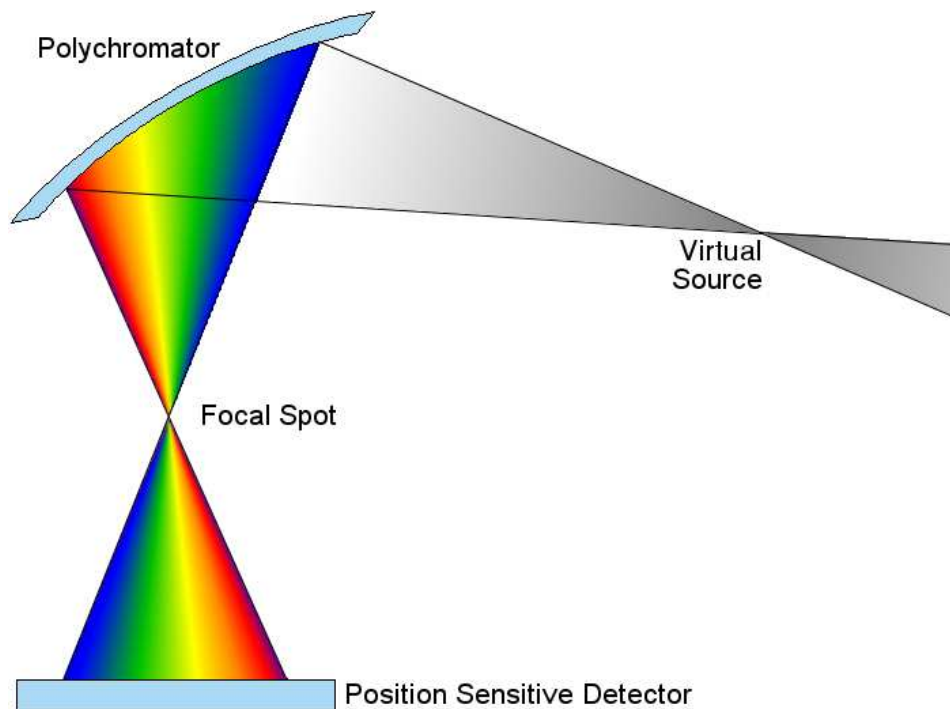


Figure 3.3: A bent crystal polychromator diffracts x-rays of a continuous range of wavelengths as the angle of incidence of impinging radiation changes along its length. The result is polychromatic illumination at the focal point rather than monochromatic as would be obtained from a flat crystal.



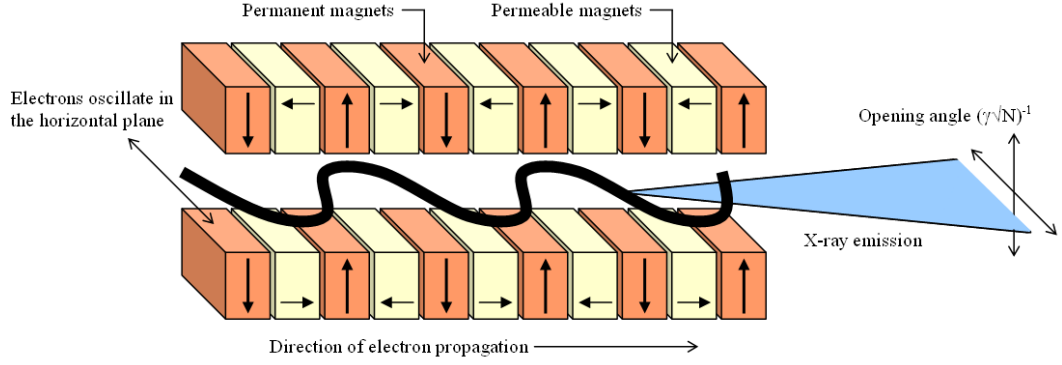


Figure 3.4: A schematic representation of an undulator/wiggler insertion device. Electrons perform small amplitude oscillations, causing the emission of radiation along the axial direction.

oscillations can be approximated by a sinusoid, the device may be characterised by the dimensionless field strength parameter [5]

$$K = \frac{eB_0\lambda_u}{2\pi mc} = 0.934B_0(T)\lambda_u(cm) \quad (3.7)$$

which in turn gives the maximum angular deviation of the electron [38]

$$\delta = \frac{K}{\gamma} \quad (3.8)$$

where  $\lambda_u$  is the undulator spatial period,  $B_0$  is the peak undulator magnetic field strength, and  $e$ ,  $m$ , and  $c$  are the electron charge and mass, and the speed of light respectively.

$K$  is much greater than one for a wiggler, and of the order of one or less for an undulator. This difference has a significant effect on the radiation output from the device. As shown in equation (3.5), the characteristic opening angle of radiation produced by an electron travelling in a circular arc, is of the order of  $\gamma^{-1}$ . Therefore, from (3.8) it can be seen that in an undulator, the cone of radiation from each electron oscillation is at least partially superimposed upon the radiation cones from previous oscillations, causing x-rays of wavelength  $\lambda_1$  and its harmonics, to add coherently from one oscillation to the next. As a result of this coherence, undulator radiation is as much as several orders of magnitude brighter than wiggler radiation, since the total intensity is proportional to

<b>ID24 Undulator Properties</b>	
K value at minimum gap (20 mm)	1.66
Magnet period	42 mm
Number of periods	42
Max. critical energy	8.9 keV
Min. energy of the fundamental	4.4 keV
Max. magnetic field	0.423 T
Source size ( $x \times z$ RMS)	$402 \times 8.4 \mu\text{m}^2$
Source divergence ( $x' \times z'$ RMS)	$12.0 \times 6.2 \mu\text{rad}^2$
Peak brilliance at min. gap and 4.5 keV	$2.6 \times 10^{19} \text{ ph s}^{-1}\text{mrad}^{-2}\text{mm}^{-2}0.1\% \text{ BW}^{-1}0.2\text{\AA}^{-1}$
Total power emitted	1.34 kW
Power density at 30 m	$50.3 \text{ Wmm}^{-2}$ (in central cone at $0.2 \text{\AA}$ )

Table 3.1: Information pertaining to the undulator source mounted on ID24. These data have been compiled from references [27] and [55].

the squared sum of amplitudes of radiated waves rather than just the sum of radiated wave intensities. Likewise, the oscillatory nature of a wiggler produces a beam as much as several orders of magnitude brighter than a bending magnet source.  $\lambda_1$  is defined by the undulator period and the electron speed,  $\beta_e = v/c$ , as [5]

$$\lambda_1(\theta) = \lambda_u \left( \frac{S}{\beta_e} - \cos \theta \right) \quad (3.9)$$

Given  $S$ , the electron path length over one undulator period, is  $S = 1 + \gamma^{-2}K^2/4$

$$\lambda_1(\theta) = \frac{\lambda_u}{2\gamma^2} \left( 1 + \frac{K^2}{2} + (\gamma\theta)^2 \right) \quad (3.10)$$

where  $\theta$  is the angle between the undulator axis and the direction of observation. This equation implies that an undulator source is quasi-monochromatic, with  $\lambda_1$  dominating the emission spectrum. The symmetry of harmonic emissions also results in the suppression of even harmonics, such that mainly odd harmonics are transmitted.

Thus, whilst the choice of an undulator source for ID24 was unconventional, both these facts provide clear advantages over other D-XAS beamlines [55]. Additionally, undulators offer a lower vertical beam divergence than bending magnets, aiding the production of a tightly focused spot at the sample; and, by altering the undulator gap and taper, and the radius of curvature of the polychromator crystal, it is possible to match the emission

bandwidth of the undulator to the acceptance of the polychromator, which results in a reduction of specific heat load on the optics.

These all make the beamline ideal for time-resolved analyses of transient chemical reactions, and for examination of tiny samples mounted inside high-pressure cells, where the beam must be both highly focused and capable of penetrating the small cell windows.

For DiffEXAFS however, these beam characteristics are advantageous for different reasons. The lower vertical divergence and resulting smaller focal spot size is ideal since it allows the use of smaller samples, which respond more quickly to small changes in environmental parameters such as temperature. The reduced specific heat load on the optics is good since it increases the stability of beamline components, minimising unwanted drifts between difference measurements. And most importantly of all, the increased flux is critical in obtaining sufficiently low statistical noise in a DiffEXAFS spectrum to allow signals from phenomena such as thermal expansion or magnetostriction to be detected.

These advantages come at a price though. The horizontal divergence of bending magnet sources are typically of the order of several milliradians. Undulator sources however, by their very nature, produce tightly collimated beams, and as such the horizontal divergence of the ID24 source is only  $12\mu\text{rad}$  RMS. This requires more complex coupling optics to be installed between the undulator and polychromator in order to generate the required, divergent beam.

ID24 employs two mirrors of Kirkpatrick-Baez (KB) type. The first, mounted 30m from the source, focuses the beam vertically and performs harmonic rejection. The second, orientated at  $90^\circ$  with respect to the first at 32.5m from the source, is elliptically bent to focus the beam horizontally. The focal point, 1.65m from the mirror, then serves as the effective source for the spectrometer, with a horizontal divergence of 1mrad. Consequently, the polychromator, which is mounted 64m from the source, is illuminated over a length of about 40mm. Additional information on the mirrors is given in tables 3.2 and 3.3.

Recently, an additional mirror has been added to the beamline at 65m from the source, between the polychromator and sample position [54]. This provides further harmonic rejection and refocuses the beam vertically. Combined with recent improvements to the

<b>Properties of Vertically Focusing Mirror (First KB Mirror)</b>	
Distance from source	30 m
Distance to image	41 m
Max. reflected photon energy	28 keV
Max. glancing angle	3.0 mrad
Slope error	1.2 $\mu$ rad FWHM
De-magnification	1.367
Shape	cylindrical
Coating	Bare (Si) / Rh / Pt
Average radius of curvature	12 km

Table 3.2: Information pertaining to the first coupling mirror mounted on ID24. These data have been compiled from references [27] and [55].

<b>Properties of Horizontally Focusing Mirror (Second KB Mirror)</b>	
Distance from source	32.5 m
Distance to image	1.65 m
Max. reflected photon energy	28 keV
Max. glancing angle	3.0 mrad
Slope error	3.3 $\mu$ rad FWHM
De-magnification	0.051
Shape	elliptical
Coating	Bare (Si) / Rh / Pt
Average radius of curvature	980 m

Table 3.3: Information pertaining to the second coupling mirror mounted on ID24. These data have been compiled from references [27] and [55].

polychromator and horizontally focusing KB mirror, the size of the focal spot at the sample position is now just  $(3.8 \times 5.1)\mu\text{m}$  [55].

Beyond the focal spot lies a position sensitive CCD matrix containing 1152 lines of 1242 pixels, coupled to the beam via a phosphor fluorescence screen and a 2x magnifying lens. Only 64 lines (or 1 stripe) of the CCD are actually exposed. The remaining 17 stripes are covered and used as parallel transfer buffers, which allows rapid acquisition of 18 spectra before the data must be read out. Charge from each exposed line can be transferred to a buffer line in about  $1.5\mu\text{s}$ , so a full stripe transfer takes about  $100\mu\text{s}$ , thus defining the time resolution of the detector. Once the CCD is full, the charge from each line in a stripe is binned in a single data register, and then read out through a serial transfer line. This effectively averages the vertical beam intensity, improving the signal-to-noise ratio. Whilst this comes at the expense of spatial resolution, the vertical profile of the beam is not important. Serial transfer of the readout register takes 12.2ms, so the entire CCD read out time is about 220ms.

The spatial resolution of the detector in the horizontal plane is a function of the CCD pixel pitch,  $22.5\mu\text{m}$ , and the point spread function of the phosphor screen,  $60\mu\text{m}$ . Given also that there is a 2x magnifying lens between the two, a beam of collimated light from a point source will appear to be  $30\mu\text{m}$  in diameter at the CCD. This will impinge on at least two CCD pixels, so it is the screen that limits the spatial resolution of the detector, and hence wavelength resolution of the spatially dispersed beam.

### 3.4.1 Extracting DiffEXAFS signals from measurements on ID24

DiffEXAFS signals are extracted from a sequence of XAS measurements in a fashion analogous to that described by Mathon et al. for XMCD measurements [47]; with DiffEXAFS dichroism being essentially the same as magnetic circular dichroism from a practical experimental standpoint.

Given that the Thermal DiffEXAFS signal is the difference between two XAS spectra at varying temperatures, it may be expressed as

$$\frac{\Delta\chi(E)}{\Delta T} = \frac{\mu^+ - \mu^-}{T^+ - T^-} = \frac{1}{\Delta T} \left( \ln \frac{I_0^+}{I_1^+} - \ln \frac{I_0^-}{I_1^-} \right) \quad (3.11)$$

<b>Properties of Detector</b>	
CCD-type	Princeton TE-CCD-1242-E-1-UV
Dimensions	1242 × 1152 pixels (64 lines unmasked)
Pixel size	22.5μm × 22.5μm
Dynamic range	16-bits at 100 kHz, 14-bits at 1MHz
Parallel transfer time	about 1.5μs per line
Serial readout time	about 12.2ms per stripe
Time resolution	100μs
Phosphors	P20 ((Zn, Cd)S:Ag) P43 (Gd <sub>2</sub> O <sub>2</sub> S:Tb) P40 (Y <sub>3</sub> Al <sub>5</sub> O <sub>12</sub> :Ce)
Point spread of screen	60μm

Table 3.4: Information pertaining to the CCD detector on ID24. These data have been compiled from references [31] and [100].

where  $\mu^+$  and  $\mu^-$  are the x-ray absorption coefficients measured at  $T^+$  and  $T^-$  respectively. Unfortunately, one current problem with wavelength-dispersive XAS, used for DiffEXAFS experiments, is the fact that it is not yet possible to make simultaneous measurements of the incident and transmitted x-ray intensities. With only one detector at the end of the beamline, it is necessary to move any sample out of the beam in order to measure  $I_0$ , and thus measurements at  $I_0$  and  $I_1$  are separated by several seconds. It would be convenient to assume that  $I_0^+$  and  $I_0^-$  are identical over a short space of time such that the DiffEXAFS signal becomes a function of the two transmitted intensities only, but in reality this is not correct. X-ray intensity decreases over time as electron beam current in the storage ring decays. However, this effect may be accounted for by making XAS transmission measurements in the following sequence

$$I^{0+}, I^{1-}, I^{2+}, I^{3-}, \dots, I^{2n-2+}, I^{2n-1-}, I^{2n+} \quad (3.12)$$

and then calculating the DiffEXAFS signal from the following algorithm.

$$\frac{\partial \chi(E)}{\partial T} = \frac{1}{2n} \ln \left( \frac{I^{0+} (I^{2+})^2 \dots (I^{2n-2+})^2 I^{2n+}}{(I^{1-})^2 (I^{3-})^2 \dots (I^{2n-1-})^2} \right) \quad (3.13)$$

The signal is then the product of transmitted intensities only and thus any linear and exponential drifts in the incident beam intensity are suppressed. An additional advantage of this scheme is that the DiffEXAFS signal may be composed of a large number

of dichroic measurements taken over time, which are effectively averaged in (3.13), suppressing inevitable statistical noise in the data. Experiments conducted to date indicate that letting  $n$  go to approximately 2000 results in a final fractional noise in the signal of about  $2 \times 10^{-5}$ , small enough to resolve atomic displacements on the femtometre scale.

### 3.5 Requirements for the Thermal Modulation Apparatus

EXAFS measurement requirements and the subsequent choice of beamline for DiffEXAFS are only part of the story. DiffEXAFS experiments also need the design and construction of sample modulation apparatus that is compatible with these requirements. It is already evident that such apparatus must be able to modify the state of a sample quickly such that two EXAFS spectra may be acquired under different conditions in the order of a second or less, but other properties are also needed.

As part of the measurement technique, it has been shown in section 3.2 that noise in a DiffEXAFS spectrum, be it from statistics or beam stability, is best minimised by averaging the difference signal over many pairs of  $+/-$  measurements. However, for such an averaging to be meaningful, the sample must be modulated reproducibly and held stable over the period of measurement. In the context of Thermal DiffEXAFS this implies being able to reliably switch the sample back and forth between two absolute temperatures. Failure to do so would cause the (un-normalised) difference signal to vary over each pair of acquisitions, such that the final spectrum is the average signal from structural changes over the mean temperature difference rather than the average signal from structural changes between two absolute temperatures. That is

$$\langle \Delta\chi \rangle = \frac{1}{N} \sum_N \frac{\partial}{\partial T} \chi(\Delta T_N) \quad (3.14)$$

is measured rather than

$$\langle \Delta\chi \rangle = \frac{1}{N} \sum_N \frac{\partial}{\partial T} \chi(T_N^+, T_N^-) \quad (3.15)$$

The difference between these two conditions is subtle and rests on the temperature dependence of the differential fine-structure. If the phenomenon inducing structural

changes can be considered temperature invariant, as is the case for thermal expansion over a small range of temperature, then the absolute values of  $T^+$  and  $T^-$  are unimportant; only the difference counts, and thus  $\partial\chi/\partial T = \partial\chi(\Delta T)/\partial T$  as is assumed in (2.14). Given also that the amplitude of the Thermal Difference EXAFS signal scales linearly with temperature, the average signal based on some mean temperature difference will be the same irrespective of the variance about the mean. In this case, so long as the apparatus records the sample temperature difference over each  $T^+$  and  $T^-$ , allowing the mean temperature difference to be found, the signal may still be reliably normalised from (3.14) to the Differential EXAFS for unit temperature modulation.

If however, the structural changes under study are temperature dependent, which is the case at, say, phase transitions, then  $\partial\chi/\partial T = \partial\chi(T^+, T^-)/\partial T$ ; the absolute values of  $T^+$  and  $T^-$  must be known and the variance of these must be minimal since the pair averaged Difference EXAFS signal can no longer necessarily be correctly normalised by a simple linear scaling of its amplitude.

The next requirement is that of ensuring the sample material is in, as near possible, an equilibrium state at the time of measurement. This implies the absence of any thermal gradients in the volume of material illuminated by the beam. A small spot size helps here since all but the steepest gradients transverse to the beam would induce only a negligible temperature difference over an area of, say  $(10 \times 10) \mu\text{ m}$ . Gradients along the line of the beam can be more problematic but can be examined with the X-ray Temperature as described in section 3.7.3.

Another final requirement, particularly for thermal experiments, is that the sample be isolated from external influence. This ties in with need for temperature stability over many pairs of measurements, since any change in ambient temperature, or the presence of changing air flows in the vicinity of the sample, can easily affect the temperature of the sample itself.



### 3.6 Design and Manufacture of the Thermal Modulation Apparatus

Given the requirements shown above, the task of designing the thermal modulation apparatus was undertaken. Several candidates presented themselves.

The first would have involved modulating the sample temperature via resistive heating. If a sufficiently large electric current were passed through a sample material, resistance alone would induce heating, thus allowing the temperature of the sample to be controlled by varying the current flowing through it. Whilst the simplest design, critical problems made it unviable. Firstly, although resistive heating is very rapid, there is no analogy to actively cool the sample, making the overall modulation cycle both slow and asymmetric. The technique also limits the choice of sample to those through which a current can be driven without damaging it. Finally, with a strong current flowing through the sample, it is impossible to say definitively that any observed differential signal is purely thermal in origin. There may also be components from, say, electrostriction due to the presence of an electric field.

Similar problems would be encountered with, say, laser heating. There is no analogy for cooling, and the sample itself affects the heating. Specifically, the heating is highly sensitive to the reflectivity of the sample surface.

The second design would have continued the idea of resistive heating, but employed it to heat a thin metal capillary down which gas would be pumped and out onto the sample. The problems of driving a current through the sample itself are eliminated, but an operational prototype showed there were extreme difficulties in both setting the gas temperature to single Kelvin accuracy, and reproducing the temperatures over many hot/cold cycles.

This prototype did however show that blowing jets of heated gas over samples of small thermal mass was a very quick and efficient method of transferring heat into the sample, with both active heating and cooling, and in a manner that would not interfere with any XAS measurements. Therefore, the final design, which was fully implemented for experiments on beam, was a dual gas jet as shown both schematically and *in situ* on

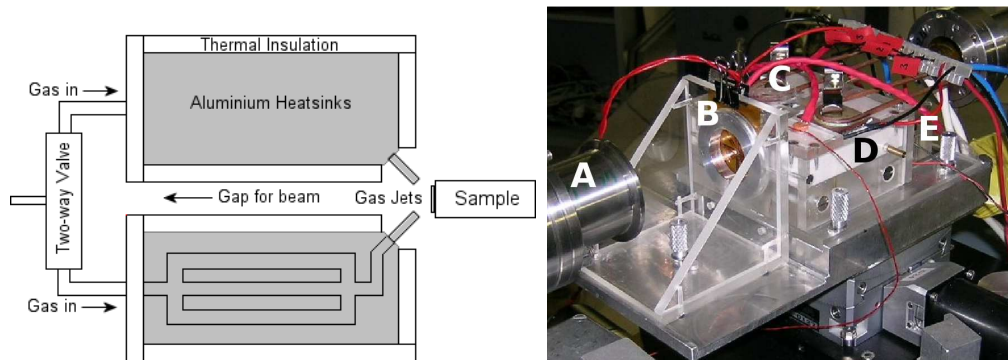


Figure 3.5: The Gas jet thermal modulation apparatus. a) A schematic of the apparatus showing the two-way valve, heatsinks with gas flow channels, and the gas output needles. b) The gas jet *in situ* on ID24 A: X-rays in, B: Thermopile, C: Heaters and temperature sensors, D: Heatsink, E: Valve behind heatsink.

ID24 in figure 3.5.

Gas from a dry nitrogen source is passed into a fast switching two-way fluidic valve mounted at the rear of the apparatus. Simply by passing a high or low voltage signal to the valve, gas is switched to flow down separate channels and into one of two identical aluminium heatsinks.

Several channels are cut inside the heatsink, which further split the gas and increases the surface area of aluminium over which it passes - increasing the rate of heat transfer between the two. The channels recombine at the far end of the heatsink, and gas is discharged through a needle, forming a jet that is targeted at the sample.

Splitting the gas into several channels in this way is more favourable than passing it into a single cavity of the same surface area, since, in the latter case, the cavity will allow a large volume of pressurised gas to accumulate, which will continue to discharge for some time after switching the two-way valve. The multi-channel solution should therefore optimise both the heat transfer rate and response time of gas jet switching.

Also cut into the heatsink are another, separate set of channels through which some desired heating or cooling fluid may be pumped in order to reach temperatures far away from room temperature. However, this fluid, or ambient conditions in its absence, only sets a rough baseline temperature. The precise temperature is instead set by a Peltier effect heater (PEH) mounted on the top of the heatsink.

Also mounted on top of the heatsink is a silicon band-gap reference temperature sensor. Both the sensor and PEH are connected to a proportional integral derivative (PID) controller, which then actively regulates the power in the PEH so as to maintain a constant temperature in the heatsink. The desired temperature may be selected on the PID controller to a precision of 0.1K and then maintained electronically to an accuracy of  $\pm 0.2\text{K}$ .

Stability of this heating feedback loop is optimised by coating the heatsink with 2mm of thermally insulating fabric and then encasing it in a shell of perspex 6mm thick, minimising heat loss to the atmosphere and protecting it from fluctuations in ambient temperature.

With this arrangement, temperature modulation is achieved by setting the two heatsink PID controllers to slightly different temperatures and then switching the two-way valve back and forth so as to cycle the gas flow through each heatsink alternately. Since the temperature of the heatsinks themselves do not require modulation between each XAS measurement, the thermal stability of the gas jets is high. Given also that the two heatsinks are totally independent, the output gas jet temperature may be cycled in a reproducible fashion upon switching of the valve.

One final point to consider is how to facilitate passage of the beam through the sample without being obstructed by the surrounding apparatus. The solution is quite simply to mount the two gas jets on a base plate that ensures a 5mm wide gap runs along the length of the apparatus, between the two heatsinks. A gap this wide is required since away from the focal spot, the dispersive geometry of the beam causes it to diverge, becoming about 2.5mm wide at the rear of the apparatus.

The full blueprints for this design are presented Appendix A, and were used by D. Sutherland of the Warwick Physics Department's Mechanical Workshop for manufacture of the actual apparatus. The PID controller and associated electronics were designed and manufactured by A. Lovejoy of the Warwick Physics Department's Electronics Workshop. Unfortunately, after manufacture, a Finite Element Analysis (FEA) of gas flow through

the heatsinks revealed a design flaw<sup>1</sup>. Figure 3.6 shows a plan view of a horizontal cross-section through the apparatus along the line of the beam. The two heatsinks with gas flow channels can be seen to the left, and the gas jets and sample environment to the right. The contour plot overlaid on the gas flow path shows the result of an FEA calculation of the gas velocity through one of the heatsinks and into the sample environment. Nitrogen gas is injected into the heatsink at 2 litres per minute (lpm) at point A. At this initial stage, the flow is assumed to be laminar with no vorticity. Fluid flow equations are then solved with continuous boundary conditions for each discrete fluid element until points B and C are reached, which are exposed to atmosphere, and hence require the gas pressure to be fixed at 1013 mbar.

The three parallel channels cut into the heatsink were intended to have the same gas flow rates. However, Figure 3.6 reveals that it is only the central channel that has any significant flux; the other two side channels are largely redundant. Figure 3.7 shows a close-up of the region at the input end of the heatsink where the gas channel splits into three. Gas velocity vectors have been plotted to highlight the direction of gas flow in addition to its speed. Again, this shows very little flux along the side channels, with the bulk of gas passing straight down the centre.

As a result of this problem, gas will flow over a smaller surface area of the heatsink than anticipated, reducing the rate of heat transfer from the heatsink to the gas. Consequently, as shown in Figure 3.8, gas traversing the heatsink from an input flow rate of 2 lpm, does not reach thermal equilibrium with the heatsink before being ejected through the gas jet; and thus the desired temperature difference, set on the gas jet PIDs, is not actually attained. Fortunately the temperature difference as displayed on the PIDs is not of critical importance. The true temperature difference at the sample is measured directly by a thermocouple attached to it (as described in section 3.7.2), with the X-ray Temperature (described in section 3.7.3) revealing whether or not the sample has reached thermal equilibrium with the flowing gas. The heatsink deficiencies may, therefore, be compensated for.

---

<sup>1</sup>This problem was discovered only days before scheduled beamtime, forcing the use of the deficient design during all experiments on beam. Fortunately, with knowledge of the flaw it could be compensated for.

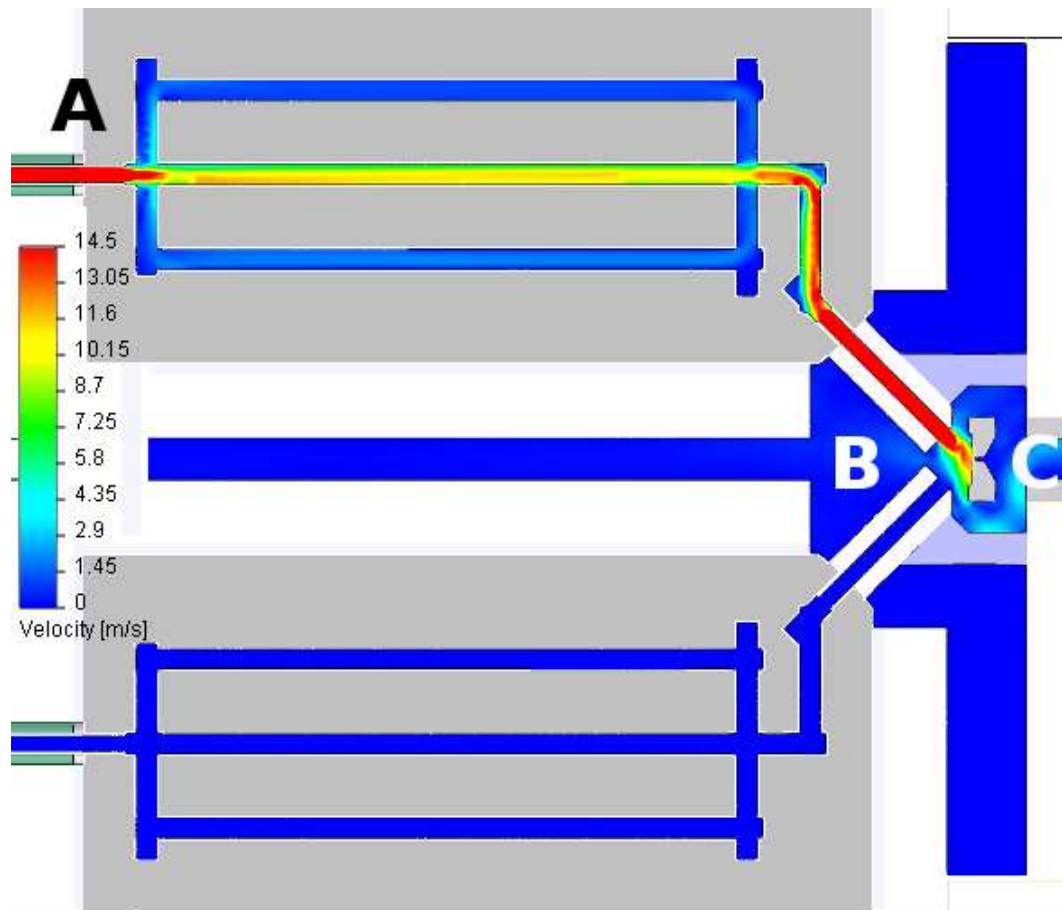


Figure 3.6: A horizontal cross-section through the gas jet apparatus along the line of the beam. The contour plot shows the velocity of gas flowing through the channels of the upper heatsink based on an input flow rate of 2 lpm.

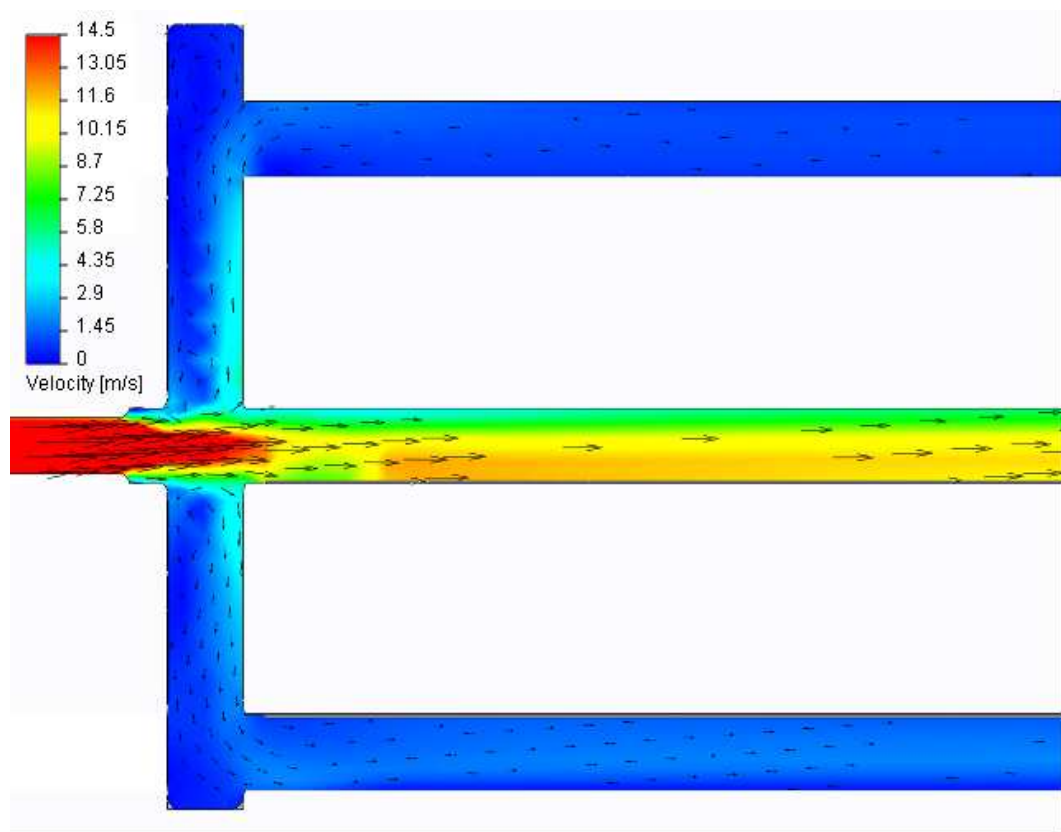


Figure 3.7: A close-up of the channels in the heatsinks in the region where gas flow is split into three. A problem with the design shows that the central channel has a significantly greater flow rate than the outer two channels.

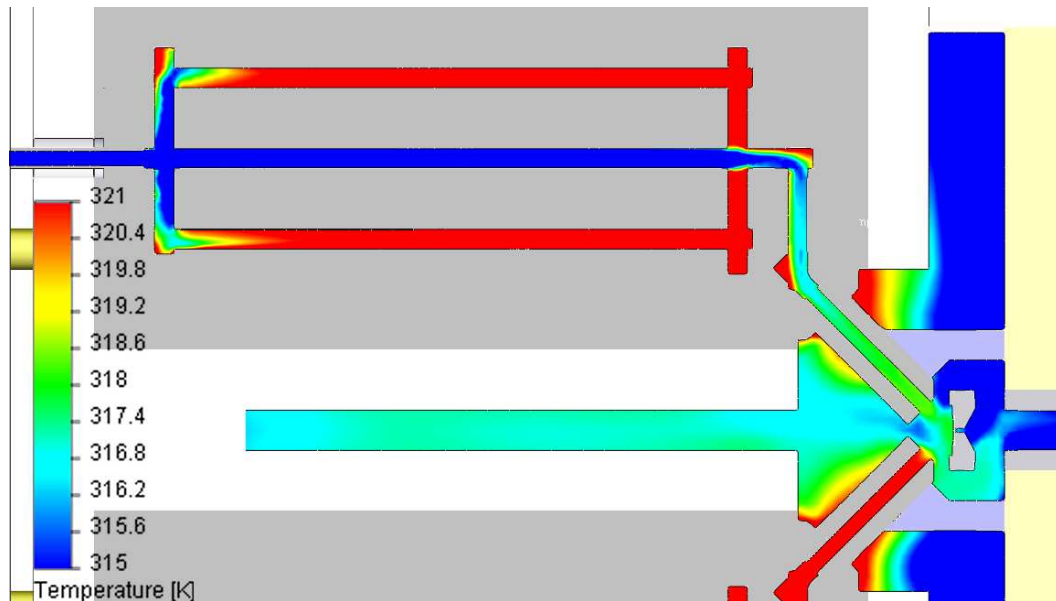


Figure 3.8: FEA of gas temperature whilst traversing the upper heatsink. The heatsink is heated to 323K, and gas injected at 2lpm. Poor flow through the outer heatsink channels results in insufficient heating, with gas being expelled at about 319K before reaching equilibrium with the heatsink.

Whilst all experiments for this thesis were conducted with the deficient heatsinks, there are two potential methods for rectifying the design in the future. The first is to, quite simply, remove the central channel altogether, thus forcing the gas to flow down the two symmetric outer channels. However, a more elegant solution would be to reduce the diameter of the central channel in accordance with Poiseuille's equation to match the flux in each. This would maintain three channels and with them a greater surface area of aluminium for heat exchange between the heatsink and gas.

## 3.7 Temperature Measurement and Sample Mounting Systems

### 3.7.1 Initial designs

An equally important component of the apparatus design involves the sample environment. Again, several possible designs were considered.

Initially, the idea of making temperature measurements with a platinum resistance thermometer (PT100) was explored. Such a device could be sputter deposited onto a thin film of Kapton, upon which the sample would then be mounted. As the sample temperature changed so too would the resistance of the device. This design was attractive in that the resistance could be calibrated as a function of temperature to give an absolute measurement. However, in practical terms it was unviable since, for the smallest device we could make (1mm by 1mm), the thickness of platinum deposited would be only 1nm for a 100 $\Omega$  device. Such a thin film could not be reliably produced and could be structurally unstable if excessively heated or cooled. Additionally, since such a device must be actively driven, it could be affected by self-heating as current flows through it. The concept of sputter depositing a sensor remained attractive however, given that a thin film sensor would have a low mass, and so, ideally, respond to changes in temperature more rapidly than the sample itself. This would ensure that it is the sample itself that dictates the thermal response of the sample environment. The Kapton film would also thermally insulate the sample from the remainder of the mount, minimising losses through conduction.

Therefore, the design accepted for initial DiffEXAFS measurements on ID24, and with which SrF<sub>2</sub> data shown in chapter 5 was acquired, involved sputtering a circular, series array of eight copper-constantan (T type) thermocouples onto Kapton as shown in Figures 3.9 and A.1. Each thermocouple has one of its junctions placed between large aluminium rings, which, being thermally massive, respond only very slowly to changes in surrounding gas temperature; much more slowly than the period of thermal modulation. The other junctions are clustered at the centre of the rings, with the sample being mounted on top of them.

Thermocouples are better than resistance devices since they do not have to be actively driven, eliminating problems with self-heating, and since the critical parameter affecting the performance of the thermocouple is not the cross-sectional area of the sputtered material, but the mismatch in thermo-EMFs between different metals. Therefore, the thickness of the film is not critical, allowing a continuous film of tens of microns to be deposited. They do however, only provide an emf proportional to the temperature



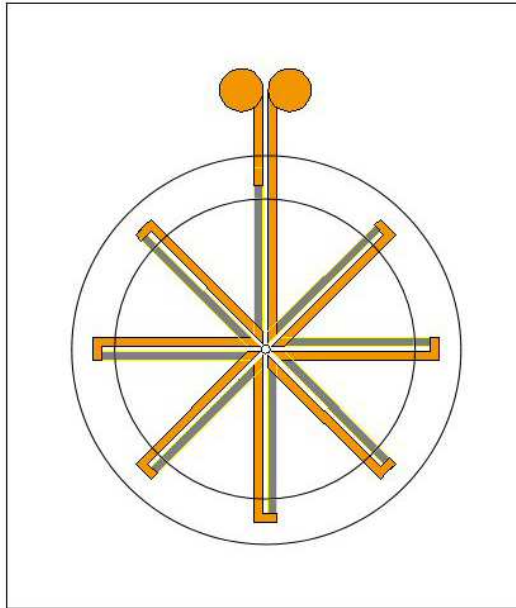


Figure 3.9: A schematic representation of the completed copper-constantan thermopile. The copper coloured lines indicate deposited copper, and the grey lines, constantan. The two concentric rings towards the outside of the device show where the thermally massive aluminium rings should be attached. The sample is attached at the centre.

*difference* between junctions, so to obtain the absolute temperature of the sample, the temperature of the junction under the rings would need to be known absolutely. This is accomplished by attaching an industrially manufactured PT100 to one of the rings.

The completed device is then mounted in front of the gas jets using the mount shown in Figure A.19. This mount and the gas jets are attached to a specially designed aluminium base (shown in Figure A.2), which ensures that when the sample is placed in front of the jets, it is positioned at their focal spot. This not only ensures optimal heat transfer between the jets and the sample, but also maintains the required symmetry between the two jets.

### 3.7.2 The revised design

The sample mount and temperature measurement design detailed above was used on beam during experiment MI-740 on ID24. However, several problems arose that required

addressing before any further experiments [76].

First and foremost, the Kapton film onto which the thermopile was sputtered had a tendency to vibrate slightly whilst in the gas flow. Although not noticeable to the naked eye, this was clearly visible in the DiffEXAFS signal, with spurious results being produced. Supporting the film with a plastic plug temporarily solved the problem. Another issue was the response time of the sample. In order to cover the central junctions of the thermopile, each sample needed to be at least 5mm in diameter. Whilst these samples could be heated to within 5% of the target gas temperature in around seven seconds, this, in practice, was not quick enough to eliminate the effect of temporal beam drifts between measurements at each of the difference temperatures. Reducing the sample mass or improving the heat transfer rate between gas and sample would improve matters. Finally, it was found that having the sample exposed to air left it open to ambient effects despite being in constant gas flow from the jets. This suggested enclosing the sample in some protective container for the duration of measurements.

Therefore, an upgraded sample mount was devised as shown in figures 3.10 and 3.11. This mount is constructed of three components, the first being the sample holder itself. This is a cylinder measuring 22mm long by 8mm diameter, into the end of which two 500 $\mu$ m deep recesses had been cut. The first, 5mm in diameter to accommodate a pellet produced by a 5mm die, and the second, 3mm in diameter to accommodate samples pressed into small gaskets. From the other end of the holder, a 4mm diameter hole was machined along the length of the cylinder up to within 2mm of the sample position, where its diameter reduced to 500 $\mu$ m. This hole allows the unhindered passage of the beam through the sample. Just behind the sample, at the point where the hole narrows, three more holes, 3mm in diameter, were drilled at 90° angular intervals from the outside curved surface of the cylinder into the internal recess. These allow gas from the jets to pass around the reverse side of the sample and out along the line of the beam, which minimises the thermal gradient between the front and back of the sample, and isolates the sample from the environment, preventing oxidation, and thermal interference. The section of cylinder without one of these exit holes had two narrow channels cut into it, running the length of the holder, into which thermocouple wires could be glued.

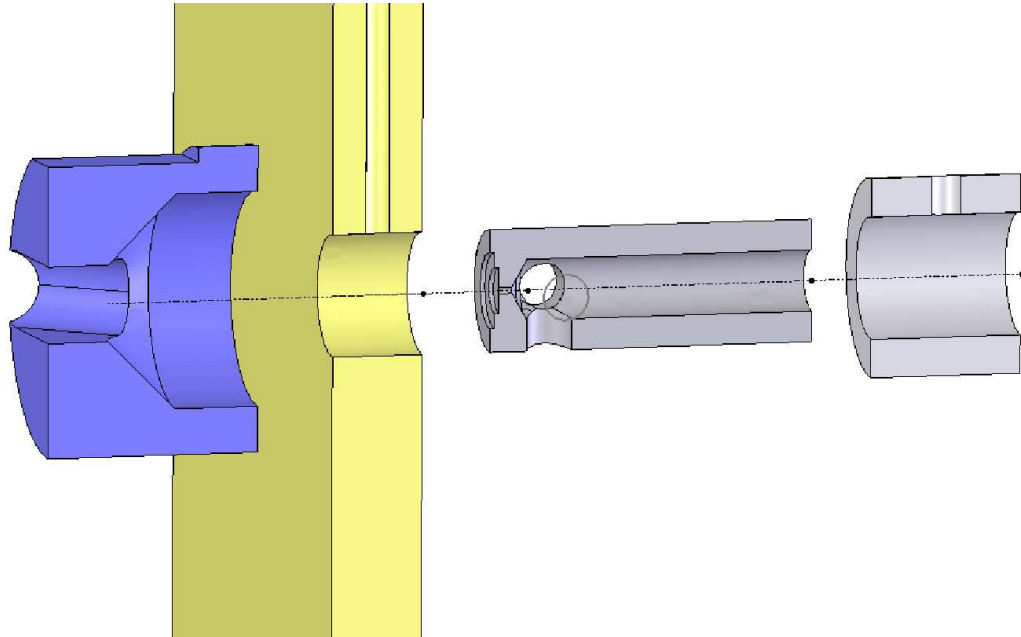


Figure 3.10: An exploded view of the upgraded sample mount. Components 1a and 1b form the sample sheath, 2 is the sample holder, and 3 is the collar for the sample holder.

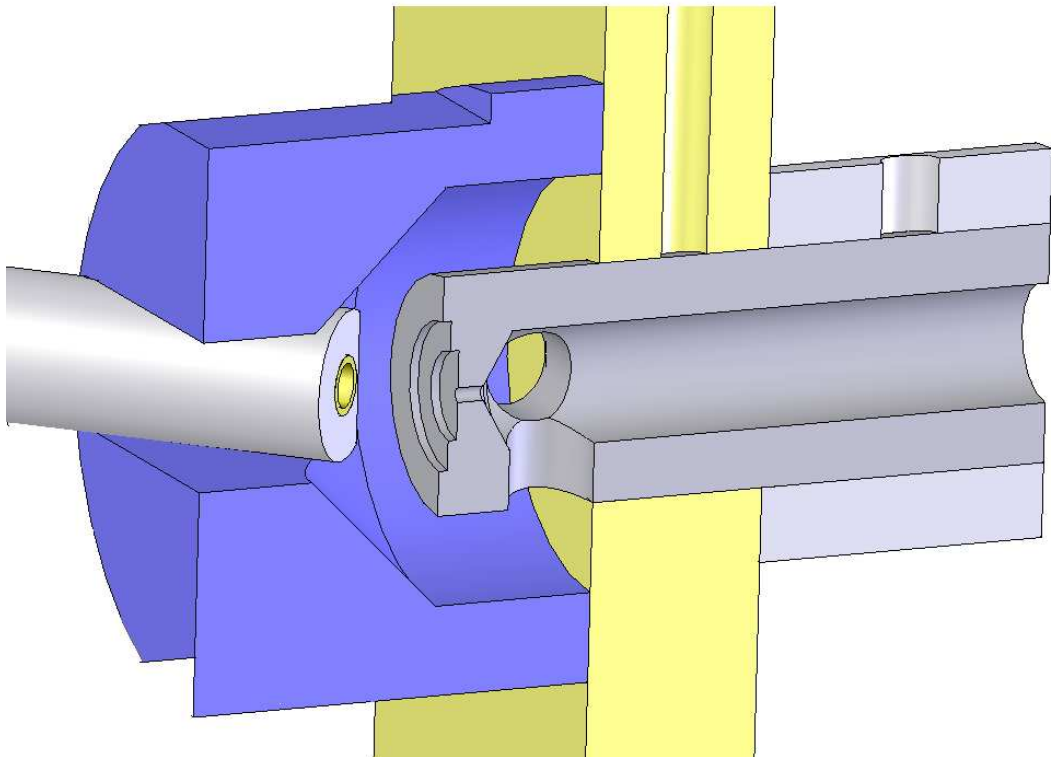


Figure 3.11: An assembled view of the upgraded sample mount with one of the two gas jets shown. 1: gas jet, 2: sample position, 3: gas exit channel.

The second component is a plastic sheath, fixed to a 6mm thick perspex sheet, into which a slot was machined to accommodate the gas jets. This sheath is slid over the jets to provide a contained environment for the gas-sample interaction. The sample is introduced to this environment via an 8mm hole in the perspex sheet, centred on the line of the beam. With this sheath in place, gas is forced to pass over the sample and out to atmosphere, either by passing between the two gas jets, or around through the exit channels cut into the sample holder.

The final component is a 10mm long collar, which is placed over the back of the sample holder such that it is flush with the end. This ensures that when the sample is pushed through the reverse of the sheath into the sample environment, it is reproducibly positioned exactly on the focal spot of the gas jets. All components of the new sample mount were made out of PEEK (Polyetheretherketone) to prevent brittleness observed in most plastics, brought about by radiation damage; and also to ensure that the holder remained structurally stable over a large range of temperatures, where other plastics would deform.

In this scheme the concept of a sputter deposited thermopile is abandoned, and instead the sample temperature is measured via a single thermocouple. These are constructed from 200 micron thick copper and constantan wires and attached to the sample with a minimal quantity of thermally conductive glue, or, in the case of metallic materials, by spot welding one of the thermocouple junctions directly onto the sample. This approach significantly reduces the size of the thermocouple junctions with which the sample must be thermally coupled; and hence allows the sample itself to be reduced in size, improving its thermal response time.

The absence of the thermopile's aluminium rings requires a new reference point for the other thermocouple junction. This is provided by attaching the junction, along with a PT100 for absolute temperature measurement, to a section of copper pipe in the cooling system for the Peltier heater, and covering the two devices with a thick layer of thermally insulating tape. Fluid flowing through the cooling system comes from a temperature regulated source, which as a consequence, provides actively controlled, and so thermally stable conditions at this temperature reference node. This arrangement

has an additional advantage over the thermopile in that the thermocouple junction and PT100 are positioned right next to one another rather than being on opposite sides of a 5mm thick aluminium ring. This minimises the probability of any thermal mismatches between the PT100 and thermocouple junction; ensuring the PT100 does indeed provide an absolute reference for the thermocouple.

Figure 3.12 shows the results of a FEA analysis of this new sample environment, taken from Figure 3.6. Again, the contours show the gas velocity, with arrows indicating the direction of flow. Gas exits the heatsink needle at about  $15 \text{ ms}^{-1}$  and forms a visible jet of high velocity gas that impinges upon the sample at a peak speed of  $12 \text{ ms}^{-1}$ . After hitting the sample, gas is indeed primarily deflected around the gas jet sheath and directed out of the reverse of the sample environment via the holes cut into the sample mount. Some gas also leaves the environment through the gap between the two gas jets, along the line of the beam.

Figure 3.13 shows the thermal profile of gas within the sample environment taken from Figure 3.8. The gas jet ejected from the heatsink needle can be seen to lose approximately 0.4K before striking the sample, most likely due to adiabatic expansion of the gas. Again, this loss is not important since the sample temperature is measured at the time of measurement by a thermocouple rather than being inferred from the PID setting.

After striking the sample, the gas cools as it flows around the reverse side of the sample, but importantly it retains around 90% of the temperature provided by the heatsink. This, therefore, keeps the entire sample environment at some mean temperature, which is close to that of the gas jets. In turn, this reduces the rate of heat loss from the sample, and so reduces the amount of heat that must be applied to the sample to maintain a stable temperature.

This upgraded sample mount was manufactured by A. Sheffield of the Warwick Physics Department's Mechanical Workshop and used on beam during experiments MI-803 and HS-2945 [78][80], discussed in Chapters 5 and 7 respectively. Again, full blueprints are shown in Appendix A.

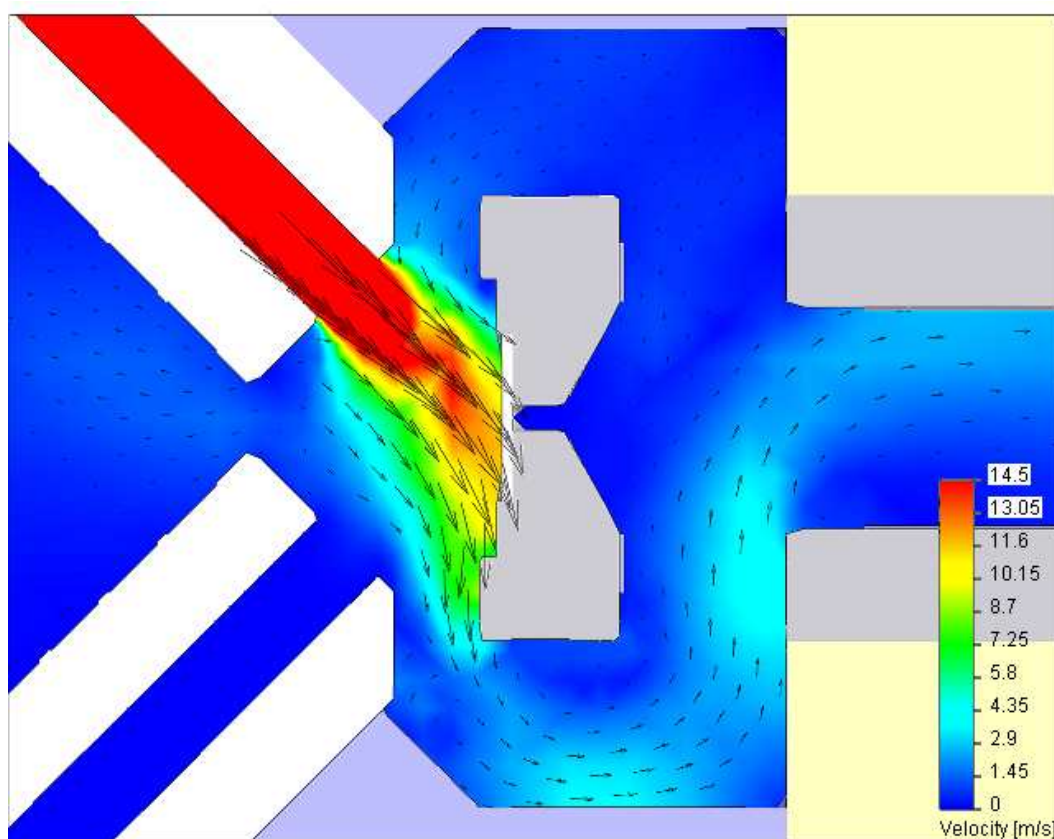


Figure 3.12: A close-up of the velocity of gas flow around the revised sample mount. Gas ejected from the needle forms a jet, hitting the sample before passing out between the needles or around the rear of the sample mount.

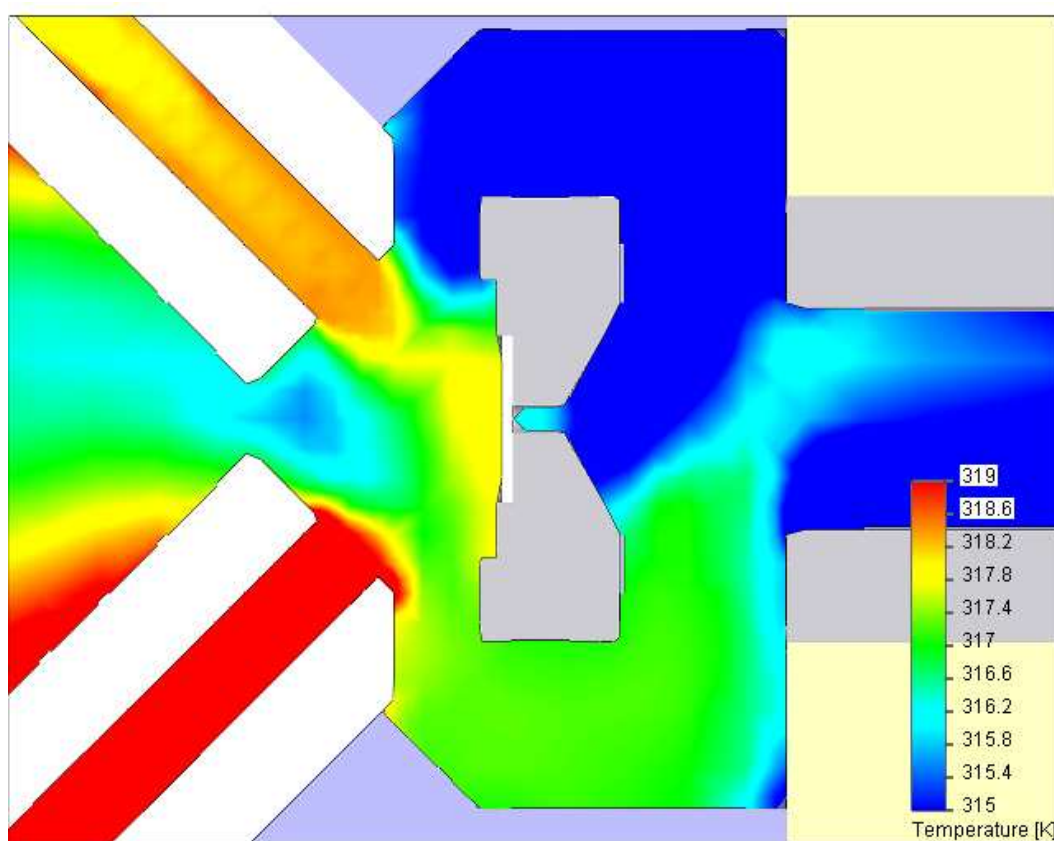


Figure 3.13: A close-up of the temperature of the gas jets around the revised sample mount.

### 3.7.3 'X-ray Temperature' Measurement

Equation (2.14) shows that the total amplitude of the difference fine-structure scales with  $\Delta T$ , being linear within the first order approximation. This feature is primarily exploited to normalise the Difference EXAFS to obtain the differential signal, but may also be used to define an 'X-ray Temperature' (XRT).

This has an extremely important use during experiments, solving a potential problem with Thermal DiffEXAFS: how to ensure that the sample is fully heated to the desired temperature at the time of measurement. The sample temperature must, therefore, be measured; but measured directly, independent of some sensor that has a thermal response characteristic of its own.

It is not enough to simply check for equilibrium via the thermocouple probe attached to the sample, since the heat capacity of the probe is likely to be comparable that of the sample itself given Thermal DiffEXAFS specimens are very small.

The solution, therefore, is to measure the Difference EXAFS amplitude as a function of modulation frequency and check for saturation. For very rapid modulation, the sample is certain to have insufficient heat input to fully raise its temperature to that of its environment. The Difference EXAFS amplitude will therefore be some (probably small) fraction of saturation amplitude. As the modulation frequency is reduced, more heat may flow into the sample before measurement, and so the Difference EXAFS amplitude will increase until, when the sample is in equilibrium with its surroundings, the amplitude increases no more.

Taking simultaneous temperature measurements with the thermocouple attached to the sample, allows its response characteristics to be independently compared to that of the sample itself. This can then verify that the thermocouple reading is representative of the sample temperature, or at least quantify differences in the two heating profiles so that the true sample temperature may be derived from that indicated by the thermocouple. This comparison, and potential mismatch between sample and sensor, was vividly displayed when measuring the thermal expansion of Fe with the sputtered thermopile sensor and then a spot-welded thermocouple as shown in Figure 3.14. The XRT indicates that the particular sample shown here is fully heated about two seconds after gas jet switch-



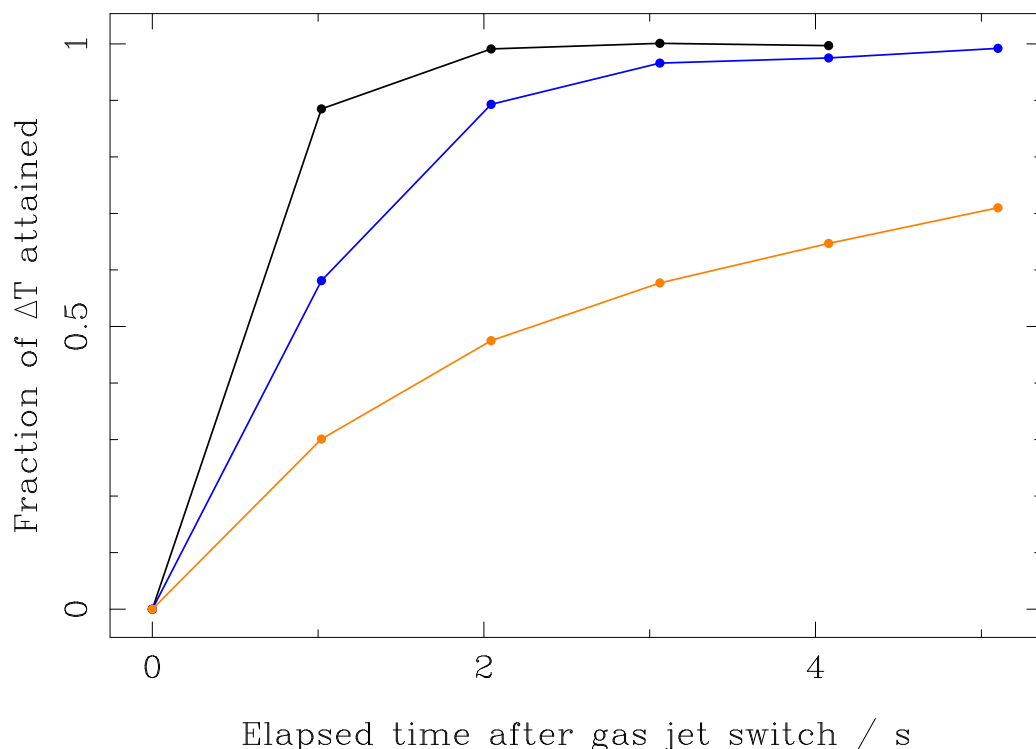


Figure 3.14: Normalised Thermal response profiles. The black line shows the fraction of  $\Delta T$  attained by an Fe foil in the beam as a function of elapsed time after gas jet switching, and is derived from its XRT. The blue line is the corresponding temperature measurement for a thermocouple spot welded to an Fe foil, and the orange line, the temperature measurement for a thermopile attached to the rear of an Fe foil with a thermally conductive compound. Whilst the response times of the sample and thermocouple are roughly comparable, the thermopile responds extremely slowly to a change in gas temperature.

ing. The thermocouple response is slower, but is fully heated after about 3 or 4 seconds. The thermopile however takes over 30 seconds to fully respond. This large mismatch meant that although the sample could be measured two seconds after gas jet switching, the temperature reading given by the thermopile at that time would only be about 50% of the true sample temperature, and thus require a re-normalisation. This was another reason for the replacement of the thermopile.

Since the response times vary somewhat between different samples, thermocouples, and thermopiles, the XRT should be checked before each measurement to ensure a sufficient delay between gas jet switching and XAS measurement is provided.

## Chapter 4

# Development of Data Analysis Techniques

### 4.1 Introduction

In a similar sense to the absence of commercial apparatus to perform DiffEXAFS experiments, the novelty of the technique means that there are no analysis packages available specifically for processing DiffEXAFS data. Indeed, no method by which to analyse Thermal DiffEXAFS data existed prior to this thesis.

This chapter therefore focuses on the efforts required to take experimental spectra and extract information on thermal atomic perturbations. The first section describes DXAS Calibration, a code developed to calibrate spectra obtained from Dispersive XAS beamlines such as ID24. Following sections then proceed to look at how to define a reference point from which to measure atomic perturbations, and ultimately, how to quantify perturbations observed in a DiffEXAFS signal. These last two stages were performed under the auspices of a new analysis code developed for this thesis, which is also described.

## 4.2 Calibration of spectra from ID24

Due to the geometry of beamline ID24, as described in section 3.4, the first important stage in data analysis is the conversion of a spectrum's 'pseudo-energy' scale, specified in CCD pixel number, to an absolute scale. Since many beamline parameters either cannot be determined to sufficient accuracy for calibration, or drift over time, calibration must be performed *a posteriori* with respect to a reference spectrum of known calibration. Such a reference spectrum could, for instance, be obtained from an ordinary step-scanning beamline using the long established technique for absolute energy calibration [63]. It then remains to fit uncalibrated ID24 spectra to this reference in order to calibrate them on an absolute scale.

### 4.2.1 Coordinate transformation

The primary task for calibration is to convert the uncalibrated ID24 energy axis to a known scale. Assuming both the ID24 and reference spectra were acquired under the same environmental conditions, from the same sample, and also, for now, that the instrument response functions of ID24 and the reference beamline were identical, then calibration is reduced to calculating the values of a set of parameters necessary to transform the channel number 'pseudo-energy' axis to an absolute energy scale, and relative absorption to absolute absorption. Algorithmically, these parameters are represented by the coefficients of two polynomials: one for energy calibration, and one for absorption normalisation, so that for each pixel  $i$

$$E'_i = a_0 + a_1 E_i + a_2 E_i^2 + \cdots + a_n E_i^n \quad (4.1)$$

$$\mu'_i = b_0 + b_1 \mu_i + b_2 \mu_i^2 + \cdots + b_n \mu_i^n \quad (4.2)$$

where  $E_i$  and  $\mu_i$  are the original energy and absorption coefficients respectively, and  $E'_i$  and  $\mu'_i$  are the transformed coordinates. As a result,  $a_0$  and  $b_0$  perform a simple translation of the spectrum,  $a_1$  and  $b_1$  stretch the spectrum in a linear fashion, and higher order coefficients induce non-linear deformations. Setting  $a_1$  and  $b_1$  to one and all other parameters to zero will return the original spectrum as it was experimentally recorded.

The order  $n$  of the polynomial is specified by the user, and is typically between 2 and 4. Given all parameters  $a_i$  and  $b_i$  are independent, they may be inserted into a single vector  $\mathbf{a}$  for use by the calibration algorithm.

#### 4.2.2 Compensating for background effects

Frequently, XAS spectra contain low frequency drifts in absorption resulting from any number of background effects.

On a step-scanning beamline these are generally temporal effects such as beam instabilities (both spatially and energetically) or changes in heat load in the beamline components, both of which vary slowly over time. On dispersive beamlines a whole spectrum is acquired simultaneously, so background effects are different in nature. For instance, the combination of the undulator source and polychromator crystal on ID24 does not produce a flat intensity profile, but one which varies as a function of energy, dropping away towards the fringes of a spectrum. Accordingly, the spectral extremities have greater statistical noise than the centre. Another example results from the finite focal spot size, which can inadvertently probe any inhomogeneities in the sample. Since the beam is dispersed in wavelength across the width of the spot, any variation in sample thickness will result in a spurious, apparently wavelength dependent absorption signal. Therefore, DXAS Calibration also provides the option of performing background correction. If activated, a Chebyshev polynomial of usually 3 to 6 coefficients is fitted through the residual absorption differences between the ID24 and reference spectra, and then subtracted to eliminate any low frequency drift.

#### 4.2.3 Handling beamline specific spectral artifacts

Frequently, coordinate transform and background correction parameters alone will suffice in generating an accurate calibration, however it is also important to consider the case where our final assumption fails, and the instrument functions of ID24 and the reference beamline differ. When this happens, such as at x-ray energies in excess of approximately  $10\text{keV}$ , it becomes necessary to include additional instrument correction parameters [35]. If BM29 is again taken to be the reference beamline, then two instrument corrections

have been found to be necessary: one for the difference in diffraction monochromaticity between the monochromator and polychromator crystals, and another for differences in x-ray penetration into the crystals.

Taking the first correction and considering a perfect crystal diffracting x-rays in compliance with Bragg's Law, there is no propagating solution to Maxwell's equations in the crystal itself, and so the x-ray reflectivity (in the absence of absorption) is unity. This perfect reflection extends for some angular deviation around the Bragg angle defined by the Darwin width, which for Si(111) illuminated with 1Å radiation, say, is about three arcseconds. Beyond the Darwin width, the diffracted x-ray intensity drops off rapidly in a Lorentzian form. The result is that, when illuminated by white light at some angle of incidence, the crystal will almost perfectly diffract a small range of wavelengths close to the Bragg condition, and then a larger range of wavelengths further away from the Bragg angle at ever smaller intensity.

These Lorentzian tails to the diffracted beam reduce its monochromaticity, and hence are undesirable. The BM29 monochromator, therefore, utilises either twin crystals of Si(111) or twin crystals of Si(311), arranged in the parallel configuration to suppress these tails. ID24 however, implements only a single Si(111) or Si(311) crystal to select x-ray wavelengths. Consequently, the tails on the angular reflectivity profile are unattenuated, broadening the fine structure.

For calibration purposes, convolving the BM29 spectrum with a normalised Lorentzian of the form

$$L(x) = \frac{1}{\pi} \frac{\frac{1}{2}\Gamma}{(x - x_0)^2 + (\frac{1}{2}\Gamma)^2} \quad (4.3)$$

will reintroduce the broadening effects eliminated by the two crystal monochromator, matching its characteristic reflectivity profile to that of ID24. At the Sr K edge, for example,  $\Gamma$  has been found to be 3.4eV.

The second correction, for differences in crystal transparency, arises due to the bending of Si crystal in the ID24 polychromator. For a perfect crystal of Si(111) on BM29, diffracting in the dynamical regime, x-ray penetration into the crystal, determined by its extinction length, is of the order of 1μm for 1Å radiation. However, on ID24 the bending of the crystal, which in turn bends the lattice planes, breaks the conditions necessary for

purely dynamical diffraction [26]. Differences in the condition of the crystal surface as a result of its preparation are also important. Thus, on ID24, x-rays penetrate significantly further into the crystal - up to  $35\mu\text{m}$ .

The result is that on ID24, x-rays of a given energy diffract from many more lattice planes of greater depth, which in turn spatially smears the diffracted beam perpendicular to the planes. These x-rays are therefore detected in several pixels along the length of the CCD, broadening the spectrum. Given also that the beam intensity decays exponentially as it penetrates the crystal, with a sharp discontinuity at the crystal surface, the smeared intensity of diffracted radiation will decay exponentially in space. This introduces an erroneous, asymmetrical energy shift in the observed structure, which, due to the geometry of ID24, is towards higher energies. To correct this, the second instrument convolution function is an exponential of the form [35].

$$\exp(z) = \begin{cases} (1/\sigma) \exp(1/\sigma z) & \text{for } z > 0 \\ 0 & \text{for } z \leq 0 \end{cases} \quad (4.4)$$

where  $\sigma$  is found to be 1.25eV at the Sr-K edge. Again, this is applied to the BM29 spectrum so that its monochromator transparency effectively matches that of ID24.

#### 4.2.4 The General Non-Linear Levenberg-Marquardt algorithm

Given the above calibration parameters, DXAS Calibration optimises them using a Levenberg–Marquardt algorithm for general non-linear least-squares fitting of an arbitrary number of parameters [1][67]. This is a widely used fitting algorithm for data analysis, and indeed is implemented in all the fitting procedures presented in the remainder of this chapter.

For the purpose of creating a calibration algorithm within the assumptions given above, we must state *a priori* that it is possible to select some set of parameters,  $\mathbf{a}$ , which when applied to an ID24 spectrum,  $f(E, \mathbf{a})$ , reduce any differences between it and the reference spectrum,  $f_{ref}(E)$ , to a minimum. We therefore define some 'cost function' that measures the spectral differences for any potential solution, and work to minimise it. Given also that the code is always supplied with sets of spectral data, discretely sampled at energies  $E_i$ , the differences can be evaluated at each data point as  $y_i(\mathbf{a}) =$

$f(E_i, \mathbf{a}) - f_{ref}(E_i)$  and inserted into a vector

$$\mathbf{y}^T = \begin{bmatrix} y_1(\mathbf{a}) & y_2(\mathbf{a}) & \cdots & y_m(\mathbf{a}) \end{bmatrix} \quad (4.5)$$

The cost function, which is simply the overall sum of these differences multiplied by some weighting function if desired, is then

$$\chi^2 = \sum_{i=1}^m y_i(\mathbf{a})^2 \quad (4.6)$$

which can be expressed in vector notation as

$$\chi^2 = \mathbf{y}^T \mathbf{y} \quad (4.7)$$

We choose to weight the differences at each data point as their square when evaluating the sum of the differences, so as to allow areas of large difference to dominate the cost function, and so be aggressively minimised when selecting a new set of parameter values. Consequently, areas of small difference only become significant when the algorithm is close to the optimal solution.

Once (4.6) has been evaluated, the algorithm is required to calculate a set of changes to the fit parameters, which, when applied to the uncalibrated spectrum, will (hopefully) reduce the overall cost of the solution. In order to do this, it is necessary to map out the polynomial coefficient parameter space by evaluating the elements of its Jacobian,  $\mathbf{g}$ , and Hessian,  $\mathbf{H}$ , which describe the partial gradient and curvature of  $\chi^2$  with respect to changes in given parameters, as follows

$$g_k = \frac{\partial \chi^2}{\partial a_k} = 2 \sum_{i=1}^m [y_i(\mathbf{a})] \frac{\partial y_i(\mathbf{a})}{\partial a_k} \quad (4.8)$$

$$H_{kl} = \frac{\partial^2 \chi^2}{\partial a_k \partial a_l} = 2 \sum_{i=1}^m \left[ \frac{\partial y_i(\mathbf{a})}{\partial a_k} \frac{\partial y_i(\mathbf{a})}{\partial a_l} + [y_i(\mathbf{a})] \frac{\partial^2 y_i(\mathbf{a})}{\partial a_k \partial a_l} \right] \quad (4.9)$$

These derivatives however, do not contain any information on how each individual data point was affected by changes in the fit parameters. It is therefore convenient to define a matrix of the variation in spectral difference at each data point with respect to a

change in each parameter.

$$\mathbf{A} = \begin{bmatrix} \frac{\partial y_1(\mathbf{a})}{\partial a_1} & \frac{\partial y_1(\mathbf{a})}{\partial a_2} & \dots & \frac{\partial y_1(\mathbf{a})}{\partial a_n} \\ \frac{\partial y_2(\mathbf{a})}{\partial a_1} & \frac{\partial y_2(\mathbf{a})}{\partial a_2} & \dots & \frac{\partial y_2(\mathbf{a})}{\partial a_n} \\ \vdots & \vdots & \ddots & \vdots \\ \frac{\partial y_m(\mathbf{a})}{\partial a_1} & \dots & \dots & \frac{\partial y_m(\mathbf{a})}{\partial a_n} \end{bmatrix} \quad (4.10)$$

This matrix is directly evaluated in the code using the symmetric numerical derivative equation

$$A_{ij} \approx \frac{y_i(\mathbf{a} + \delta a_j) - y_i(\mathbf{a} - \delta a_j)}{2\delta a_j} \quad (4.11)$$

where  $\delta a_j$  is selected to be no larger than the distance (in either units of absorption or energy) between adjacent points in the spectrum data set. Using  $\mathbf{A}$ , the Jacobian and Hessian can be expressed in matrix notation and evaluated likewise in the code. The second derivative term of the Hessian is ignored since it is negligible when compared to the first derivative term.

$$\mathbf{g} = 2\mathbf{A}^T \mathbf{y} \quad (4.12)$$

$$\mathbf{H} \approx 2\mathbf{A}^T \mathbf{A} \quad (4.13)$$

With the Jacobian and Hessian known, the required changes to each fit parameter,  $\Delta a_i$ , can be calculated. Consider a second order Taylor expansion of the cost function in the region of the best solution  $\mathbf{a}_{best} = \mathbf{a} + \Delta \mathbf{a}$

$$\chi^2(\mathbf{a}_{best}) \approx \chi^2(\mathbf{a}) + \mathbf{g} \cdot \Delta \mathbf{a} + \frac{1}{2} \Delta \mathbf{a} \cdot \mathbf{H} \cdot \Delta \mathbf{a} \quad (4.14)$$

If the approximate solution is sufficiently close to the optimal solution, then it may be reached in one step by differentiating (4.14) with respect to  $\Delta \mathbf{a}$  and rearranging to obtain.

$$\Delta \mathbf{a} = -\mathbf{H}^{-1} \mathbf{g} \quad (4.15)$$

In reality however, the approximation in (4.14) is not sufficiently good to reach the minimum in a single step, so therefore, the best approach is to take a smaller than calculated step in the direction of the minimum and iterate until the cost function stops (or effectively stops) decreasing.



In this sense, Levenberg [43], and later Marquardt [45], suggested scaling the steps as

$$\Delta \mathbf{a} = -(\lambda \mathbf{I} + \mathbf{H})^{-1} \mathbf{g} \quad (4.16)$$

where  $\lambda$  is an order of magnitude scaling parameter, and  $\mathbf{I}$  is the identity matrix. The calibration then proceeds by choosing an initial set of parameters,  $\mathbf{a}_0$ , believed to be close to the optimal solution, and setting  $\lambda$  to an order of magnitude comparable to the expected scale of the solution.  $\Delta \mathbf{a}$  is then calculated using (4.16) and applied to  $\mathbf{a}$ . If the cost function is reduced with the new parameters, they are accepted, and  $\lambda$  is reduced by a factor of 10. If however the cost function fails to decrease, the new parameters are rejected and  $\lambda$  is increased by a factor of 10.  $\Delta \mathbf{a}$  is then calculated again, and so on. If a user specified number of consecutive iterations fail to improve the cost function, the best solution is assumed to have been reached, and the calibration terminates.

## 4.3 Fitting EXAFS spectra to theory

### 4.3.1 *ab initio* EXAFS spectra using the FEFF code

FEFF is a program developed by the University of Washington to calculate *ab initio* x-ray phase and amplitude information for XAFS spectra [71] [72]. These calculations are based on an all-electron, relativistic Green's function formalism, and are performed using a self-consistent, real-space multiple scattering (RSMS) approach for atomic clusters; they also take x-ray polarisation dependence, core-hole effects, and local field corrections into account [6]. What follows in this section is a precis of FEFF's operation from descriptions given in the FEFF manual [7]. The reader is referred to that manual for more detailed information.

Each calculation performed by FEFF is composed of six stages. The first of these is to calculate the scattering potentials for each atomic species present in the sample material. These species are listed in the FEFF input file 'feff.inp' along with the type of core hole under study (i.e. K, L<sub>1</sub>, L<sub>2</sub> etc). Firstly, the free atom potentials are calculated for each atomic type using a relativistic Dirac-Fock code. This information is then used,

within the muffin-tin approximation, to determine scattering potentials according to the Mattheiss prescription [48]. Finally, the Hedin-Lundqvist/Quinn self-energy for excited states is included [29].

Next, scattering phase shifts, and x-ray cross-sections are calculated. The (relativistic) matrix for dipole transitions is evaluated using atomic core and normalised continuum wave functions. Several options exist at this stage for optimising the calculation for specific XAFS regimes. For work in this thesis the EXAFS flag was used, so as to perform calculations out to  $k = 20 \text{ \AA}^{-1}$ .

The third stage performs full multiple-scattering calculations, summed to infinite order via the Rehr-Albers formalism [71], for a cluster of atoms centred on the absorbing atom. This process focuses on the XANES region of the fine-structure out to about  $4 \text{ \AA}^{-1}$ , and is therefore not of particular importance in the EXAFS region.

Following this, photo-electron scattering paths are enumerated. Since the number of scattering paths is potentially huge, increasing exponentially with atomic shell radius, this module employs several path importance filters to find all significant multiple-scattering paths. These work in order of increasing path length, and are combined with a degeneracy checker to identify equivalent paths. The paths themselves are constructed based upon a list of coordinates, in Cartesian space, for all of the atoms considered in the calculation.

With the significant scattering paths found, the effective scattering amplitudes, total scattering phase shift, and other XAFS parameters are calculated for each scattering path. For calculations performed in this thesis, the NLEG flag was specified at this stage (in 'feff.inp') to limit the maximum number of scattering path legs to six.

Finally, once all the calculations above are complete, the *ab initio* XAS spectrum,  $\chi(k)$ , is constructed. Debye-Waller factors for both single- and multiple-scattering paths may be introduced via the Correlated Debye Model (CDM), Equation of Motion (EM) method, or Recursion (RM) method. As well as outputting  $\chi(k)$ , the individual  $\chi_j(k)$  may be produced for each scattering path. Such output was requested for calculations in this thesis since additional, experimentally determined parameters had to be found for each path.

### 4.3.2 Extraction and normalisation of experimental XAFS signals

Prior to fitting any XAFS signal it is necessary to extract the normalised oscillatory component of the measured x-ray absorption above the edge. This is  $\chi(E)$ , as defined, in the general case, by equation (2.9).

Experimentally,  $\mu(E)$  may be obtained from the familiar absorption relation  $I = I_0 e^{-\mu z}$ , where  $I_0$  and  $I$  are the x-ray intensities before and after passing through a sample of thickness  $z$ . The other terms in (2.9) are much harder, or indeed, impossible to obtain from direct measurements.

However, whilst (2.9) is a rigorous definition of  $\chi$ , it is important to remember that, conceptually,  $\chi$  is nothing more than the oscillatory part of the post-edge absorption spectrum, normalised to unit amplitude. Likewise, the  $\mu_{0i}(E)$  and  $\mu_{en}(E)$  are just present to compensate for the background about the measured absorption edge.

Bearing this in mind,  $\chi$  can be obtained if two conditions hold. Firstly, the edge under study must be far from any other edges. The sum of  $\mu_{en}(k)$  can then be modelled as a smoothly varying function, such that a spline, fitted to the pre-edge region of the spectrum, can be extended under the studied edge and its fine-structure<sup>1</sup>. Call this spline  $S_{pre}(E)$ .

This can not be done if edges are close together, as can be the case at, say, L-edges, since the fine-structure from one edge can overlap that from another requiring explicit knowledge of each  $\mu_{en}(k)$ .

The second condition is similar. One must assume that the sum of  $\mu_{0i}$  is also a smoothly varying function, this time over the whole post-edge region. It is then possible to take a large range of data above the edge, which extends to well beyond the point where any EXAFS oscillations disappear, fit a spline to this region, and then extend it back to the edge. Call this spline  $S_{post}(E)$ .

This concept is shown in Figure 4.1. With the splines fitted, it is possible to obtain  $\chi$

---

<sup>1</sup>Extrapolation of splines is not possible. Thus in order to extend the spline under the edge, an additional knot point must be placed by eye in the high- $k$  region, where it is anticipated the background absorption would be in the absence of the edge. Thus the spline is extended by interpolating between the pre-edge region and this high- $k$  knot. Although this requires an element of human judgement, this approach is sufficiently good to normalise the spectrum. Any background errors can be removed later whilst fitting the fine-structure

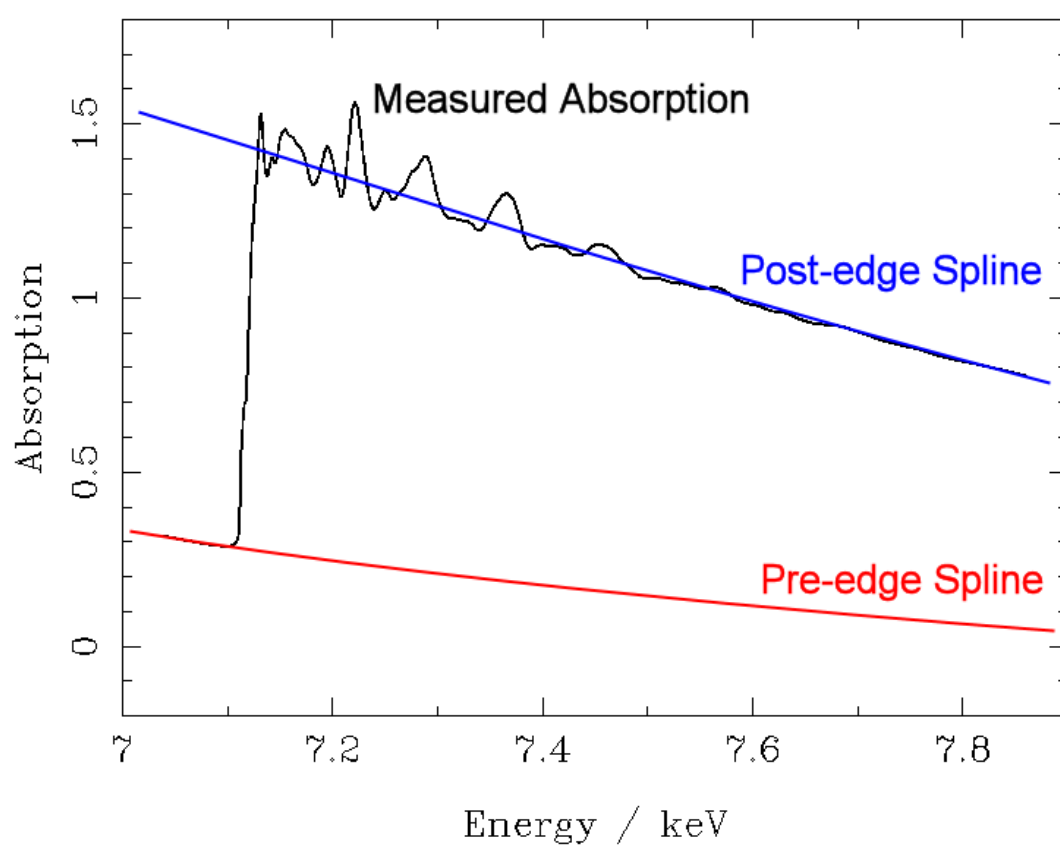


Figure 4.1: A typical X-ray absorption spectrum, taken on BM29 of the ESRF, with splines fitted to the pre- and post-edge regions to enable extraction of the observed fine-structure.

in the post edge region by

$$\chi(E) = \frac{\mu(E) - S_{post}(E)}{S_{post}(E) - S_{pre}(E)} \quad (4.17)$$

which is of a similar form to equation (2.8).

It is worth pointing out that a qualitative form of the normalised fine-structure can be obtained simply by subtracting any pre-edge absorption such that the bottom of the studied edge lies at  $\chi \simeq 0$ , and then dividing the residual absorption by the perceived magnitude of the edge jump. This can be useful in providing a quick comparison for the eye between different spectra, but should not be used in any quantitative data analysis.

### 4.3.3 Fitting conventional EXAFS spectra to theory

With the experimental  $\chi(E)$  obtained from (4.17), it is possible to convert to  $\chi(k)$  by virtue of equation (2.7) and then fit the resulting data to the fine-structure function (2.11).

The primary goal here is to acquire values for all structural parameters that contribute to the fine-structure, and then fix them. This provides a reference point from which to measure the thermally induced atomic perturbations observed in corresponding DiffEXAFS spectra. For such a reference to be valid,  $\chi(E)$  must have been extracted from a spectrum taken at close to the same temperature as the DiffEXAFS measurements.

This reference is obtained by firstly using FEFF to determine which scattering paths in the sample are significant and to generate their phase and amplitude information. Scattering path lengths,  $s_j$ , and shell coordination numbers,  $N_j$ , are fixed from the outset by providing FEFF with a list coordinates for the position of each atom surrounding the absorbing atom. The Debye-Waller factors,  $\sigma_j^2$ , may also be calculated by FEFF via the Correlated Debye Model<sup>2</sup>, which provides a good initial approximation to each  $\sigma_j^2$ . These are not, however, sufficiently good to serve as a reference, and so must be improved by fitting  $\chi(k)$ .

---

<sup>2</sup>FEFF may also calculate  $\sigma_j^2$  through either the Equation of Motion or Recursion methods. These both tend to be more accurate than the Correlated Debye Model, but require knowledge of the sample's phonon spectrum.

It is important to stress that this fitting process works on a restricted number of parameters. Only the  $\sigma_j^2$  are fitted, along with the experimental shake-off,  $S_0^2$ , and absolute edge energy,  $E_0$ <sup>3</sup>. All other components of the fine-structure function are either fixed or calculated from first principles. This approach can therefore be considered 'pseudo-*ab-initio*'. It also serves to mitigate any deficiencies in theoretically calculated spectra by absorbing them into the fitted parameters.

The fitting itself is performed with FitChi2, a new code developed for this thesis that is based in part upon the FitChi code [58]. Like DXAS Calibration, it utilises the Levenberg-Marquardt algorithm to determine the optimal parameter values. Parameter errors are also calculated, and are discussed in more detail in section 4.4.2. By default, every significant scattering path returned by FEFF is considered by FitChi2 irrespective of path length or whether it is a single or multiple scattering path. This typically results in many tens of fitting parameters, which can potentially present a problem with conditioning the fit so as to maximise orthogonality between different parameters.

To help identify any such problems, FitChi2 outputs the full fit correlation and variance/covariance matrices, and plots containing each individual path contribution to the overall fine structure. In the event of poor fit conditioning, paths of negligible amplitude may be discarded, and then, if conditioning is still poor, the experimental spectra may be Fourier filtered to limit the maximum scattering path length to further reduce the number of parameters. Experience gained from fitting Fe, SrF<sub>2</sub>, and Ni<sub>2</sub>MnGa data has indicated that Fourier filtering spectra to eliminate contributions beyond the fourth or fifth single-scattering path, leaving around ten paths to consider, produces the best results. However, some degree of trial-and-error is necessary to obtain optimal fits.

Once a good fit is found. Just one problem remains, which relates to the representation of the Debye-Waller factors. FitChi calculates them as  $\exp(-2\sigma_j^2 k^2)$ , based upon  $k$ , the photoelectron momentum. However, FEFF generates scattering phase and amplitude information in more general terms, based upon a complex local momentum  $p^2 = k^2 + k_F^2 - (\Sigma(E, p) - \Sigma(E_F, p_F))$  (in atomic units), where the  $F$  subscripts denote  $k$ ,  $E$ ,

---

<sup>3</sup>Although not strictly structural parameters,  $S_0^2$  and  $E_0$  must be known since  $\alpha$  and  $\partial\sigma_j^2/\partial T$  scale with signal amplitude, and hence also with  $S_0^2$ , and since previous work [61] has shown that when varying scattering path lengths - as is the case in determining  $\alpha$  - parameter correlation with  $E_0$  is extremely strong.

and  $p$  at the Fermi energy. This includes many-body effects from the 'dressing' of the electron. The Debye-Waller factor is therefore  $\exp(i\mathbf{p}\cdot\mathbf{r})$ , and there is thus a correction for the inner atomic potential, which is  $\sigma_j^2$  dependent [70]. The difference in results between these two treatments is small, particularly in the EXAFS regime. However, since the complex local momentum treatment results in a small phase correction, it is important include this in subsequent analysis in order to obtain the correct thermal expansion coefficient.

It is therefore necessary to ensure self-consistency is achieved between the FitChi results and FEFF. The Debye-Waller factors are taken from FitChi, and inserted back in to FEFF so that it may re-generate the scattering phase and amplitude information with the experimental parameters included. This new information is then passed back to FitChi, and another, identical, fit performed in order to obtain a correction to the FEFF Debye-Waller factors. These corrections are applied to those already in FEFF, another set of phase and amplitude information generated, and so on until self-consistency is reached, and FitChi no longer changes any of the Debye-Waller factors.

## 4.4 Fitting Differential EXAFS spectra to theory

Once a good conventional EXAFS reference has been obtained, the thermal components  $\alpha$  and  $\partial\sigma_j^2/\partial T$  of the DiffEXAFS spectra may be found relative to  $s_j$  and  $\sigma_j^2$  respectively. As with the conventional EXAFS, the experimental DiffEXAFS,  $\partial\chi(E)/\partial T$ , is first converted to k-space using (2.7) and then fitted, this time to the differential fine-structure function (2.14).

### 4.4.1 Fitting paradigm and considerations for fit conditioning

In conventional EXAFS fitting, as described in section 4.3, the approach is to generate *ab initio* scattering phase and amplitude information for each significant scattering path, and fit them directly to the experimental fine-structure to determine parameters such as Debye-Waller factors. The number of paths considered in the fit is based upon the quality of previous fits; more paths being added if the fit itself is poor, and paths being

removed if fit conditioning becomes poor.

Such an approach was also tried for Thermal DiffEXAFS analysis. However, it soon became clear that successfully conditioning such a fit was virtually impossible. Paths contributing to the differential fine-structure increase in amplitude both with increasing path length,  $s_j$ , and with increasing x-ray wavenumber,  $k$ . The first has the effect of amplifying the significance of paths far away from the source atom, which would normally not be considered in a conventional EXAFS fit. And the second has the effect of counteracting, to a certain degree, the effect of the Debye-Waller factor, causing EXAFS oscillations to remain significant out to a higher  $k$  than would be observed in conventional EXAFS.

Consequently, so many paths must be considered in a plain *ab initio* fit to experiment that maintaining low correlation between fit parameters becomes impossible. As a result of this, the fitting algorithm must include a Fourier filter operation at the beginning to remove the numerous paths with very large lengths. Suitable positioning of the filter reduced the number of paths from a value approaching a hundred to around about ten. The fitting procedure is therefore as follows. Firstly, the experimental spectrum is Fourier transformed. A simple, rectangular filter is positioned at some convenient location, all data at higher radii deleted, and the spectrum back-transformed. The location of the window is selected by trial-and-error, but should, as near as possible, be positioned in a trough between Fourier peaks to minimise the leakage of high- $R$  paths into the filter region. The window should also be sufficiently large that the filtered spectrum retains enough independent data points to permit fitting all the required theory parameters, namely  $\partial\sigma_j^2/\partial T$  for each path,  $\alpha$  (just one in the case of a cubic crystal), and some background parameters. For a Fourier filtered spectrum, the number of independent data points is given by [86]

$$N_{ind} = \frac{2\Delta k \Delta R}{\pi} \quad (4.18)$$

where  $\Delta k$  is the range of data initially passed into the filter,  $\Delta R$  is the range of radii allowed to pass through the filter, and where  $N_{ind}$  is rounded to the nearest integer. For a viable fit

$$N < N_{ind} \quad (4.19)$$



where  $N$  is the number of fitting parameters.

Once the experimental spectrum has been filtered, the FEFF phase and amplitude information for the scattering paths that are allowed through the filter are taken, and this information used to generate theory spectra that are fitted to the filtered experimental spectra (back in  $k$ - or  $E$ -space).

Importantly, each theory spectrum generated by the fitting algorithm is passed through the same Fourier window as the experimental spectrum. This has the effect of introducing similar Fourier defects to the theory spectra as were introduced when filtering the experimental spectrum.

Once the fitting algorithm has converged, a similar analysis of the fit is performed as described in section 4.3 to assess the quality of the fit. Namely, are the fit residuals low, and the fit conditioning good?

In contrast to this approach, Fourier filter windows could be selected to extract information from specific shells or scattering paths at a time, which are then analysed via, say, the ratio method [13]. However, such an approach is not advisable since scattering paths, particularly away from the first or second shell single-scattering radii, are neither orthogonal nor discrete in  $R$ -space. Fourier transform peaks have a Gaussian shape, describing some variance in scattering radius for a given path. These peaks overlap in  $R$ -space, sometimes even forming a continuum at high radii, making path selective filter windows near impossible to define.

Such an approach may work for first or second shell single-scattering, but it should be remembered that the expansion term in the differential fine-structure (2.14) scales with increasing path length, meaning high- $R$  paths should also be considered.

Additionally, and as always in spectral applications, Fourier transform operations introduce artifacts into the spectra by virtue of the finite range of data available. Whilst specialised filters may be selected to minimise such artifacts, they cannot be completely eliminated. Therefore, it is advisable to perform as few filter operations as possible to prevent the introduction of too many spectral defects.

#### 4.4.2 Analysis of fitting errors

In fits to conventional EXAFS spectra, errors are obtained by simply calculating the variance/covariance matrix from the Marquardt fitting algorithm. Since the noise in the spectrum is very low, each data point is considered to have the same statistical noise associated with it, and as such, the Marquardt cost function is as shown in (4.6). In the DiffEXAFS spectra however, the noise is firstly a much larger fraction of the measured signal, but also varies across the spectrum; the dispersive geometry produces a continuous range of diffracted wavelengths, but not all wavelength components carry the same intensity. At the extremities of the spectrum, noise is higher since the polychromator crystal produces fewer photons there, and lower in the central region where the flux is greatest.

Consequently, when evaluating the fitting cost function, each data point must be given a relative weighting based on the amount of noise associated with it. (4.6) becomes

$$\chi^2 = \sum_{i=1}^m \frac{y_i(\mathbf{a})^2}{\sigma_i^2} \quad (4.20)$$

where  $\sigma_i^2$  is the variance of  $y_i(\mathbf{a})$  at point  $i$ . In order to evaluate each  $\sigma_i^2$ , it becomes necessary to estimate the noise at each point in a measured spectrum.

This can be achieved by defining a maximum effective scattering radius for EXAFS contributions,  $R_{max}$ , beyond which the remaining, structureless components can be extracted and considered purely noise. Assuming the noise is white, these components are indicative of the noise over all R-space and so can be bandwidth corrected to compensate for unrejected noise in the region where  $R < R_{max}$ .

This will extract the high frequency noise only. A similar filter could be applied to low radii noise by eliminating contributions from radial components less than the first shell single-scattering radius. However, better results tend to be obtained when background features are subtracted using a Chebyshev polynomial incorporated into the fit.

Rather than filtering the noise in R-space, the Fourier transform relation  $R = \pi/2\Delta k$  should be used to fit smoothed, piecewise-continuous, natural cubic splines - with knots positioned such that  $\Delta k$  corresponded to  $R = R_{max}$  - to the spectra to define the EXAFS components. The fit residuals then define the noise. This approach is more

favourable to Fourier filtering since it preserves the  $k$ -dependence of the noise, and hence, directly yields the required  $\sigma_i^2$ .

Once  $\sigma_i^2$  is known for all  $i$ , the Marquardt algorithm can proceed according to (4.20), and the parameter fitting errors again acquired from the Marquardt variance/covariance matrix.

One final point to note is that spectra are acquired on ID24 with data points spaced linearly in energy. Fitting the noise extracting spline described above though, requires knots to be positioned evenly in  $k$ -space. A spectrum can easily be converted from  $E$ -space to  $k$ -space and vice versa using equation (2.7), but care must be taken. Since  $E \propto k^2$ , and thus  $\Delta E \propto k$ , the data sampling rate apparently changes when switching between the two spaces. If a spectrum is acquired in constant energy steps and converted to  $k$ -space, the density of data points increases proportional to  $k$ . At low- $k$ , there are fewer data points between two knots than there are at high- $k$ .

Since each individual data point has the same statistical significance, the spline fit must be weighted such that it becomes increasingly important to obtain a good fit between two knots,  $\Delta k$  apart, at high- $k$  than at low. The cost function then becomes

$$\chi^2 = \sum_{i=1}^m y_i(\mathbf{a})^2 k^2 \quad (4.21)$$

Performing Fourier filtering instead of fitting a spline at this stage will not help, since Fourier transforms from  $k$ - to  $R$ -space again require the input spectrum to be sampled in steps of constant  $k$ .

A similar situation can arise when spectra acquired in constant  $k$  steps are converted to, and analysed in,  $E$ -space.

## Chapter 5

# Differential EXAFS to Measure Thermal Expansion

### 5.1 Introduction

The first task in assessing the viability of Thermal DiffEXAFS was to perform a simple, proof of concept experiment; taking measurements from an already characterised material of well known thermal properties, and analysing them to see if those characteristics could be reproduced and to what accuracy.

Thermal expansion measurements fitted this mandate nicely. Such measurements have been performed with a multitude of techniques over many decades, especially with respect to the elements and simple compounds, providing highly accurate expansion coefficients.

Thermal expansion also has the advantage that away from any features such as phase-transitions, it describes a linear change in crystal dimensions as a function of temperature. This simplifies the analysis of DiffEXAFS data.

This chapter describes the process by which samples were selected for DiffEXAFS thermal expansion measurements, provides the results of those measurements and the subsequent analysis, and culminates in the derivation of coefficients of thermal expansion for strontium fluoride and alpha iron.

## 5.2 Selection of samples for Thermal Expansion measurements

Since the measurements described here would present the first test for Thermal DiffEXAFS, it was important to select samples that would provide the best chance of resolving the thermal expansion component of the differential fine-structure.

Based on previous Differential EXAFS experiments [64], mean atomic displacements of the order of one femtometre may be expected to be resolved in a Thermal DiffEXAFS measurement. In terms of thermal expansion, and given inter-atomic distances are of the order of a few angstroms, this corresponds to a minimum detectable thermal expansion coefficient of approximately  $10^{-5} K^{-1}$  for a temperature modulation of 1K. Numerous materials exist with a thermal expansion of this order, presenting many targets for measurement. Indeed, even those with a lower thermal expansion need not necessarily be ruled out, since it is always possible to increase the degree of temperature modulation between each of the difference spectra in a DiffEXAFS measurement.

However, thermal disorder must also be considered, and so a material's phonon spectrum examined. As described in section 2.3, thermal disorder washes out x-ray fine-structure - particularly when this is associated with high-frequency modes of vibration. As the absolute temperature of a sample is increased, more phonon states become excited, increasing  $\sigma_j^2$ , and so reducing the fine-structure amplitude according to  $\exp(-\sigma_j^2 k^2)$ . Since  $\sigma_j^2$  should be as small as possible, samples should be selected, to a first approximation, with high Debye temperatures; higher than the measurement temperature, such that high-frequency phonon states are not excited.

Care should also be taken to select samples where  $\sigma_j$  varies slowly with temperature, reducing the thermal disorder component of the differential fine structure, and so increasing the proportion of the total DiffEXAFS signal described by thermal expansion.

One final parameter to consider is the crystallographic symmetry of the chosen sample material. As explained in Section 2.5, von Neumann's Principle may be used to reduce the number of independent thermal expansion coefficients. Thus, for simplicity, cubic systems should be examined first, where only one thermal expansion coefficient is

required, which may be applied to all DiffEXAFS scattering paths.

The viability or otherwise of potential samples was established prior to experiments on beam, by using FEFF to generate anticipated Thermal DiffEXAFS signals. Two targets initially considered were the Alkali Halides Rubidium Fluoride (RbF) and Lithium Bromide (LiBr), which have thermal expansion coefficients of  $3.86 \times 10^{-5} K^{-1}$  and  $4.87 \times 10^{-5} K^{-1}$  [68] respectively. However, with Debye temperatures of only 272K [69] and 246K [15] respectively, the overall anticipated DiffEXAFS signal quickly decays with increasing  $k$ , dropping below the predicted noise limit of ID24 before a suitably large range of data is acquired.

As a result, these materials were discarded. Much better samples proved to be Strontium Fluoride ( $SrF_2$ ) and Iron ( $\alpha$ -Fe), shown in Figure 5.1.

### 5.3 Strontium Fluoride and Alpha-Iron

The thermal expansion coefficients and Debye temperatures for  $SrF_2$  and  $\alpha$ -Fe are shown in Table 5.1.

The thermal expansion coefficients are clearly a factor of two to five smaller than those of LiBr and RbF, and are only just above the 1K modulation limit of  $10^{-5} K^{-1}$ . However, the higher Debye temperature results in the anticipated signals remaining above the ID24 noise limit up to approximately 550eV, providing numerous high- $k$  oscillations that may be fitted during data analysis. These are shown in Figure 5.1.

Another interesting and useful feature of the Thermal DiffEXAFS signals can be seen in figure 5.1. Taken alone, the desired thermal expansion component of the signal soon falls below the ID24 noise limit as  $E$  increases. It may, however, still be resolved as a peak shift with respect to the standard EXAFS when superimposed upon the larger thermal disorder component. In effect, this means that for thermal signals it is possible to resolve mean atomic displacements fractionally smaller than a femtometre in spite of the previously stated noise limit.

A small crystal of strontium fluoride was ground to a fine powder for DiffEXAFS measurements. 19.8mg of this powder was mixed with 111mg of Boron-Nitride and pressed

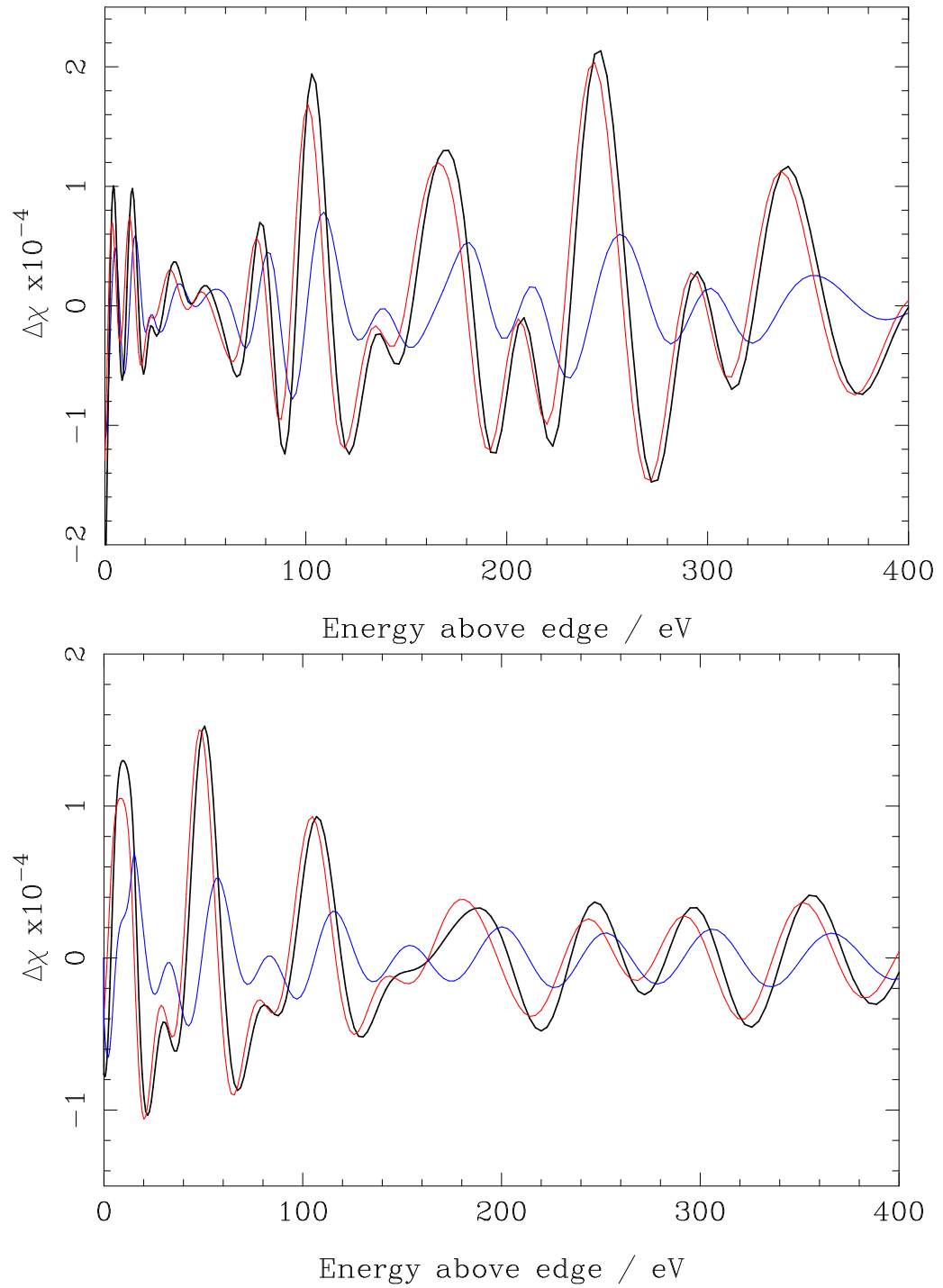


Figure 5.1: Anticipated DiffEXAFS signals, calculated using *ab initio* theory for a 1K change in  $\alpha$ -Fe (top) and  $\text{SrF}_2$  (bottom). In each graph, the blue line is the thermal expansion component of the differential fine-structure function, the red line the disorder component, and the black line the sum of the two.

	SrF <sub>2</sub>	$\alpha$ -Fe
Structure	Face-centre cubic (Fm-3m)	Body-centre cubic (Im-3m)
$a/\text{\AA}$	5.7996 [90]	2.8665 [57]
$\alpha/10^{-5} K^{-1}$	1.81 [74]	1.18 [33]
$\Theta_D/K$	420 [22]	470 [34]

Table 5.1: Crystal structure with lattice parameter,  $a$ ; thermal expansion coefficient,  $\alpha$ ; and Debye temperature,  $\Theta_D$ ; of SrF<sub>2</sub> and  $\alpha$ -Fe. References are shown in brackets.

in a 13mm die to produce a pellet 0.5mm thick, with an absorption jump of 1.0 at the Sr-K edge.

A polycrystalline iron foil was obtained from Goodfellows that had been rolled to a thickness of 9 $\mu$ m, giving an absorption jump of 2.6 at the Fe-K edge. To relieve any strain present in the material, the sample was annealed in an atmosphere of 5% hydrogen in nitrogen at 500°C for half an hour, and then cooled in freefall to room temperature at an initial rate of 2°C/min. Finally, the sample was covered with a thin coat of lacquer to protect it from oxidation. This was removed immediately before measurements were made.

## 5.4 Ensuring Observed Structure is Thermal in Origin

### 5.4.1 Checking the DiffEXAFS Baseline

Given the stringent DiffEXAFS requirements laid out in section 3.2, it is important to ensure that structure seen in a Thermal DiffEXAFS spectrum is indeed thermal in origin. There are two ways in which this can be accomplished. The first is to ensure that the DiffEXAFS is structure-less and passes through  $\Delta\chi = 0$  when  $\Delta T = 0K$ , or, quite simply, to check that there is no signal when there is no temperature modulation.

Figures 5.2 and 5.3, taken through an Fe foil, clearly breach this requirement, indicating that the beamline and modulation apparatus are not properly configured. They do however, serve to show how tricky it can be to obtain a good Thermal DiffEXAFS spectrum. Figure 5.2 shows some fraction of the Fe EXAFS leaking through into the DiffEXAFS spectrum. Examination revealed that this problem originated from the supply



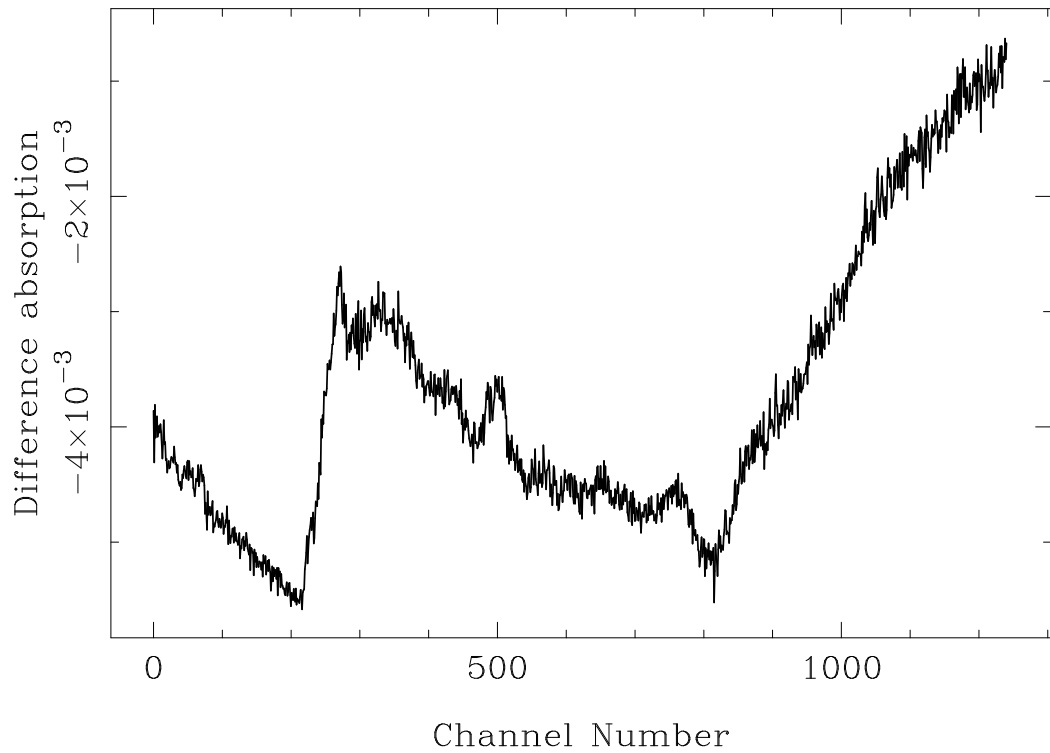


Figure 5.2: A spurious DiffEXAFS spectrum taken through Fe foil for  $\Delta T = 0\text{K}$ . The structure seen is Fe EXAFS leaking into the DiffEXAFS as a result of a change in gas pressure in ID24's third mirror upon switching the gas jets. This pressure change is about 10mbar, resulting in a change in beam attenuation of about 0.2% along the length of the mirror.

line that was providing nitrogen to both the gas jet apparatus and to ID24's third mirror. It was found that switching the gas jets back and forth induced subtle changes to the gas pressure in the supply line, which in turn changed the pressure of gas inside the third mirror, affecting the attenuation of x-rays passing through it. This change in pressure amounted to about 10mbar, inducing a change in x-ray absorption across the length of the mirror of about 0.2%. Under normal conditions, such a small change would not be detectable, but when looking at differences in absorption, the change generates a spurious signal that is two orders of magnitude larger than the Thermal DiffEXAFS signal from the sample itself, completely masking it.

Isolating the two beamline components rectified this problem, but, as seen in Figure 5.3, the baseline was still not flat. This problem also arose from beam attenuation by the nitrogen gas, but was even more subtle in origin than the first. Referring back

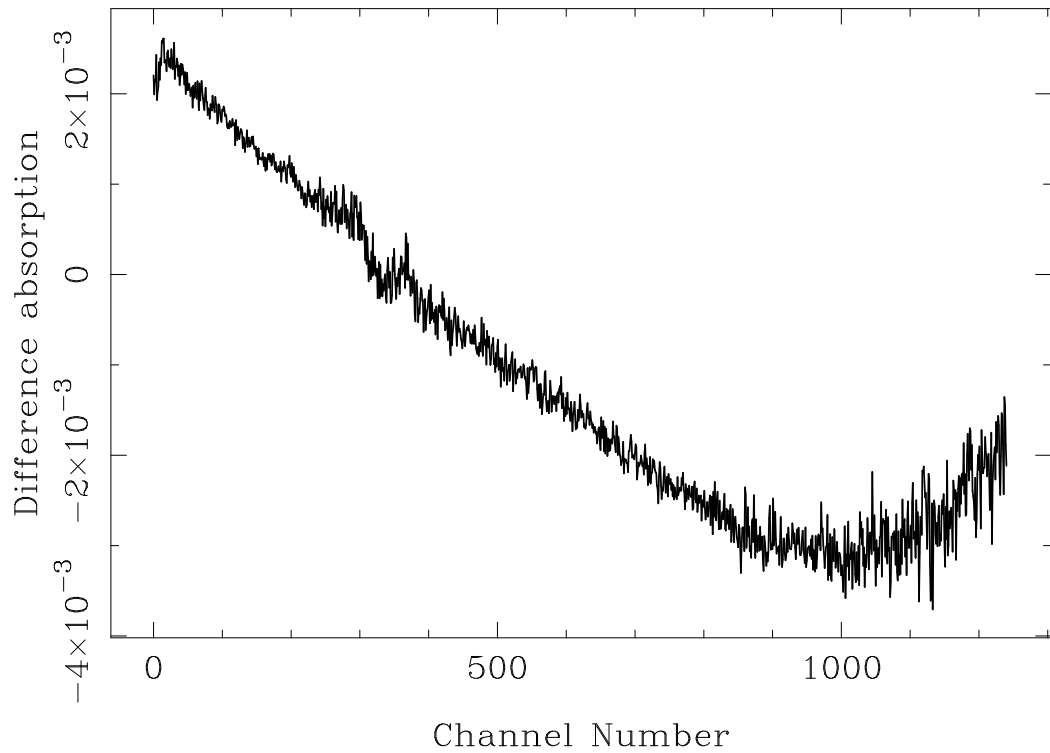


Figure 5.3: A spurious DiffEXAFS spectrum taken through Fe foil for  $\Delta T = 0\text{K}$ . Once the problem shown in Figure 5.2 was eliminated the resulting DiffEXAFS baseline was still not flat. This was due to changes in gas pressure across the spatially dispersed beam inside the sample mount.

to Figure 3.12, it can be seen that, at the reverse side of the sample mount, the gas flow is not uniform in the plane of the beam. Again, this induces changes in local gas pressure of a few mbar. Normally, on, say, a step scanning beamline, this would not be problematic, but in D-XAS, the wavelength components of the beam are correlated in the horizontal plane, and are dispersed away from the focal spot. Consequently, the asymmetric gas pressure across the beam profile causes greater attenuation at one end of the spectrum than at the other. Critically, this profile is reversed upon switching the gas jets, generating an absorption difference between the two state measurements.

This situation was remedied by blocking the central gas channel cut into the side of the sample mount, and arranging the other two such that gas flowed around the reverse side of the sample in the vertical plane rather than the horizontal. In future, this effect could also be reduced by using a lighter gas such as helium, which will have less of an

effect on the beam.

### 5.4.2 Checking the Phase-Reversed Signal

Once a flat baseline is obtained, the next task is to show that any structure seen in a Thermal DiffEXAFS spectrum is genuinely thermal in origin rather than from some other source that is correlated with the gas jet switching. This can be achieved by measuring and comparing both the standard DiffEXAFS, and the phase-reversed DiffEXAFS. In this sense, a DiffEXAFS spectrum is acquired with a  $T^+$  measurement first - such that the spectrum is then based on  $T^+$  minus the  $T^-$  measurement - and then taking another spectrum with the gas jet phase reversed, that is, by taking a  $T^-$  spectrum first. Since this changes the sign of  $\Delta T$ , equation (2.14) predicts that the observed structure should be perfectly inverted about  $\Delta\chi = 0$ . Any part of the spectrum that does not invert cannot be thermal in origin, and is therefore spurious.

Such measurements can be seen in the example shown in Figure 5.4. The inversion of the phase-reversed signal produces the distinctive eye-pattern shown. Taking the red line from Figure 5.4 and inverting it produces Figure 5.5. Since all the structure shown the two spectra are then coincident, it is all thermal in origin. These are thus good Thermal DiffEXAFS spectra.

## 5.5 Experimental Results

Figure 5.6 is a plot of both the Fe-K and Sr-K edge EXAFS (scaled in amplitude) and the associated Thermal DiffEXAFS for modulation of the order of 1K at room temperature. The spectra were put on a known energy scale using reference spectra from BM29 and the DXAS Calibration code described in section 4.2.

The time between measurements at  $T^+$  and  $T^-$  was 1.5s for the Fe measurements and 3s for the Sr measurements, with each pair of measurements repeated six hundred times and averaged to minimise statistical noise. Each complete difference measurement was repeated with the initial gas jet phase reversed, causing all observed structure to invert about  $\Delta\chi = 0$ , proving its thermal origin. These spectra have themselves been

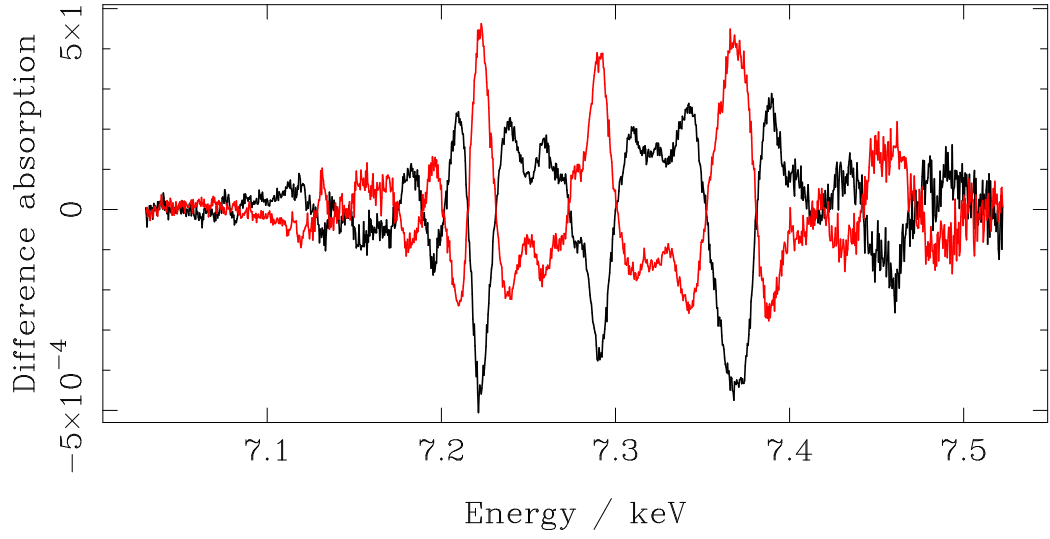


Figure 5.4: Two DiffEXAFS signals, in this case taken at the Fe-K edge in  $\alpha$ -Fe, showing the effect of gas jet phase inversion. The black plot was produced based upon  $T^+ - T^-$ , and the red upon  $T^- - T^+$ . The structure in the latter is thus inverted about  $\Delta\chi = 0$ , producing this distinctive eye-pattern.

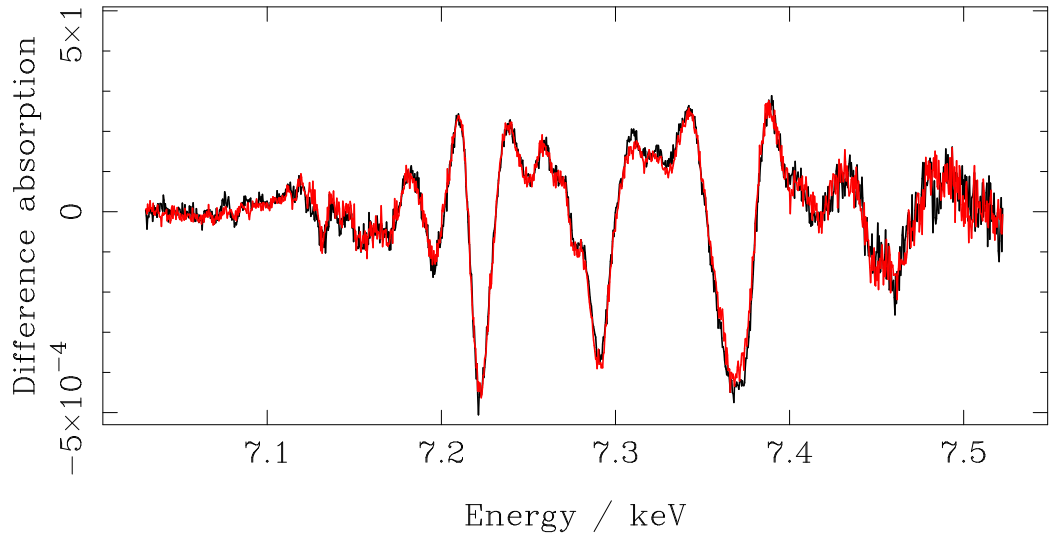


Figure 5.5: Taking the data from Figure 5.4 and inverting the phase-reversed signal shows the structure in two spectra is identical. It can therefore be stated that this structure is entirely thermal in origin, with no corruption from non-thermal sources.

inverted and plotted as the grey lines on Fig 5.6. Additional control measurements with  $\Delta T = 0.0\text{K}$  yielded no structure larger than that anticipated from our  $0.2\text{K}$  temperature error, further demonstrating the signals are thermally generated. A strong dominance of the DiffEXAFS disorder component is clearly observed given the signals are largely in phase with the original EXAFS. However, the vertical dashed-grey lines, which are centred on the three largest EXAFS peaks, reveal that the DiffEXAFS spectra are phase shifted - indicating the thermal expansion component has also been detected. As  $\Delta T$  increases, so does the amplitude of the difference signal. Normalising each to a unit temperature modulation yields the Differential EXAFS, which shows that the amplitude follows a linear scaling relationship with temperature as predicted by (2.14).

The absence of any sharp features at the edge energy, where the XAFS derivative is maximal, is testament to energy stability between  $T+$  and  $T-$  measurements of better than  $1\text{meV}$ , as required [64].

Some other spectral characteristics predicted by (2.14) are also visible. Firstly, the  $k$  and  $k^2$  dependency of the DiffEXAFS expansion and disorder terms respectively, especially in the Fe data. Whereas the three marked peaks in the EXAFS plot get progressively smaller with increasing energy, the same peaks in the DiffEXAFS plots are all of similar amplitude.

The  $s_j$  dependency of the thermal expansion term can be seen by virtue of the additional high frequency structure present in the DiffEXAFS, indicative of scattering from paths with large  $s_j$ , that is not seen in the conventional EXAFS.

The  $\text{SrF}_2$  data shown in Figure 5.6 were acquired during ESRF experiment MI-740, the first ever Thermal DiffEXAFS experiment, using the sputtered thermopile sample mount described in section 3.7.1. By contrast, the Fe data were taken during experiment MI-803, which exploited the upgraded sample mount described in section 3.7.2. Some Fe data were also taken with the sputtered thermopile during MI-740, and are shown alongside Fe data from MI-803 in Figure 5.7. The signal from the latter experiment is clearly an improvement on the initial signal. Some of the improvement, in terms of statistical noise for instance, is due to beam differences between experiments; MI-740 being carried out during the ESRF's 16-bunch operation mode at  $100\text{mA}$  ring current,

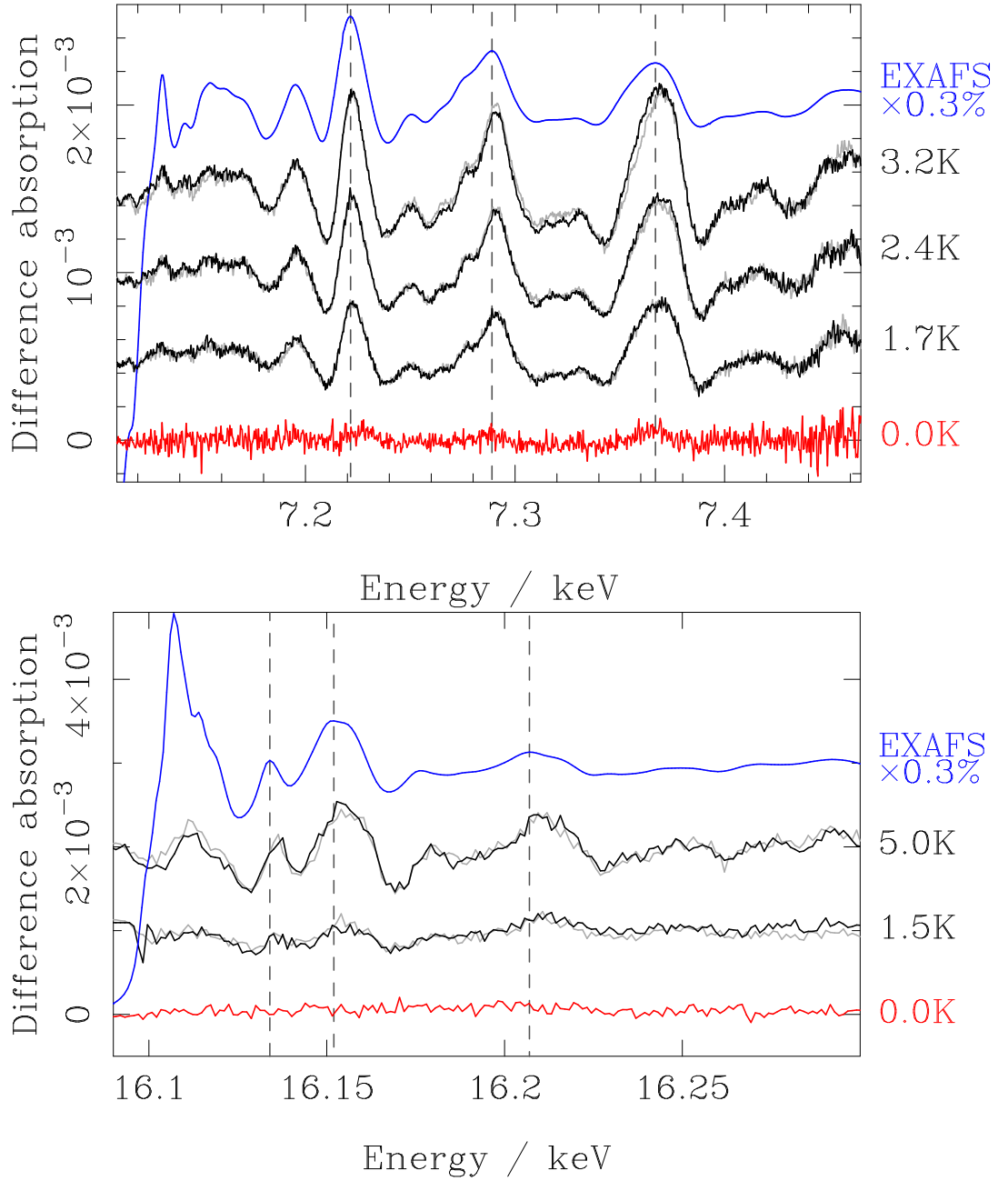


Figure 5.6: Experimental EXAFS and DiffEXAFS for the K-edges of  $\alpha$ -Fe (top graph) and  $\text{SrF}_2$  (bottom graph) at room temperature. The EXAFS plots have been scaled to 0.3% of their original amplitude so as to be of comparable size to the difference signals. Temperature modulation in the difference spectra is accurate to  $\pm 0.2\text{K}$ . The gray plots are the inverted gas jet phase-reversed signals, which are essentially identical to the black plots, proving the thermal origin of the signal. The dashed vertical lines, which are centred on peaks in the EXAFS plots, highlight the phase shift of the difference signals with respect to the EXAFS.

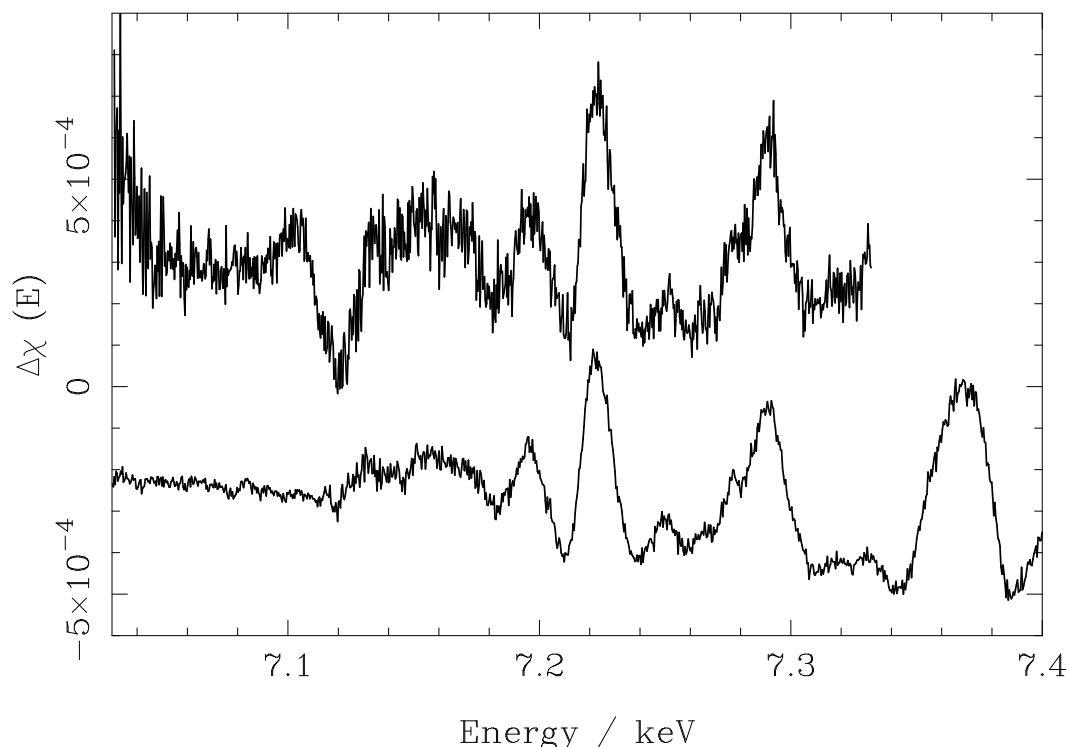


Figure 5.7: A comparison between Difference EXAFS data taken, under similar conditions, through Fe foil during experiment MI-740 (top) and MI-803 (bottom). The upgraded sample mount used in MI-803, which allowed the time between measurements to be reduced to about 1.5s, yielded significantly better data.

and MI-803 during Uniform filling mode at 200mA. However, other improvements result from the upgraded sample environment.

Samples used during MI-803 were about four to five times smaller in mass than could have been used with the sputtered thermopile. This reduction, combined with the upgraded mount's back-face sample heating, improved the thermal response time of the sample when switching gas jets, allowing the delay between + and - measurements to be reduced from 4.0s to 1.5s. This reduced the influence of beam drift between the two measurements removing some spurious spectral features seen when using the thermopile. The protective sheath of the upgraded mount improved the thermal stability of the sample by eliminating atmospheric effects, resulting in greater reproducibility between different DiffEXAFS spectra, and a reduction in temperature measurement errors that affect normalisation of the signal.

## 5.6 Extraction of the Thermal Expansion Coefficients

### 5.6.1 Generation of Theory Phase and Amplitude Information

As described in section 4.3.3, the first stage to extracting thermal expansion coefficients is to use FEFF to generate scattering phase and amplitude information.

For analysis of the Fe data, this information was calculated in the range  $0 \leq k \leq 20 \text{\AA}^{-1}$ . The  $\alpha$ -Fe BCC crystal structure supplied to FEFF was generated using the lattice parameter at room temperature  $a = 2.8665 \text{\AA}$  [57]. Atomic potentials were modelled according to Hedin and Lundqvist [29]. Calculated scattering paths (which included multiple scattering paths) were filtered, limiting the minimum path amplitude to 4% of the largest path amplitude and the maximum total path length to  $5.0 \text{\AA}$ , leaving 12 significant paths. This relatively low maximum scattering path length was selected in anticipation of Fourier filtering the experimental data to  $5.0 \text{\AA}$ , or the first 5 single-scattering paths, when fitting the conventional EXAFS.

Similarly, for  $\text{SrF}_2$ , FEFF calculated the phase and amplitude information, again between  $0 \leq k \leq 20 \text{\AA}^{-1}$ , using the lattice parameter at room temperature  $a = 5.7996 \text{\AA}$  [90]. Filtering limited paths to no more than  $9.1 \text{\AA}$  in length, and again required their amplitude to be at least 3% the amplitude of the largest path; producing 38 significant paths.

The FEFF input files used to generate these data, along with lists of the scattering paths returned, are given in Appendix C.1.

### 5.6.2 Establishing a Perturbation Reference Point

Once the scattering phase and amplitude information has been calculated, FitChi2 was used to find the remaining EXAFS factors, again described in section 4.3.3.

As shown in Figure 5.8, the Fe and  $\text{SrF}_2$  data were fitted from  $60 \leq E' \leq 740 \text{eV}$  and  $40 \leq E' \leq 450 \text{eV}$  respectively, where  $E'$  is the energy above the edge. Treatment of the scattering paths contributing to the fine-structure was different in each case.

At the Sr-K edge in  $\text{SrF}_2$ , a good fit was obtained without the need for Fourier filtering to eliminate high-order paths, and so all 38 paths returned by FEFF up to  $9.1 \text{\AA}$  were considered. Parameter correlation remained low, with the typical inter-parameter cor-



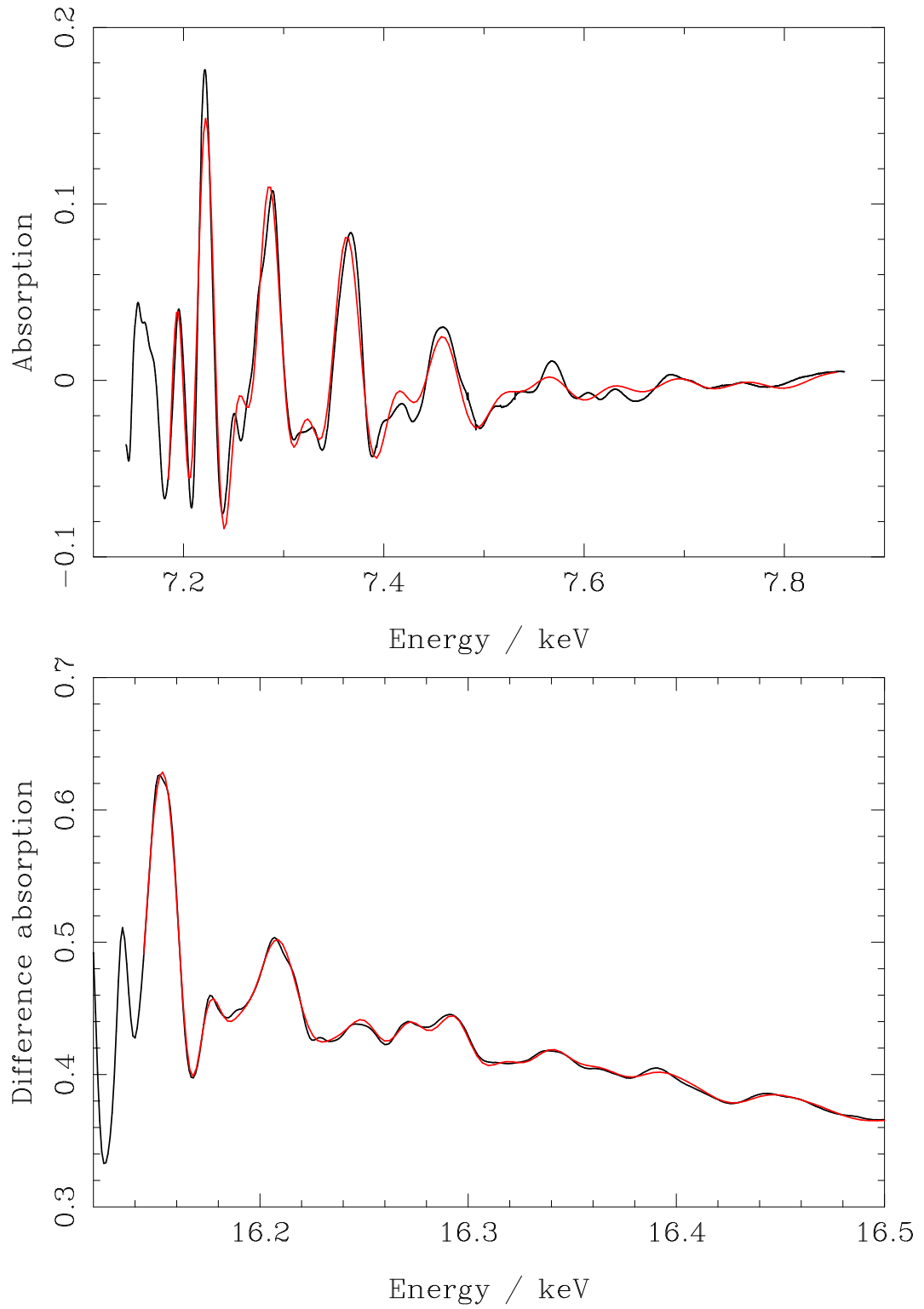


Figure 5.8: Theory fit to experimental EXAFS, taken on BM29, at the Fe-K edge in  $\alpha$ -Fe (top) and the Sr-K edge in  $\text{SrF}_2$  (bottom). The theory spectra, shown in red, were calculated as described in section 5.6.2. The experimental spectra are shown in black.

Fe EXAFS		SrF <sub>2</sub> EXAFS	
Parameter	Fitted value	Parameter	Fitted value
$\sigma_1^2/10^{-3}\text{\AA}^2$	$6.5 \pm 0.2$	$\sigma_1^2/10^{-3}\text{\AA}^2$	$9.6 \pm 0.1$
$\sigma_2^2/10^{-3}\text{\AA}^2$	$5.8 \pm 0.2$	$\sigma_2^2/10^{-3}\text{\AA}^2$	$7 \pm 3$
$\sigma_3^2/10^{-3}\text{\AA}^2$	$7.2 \pm 0.4$	$\sigma_3^2/10^{-3}\text{\AA}^2$	$10.4 \pm 0.4$
$S_0^2$	$0.94 \pm 0.02$	$S_0^2$	$0.88 \pm 0.02$
$E_0$ eV	$7121^1$	$E_0$ eV	$16103.7 \pm 0.1$

Table 5.2: The primary parameters found when fitting the Fe and SrF<sub>2</sub> conventional EXAFS. The  $\sigma_j^2$  shown are for the first three single-scattering paths, where  $j = 1, 2, 3$  respectively.

relation coefficient being around 0.2. The most significant fit parameters are shown in Table 5.2.

By contrast, a Fourier filter at the Fe-K edge was found to be absolutely necessary. Here, scattering paths were limited a maximum length of  $5.0\text{\AA}$ . Again the typical inter-parameter correlation coefficient was around 0.2, which, along with the satisfaction of equation 4.19, testifies to good fit conditioning. The results for  $\sigma_j^2$  were returned to FEFF, as described in section 4.3.3, and the fit iterated 21 times to reach self-consistency in Debye-Waller factors based on the FEFF and FitChi representations. The most significant parameters are again shown in Table 5.2, which reveals an interesting trend.

From harmonic theory, and based upon a model such as the Correlated Debye Model [83], Debye-Waller factors should, for single-scattering paths at least, increase monotonically with increasing scattering path length. This would make  $\sigma_j^2$  for the second shell single-scattering anomalously low. However, such a trend is consistent with Born-von Karman lattice dynamics calculations performed by Jeong et al. [32], apparently confirming their results (for Fe at least). As a consequence, changes to Debye-Waller factors, observed through  $\partial\sigma_j^2/\partial T$ , should also exhibit this trend.

The full configuration files for these fits, along with the output data, are given in Appendix C.1.

### 5.6.3 Fitting the Differential Fine-Structure

With a reference point defined, the thermally induced perturbations of (2.14) were determined.

For the Fe data, the experimental DiffEXAFS spectra were Fourier filtered to the region  $0 \leq R \leq 5\text{\AA}$  - the upper limit being selected to eliminate paths with low orthogonality in R-space. Theory spectra, generated from the 12 significant scattering paths calculated by FEFF for the same region, were then fitted to these filtered DiffEXAFS spectra in order to determine  $\alpha$  and  $\partial\sigma_j^2/\partial T$ . These corresponded to both single and multiple scattering paths out to the 5th coordination shell, although only the first four single-scattering paths were found to contribute significantly to the DiffEXAFS signal.

The statistical noise in each experimental spectrum was estimated by defining a maximum effective scattering radius for EXAFS contributions of  $30\text{\AA}$ , and then processing the spectrum as described in section 4.4.2

Similarly, for  $\text{SrF}_2$ , the DiffEXAFS were Fourier filtered to  $0 \leq R \leq 4.57\text{\AA}$ , leaving 3 significant paths - the first three single-scattering paths - and the noise extracted based on a maximum EXAFS scattering radius of  $15\text{\AA}$ .

Figure 5.9 shows the theory fit to experiment for the filtered Fe and  $\text{SrF}_2$  DiffEXAFS data based on equation (2.14). The corresponding parameters are shown in Table 5.3. Averaging the thermal expansion coefficient for each sample material over all its DiffEXAFS measurements yields  $\alpha = (11.6 \pm 0.4) \times 10^{-6} K^{-1}$  for Fe and  $\alpha = (19 \pm 2) \times 10^{-6} K^{-1}$  for  $\text{SrF}_2$ , which agree with the accepted values of  $\alpha = 11.8 \times 10^{-6} K^{-1}$  and  $\alpha = 18.1 \times 10^{-6} K^{-1}$  respectively [52] [74]. Given the error of  $5 \times 10^{-7} K^{-1}$  in the Fe thermal expansion coefficient over an average  $\Delta T$  of  $2.6 K$ , we claim to be able to resolve thermally induced atomic displacements to an accuracy of about  $0.3 fm$ .

## 5.7 Discussion of Thermal Expansion Measurements

With the results shown above, it is possible to conclude that DiffEXAFS is a viable technique for the measurement of thermally induced atomic displacements. Here mea-

---

<sup>1</sup>Best results were produced when  $E_0$  was fixed at 7121eV, corresponding to the inflection point on the dipole absorption edge.

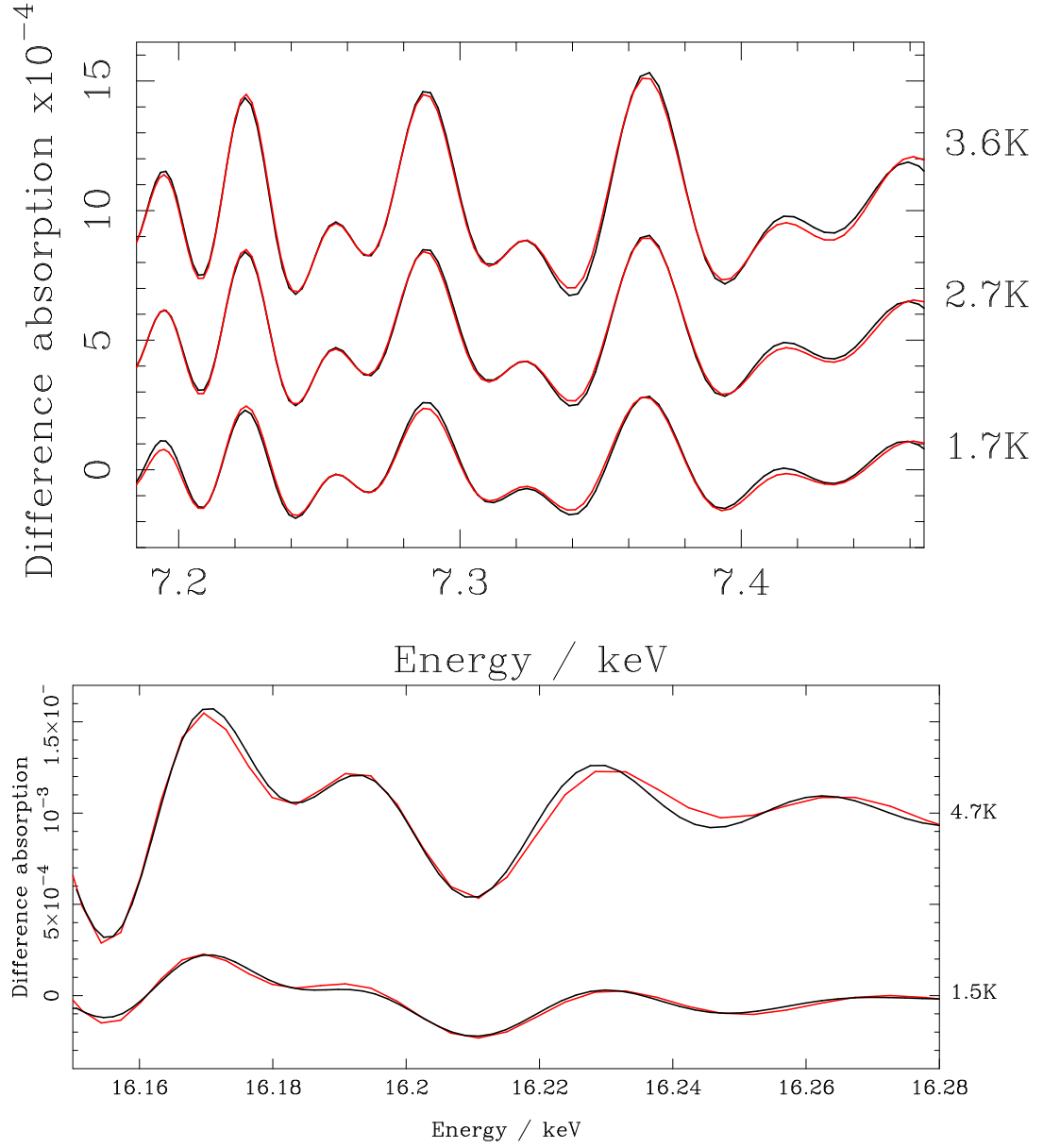


Figure 5.9: Fourier filtered experimental Difference EXAFS spectra (black lines) for  $\alpha$ -Fe (top graph) and SrF<sub>2</sub> (bottom graph), which have been fitted to the DiffEXAFS fine-structure function (2.14) (red lines).  $\Delta T$  for each spectrum is given to the right. The associated fit parameters are shown in table 5.3.

Fe DiffEXAFS			
Parameter	$\Delta T/K$		
	$1.7 \pm 0.2$	$2.7 \pm 0.2$	$3.6 \pm 0.2$
$\alpha$	$11.1 \pm 0.9$	$12.1 \pm 0.6$	$11.5 \pm 0.5$
$\partial\sigma_1^2/\partial T$	$1.48 \pm 0.04$	$1.38 \pm 0.03$	$1.33 \pm 0.02$
$\partial\sigma_2^2/\partial T$	$1.34 \pm 0.08$	$1.04 \pm 0.06$	$1.09 \pm 0.04$
$\partial\sigma_3^2/\partial T$	$2.2 \pm 0.1$	$1.60 \pm 0.07$	$1.47 \pm 0.06$
$\partial\sigma_4^2/\partial T$	$2.0 \pm 0.1$	$1.5 \pm 0.1$	$1.38 \pm 0.08$

SrF <sub>2</sub> DiffEXAFS		
Parameter	$\Delta T/K$	
	$1.5 \pm 0.2$	$4.7 \pm 0.2$
$\alpha$	$20 \pm 3$	$18 \pm 1$
$\partial\sigma_1^2/\partial T$	$2.04 \pm 0.09$	$1.85 \pm 0.05$
$\partial\sigma_2^2/\partial T$	$3.1 \pm 0.4$	$2.0 \pm 0.2$
$\partial\sigma_3^2/\partial T$	$2.2 \pm 0.5$	$3.4 \pm 0.2$

Table 5.3: The DiffEXAFS parameters for  $\alpha$ -Fe and SrF<sub>2</sub>.  $\alpha$  is in units of  $10^{-6}K^{-1}$  and  $\partial\sigma_j^2/\partial T$  in  $10^{-5}\text{\AA}^2K^{-1}$ . Note that errors for  $\alpha$  and the  $\partial\sigma_j^2$  are based on the fit errors only and do not include possible errors from  $\Delta T$ .

measurements of thermal expansion in some simple materials has been demonstrated. The technique presented may also be applied to more complex crystalline systems or even amorphous systems, with minimal changes. Indeed, the potential for studying amorphous systems presents numerous opportunities where other techniques, such as diffraction, struggle.

Presently, the factors limiting the accuracy of the measured thermal expansion coefficients come partly from the modulation apparatus and partly from the beamline.

The modulation apparatus is currently only able to set the sample temperature with an accuracy of 0.2K (although the actual temperature may be measured more accurately with the thermocouple attached to the sample). Improving this will improve the average DiffEXAFS signal calculated over many pairs of +/- measurements. The speed at which the sample temperature may be changed defines the modulation period, and so the degree of beam drift between measurements at + and - states. Although the upgraded sample mount reduced the modulation period over that of the initial, thermopile design, a further reduction in the modulation period would improve the signal further.

As for the beamline, fractional statistical noise in the measured spectra is not currently limited by the flux emitted from ID24's source, but by the sensitivity of its detector. The CCD detector currently in use employs a 16-bit buffer for data storage and transfer, limiting the CCD to just 65536 discrete digital levels, and thus its sensitivity to one part in  $10^{-5}$ . Reducing the quantisation limit of the CCD could potentially improve the the statistical noise by an order of magnitude since flux is available for fractional statistical noise in photon counting of the order of  $10^{-6}$  in a few hours.

Whilst, in this chapter, Thermal DiffEXAFS has been proven to work in practice rather than just in theory, the true power of the technique lies in the measurement of non-linear phenomena such as phase-transitions. With displacements detectable over temperature changes of about one Kelvin, high-resolution measurements of atomic motion may be made through transition regions, which until now has not been possible with any other x-ray spectroscopic technique.

## Chapter 6

# Differential XRD to complement DiffEXAFS

### 6.1 Introduction

Differential X-ray Diffraction (DiffXRD) was discovered by chance during initial Thermal DiffEXAFS measurements on ID24, but has since proven to be a useful tool to complement information obtained from DiffEXAFS data [77].

DiffXRD uses the same experimental apparatus and measurement technique as its EXAFS counterpart. The difference however, is that the sample through which transmission absorption measurements are taken (normally polycrystalline or amorphous) is replaced with its single crystal counterpart.

In kinematic diffraction theory, this introduces Laue diffraction features to the measured transmission intensity, where x-rays at certain energies are scattered out of the main line of the beam. These scattered photons do not enter the detector at the end of the beamline, causing an anomalous drop in transmitted intensity. This is seen as an apparent increase in x-ray absorption, which is observed as a discrete peak, independent of any true absorption fine-structure.

Such features make XAFS analysis difficult<sup>1</sup>. However, being from diffraction in origin,

---

<sup>1</sup>Diffraction features may be removed from XAS spectra with, for instance, the technique given in [91].

they contain information on the structure of the sample material, and hence are sensitive to atomic perturbations in the same way as DiffEXAFS, albeit on a structurally averaged scale rather than a local atomic scale.

From Bragg's law and  $E = hc/\lambda$  it is easy to show that for a given diffraction peak

$$\left(\frac{\Delta E}{E}\right)_{hkl} = -\left(\frac{\Delta d}{d}\right)_{hkl} \quad (6.1)$$

Where  $\Delta E/E$  is the observed fractional change in peak position due to a relative change in inter-planar spacing,  $\Delta d/d$ , corresponding to the Miller indices  $hkl$ . In the case of, say, thermal expansion, this change is in turn

$$\left(\frac{\Delta E}{E}\right)_{hkl} = -\alpha_{ij}\Delta T \quad (6.2)$$

where, as in (2.14),  $\alpha_{ij}$  are the coefficients of the thermal expansion tensor, each of which can be obtained by the analysis of an appropriate diffraction peak. Again, von Neumann's Principle may be applied to reduce the number of independent coefficients. For cubic crystals, this again results in one independent parameter, so  $\Delta E/E$  is the same for all diffraction peaks.

In order to accurately determine  $\Delta d$  using conventional XRD techniques, it is typically necessary to vary the temperature of the sample by many tens of Kelvin between measurements such that a clear peak shift can be observed and thus measured. However, by utilising the same measurement technique as DiffEXAFS - namely taking the difference between two spectra acquired in a short space of time in high stability, low noise conditions, where the only change between measurements is the modulation of a given sample property - then it is possible to detect extremely subtle shifts, and so obtain  $\Delta E$  over temperature changes of the order of 1K or less.

Thus, simply by substituting a DiffEXAFS sample with its single crystal counterpart, it is possible to obtain an independent measure of crystal perturbations without having to change any other part of the experimental setup.



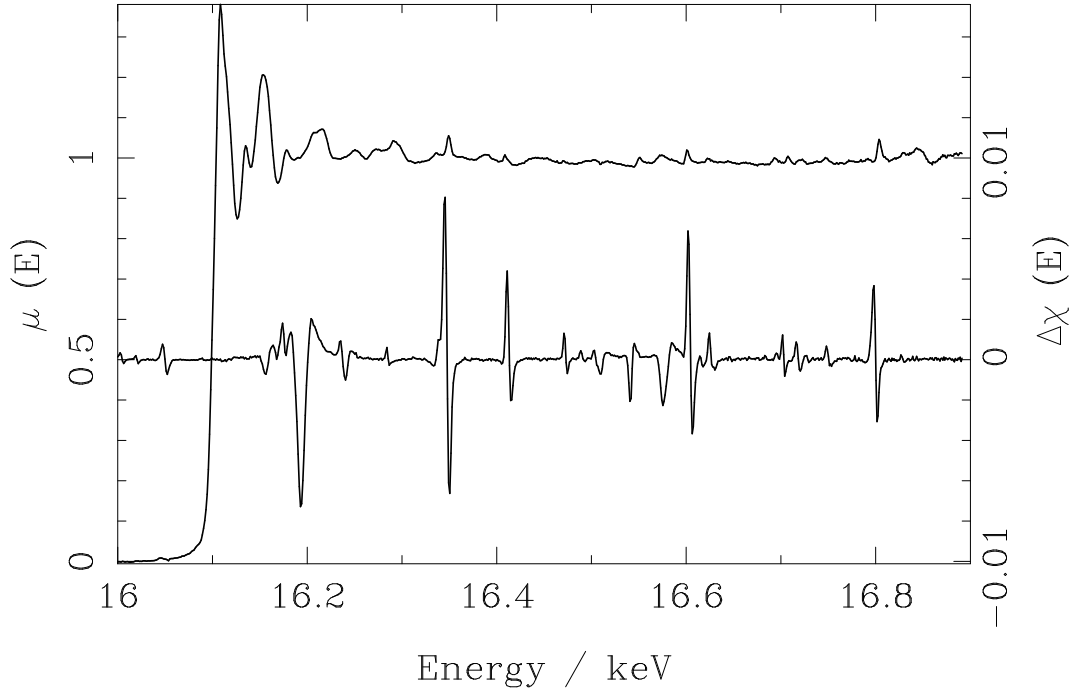


Figure 6.1: The Sr-K edge measured in transmission on ID24 through a single crystal of  $\text{SrF}_2$  (top plot with left scale). The amplitude has been normalised to unit edge jump. Diffraction glitches are clearly present on the absorption fine-structure. As the temperature of the specimen is changed by 1K at room temperature, these glitches shift in energy due to thermal expansion in the crystal, producing the DiffXRD signal shown below (right scale).

## 6.2 Experiment

The powdered  $\text{SrF}_2$  sample used for DiffEXAFS measurements was replaced with a single-crystal sample, cleaved along its 111 lattice planes, producing a section about  $5 \times 5$  mm big and  $70\mu\text{m}$  thick, with an absorption jump of 1.9 at the Sr-K edge. The normalised absorption spectrum from this sample is plotted in Figure 6.1 along with its corresponding DiffXRD signal for a 1K modulation. Peaks generated by the effect of Laue diffraction removing flux from the beam are clearly present in the observed signal.

Given  $\text{SrF}_2$  has a cubic crystal structure, the thermal expansion is described by just one coefficient. The temperature shifts of all the diffraction peaks will, therefore, exhibit the same change in position independent of the Miller indices of the reflections.

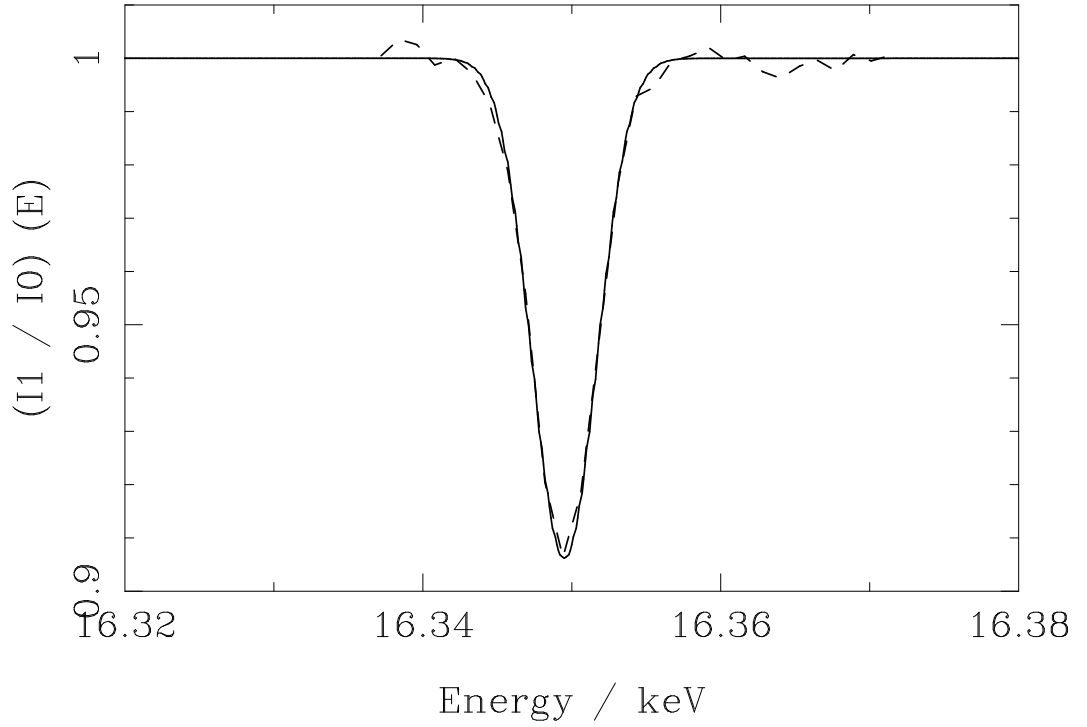


Figure 6.2: The diffraction glitch (dashed line) at about 16.35keV is extracted from the x-ray *transmission* spectrum, and the background subtracted. A Gaussian is fitted to the glitch (solid line) to determine its centroid energy, width at half maximum, and relative height.

The absence of any difference features at the same energy as the Sr-K edge in Figure 6.1 is testament to energy stability of the beam between the two absorption measurements used to construct the DiffXRD signal. The observed differences are therefore from a genuine change in observed x-ray absorption rather than from drifts in the beam between measurements.

The diffraction peak at 16.35keV, corresponding to the largest feature in the DiffXRD signal, was extracted and transformed back to transmission space using  $I_1/I_0 = \exp(-\mu x)$ . A normalised Gaussian was then fitted to the transmission spectrum to determine its centroid energy, width at half-maximum, and height. This fit is shown in Figure 6.2, with the parameters listed in Table 6.1.

Whilst diffraction peaks themselves are Lorentzian in form, the energy resolution of a beamline can, under certain conditions, cause some broadening of the peaks, transforming them to Gaussians. This is the case on ID24 at energies in excess of about

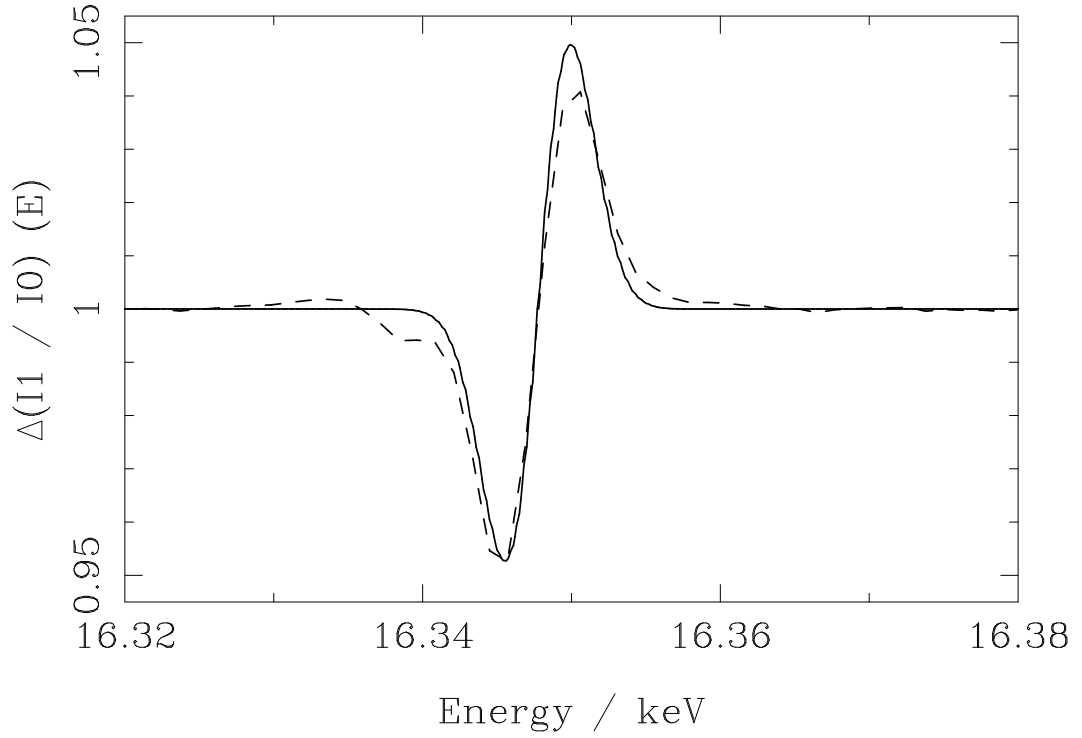


Figure 6.3: The DiffXRD transmission signal obtained for  $\Delta T = 6K$  in the energy region of the glitch shown in Fig 6.2 (dashed line). The difference between a pair of Gaussians of width and height determined by the fit in Fig 6.2, and offset in energy relative to one another, are fitted to the feature (solid line); the energy offset being related to the fractional change in lattice spacing.

15keV.

Although the convolution of an instrument function with the diffraction signal clearly alters the peak's observed width and height and thus any fitted parameters, this is not a problem from the point of view of DiffXRD. As shown in equation (6.1), structural changes in the sample material are derived from a change in the measured energy of a given peak. Therefore, the only requirement for DiffXRD is that the peak retains its shape between the two measurements under different sample conditions, allowing this shift to be determined.

The DiffXRD signal, shown in Figure 6.3, was obtained for a temperature change in the sample of 6K rather than 1K; increasing the degree of peak movement between measurements, and thus making the difference feature larger and easier to define. Given the degree of movement is linearly related to the change in temperature by (6.2) (for

<b>Conventional Gaussian Fit</b>	
Parameter	Value
Centroid / eV	$16349.505 \pm 0.002$
FWHM / eV	$2.137 \pm 0.002$
Relative height	$(-9.3782 \pm 0.0003) \times 10^{-2}$

<b>DiffXRD Fit</b>	
Parameter	Value
Centroid / eV	$16347.74 \pm 0.07$
Gaussian Separation / eV	$1.84 \pm 0.08$
Thermal Expansion / $\times 10^{-6} \text{K}^{-1}$	$18.7 \pm 0.8$

Table 6.1: Fitted parameters for the diffraction peak shown in Figure 6.2 and for the corresponding DiffXRD feature shown in Figure 6.3. The thermal expansion coefficient has been derived using equation (6.2). Energies shown are not absolute energies, but based on a calibration with respect to another spectrum of known calibration. The errors shown are for the Gaussian and DiffXRD fits only and do not incorporate errors in calibration.

small temperature changes), the energy shift per Kelvin may be restored by dividing the observed shift by the temperature difference. Using the Gaussian width and height parameters from Table 6.1 to fix the shape of the diffraction peak to that seen in Figure 6.2, the DiffXRD feature was characterised by calculating the difference in observed absorption between two such peaks, slightly offset in energy relative to one another, giving the separation shown at the bottom of Table 6.1. The centroid of the difference feature is defined as half way between the two constituent peak centroids, and thus is not the same as that of the initial, single Gaussian fit.

Using equation (6.2), the thermal expansion coefficient of  $\text{SrF}_2$  was found to be  $(18.7 \pm 0.8) \times 10^{-6} \text{K}^{-1}$ ; in agreement with the published value of  $18.1 \times 10^{-6}$  at 300K [74], and in agreement with the corresponding DiffEXAFS measurements in section 5.6.

### 6.3 Discussion

Clearly, one advantage of DiffXRD over DiffEXAFS is the sheer simplicity of the technique; equation (6.1) being considerably more straightforward to extract structural changes from than (2.14).

However, DiffXRD cannot be considered a replacement for DiffEXAFS, in spite of this, since it is hindered by the same limitations that affect standard XRD measurements. Firstly, the technique cannot be applied to disordered or amorphous systems unlike EXAFS, but most importantly, structural information derived from DiffXRD is based on mean atomic perturbations over a periodic crystal structure. It does not yield information on *local* atomic perturbations - one of the real strengths of DiffEXAFS.

DiffXRD should therefore be considered complementary to DiffEXAFS. Simply by substituting a DiffEXAFS sample with its single crystal counterpart (where available) and taking the same difference measurements with the same experimental apparatus, it is possible to obtain an independent measure of atomic perturbations to verify those from DiffEXAFS. Conversely, it could also be used to identify and quantify any discrepancies between local atomic perturbations and average (macroscopic) perturbations via a common experimental arrangement.

## Chapter 7

# Differential EXAFS to Study Phase Transitions

### 7.1 Introduction

In Chapter 5, thermal expansion measurements proved the viability of Thermal DiffEXAFS in measuring atomic perturbations on a femtometre scale. This chapter takes Thermal DiffEXAFS further, with a study of thermally induced structural changes around the Martensitic phase transition in  $\text{Ni}_2\text{MnGa}$  [98]. Samples for this experiment were supplied by M. Pasquale of IEN Galileo Ferraris, Torino, Italy.

Such studies are where the true power of Thermal DiffEXAFS is exploited. No other spectroscopic technique is capable of probing atomic perturbations in the region leading up to, through, and beyond a phase transition with single Kelvin precision. Other techniques that are capable of similar resolution, such as diffraction, do not reveal information on *local* atomic structure.

Even if some transition were found to induce perturbations large enough to be probed in a number of individual steps with conventional EXAFS, DiffEXAFS will always still offer around two orders of magnitude greater sensitivity and thus, potentially, a hundred times more sampling points across that transition region. Thus, DiffEXAFS presents a unique opportunity to develop a better understanding of phase transitions from a local perspective.

At the same time, though, several points must be taken into consideration regarding the theoretical model of Thermal DiffEXAFS laid out in section 2.5.

Firstly, with thermal expansion measurements, it was reasonable to assume that the coefficients of the thermal strain tensor,  $\alpha_{mn}$  in equation (2.14), held a constant value over some small range of temperature. This approximation can be extended to regions surrounding phase transitions, but only with care. In the region of the primary transition temperature  $T_p$ , structural changes become significantly dependent upon the absolute temperature of the sample. Therefore, this approximation will become progressively worse as  $T$  goes to  $T_p$ , and the structural discontinuity represented by the transition, approached.

The effects of this can be mitigated to a certain extent by progressively reducing the magnitude of temperature modulation when approaching  $T_p$ , but such a reduction is reliant upon the precision with which the sample temperature may be set, and its subsequent stability.

Should this approximation fail, higher order terms must be considered in the thermal Taylor expansion of the fine-structure function. However, for a suitably small temperature modulation it is still possible to approximate the differential fine-structure by a first order Taylor expansion as laid out in equation (2.14).

Even in this case though, the differential structure is now dominated by atomic strains relating to the phase transition rather than thermal expansion. As a result, the strain tensor  $\alpha_{mn}$  in (2.14) is no longer the linear thermal expansion tensor, but a general thermal strain tensor incorporating the phase transition. Indeed, thermal expansion contributions under these conditions are negligible.

Further complications may arise in that previously, since the point group symmetry of the crystal under study was known, it was possible to reduce the number of independent parameters in  $\alpha_{mn}$  by virtue of von Neumann's Principle. Close to a phase transition however, where the structure is inherently unstable, such symmetry may be broken; not just in the sense of changing from some low-T to some high-T structure, but also in the presence of onset phenomena.

For instance in  $\text{Ni}_2\text{MnGa}$ , the structure changes from a body-centred tetragonal Marten-

site to an  $L2_1$  cubic Austenite around the Martensitic transition, but depending upon the exact composition of the sample, some studies have revealed varying tetragonal or orthorhombic structures close to the high-T side of the transition. These include [94][101][88].

## 7.2 $Ni_2MnGa$ and its Martensitic Phase Transition

$Ni_2MnGa$  is a Heusler-alloy [30], one of the ternary inter-metallic compounds with composition  $X_2YZ$  and an  $L2_1$  cubic structure. This is true for  $Ni_2MnGa$  at room temperature at least, but neutron diffraction data taken at 77K reveals a complex, tetragonally based structure [97]. This structural transition was suspected to occur in association with a discontinuity in magnetic properties at just above 200K, which was confirmed by Webster et al. [98], who found that in stoichiometric  $Ni_2MnGa$ , a Martensitic phase transition occurs at 202K.

Unfortunately, 202K was beyond the reach of our thermal modulation apparatus, so we arranged for our samples to be slightly Ni rich, with composition  $Ni_{53}Mn_{24}Ga_{23}$ , and formed as a melt-spun ribbon [3][4]. This had the effect of increasing the transition temperature to about 324K. Throughout the remainder of this chapter, the term  $Ni_2MnGa$  will be used in reference to the sample, though this sample is in practice the Ni rich foil. Martensitic transitions are of the first-order and diffusionless. In this sense, the change in crystal structure is triggered by a change in entropy, and achieved through deformations of the parent phase. The high temperature phase is referred to as an Austenite and denoted with a  $\gamma$ , whereas the low temperature phase is a Martensite, denoted  $\alpha'$ .

Like all first-order transitions, the change in latent heat of a specimen cannot occur instantaneously, and therefore, it is possible for a mixture of phases to be present. If a Martensite is formed in a specimen by quenching, such a mixture can be frozen into its crystal structure. This then shows that the Martensitic phase exists within the specimen in the form of plates that are embedded into the residual Austenite along certain well-defined planes. These interface planes are referred to as *habit planes*, and indicate the particular habit of the Martensite relative to the phase from which it formed [95].



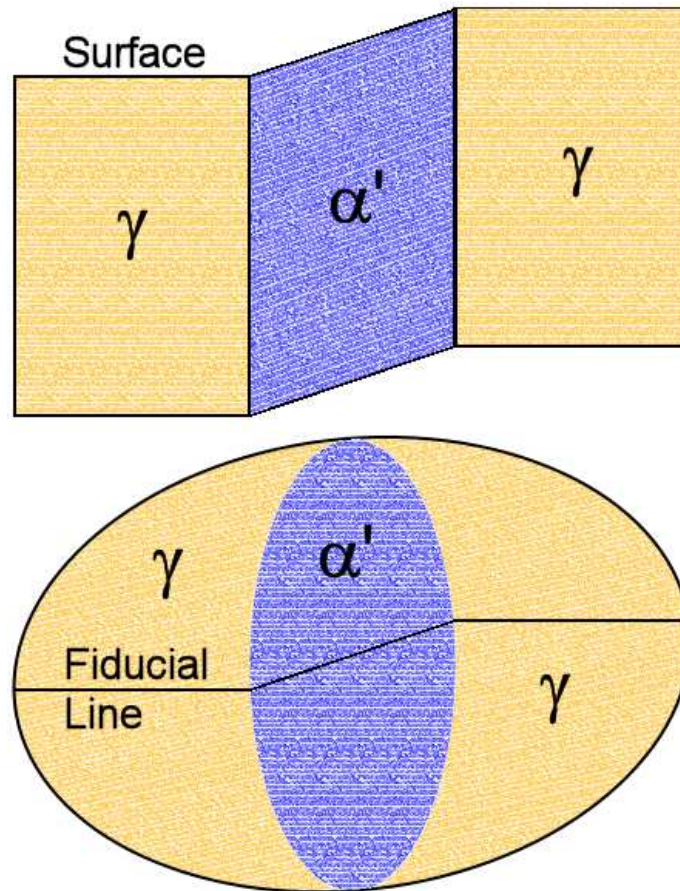


Figure 7.1: A schematic representation of shape changes observed in specimens containing Martensites. The top diagram shows the effect of surface upheaval in the region of a Martensite, and the bottom, surface skewing, which bends any fiducial lines. Both the upheaval and skewing are regular and without distortion.

At the surface of the specimen, these planes can denote regions of varying relief. Assuming the original Austenite had a plane surface, upheavals occur where Martensites are formed as shown schematically in Figure 7.1. Similarly, an initially straight fiducial line can become bent when the surface runs along a crystallographic plane perpendicular to this. Neither of these deformations are irregular; the deformed surface remains plane, and deformed line remains straight, each with a definite angle across the habit plane.

This, therefore, requires definite orientation relations to exist between the Martensite and Austenite. Thus, Martensitic transitions are *linear*; vectors and planes in one phase

can be transformed to vectors and planes in the other via a linear matrix [96].

This also leads to the conclusion that Martensitic transitions result from coordinated and ordered rearrangement of the atomic configuration [49]. Therefore, atomic movements are not free, but the motion of neighbouring atoms are coordinated as the transition interface moves. Indeed, this in turn, leads to the definition of a Martensitic transformation. A Martensitic transformation is a phase transformation that occurs by cooperative atomic movements [50], with the product being a Martensite. The features described above are criteria for assessing the presence of a Martensite.

However, the question remains as to how - in the case of, for instance,  $\text{Ni}_2\text{MnGa}$  - the Austenite face-centred cubic phase transforms into a body-centred tetragonal Martensite. In 1924, Bain proposed that the f.c.c. structure could be considered tetragonal, with a  $c/a$  ratio of one [9]. Thus, the b.c.t. structure could be obtained by a compression along one axis, and uniform expansion along the two perpendicular to it, thus reducing the axial ratio. This is the so called *Bain strain*. It is a key part of Martensitic transformations, but is not enough by itself to describe all the associated phenomena.

Since Martensitic transitions occur by cooperative atomic motion, the presence of habit planes requires the interface between Austenite and Martensite phases to be highly coherent, with no distortions or rotations. There must, therefore, be an *invariant plane*, along which deformations are referred to as *invariant plane strains*. However, it can be shown [51] that Bain strain alone cannot guarantee the presence of such invariant planes. Thus, in order for the Martensite to possess both the correct crystal structure *and* the correct shape to satisfy boundary conditions observed along habit planes, internal shearing must occur in addition to Bain strain related deformations.

This shearing must be microscopically inhomogeneous such that it does not change the crystal structure, but homogeneous on a macroscopic scale. This may be accomplished by either *slipping* or *twinning* as shown schematically in Figure 7.2. In  $\text{Ni}_2\text{MnGa}$ , the primary mechanism for this lattice-invariant shear is twinning [12], which makes it an attractive shape memory alloy [92][14].

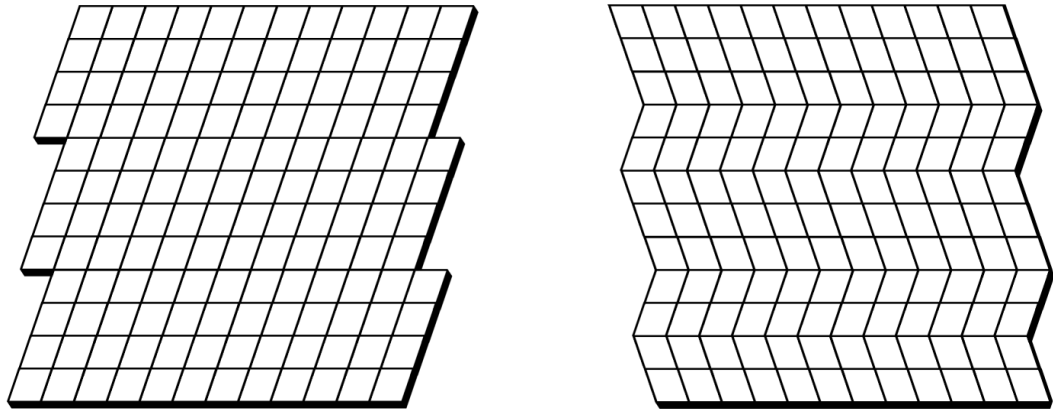


Figure 7.2: A microscopic schematic representation of lattice invariant shears that must occur as part of a Martensitic phase transformation. On the left are slip shear planes, and on the right twinned shear planes. Habit planes can be imagined to run roughly vertically along each side of these units, appearing homogeneous on a macroscopic scale. In  $\text{Ni}_2\text{MnGa}$ , the primary mechanism for lattice-invariant shear is twinning [12].

### 7.3 Experimental Results

Figure 7.3 shows Differential EXAFS spectra (i.e. normalised to a 1K modulation) taken at the Ni-K edge and heating through the Martensitic phase transition in  $\text{Ni}_2\text{MnGa}$ . Each spectrum was acquired for temperature modulation of between 1.1 and 3.3K, with the mean absolute temperature shown next to each spectrum. The time between taking spectra at  $T+$  and  $T-$  (and vice versa) was 1.5s. As with the thermal expansion measurements, the error in setting each gas jet temperature was  $\pm 0.2\text{K}$ .

The six spectra just below the horizontal grey line were taken in the Martensite phase, and the four above, in the Austenite phase. The primary transition,  $T_p$ , occurs at about 324K, but related structural perturbations can clearly be seen as much as 20K below that. It is worth noting that the spectrum at 305K, though small compared to those closer to  $T_p$ , is actually still ten times larger in amplitude than signals shown in Fig 5.6. The bottom plot is the conventional Ni-K edge EXAFS for the Martensite phase, scaled to 5% of its actual amplitude. Comparing this to the DiffEXAFS signals, it is clear that the observed atomic strains are from the phase transition rather than just from thermal expansion and disorder. This is partly by virtue of the order of magnitude difference in signal amplitude between these and the thermal expansion measurements, but also

because the DiffEXAFS structure differs significantly from that of the conventional EXAFS. None of the spectra resemble the conventional EXAFS plus a slight phase shift.

One would expect that if more data were obtained out to lower, or indeed higher, temperatures, the structure would eventually return to a state similar to that reported for the simple, thermal expansion case. Whilst these data are not available here, they would be useful to obtain in future experiments, since finding the transition between these two regimes will identify the onset of the phase transition from a local atomic perspective.

Starting from the spectrum taken about 305K and working towards  $T_p$  in the Martensite phase, it is clear that the fine-structure remains constant in phase, but increases significantly in amplitude. This indicates that the DiffEXAFS signal originates primarily from changes in thermal disorder rather than from thermal strains, with the increase in atomic vibrations as a function of  $T$  becoming much larger close to  $T_p$ .

Above  $T_p$ , in the Austenite phase, it is clear that the fine-structure is radically altered. The conventional EXAFS shown at the top of the plot is significantly different to its Martensite counterpart at the bottom of the plot. As for the DiffEXAFS, the region between 8.38 and 8.55keV bears a close similarity to the same region in the Martensite phase, albeit with oscillations showing a significantly reduced amplitude. The remainder of the spectrum is, however, completely different.

Indeed, the region beyond about 8.55keV shows sharp structure in contrast to the smooth oscillatory structure expected from EXAFS. This would first suggest some error occurred while acquiring the spectra, but this can be eliminated since the observed structure is reproducible. During the experiment, data were taken whilst cycling through the transition a number of times, and each time, the Austenite structure possessed the sharp peaks shown in Fig 7.3. The structure also exhibits inversion upon gas jet phase reversal, as shown in Figure 7.5, indicating it is indeed thermal in origin.

The origin of this structure is not known at present, and should therefore be the focus of future research. Unfortunately, it is not possible to analyse such structure within the current theory laid out for Thermal DiffEXAFS. Therefore, analysis here has been

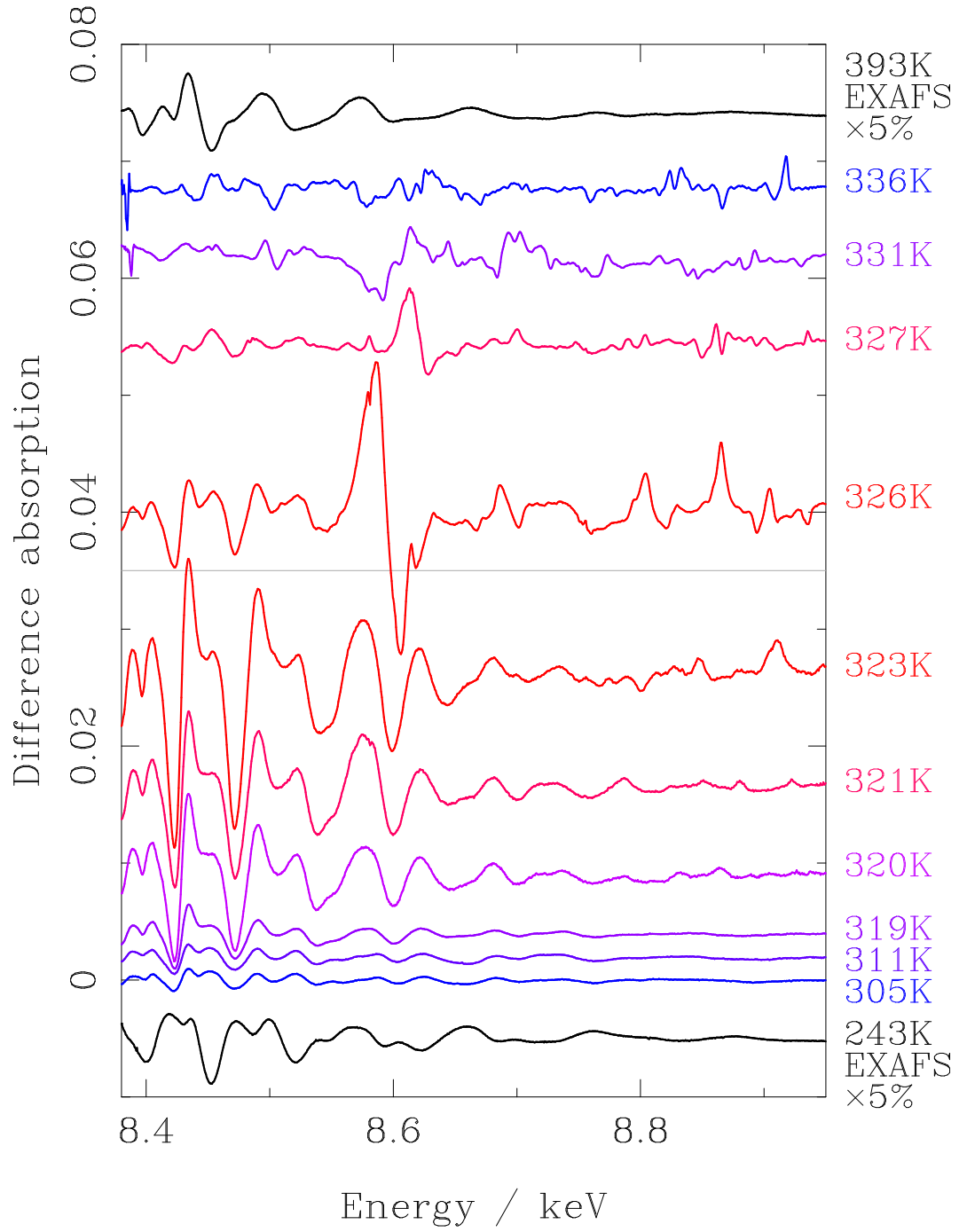


Figure 7.3: Differential EXAFS spectra (i.e. normalised to a 1K modulation) taken at the Ni-K edge and heating through the Martensitic phase transition in  $\text{Ni}_2\text{MnGa}$ . The six spectra below the horizontal grey line were taken in the Martensitic phase, and the top four in the Austenite phase. The lowermost and uppermost spectra are the conventional EXAFS for the corresponding phases, scaled to 5% of their actual amplitude.

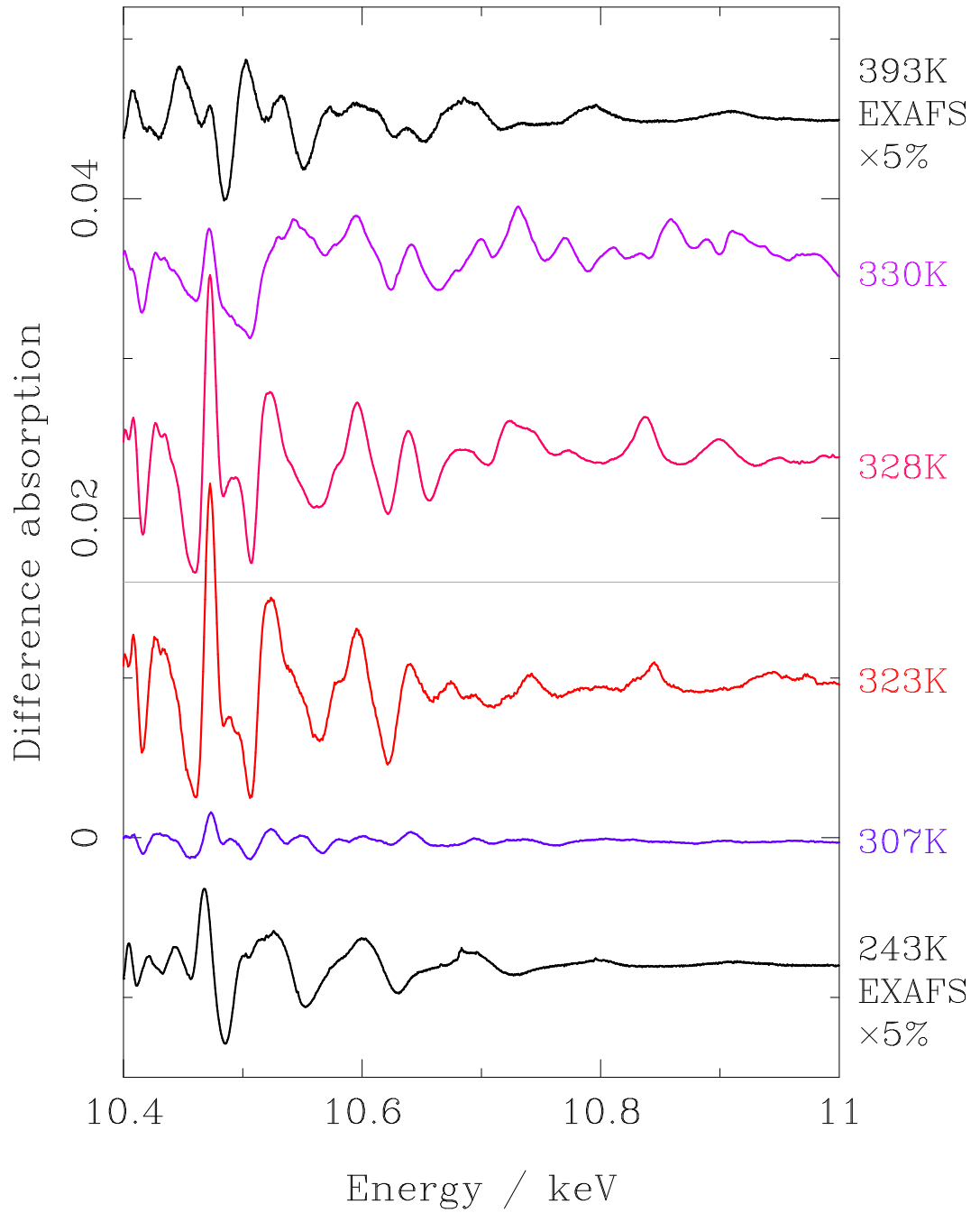


Figure 7.4: Differential EXAFS spectra (i.e. normalised to a 1K modulation) taken at the Ga-K edge and through the Martensitic phase transition in  $\text{Ni}_2\text{MnGa}$ . The spectra below the horizontal grey line were taken in the Martensitic phase, and those above in the Austenite phase. The lowermost and uppermost spectra are the conventional EXAFS for the corresponding phases, scaled to 5% of their actual amplitude.

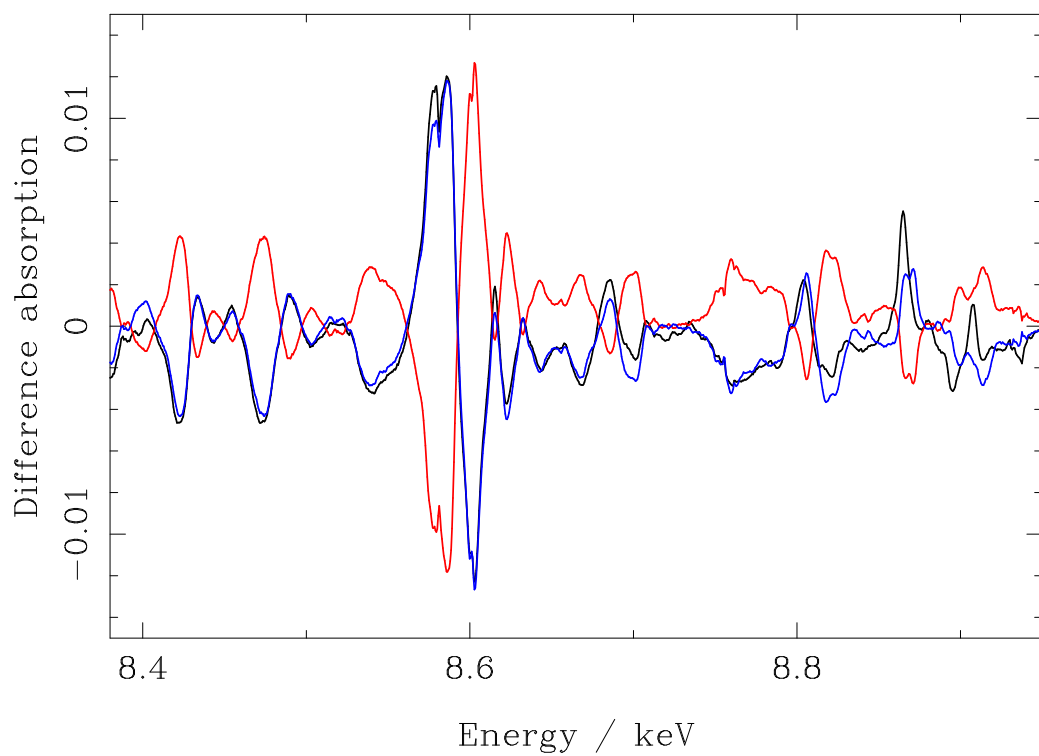


Figure 7.5:  $\text{Ni}_2\text{MnGa}$  Ni-K edge DiffEXAFS taken at 326K in the Austenite phase. The red signal was obtained with the gas jet phase reversed with respect to the black signal. The blue line is the inverted phase reversed signal, which reveals good agreement between the spectra taken with each gas phase. The two differ slightly, particularly at high energies, but are sufficiently similar to state that the structure is thermal in origin.

restricted to the low temperature, Martensite phase.

The presence of hysteresis in the transition was examined by taking data whilst moving from the Martensite to Austenite phase and vice versa. No difference was observed between spectra taken at similar temperatures in each direction, indicating minimal hysteresis or no hysteresis at all. Since the data were directionally invariant, only the spectra acquired with ascending temperature are shown in Fig 7.3.

Similar data were also acquired at the Ga-K edge, as shown in Figure 7.4. The delay between measurements was, again, 1.5s, with temperature modulation ranging from 0.8 to 3.1K. As in Figure 7.3, the spectra above the grey line show data taken in the Austenite phase, and spectra below, in the Martensite phase.

As with the Ni-K edge data, there is marked evolution of the differential structure as a function of temperature, with the signal amplitude much greater closer to  $T_p$  than further away. However, unlike the Ni-K data, the fine-structure varies much more smoothly through  $T_p$  itself. The structure just above varies only slightly compared to just below, and even at 330K, there are still features that correspond to those in the Martensite spectra. This suggests that structural changes from the point of view of the Ga atoms are less severe than they are from the Ni atoms.

Unfortunately, available beamtime did not permit the experiment to be repeated with measurements taken at the Mn-K edge. Whilst this would have provided a complete picture of structural changes from the point of view of each atomic species, the Mn atoms occupy similar positions within the crystal lattice as the Ga atoms, and so could be expected to provide similar structural information.



## 7.4 Analysis of the Low Temperature Martensite Phase

### 7.4.1 Conventional EXAFS

As with the thermal expansion analysis, a perturbation reference point had to be defined prior to fitting the DiffEXAFS itself. In the Martensite phase, conventional EXAFS spectra were acquired on BM29 at 293K at the Ni-K edge in the same  $\text{Ni}_2\text{MnGa}$  sample used for DiffEXAFS studies on ID24. Additional EXAFS spectra were also taken at 243K, 150K, and 60K, not to provide DiffEXAFS reference points, but to establish the trends in  $\sigma_j^2$  away from the phase transition.

Similar to the Fe data, fitting the EXAFS in the Martensite phase required the experimental data to be Fourier filtered. In this case, only radii up to  $3.0\text{\AA}$  were considered, which corresponded to the first four single-scattering paths only. At the Ni-K edge, and in increasing radii, these were Ni-Mn, Ni-Ga, Ni-Ni 1, and Ni-Ni 2 for  $j = 1, 2, 3, 4$  respectively. This is shown schematically in Figure 7.8. The two Ni-Ni paths would be identical in the Austenite phase, but are distinct in the Martensite due to the tetragonal distortion present.

The  $\text{Ni}_2\text{MnGa}$  Martensite crystal structure supplied to FEFF in order to calculate scattering phase and amplitude information was based upon that given by Martynov & Kokorin [46]. This is shown in detail in Appendix B.

Figure 7.6 shows the results of fitting these Martensite spectra in the range  $70 \leq E' \leq 550\text{eV}$ , where, again,  $E'$  is the x-ray energy above the edge. The fitted parameters are shown in Table 7.1, with configuration files and additional output in Appendix C.2. These fits indicate that the  $\sigma_j^2$  increase with  $T$  as is predicted by harmonic theory.

Given the magnitude of fine-structure changes as a function of temperature, seen in Figure 7.3, several conventional EXAFS spectra were also acquired up to the primary transition temperature at 324K. Whilst such spectra are insensitive to the small changes in scattering path lengths due to strain, the disorder signal is sufficiently large to allow a comparison between EXAFS and DiffEXAFS techniques. These spectra were taken *in situ* at the same time as the DiffEXAFS.

Treating these spectra in the same manner as those away from the primary transition

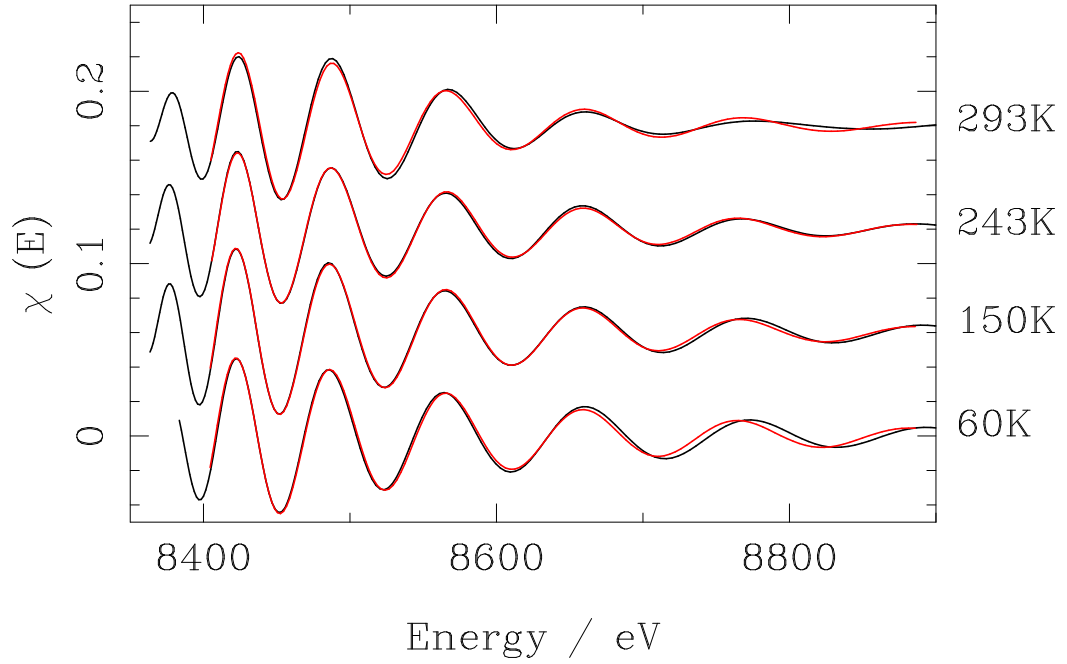


Figure 7.6: BM29 Conventional EXAFS spectra of  $\text{Ni}_2\text{MnGa}$  at the Ni-K edge for various temperatures away from the transition temperature in the Martensite phase (black lines). Each has been Fourier filtered to the first four single-scattering paths only. Overlaid in red are theory spectra, generated for the same scattering paths, fitted to experiment between  $70 \leq E' \leq 550\text{eV}$ .

Fit parameters away from $T_p$				
Parameter	Sample Temperature			
	60K	150K	243K	293K
$\langle \sigma_1^2, \sigma_2^2 \rangle \times 10^{-3} \text{\AA}^2$	$6.2 \pm 0.6$	$6.6 \pm 0.4$	$7.4 \pm 0.3$	$9 \pm 2$
$\sigma_3^2 \times 10^{-3} \text{\AA}^2$	$5 \pm 1$	$7.9 \pm 0.7$	$7.5 \pm 0.5$	$10 \pm 3$
$\sigma_4^2 \times 10^{-3} \text{\AA}^2$	$23 \pm 4$	$31 \pm 3$	$29 \pm 2$	$19 \pm 3$
$S_0^2$	0.8	0.8	0.8	0.8
$E_0$ eV	$8337.3 \pm 0.4$	$8337.4 \pm 0.2$	$8338.5 \pm 0.2$	$8337.8 \pm 0.6$

Table 7.1: Fitted parameter values for  $\text{Ni}_2\text{MnGa}$  EXAFS at the Ni-K edge for a range of temperatures away from the transition in the Martensite phase. In each fit,  $S_0^2$  was fixed at 0.8. It is important to note that given the first two Debye-Waller factors correspond to Ni-Mn and Ni-Ga, which have equivalent radii, and also that there is little phase contrast between these two paths, FitChi2 is unable to accurately distinguish one from the other. Therefore, it is only the average of these two parameters that is meaningful; hence  $\langle \sigma_1^2, \sigma_2^2 \rangle$ . Errors are based on the fit only, and do not include other sources such as  $T$  or  $E_0$  drift.

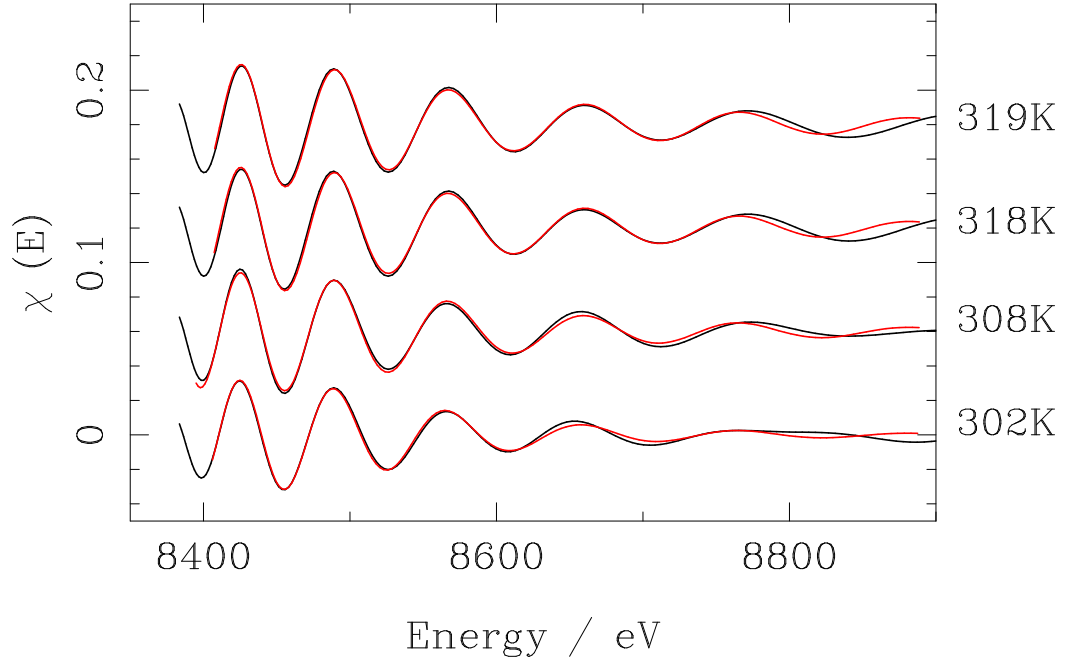


Figure 7.7: ID24 Conventional EXAFS spectra of Ni<sub>2</sub>MnGa at the Ni-K edge for various temperatures close to the transition temperature in the Martensite phase (black lines). Each has been Fourier filtered to the first four single-scattering paths only. Overlaid in red are theory spectra, generated for the same scattering paths, fitted to experiment between  $70 \leq E' \leq 550$  eV. The apparently poor fit at high energies is due to larger experimental noise on ID24 (from a lower x-ray flux) in this region.

Fit parameters in the region of $T_p$				
Parameter	Sample Temperature			
	302K	308K	318K	319K
$\langle \sigma_1^2, \sigma_2^2 \rangle \times 10^{-3} \text{\AA}^2$	$11.8 \pm 0.9$	$9.7 \pm 0.7$	$8.6 \pm 0.7$	$8.7 \pm 0.6$
$\sigma_3^2 \times 10^{-3} \text{\AA}^2$	$10 \pm 2$	$6 \pm 1$	$4 \pm 1$	$4 \pm 1$
$\sigma_4^2 \times 10^{-3} \text{\AA}^2$	$18 \pm 3$	$18 \pm 3$	$16 \pm 3$	$16 \pm 3$
$S_0^2$	0.8	0.8	0.8	0.8
$E_0$ eV	$8337.4 \pm 0.5$	$8338.5 \pm 0.4$	$8339.6 \pm 0.5$	$8339.0 \pm 0.5$

Table 7.2: Fitted parameter values for Ni<sub>2</sub>MnGa EXAFS at the Ni-K edge for a range of temperatures close to the transition in the Martensite phase. In each fit,  $S_0^2$  was fixed at 0.8. Again, errors come from the fit only.

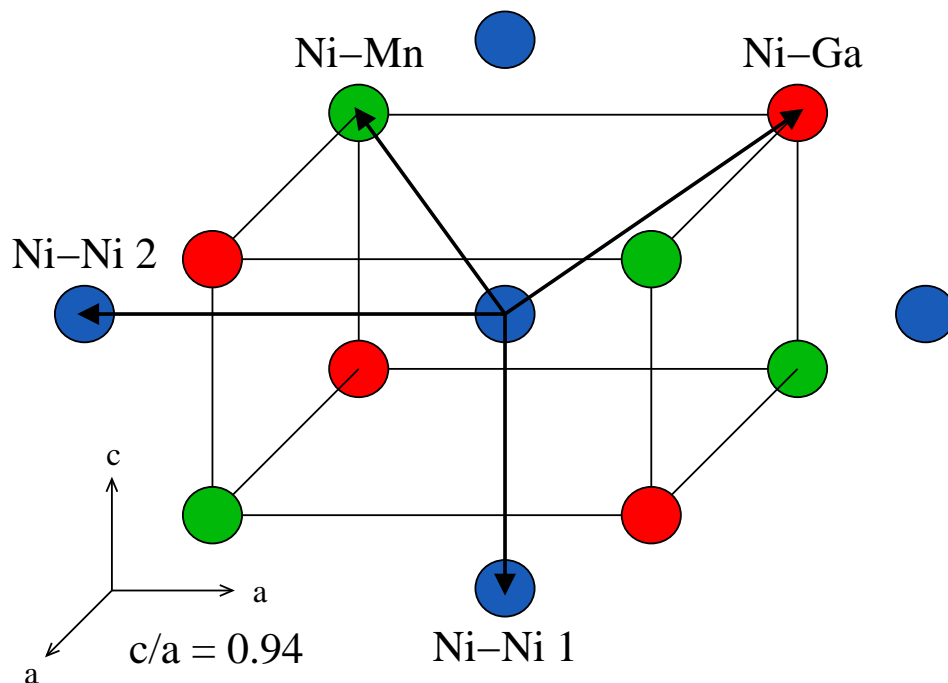


Figure 7.8: A schematic representation of the photoelectron scattering paths considered during Ni-K edge EXAFS and DiffEXAFS analysis of the Martensite phase of  $\text{Ni}_2\text{MnGa}$ . The Ni-Mn and Ni-Ga paths are of the same length and are closest to the emitter atom, Ni-Ni 1 is next in length, and Ni-Ni 2 the longest. The precise crystal structure is given in Appendix B.

temperature produced the results shown in Table 7.2 and Figure 7.7. These indicate that thermal disorder continues to rise until about 25 to 30K below the transition, when it starts to fall. This trend may be confirmed by a simple examination of each spectrum's Fourier transform, shown in Figure 7.9 for data both away from and close to the transition. These are important in that they confirm the trend independent of any fitting or other such analysis.

Away from  $T_p$ , the peak amplitude for those corresponding to the first four single-scattering paths, decays as  $T$  increases, indicating a reduction in amplitude of each EXAFS component, consistent with an increase in thermal disorder. Close to the transition however, these peaks rise as the sample temperature approaches  $T_p$ , indicating the opposite.

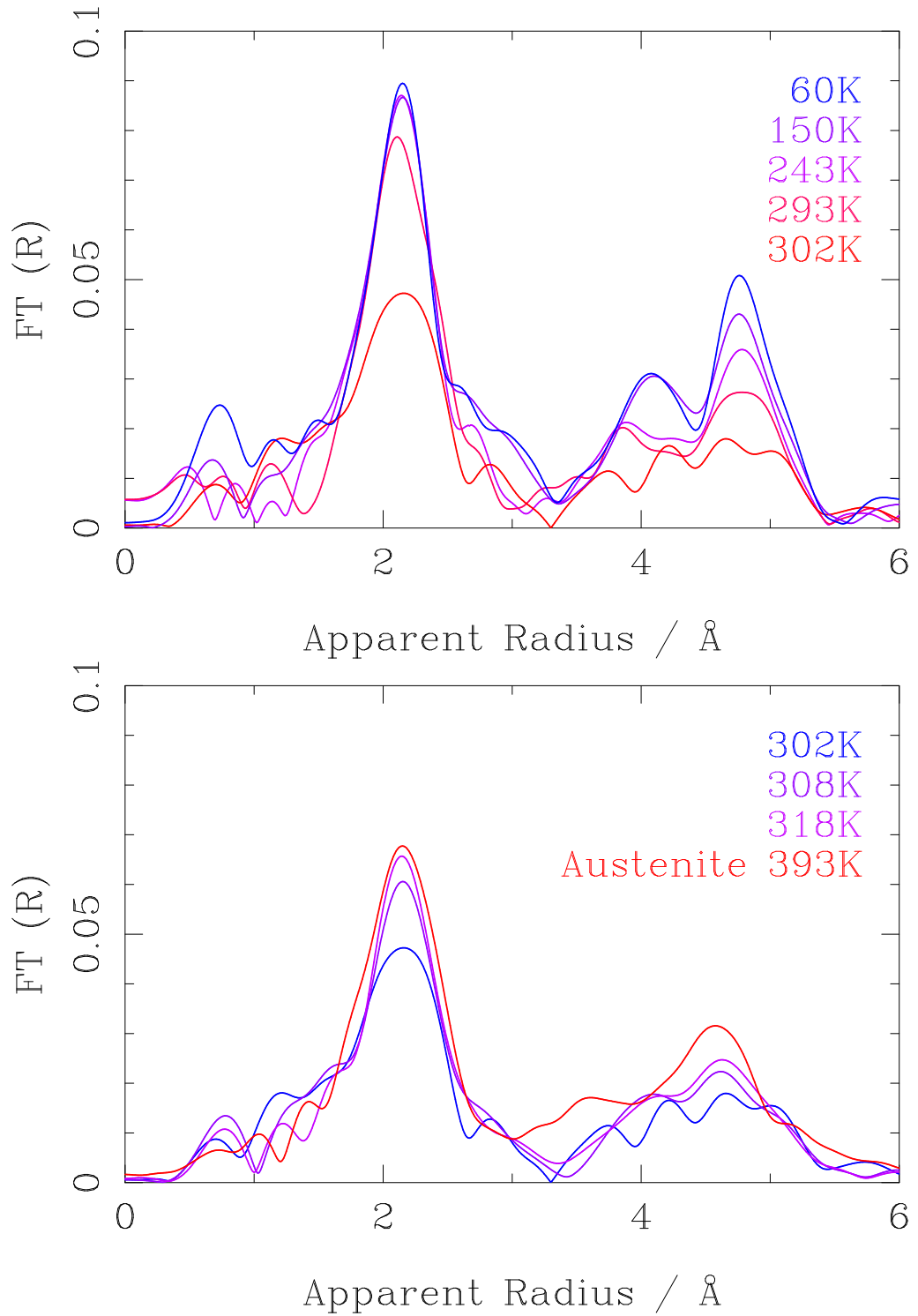


Figure 7.9: Fourier transform of experimental Ni-K edge EXAFS in  $\text{Ni}_2\text{MnGa}$  taken away from (top) and close to (bottom)  $T_p$ . The transform was performed with a Hann window to reduce termination effects. It must be noted that the abscissa is the apparent atomic radial distribution function (RDF) rather than the real RDF. The two differ by an offset of approximately  $0.3\text{\AA}$  due to phase shifts experienced by the photoelectron.

### 7.4.2 Differential EXAFS

Taking the EXAFS parameters at 293K as a reference, the Martensite DiffEXAFS spectra at the Ni-K edge, shown in Figure 7.3, were fitted to determine the structural characteristics in the region of the phase-transition. Here, since onset features may distort the lattice, breaking the crystal symmetry and thus von Neumann's Principle, a separate thermal strain  $\alpha_j$  was considered for each scattering path. The  $\partial\sigma_j^2/\partial T$  were fitted as in the thermal expansion case.

These fits are plotted in Figure 7.10, with the fitted parameters shown in Table 7.3. Integrating these parameters as a function of  $T$  and adding an offset to pin each parameter to a known value for a known  $T$ , yields their absolute values in the region of the phase transition. These are shown in Figures 7.11 and 7.12.

The negative  $\partial\sigma_j^2/\partial T$  in Table 7.3 confirm the trend of decreasing Debye-Waller factors for increasing temperature, seen both from Fourier transforming and from fitting conventional EXAFS spectra in the region of the phase transition. However, a problem becomes evident upon examination of the absolute  $\sigma_j^2$  obtained after integration.

The  $\sigma_j^2$  for both of the Ni-Ni scattering paths goes negative beyond about 308K, which is impossible since it implies an imaginary variance in atomic positions. These results must therefore be considered incorrect.

The cause for this problem is not understood at present. The raw DiffEXAFS data for all Martensite spectra are of a high quality, and the algorithm used for fitting these data close to  $T_p$  produced good results for thermal expansion studies, and for Ni<sub>2</sub>MnGa further than about 10K from the phase transition. The trends seen from the DiffEXAFS are also in agreement with the conventional EXAFS. This leads to the conclusion that the poor absolute  $\sigma_j^2$  very close to  $T_p$  are most probably the result of a failure of at least one of the approximations upon which the current theory of Thermal DiffEXAFS is based.

Some possibilities present themselves, the first being that the fitted parameters are no longer linear between  $T^+$  and  $T^-$  close to  $T_p$ . Consequently, higher order terms would be required in the differential fine-structure function (2.14) in order to accurately model the observed changes.

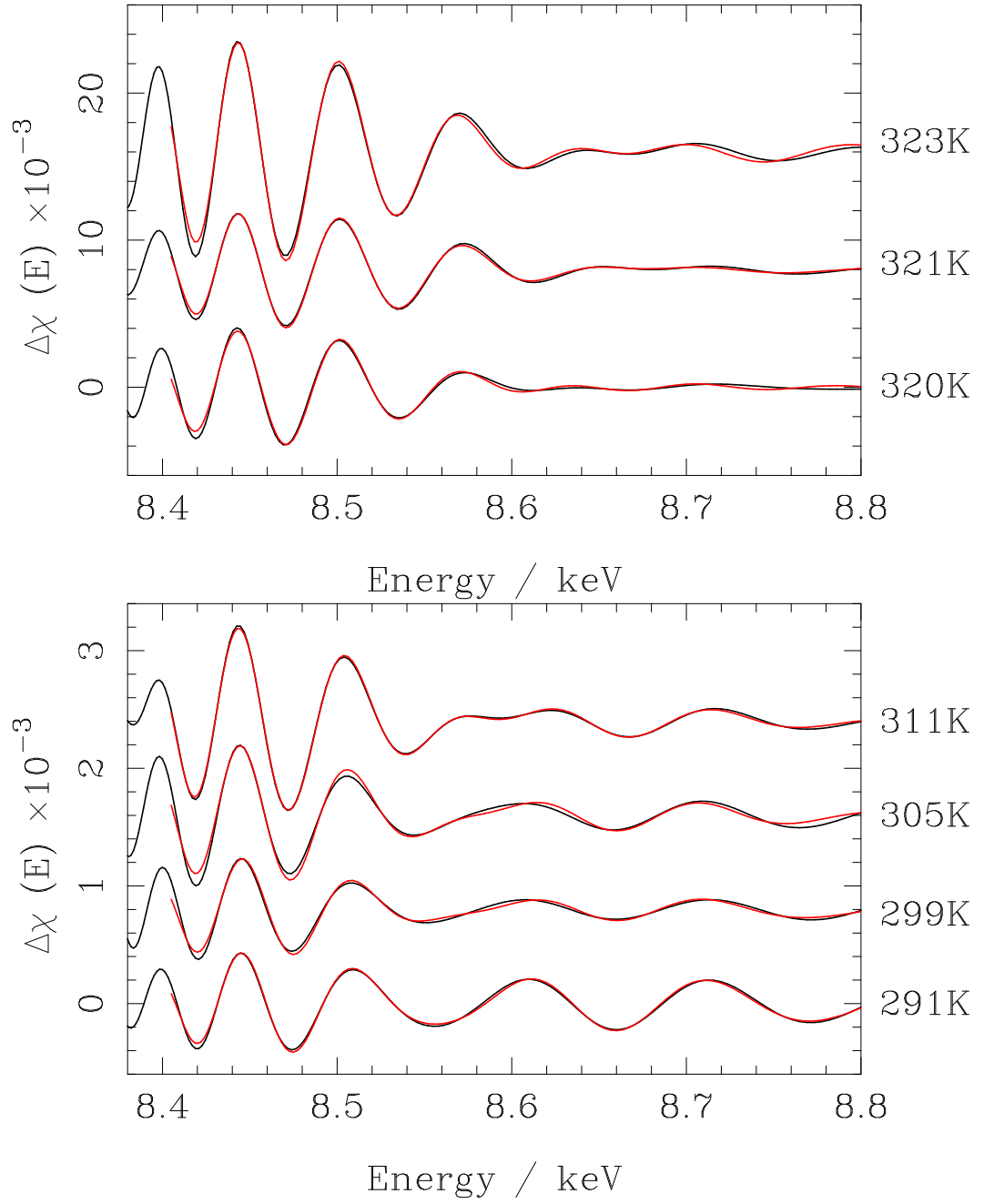


Figure 7.10: DiffEXAFS spectra from  $\text{Ni}_2\text{MnGa}$  at the Ni-K edge approaching  $T_p$  in the Martensite phase (black lines). Each has been Fourier filtered to the first four single-scattering paths only. Overlaid in red are theory spectra, generated for the same scattering paths and fitted to experiment.

DiffEXAFS fit parameters for $T$ approaching $T_p$			
Temperature	$\langle \partial\sigma_1^2/\partial T, \partial\sigma_2^2/\partial T \rangle \times 10^{-4} \text{\AA}^2$	$\partial\sigma_3^2/\partial T \times 10^{-4} \text{\AA}^2$	$\partial\sigma_4^2/\partial T \times 10^{-4} \text{\AA}^2$
291K	$-3.3 \pm 0.6$	$-9.7 \pm 0.4$	$-10.3 \pm 0.3$
299K	$-4 \pm 1$	$-10.4 \pm 0.8$	$-9.3 \pm 0.6$
305K	$-7 \pm 2$	$-13.0 \pm 1$	$-12.3 \pm 0.6$
311K	$-2.2 \pm 0.6$	$-8.1 \pm 0.6$	$-10.8 \pm 0.4$
320K	$-5.2 \pm 0.6$	$-24 \pm 1$	$-48.6 \pm 0.8$
321K	$-4.1 \pm 0.3$	$-14 \pm 1$	$-32 \pm 1$
323K	$2.4 \pm 0.5$	$-52 \pm 1$	$-78 \pm 1$
Temperature	$\langle \alpha_1, \alpha_2 \rangle \times 10^{-4}$	$\alpha_3 \times 10^{-4}$	$\alpha_4 \times 10^{-4}$
291K	$-14.3 \pm 0.7$	$-17 \pm 1$	$-1.3 \pm 0.7$
299K	$-6 \pm 1$	$-10 \pm 3$	$-2 \pm 2$
305K	$-7 \pm 2$	$-20 \pm 7$	$-8 \pm 3$
311K	$-0.7 \pm 0.7$	$7 \pm 1$	$1.4 \pm 0.6$
320K	$-42 \pm 2$	$33 \pm 3$	$29 \pm 2$
321K	$-36 \pm 1$	$154 \pm 4$	$76 \pm 3$
323K	$-17 \pm 2$	$241 \pm 4$	$133 \pm 3$

Table 7.3: Fitted parameter values for Ni<sub>2</sub>MnGa DiffEXAFS at the Ni-K edge approaching the transition in the Martensite phase. The lack of contrast between the Ni-Mn and Ni-Ga paths again requires their results to be averaged. Errors quoted arise from the fits only.

However, the effects of premature truncation of the Taylor expansion may be mitigated in code by calculating the DiffEXAFS, not from Equation (2.14), but by generating two complete EXAFS spectra - one with, and one without changes to  $\sigma_j^2$  and  $s_j$  considered - and then taking their difference. In this treatment, the resulting DiffEXAFS signal will contain all terms of the Taylor expansion out to infinity.

Implementing and then comparing both methods of calculation, however, showed no significant difference between the two approaches. The  $\sigma_j^2$  and  $s_j$  therefore remain linear close to  $T_p$  for the  $\Delta T$  used here.

The second possible failure may be in the model adopted to represent Debye-Waller factors. In equation (2.11), Debye-Waller factors are modelled with Gaussians; thus thermal vibrations are represented by some symmetric variance about a mean atomic position.

Anharmonicity of the atomic pair-correlation function, required for thermal strain to



exist, is modelled in (2.14) according to the quasi-harmonic approximation [42]. Should this approximation fail, anharmonicity would need to be modelled explicitly. Thus, thermal perturbations to the crystal structure would need to be treated within, say, a cumulant expansion of the fine-structure function [72]. It is unlikely that anharmonicity would produce an error sufficiently large to produce the effect seen here, but further work should be conducted to ascertain whether a more explicit approach is necessary.

The most likely cause, therefore, would be an error in the reference structure from which the thermal perturbations are measured. Should the structure supplied to FEFF be incorrect, there would be an apparent static disorder within the lattice due to the difference between real and anticipated mean atomic positions. This would clearly affect the absolute Debye-Waller factor, but should leave mean changes in path length untouched as well as the trends seen in the  $\partial\sigma_j^2/\partial T$ . In order to verify the mean crystal structure in the vicinity of the phase transition it would be desirable to, in the future, conduct high resolution x-ray diffraction measurements on the sample as a function of temperature, and perform a Rietveld refinement to determine atomic positions.

In spite of this problem some observations may still be made. Shown alongside the DiffEXAFS  $\sigma_j^2$  in Figure 7.11 are the  $\sigma_j^2$  obtained from the conventional EXAFS parameters in Table 7.2. The two data sets are coincident at 303K as a result of using the conventional EXAFS parameters at that temperature for the DiffEXAFS integration offsets.

These show reasonable agreement between the  $\sigma_j^2$  obtained from each method for the Ni-Mn and Ni-Ga paths. The two data sets agree within error up to about 310K, and within twice the error up to 320K.  $\sigma_j^2$  for the first Ni-Ni path also agrees within error up to about 310K<sup>1</sup> but becomes unphysical after that.  $\sigma_j^2$  for the second Ni-Ni path exhibit little or no agreement between the two measurement techniques.

Both the EXAFS and DiffEXAFS data indicate that  $\sigma_j^2$  for the first Ni-Ni path actually falls below that of the Ni-Mn and Ni-Ga paths despite being of greater length. Since the  $\sigma_j^2$  for EXAFS fits away from the transition, in Table 7.1, show a monotonic increase with path length, this provides further evidence for onset of the phase transition out to

---

<sup>1</sup>When remembering to add on the error in the integration offset, which is that for the EXAFS at 303K. This additional error is not shown on the DiffEXAFS error bars.

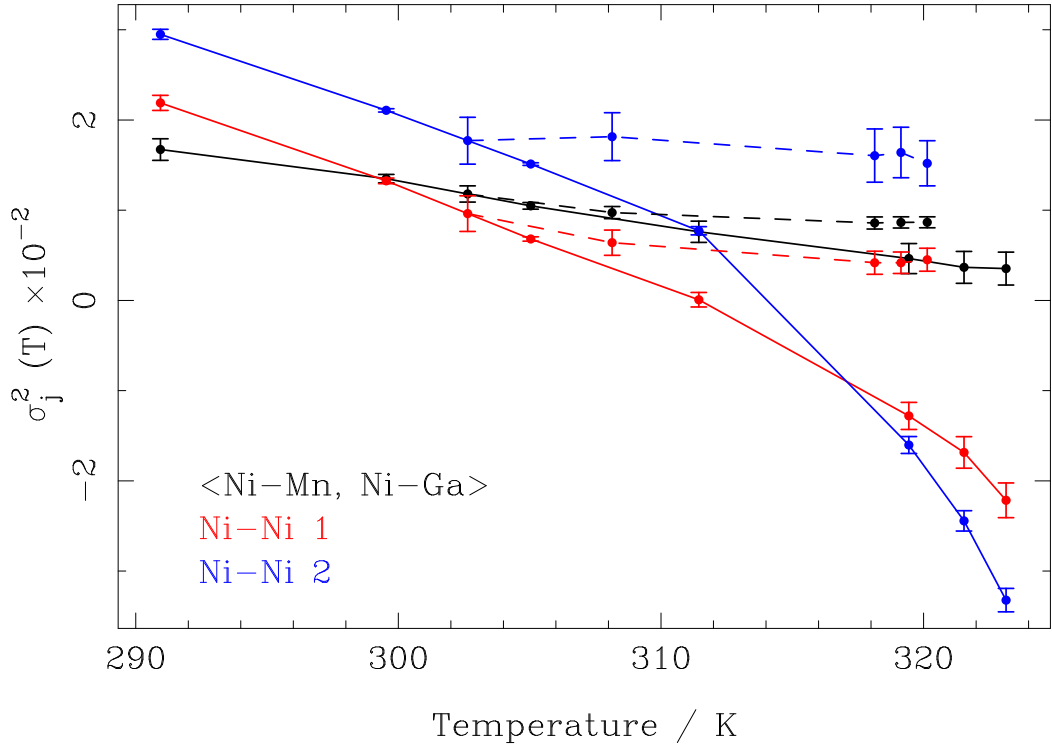


Figure 7.11: Absolute  $\sigma_j^2$  for each of the first four single-scattering paths in  $\text{Ni}_2\text{MnGa}$ , determined by DiffEXAFS (solid lines) and conventional EXAFS (dashed lines) in the region of the phase-transition. DiffEXAFS results were obtained by integrating  $\partial\sigma_j^2/\partial T(T)$  and offsetting to  $\sigma_j^2(303K)$  found from conventional EXAFS. All paths show the correct, descending trend, but values for Ni-Ni 1 and Ni-Ni 2 are clearly unphysical for  $T$  greater than about  $308K$ . This suggests a breakdown of the present theory close to  $T_p$ . Errors in  $T$  are smaller than the point size.

at least 20K below  $T_p$ .

Figure 7.12 shows how scattering path lengths vary as a function of temperature. Each plot is given with respect to the known path lengths at 293K, which are given in the associated caption. These show that each scattering path contracts as the sample temperature increases up to about 312K.

Beyond this point, the Ni-Mn and Ni-Ga paths continue to contract whilst the two Ni-Ni paths expand significantly, indicating a net increase in path length. Examining the Martensite and Austenite crystal structures [46], and also considering the Bain strain, reveals that over the transition as a whole, Ni-Mn, Ni-Ga, and Ni-Ni 1 distances must increase, whilst Ni-Ni 2 must decrease. Therefore, these trends observed in the

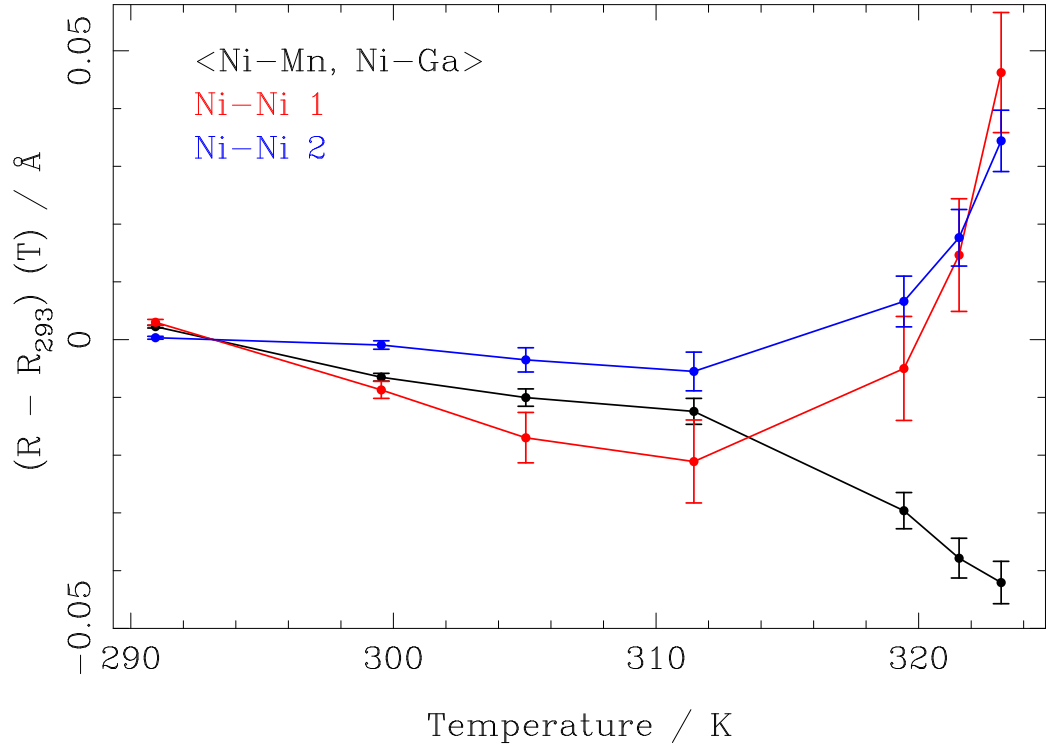


Figure 7.12: Absolute  $s_j$  for each of the first four single-scattering paths in  $\text{Ni}_2\text{MnGa}$  relative to their values at  $293\text{K}$ . These are  $2.5039\text{\AA}$  for Ni-Mn and Ni-Ga,  $2.7700\text{\AA}$  for Ni-Ni 1, and  $2.9500\text{\AA}$  for Ni-Ni 2. These reveal that each scattering path shortens at  $T$  increases. The last three points for both Ni-Ni paths should not be considered meaningful given unphysical values were obtained for  $\sigma_j^2$  from the same fits. Errors in  $T$  are smaller than the point size.

DiffEXAFS are indicative of some final onset feature before  $T_p$ , rather than of the primary transition itself.

## 7.5 Discussion of Phase Transition Studies

With the results shown above, several definitive conclusions regarding the nature of the Martensitic transition in  $\text{Ni}_2\text{MnGa}$  may be drawn.

Firstly, close to the transition, all data acquired from both EXAFS and DiffEXAFS measurements reveal a reduction in Debye-Waller factor as the phase transition is approached upon heating. This indicates that there is a hardening of the crystal structure. Conversely, away from the transition region, EXAFS Debye-Waller factors increase with

temperature as would be expected in the linear regime.

Qualitatively, if disorder is assumed to arise solely from the vibrational motion of atoms, then  $\Delta\sigma^2$  is proportional to  $\Delta S$ , the change in entropy of the crystal. A reduction in Debye-Waller factor therefore describes a reduction in vibrational entropy of the atoms. Since the specific heat capacity of the sample  $c_p = T(\partial S/\partial T)_p$ , a reduction in entropy will cause a reduction in  $c_p$  and vice versa.

Therefore, the DiffEXAFS indicates that away from the transition region in the Martensite phase, the heat capacity of the sample should be observed to rise, and then fall sharply as  $T \rightarrow T_p$  close to  $T_p$ . This is in agreement with behaviour reported from differential scanning calorimetry (DSC) measurements for a variety of  $\text{Ni}_2\text{MnGa}$  samples of similar composition to that used here [93].

In these DSC measurements, heat capacity is seen to rise at a rate of approximately  $0.01\text{mWK}^{-1}$  up to about 20 to 30K below  $T_p$ , beyond which it drops rapidly. Once  $T_p$  is crossed, the signal returns to a similar value it held prior to the onset of the phase transition. Across the transition as a whole, Pasquale et al. report a net drop in entropy of  $24\text{ J kg}^{-1}\text{K}^{-1}$  on changing from the Martensite to Austenite phase [56], again for a sample of similar composition to that used here.

Since the location of transition features in  $\text{Ni}_2\text{MnGa}$  is heavily dependent upon sample composition and preparation (see [93] or [3] for instance), a more quantitative analysis will require similar DSC measurements on the particular sample studied here. In conjunction with a greater number of DiffEXAFS measurements, both in terms of density and temperature range, these will then serve as a comparison to features observed in the DiffEXAFS and, if equivalent, further justify its use to study phase transitions.

In terms of mean, temperature-induced strains, DiffEXAFS demonstrates a contraction in all scattering path lengths as  $T$  approaches  $T_p$ , with the Ni-Ni scattering paths then lengthening very close to  $T_p$ .

To the author's knowledge no similar work, with which these observations may be confirmed or refuted, has been published on structural changes in  $\text{Ni}_2\text{MnGa}$  as a function of temperature with the resolution reported here. However, reports on the equilibrium structure of the Martensite and Austenite phases [98][46] (and including possible pre-

martensitic phases) indicates that the tetragonal  $c/a$  ratio changes from about 0.94 for the Martensite to 1.00 in the Austenite. Mapping this distortion onto the scattering paths considered here requires an expansion of the Ni-Mn, Ni-Ga, and Ni-Ni 1 scattering paths, and a contraction of the Ni-Ni 2 path.

Thus in order for the observations made here to be consistent with these reported values, there must be a sharp structural change upon switching from a Martensite to Austenite - narrowly defined in temperature as opposed to a gradual change - which has not been detected with the DiffEXAFS measurements conducted to date.

Finally, work must be undertaken in future to explain the nature of the DiffEXAFS structure observed at the Ni-K edge of the Austenite. Such structure is not predicted by the present thermal differential fine-structure function, thus requiring a refinement of the fundamental theory of Thermal DiffEXAFS. In addition to this work, results obtained to date would benefit from an analysis of measurements taken at both the Mn-K and Ga-K edge. Clearly, results obtained from the Ni site should be reciprocated for equivalent scattering paths at other atomic sites.

## Chapter 8

# General Discussion and Future Outlook

### 8.1 DiffEXAFS vs. Conventional EXAFS

DiffEXAFS and conventional EXAFS signals, though from similar origins, have very different characteristics when it comes to the detection and measurement of atomic perturbations. This is evident from the raw data alone. Conventional EXAFS spectra change only subtly in response to small changes in the sample, with the signal, seen across the  $\text{Ni}_2\text{MnGa}$  phase transition for instance, evolving slowly as successive perturbations accumulate. In the DiffEXAFS however, small changes to the sample structure generate huge changes to the measured spectrum. This is particularly clear in Figure 7.3, where, in the region of the  $\text{Ni}_2\text{MnGa}$  phase transition, small changes in absolute temperature about which the DiffEXAFS is taken, cause the signal to significantly alter; starting small in amplitude 20K below  $T_p$  and increasing by over an order of magnitude as  $T_p$  is approached before changing in structure entirely when  $T_p$  is crossed. Therefore, even prior to data analysis, trends associated with the atomic perturbations are considerably easier to see.

When data is analysed, DiffEXAFS, thermal or otherwise, has its greatest advantage over conventional EXAFS in the detection and measurement of atomic strains, which for most phenomena, such as thermal expansion reported here, are of the order of  $10^{-5}$  per unit

change in parameter. The reason for this is that changes in scattering path length, normally observed as small phase changes, are converted to an amplitude signal with  $dR \propto dA$  in quadrature with the conventional EXAFS. Assuming two measurements can be made under differing sample conditions without drift of the beam in either space or energy, strain resolution is therefore limited only by the fractional statistical noise in the spectrum. For DiffEXAFS on ID24, this is of the order of  $10^{-5}$ , allowing displacements to be detected for modulation of the order of just 1K in the thermal case.

To detect a similar strain from the phase shift of a conventional EXAFS spectrum would require sample modulation to be around a hundred times greater; 100K as opposed to 1K. This is partly due to the lower signal-to-noise ratio attainable from conventional EXAFS, but primarily due to instabilities in edge energy over the period of spectrum acquisition.

The result is that for a given 100K temperature range, Thermal DiffEXAFS could make 101 independent strain measurements compared to only 2 from conventional EXAFS. DiffEXAFS then yields not just the net structural change over the whole region, but precise incremental perturbations as a function of temperature.

It is true that such resolution may not be required in all situations, particularly where phenomena inducing structural changes are either linear or vary only weakly as a function of the modulated sample property. However, many phenomena do not conform to these restraints; most notably non-linear phenomena such as phase transitions. In these situations the ability to detect atomic displacements over small changes in sample parameters is an absolute necessity.

Whilst conventional EXAFS will be able to detect net perturbations across some such discontinuity, and describe the sample structure in the stable region either side, it is generally not possible to look at how the sample responds approaching and receding from the transition - to say whether there are any onset features, or whether any particular structural instabilities become evident close to the primary transition itself. Even if a given transition were to induce perturbations large enough to be probed in a number of individual steps with conventional EXAFS, DiffEXAFS will always still offer around two orders of magnitude greater sensitivity and thus potentially a hundred times more

sampling points across the transition region. No other XAFS technique offers this potential.

In terms of changes to vibrational disorder seen in Thermal DiffEXAFS, the two techniques are more evenly matched. Changes to Debye-Waller factors manifest themselves as amplitude changes in both DiffEXAFS and conventional EXAFS, and given they are typically of the order of  $10^{-4} \text{\AA}^2 K^{-1}$ , conventional EXAFS may detect them with temperature changes of the order of 10K. However, as seen for  $\text{Ni}_2\text{MnGa}$  in Chapter 7, in the region of phase-transitions, these changes are as much as an order of magnitude larger, making it possible to detect  $\partial\sigma_j^2/\partial T$  with conventional EXAFS for temperature steps of the order of 1K.

Considering beamline components and available flux on ID24, Thermal DiffEXAFS remains two orders of magnitude more sensitive than conventional EXAFS, implying that changes in Debye-Waller factor may be detected from a temperature modulation of just 0.1K in the general case, or 0.01K at a phase transition similar to that in  $\text{Ni}_2\text{MnGa}$ . However, in practice, such a small modulation is not possible with the present gas jet apparatus. Consequently, conventional EXAFS is not currently far behind DiffEXAFS in terms of sensitivity to changes in vibrational disorder, and is even comparable to DiffEXAFS at the phase transition shown in this thesis.

However, since DiffEXAFS is limited by the gas jet apparatus rather than the beamline itself, there is considerably more prospect of improving the sensitivity of DiffEXAFS in the future than there is of conventional EXAFS.

## 8.2 Future work

Work in this thesis has demonstrated that Thermal DiffEXAFS is a viable experimental technique for measuring atomic perturbations, with clear advantages present over conventional EXAFS techniques. However, this work has also shown that the technique will benefit from some refinement in the future.

In terms of experimental apparatus, the first concern should be to upgrade the gas jet apparatus (or even replace it entirely) in order to improve upon the current 0.2K



temperature stability, reduce the time required to change between  $T^+$  and  $T^-$  states, and - most importantly from the point of view of allowing the technique to be applied in many situations - extend the temperature range currently accessible by the apparatus; allowing measurements to be made far away from room temperature.

These upgrades will improve the quality of experimental spectra, but strain resolution will still be limited to around one femtometre. Therefore, the next change should be to obtain new detectors with, say, a more sensitive CCD that will allow for single photon counting. With the flux currently available on ID24, this should make strains detectable on a 0.1fm scale if pairs of  $T^+$ ,  $T^-$  spectra are averaged over a few hours. Further, incremental improvements in sensitivity will then be subject to improvements to synchrotrons themselves, with step changes not likely until the advent of 4<sup>th</sup> generation light sources.

Work must also be carried out to refine the present theoretical model of Thermal DiffEXAFS. Measurements of the Austenite phase of  $\text{Ni}_2\text{MnGa}$  have clearly demonstrated that in some instances the DiffEXAFS contains features that are not currently predicted by Equation 2.14. Additionally - whilst the experimental  $\text{Ni}_2\text{MnGa}$  data was of a very high-quality, with trends clearly visible and in agreement with EXAFS results - the negative absolute Debye-Waller factors obtained upon integrating DiffEXAFS results require further investigation.

To help develop the  $\text{Ni}_2\text{MnGa}$  phase transition results, future work should assess the effect of magnetisation of the sample via, say, XMCD measurements, and again with DiffEXAFS and an applied external field. It is known that magnetisation of the sample has a significant effect on the properties of the phase transition, which should be studied with DiffEXAFS. Additionally, knowledge of the magnetism at each atomic site from XMCD may help explain the observed DiffEXAFS trends should there be, for instance, something like an invar effect in the material.

### 8.3 Extension to Studies of Non-Thermal Phenomena

It is important to remember that DiffEXAFS is not limited to the study of any particular set of materials or to the study of any given type of phenomenon. In principle it may be used to examine *any* situation where the modulation of a sample property results in some small degree of atomic perturbation on a local scale. This means that there are numerous potential applications for the future.

For instance, initial data from [64] demonstrated the measurement of magnetostriction by DiffEXAFS, which should be of great interest to those wishing to examine the atomic origins of this and other -striction type phenomena.

Additionally, much work is conducted at present to see how material structures respond to large changes in pressure, but with DiffEXAFS, comes the potential of studying responses to small changes in pressure. Whilst this would be unlikely to reveal anything interesting in a linear regime, it could yield important information on non-linear strain mechanisms close to, say, elastic/plastic deformation limits in solids, and pressure induced phase-transitions, especially at interfaces containing liquid phases that are not examinable with techniques such as diffraction.

In general terms however, the real interest will lie in one of two areas. Firstly, in the study of non-linear phenomena as already described. Then in the examination of disordered or amorphous systems, where not only do other techniques such as diffraction fail, but where macroscopic measurements of sample properties may not necessarily scale down to the locally observed atomic perturbations due to the presence of intermediate scale deformations, such as the relief of microscopic strain by sample defects.

## **Appendix A**

### **Gas Jet Blueprints**

Figure A.1: Sputter Masks for deposition of an eight element copper-constantan thermopile. These masks should be laser etched from sheet aluminium of no more than 200 $\mu\text{m}$  thick. Constantan should be deposited first, and then copper over the top.

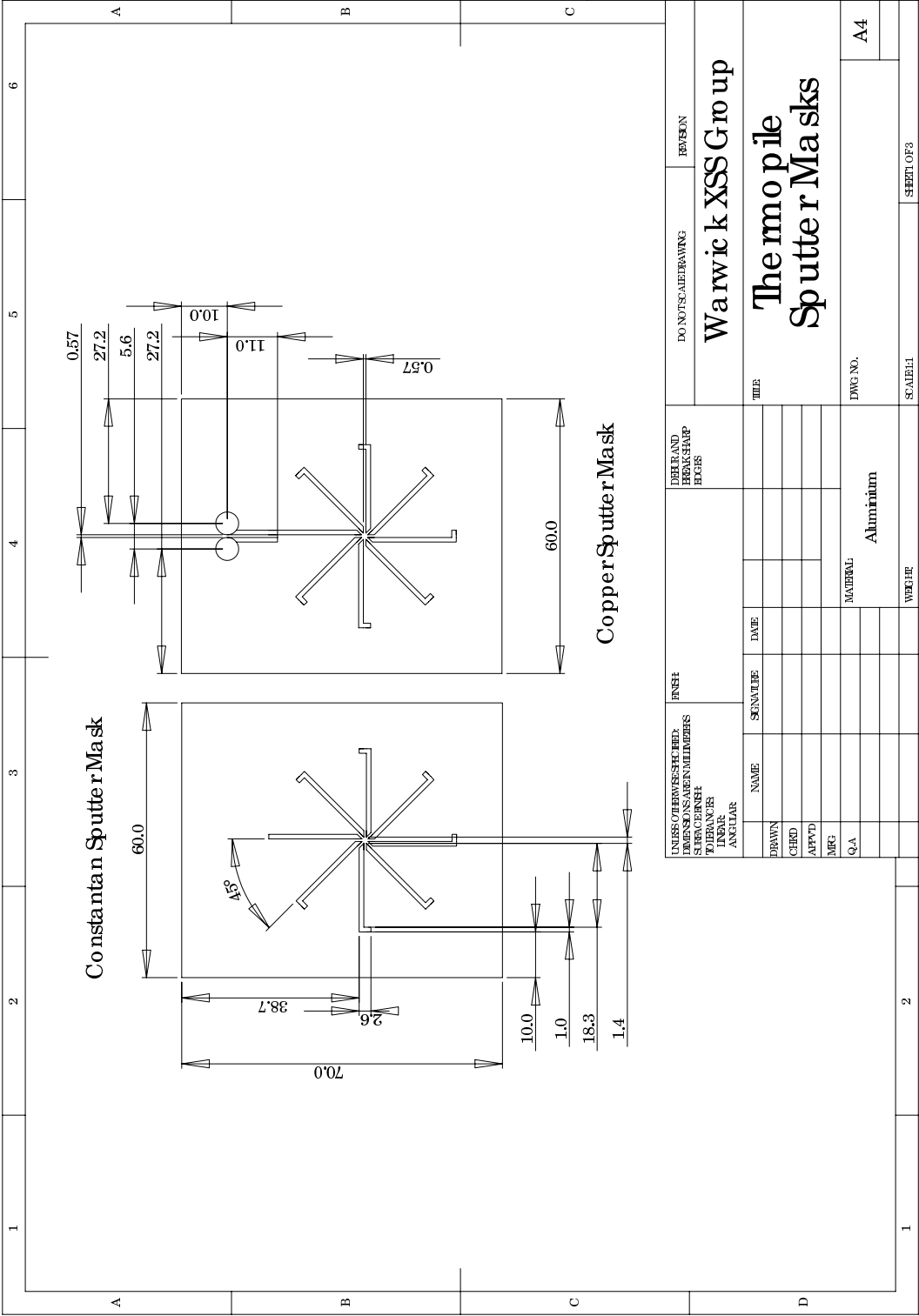


Figure A.2: A base plate onto which the gas jet and sample holder components are mounted. It is carved from a single piece of aluminium and may be attached directly to any of the beamline apparatus tables.

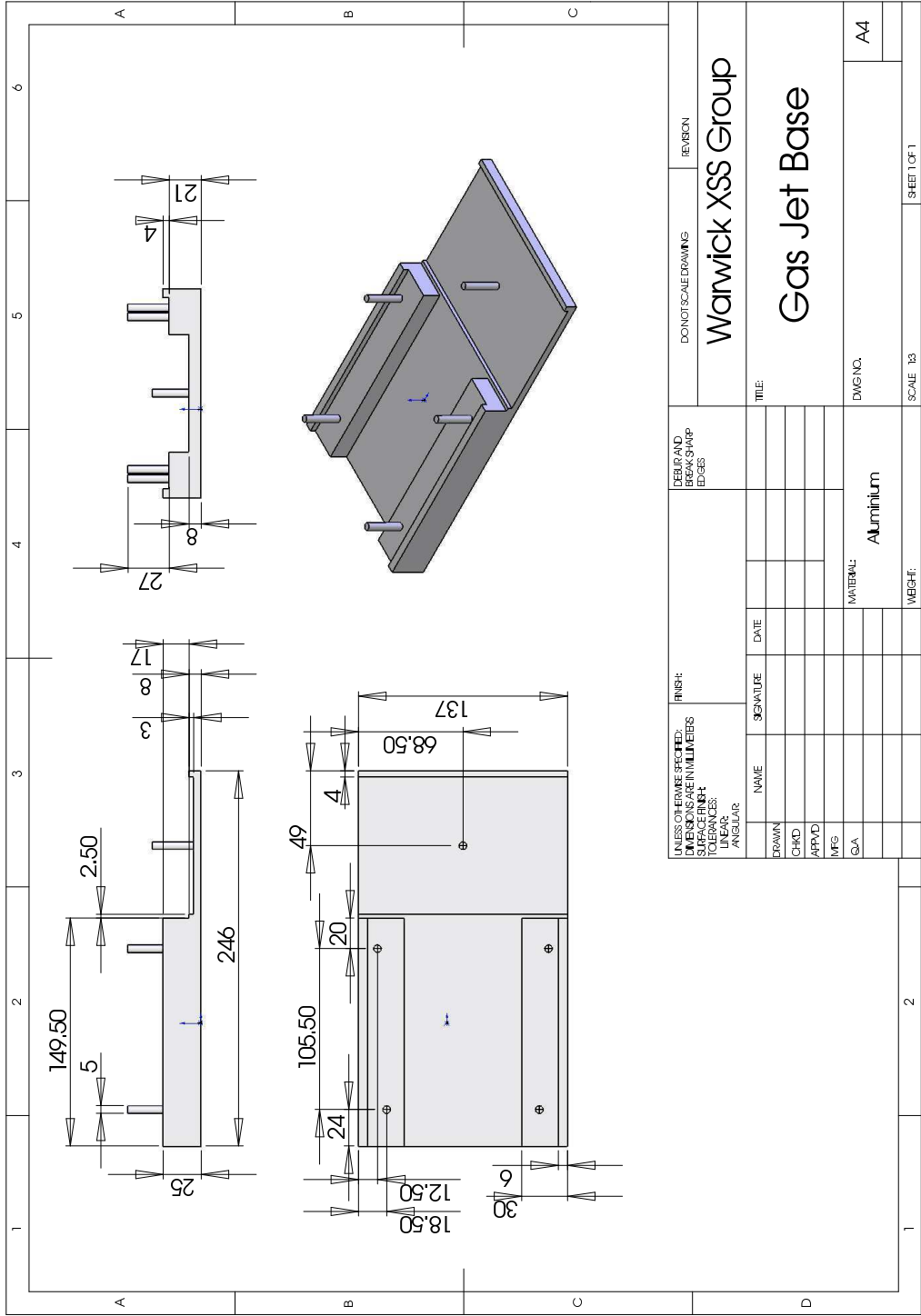
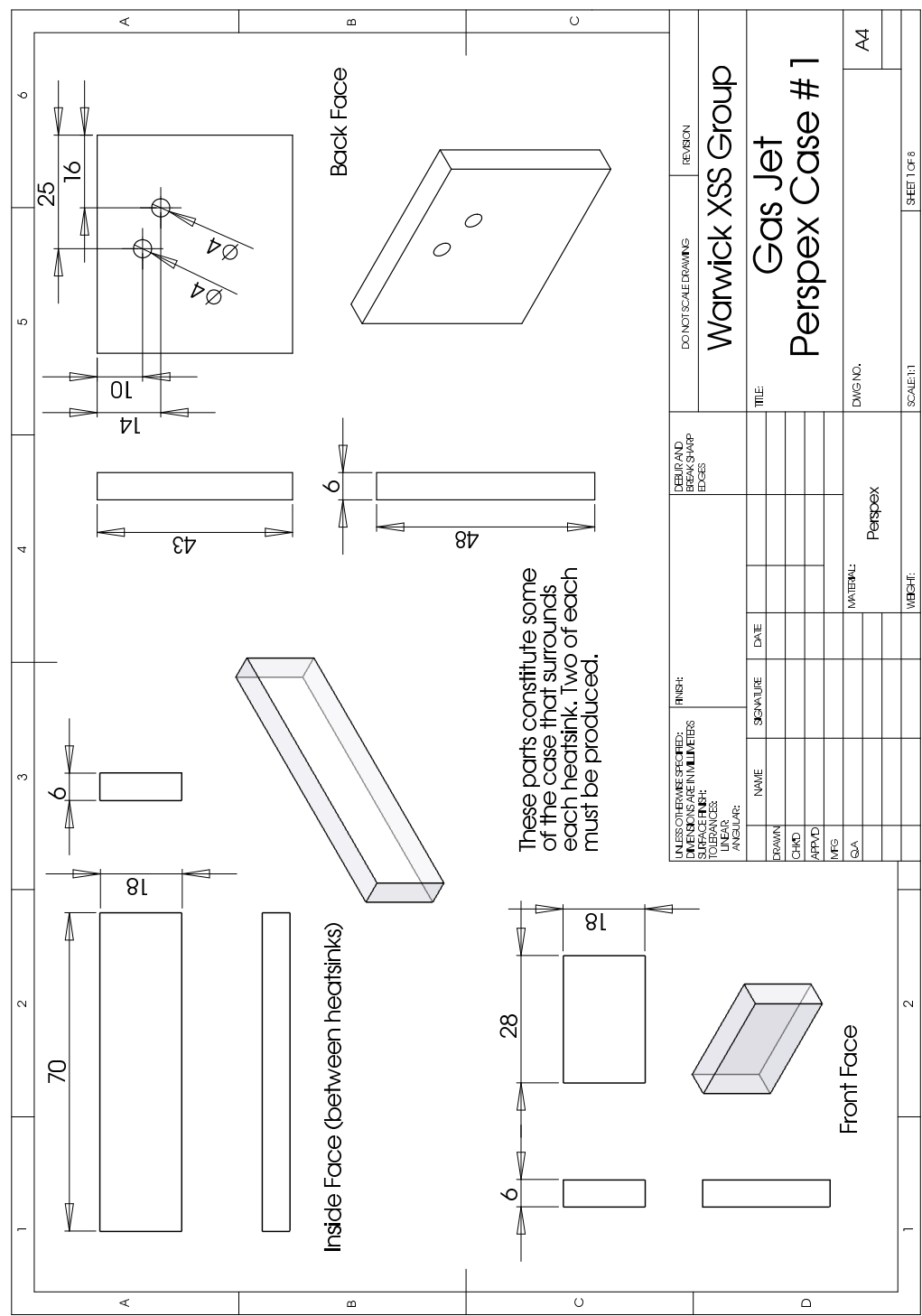
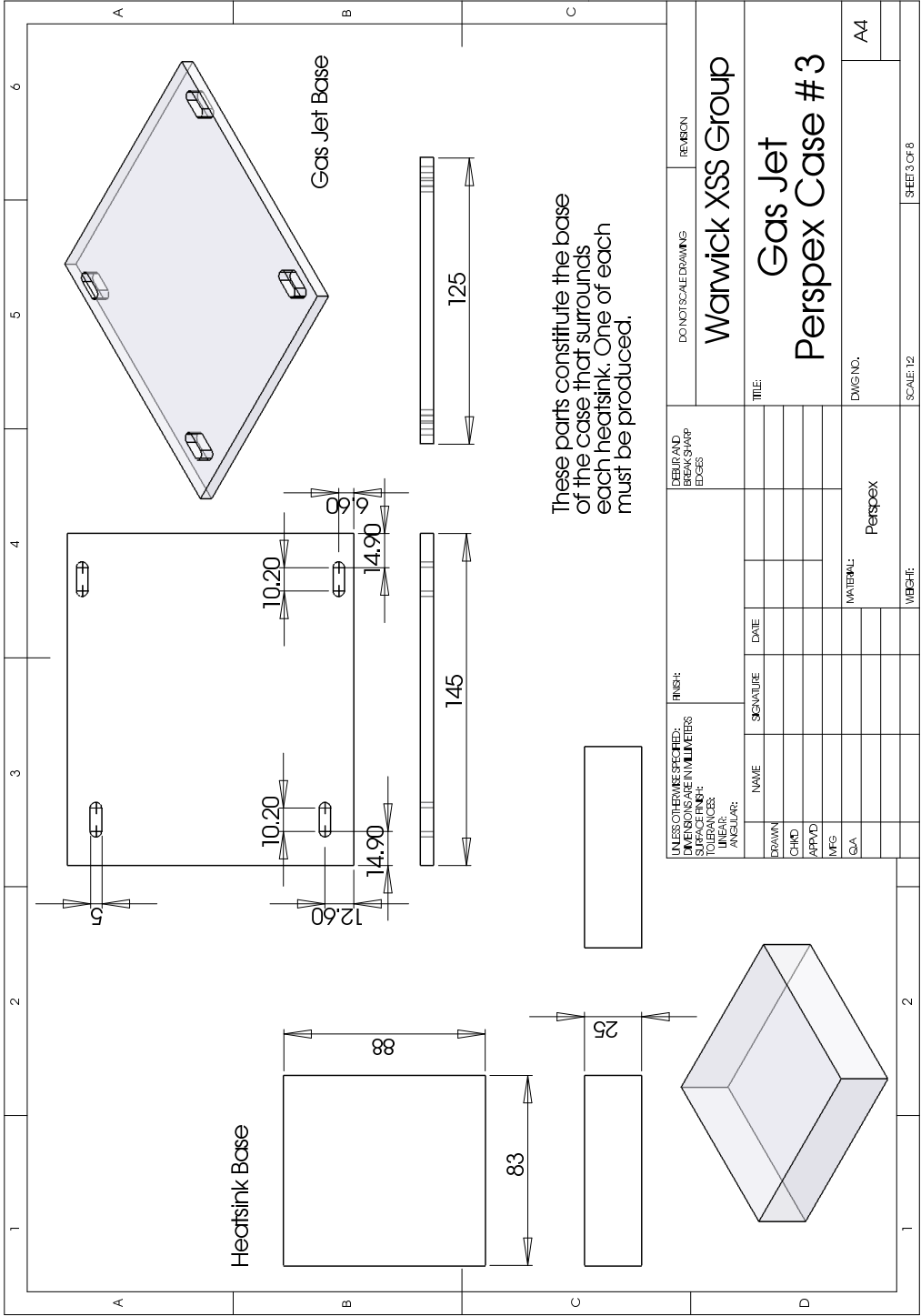


Figure A.3: Some of the parts that construct a thermally insulating case around the aluminium heatsinks. Two of each must be produced - one for each heatsink.



[illegible]

Figure A.5: The remaining parts that construct a thermally insulating case around the aluminium heatsinks. These parts make a base for the heatsinks. Only one of each is needed.





1	2	3	4	5	6
A	B	C	D	E	F

Top View

Front View

Isometric View

UNLESS OTHERWISE SPECIFIED: DIMENSIONS ARE IN MILLIMETERS		FINISH		DEBUR AND BREAK SHARP EDGES		DO NOT SCALE DRAWING		REVISION	
DRAWN	NAME	SIGNATURE	DATE	SURFACE FINISH:	TOLERANCES:				
CHKD	NAME	SIGNATURE	DATE	LINEAR:	ANGULAR:				
APPRD				MFG	MATERIAL:				
QA				MATERIAL:	Aluminium				
<div style="display: flex; justify-content: space-between;"> <div> <p>WARWICK XSS GROUP</p> <p>GAS JET HEATSINK</p> <p>REAR PROJECTION</p> </div> <div> <p>DWG NO.</p> <p>A4</p> </div> </div>				<p>SCALE: 1:1</p> <p>SHEET 1 OF 8</p>					

Figure A.7: Front projection of the aluminium heatsink. It is produced from a single piece of aluminium with channels cut into it for gas flow. The gas hose attachment nipples and gas jet needle are also shown.

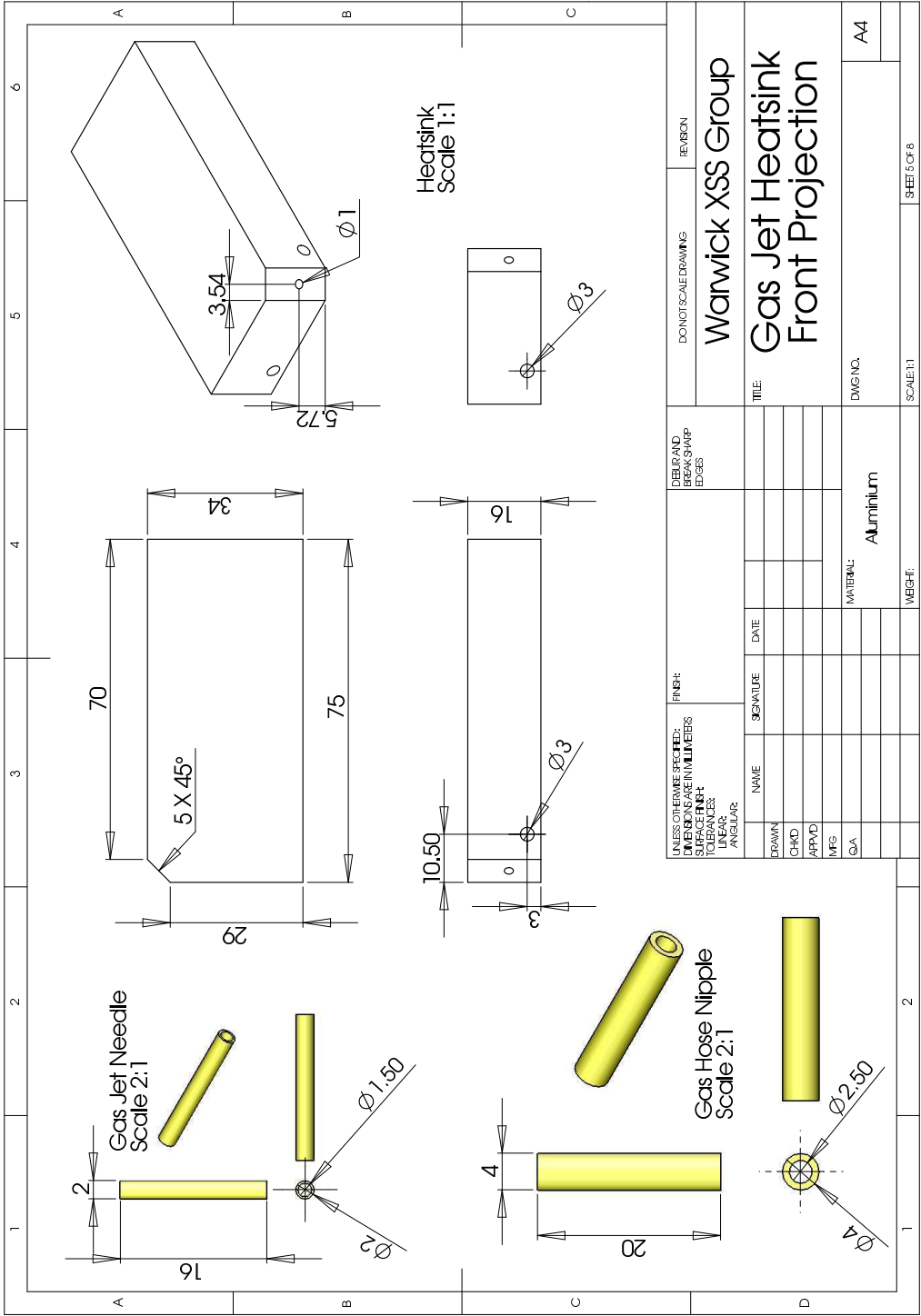


Figure A.8: A cross-section through the heatsink showing the Nitrogen gas flow channels that are used to form the gas jets.

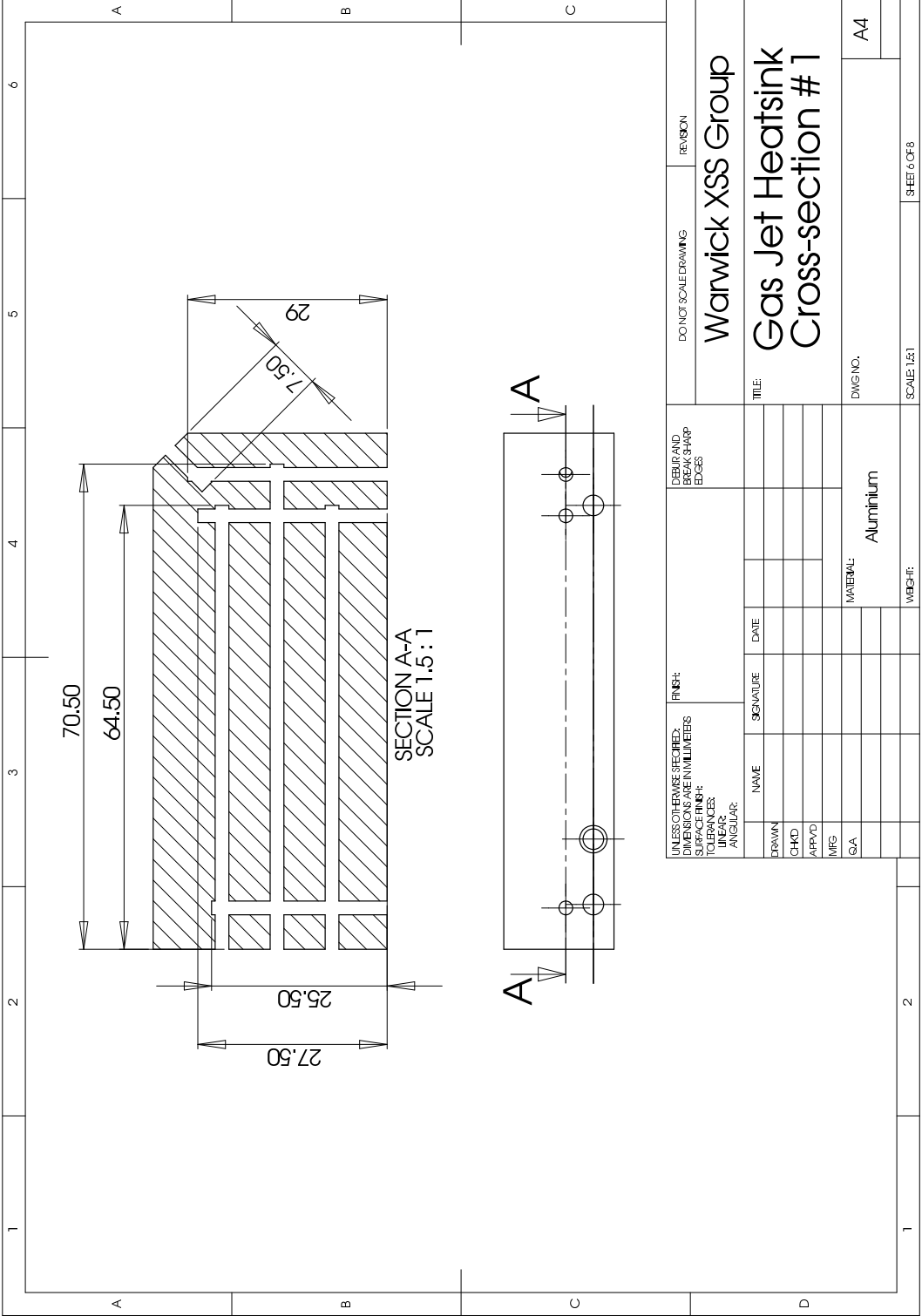


Figure A.9: A cross-section through the heatsink showing the cooling fluid channels.

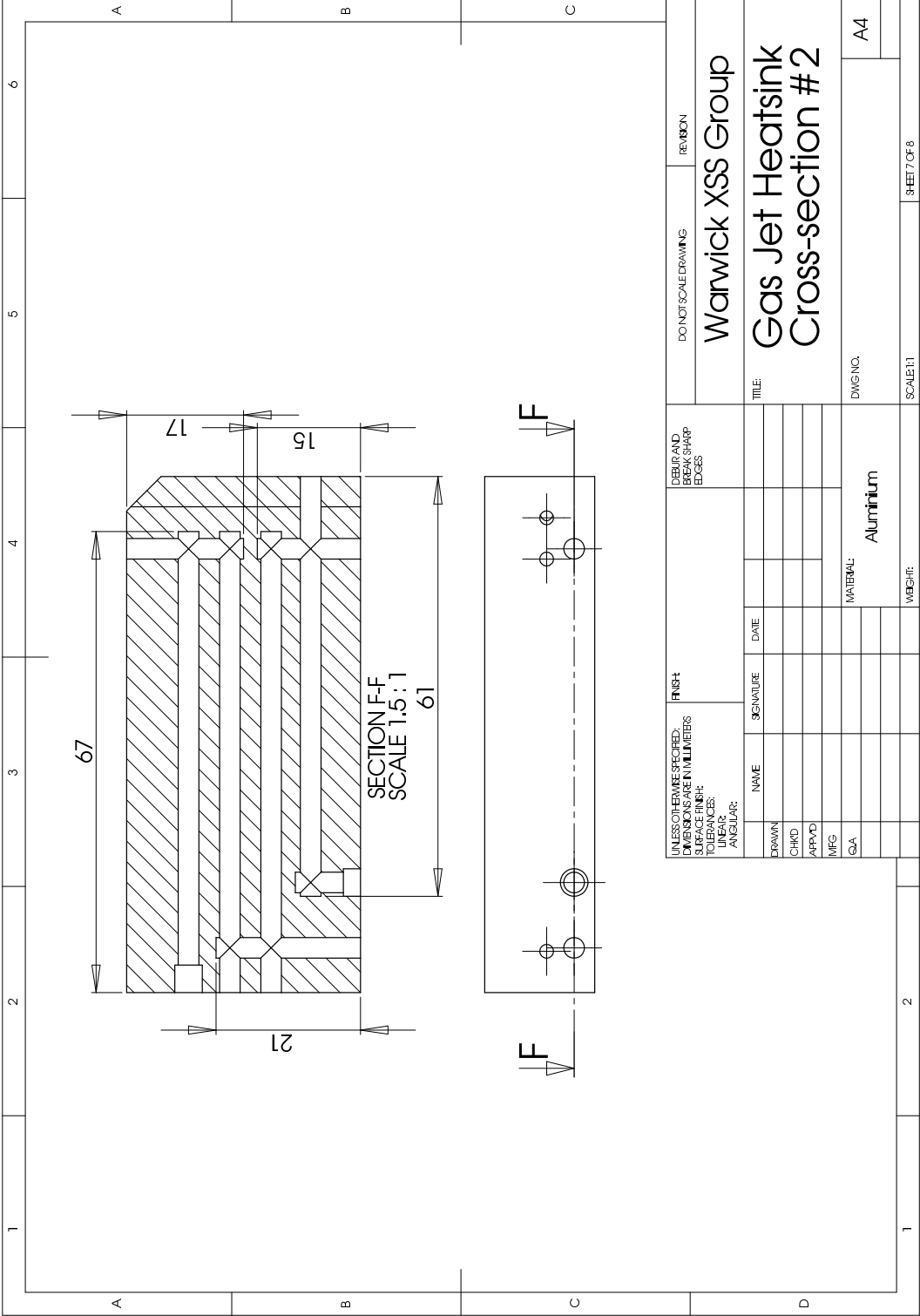


Figure A.10: The completed pair of heatsinks with brass nipples attached. Any hole shown drilled through the heatsink in Figures A.8 and A.9 that does not have a nipple attached is blocked with an aluminium plug.

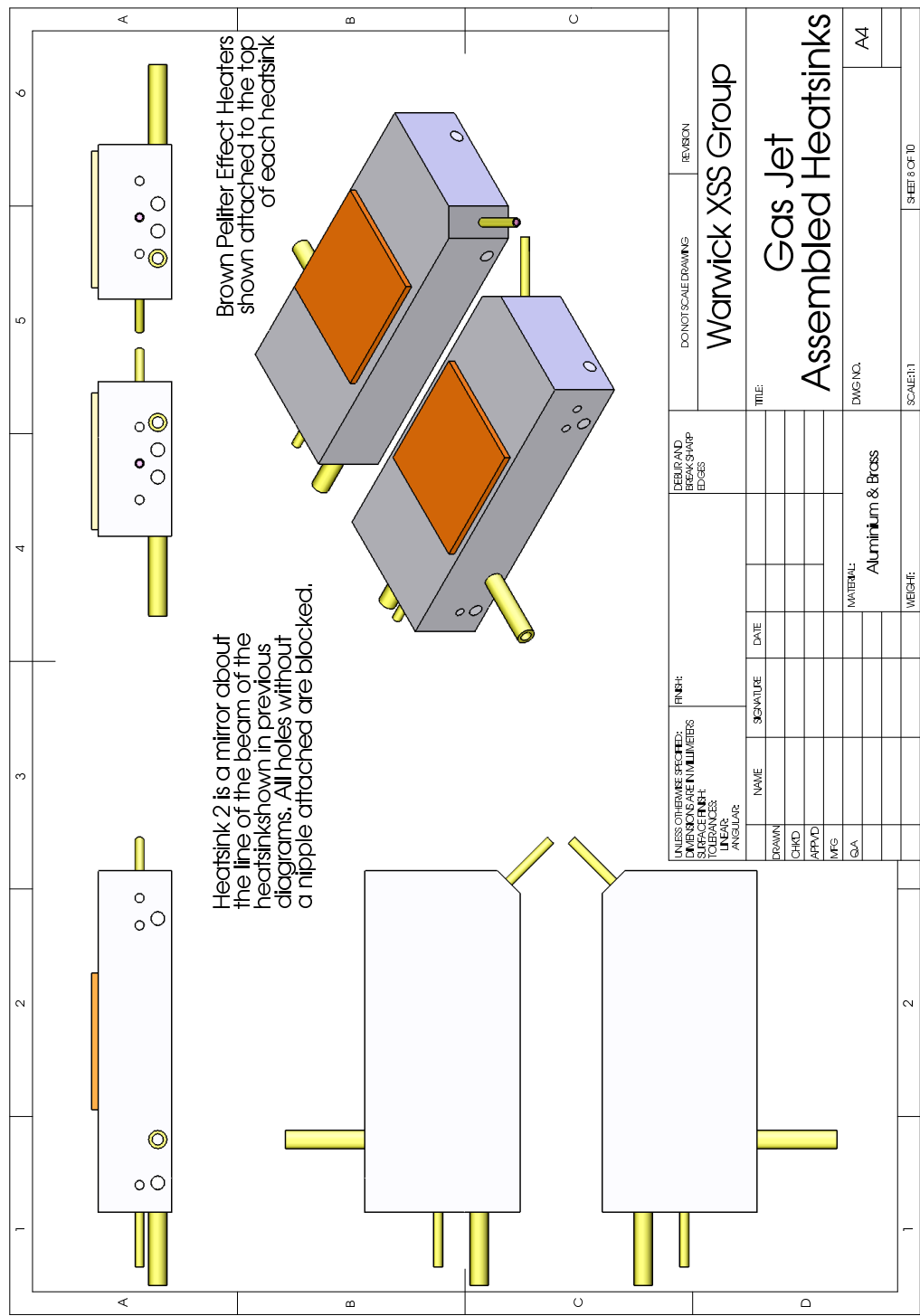


Figure A.11: The completed pair of heatsinks with perspex case, ready to mount on the base plate shown in Figure A.2.

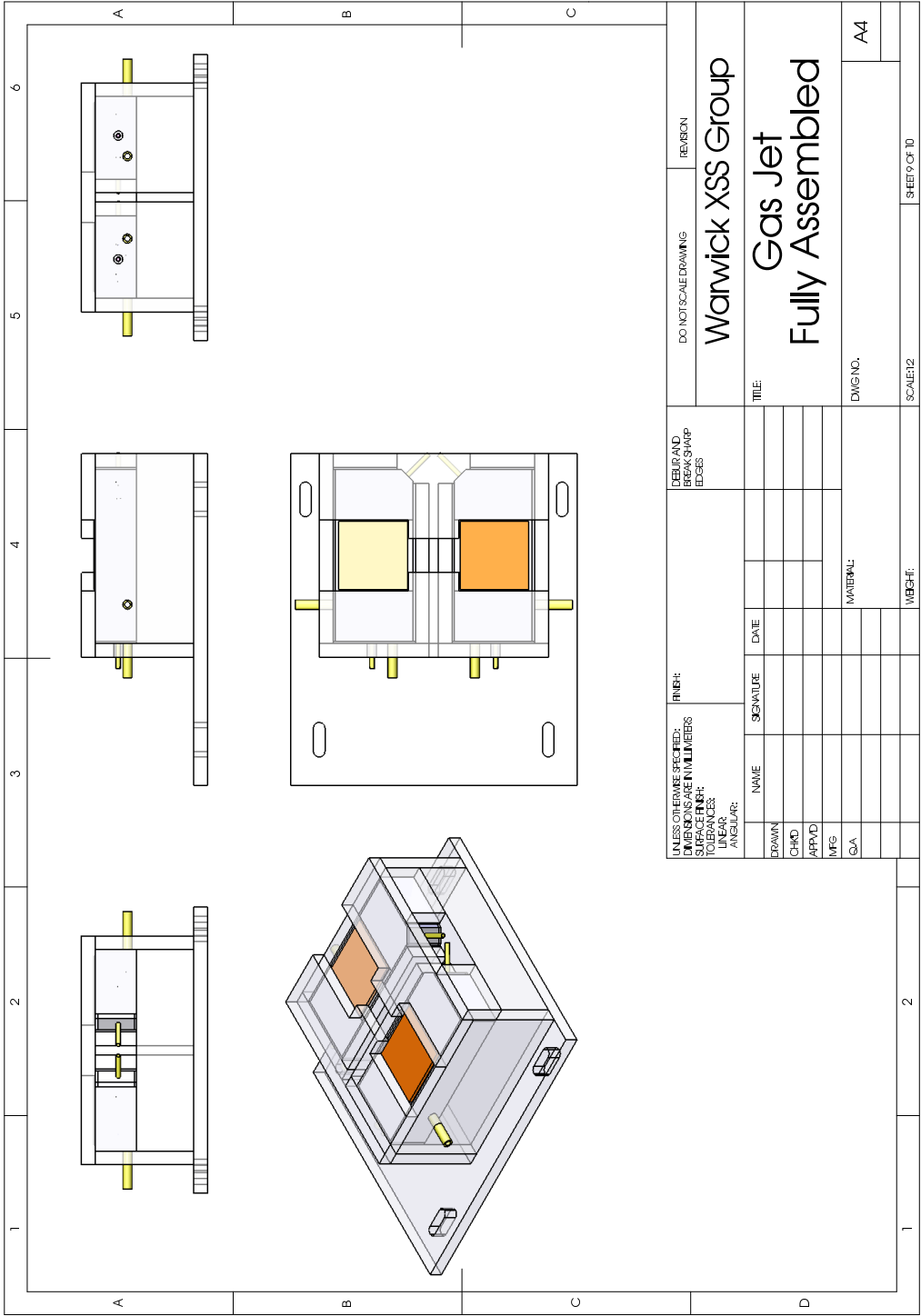
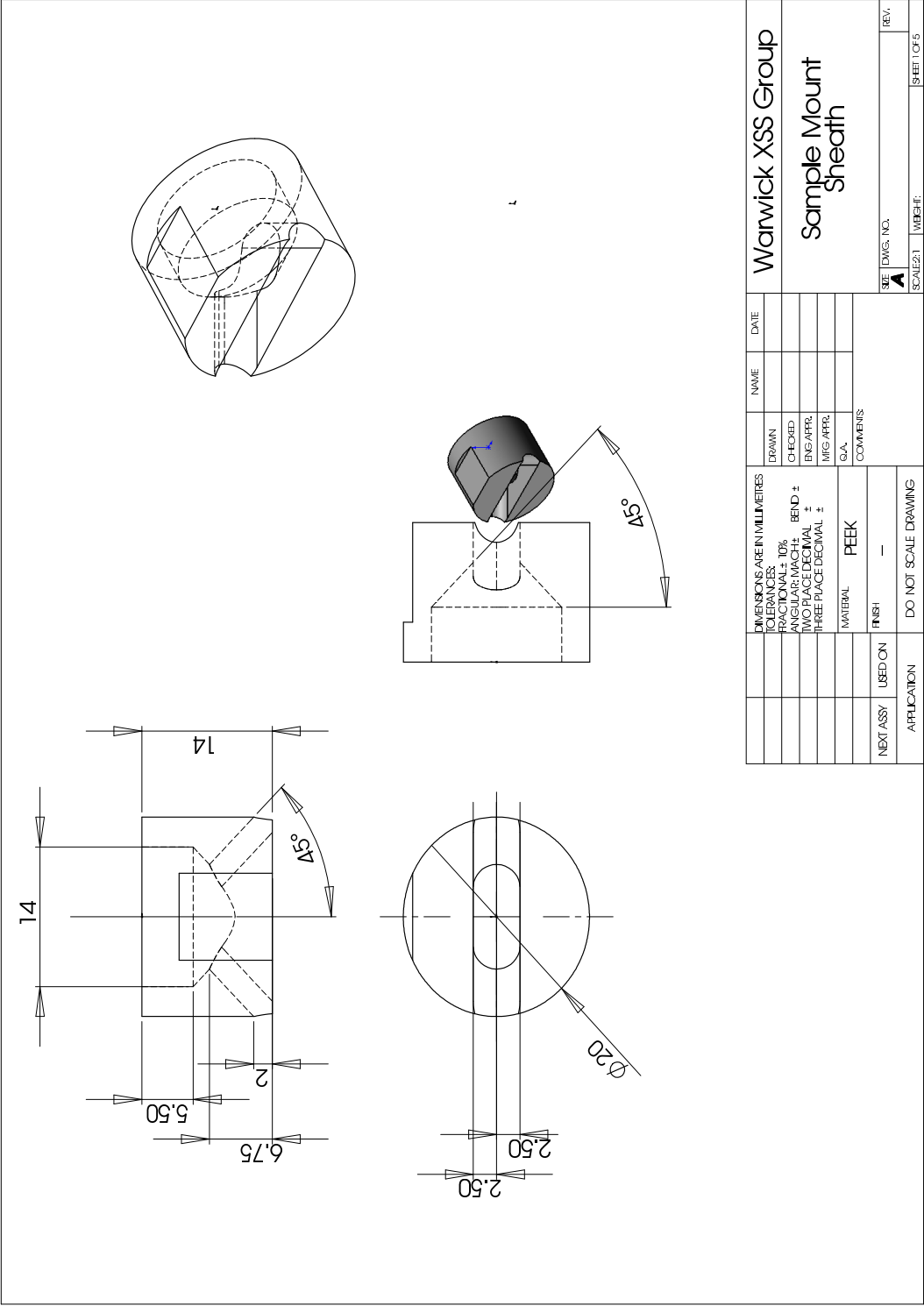


Figure A.12: The sample sheath for the revised sample mount described in Section 3.7.2.

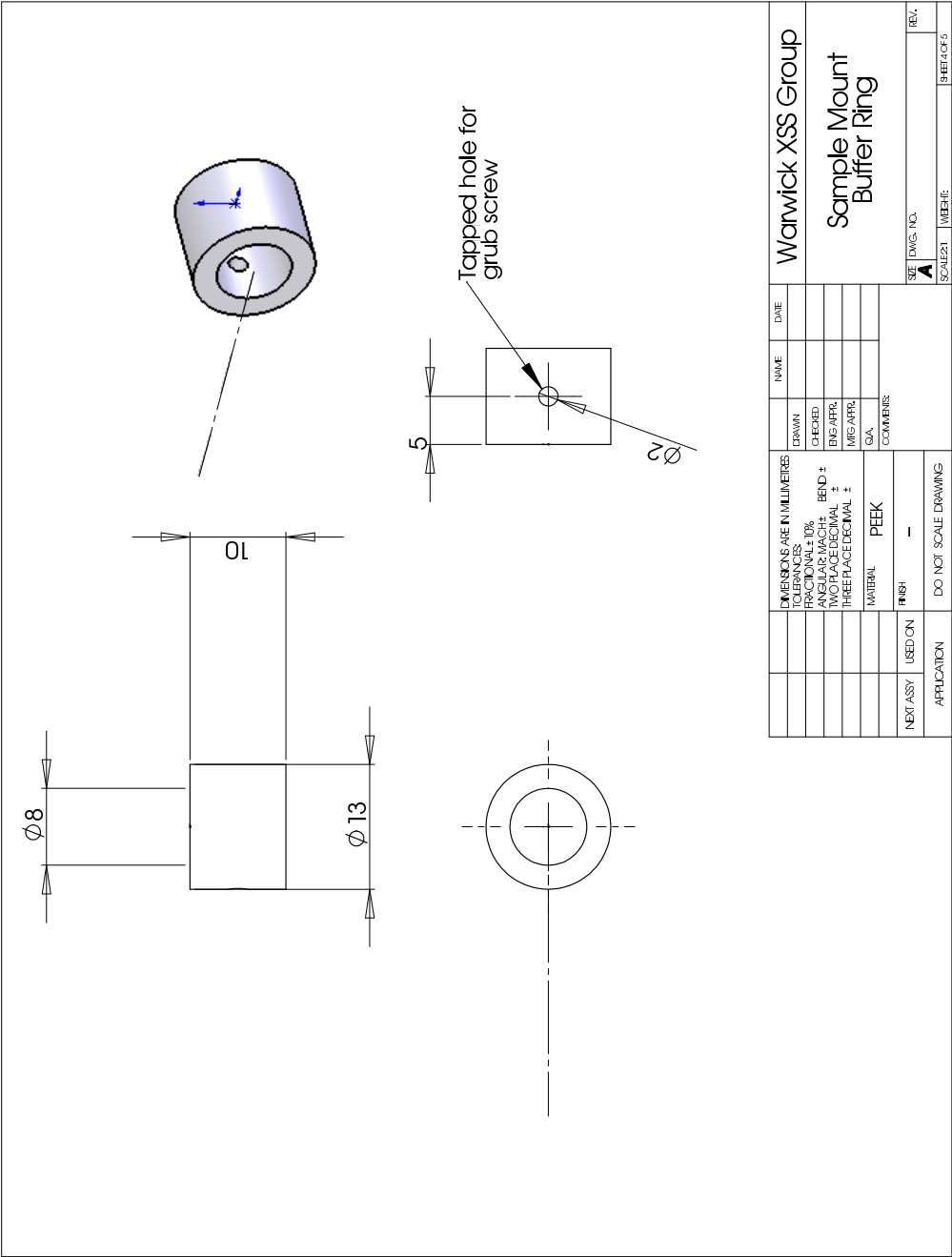


[illegible]



[illegible]

Figure A.15: The sample support buffer ring described in Section 3.7.2.



[illegible]

Figure A.17: Base section of the sample holder. This plate has a slot cut into it so that it may be attached to the aluminium base plate shown in Figure A.2.

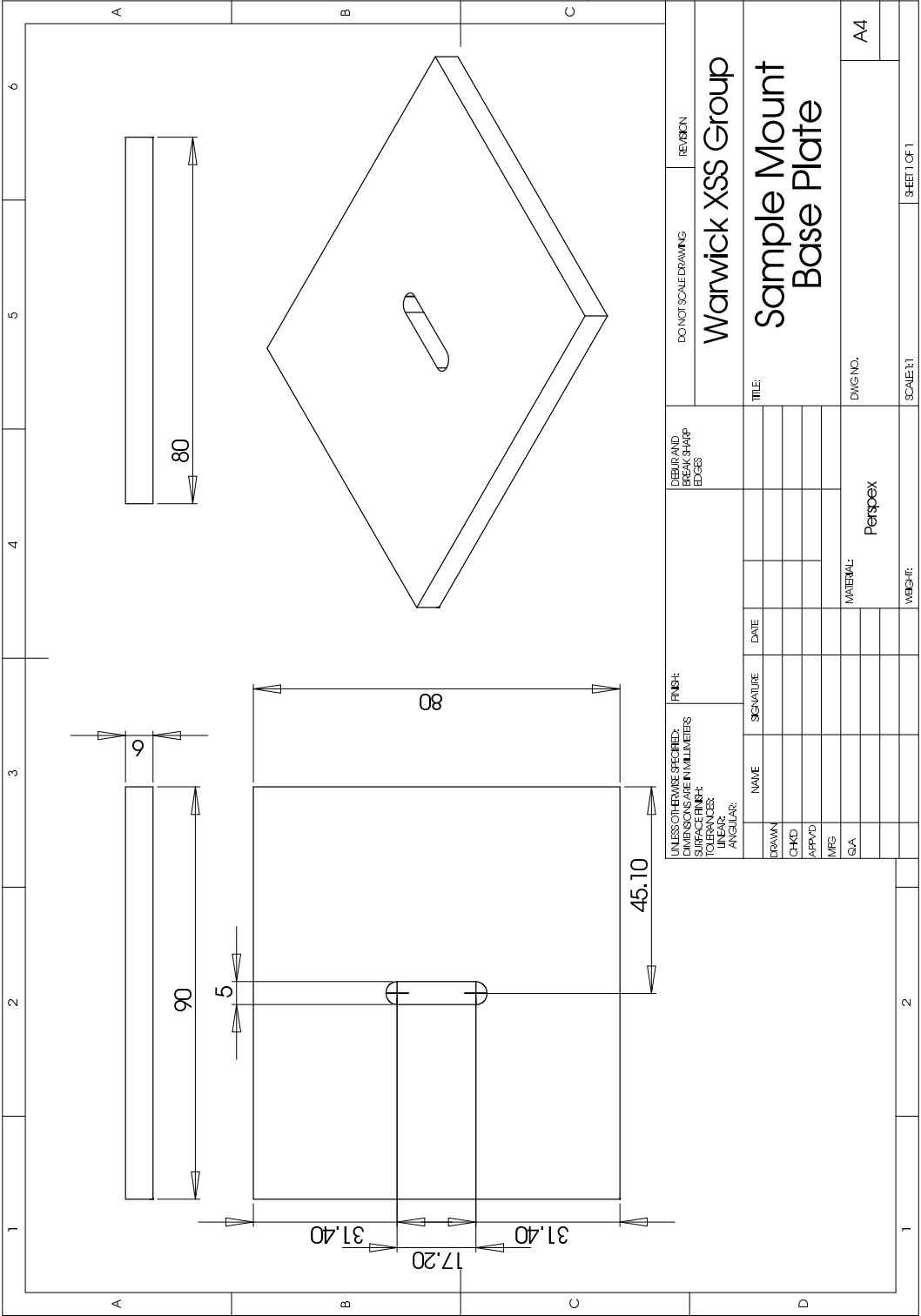


Figure A.18: Lateral support struts attached between the sample holder base plate in Figure A.17, and the front plate in Figure A.13

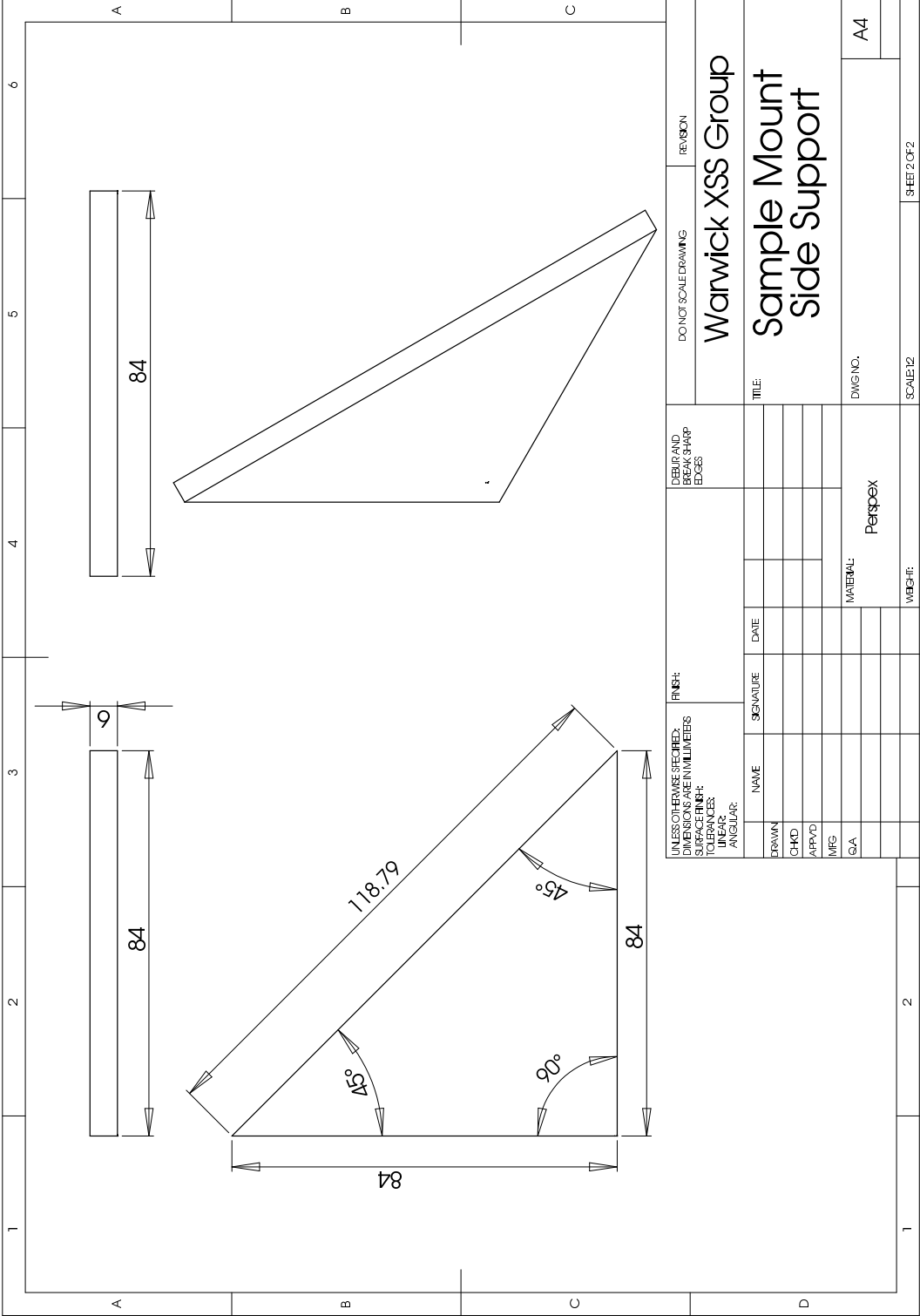


Figure A.19: The complete sample mount, ready to be attached to the aluminium base plate shown in Figure A.2.

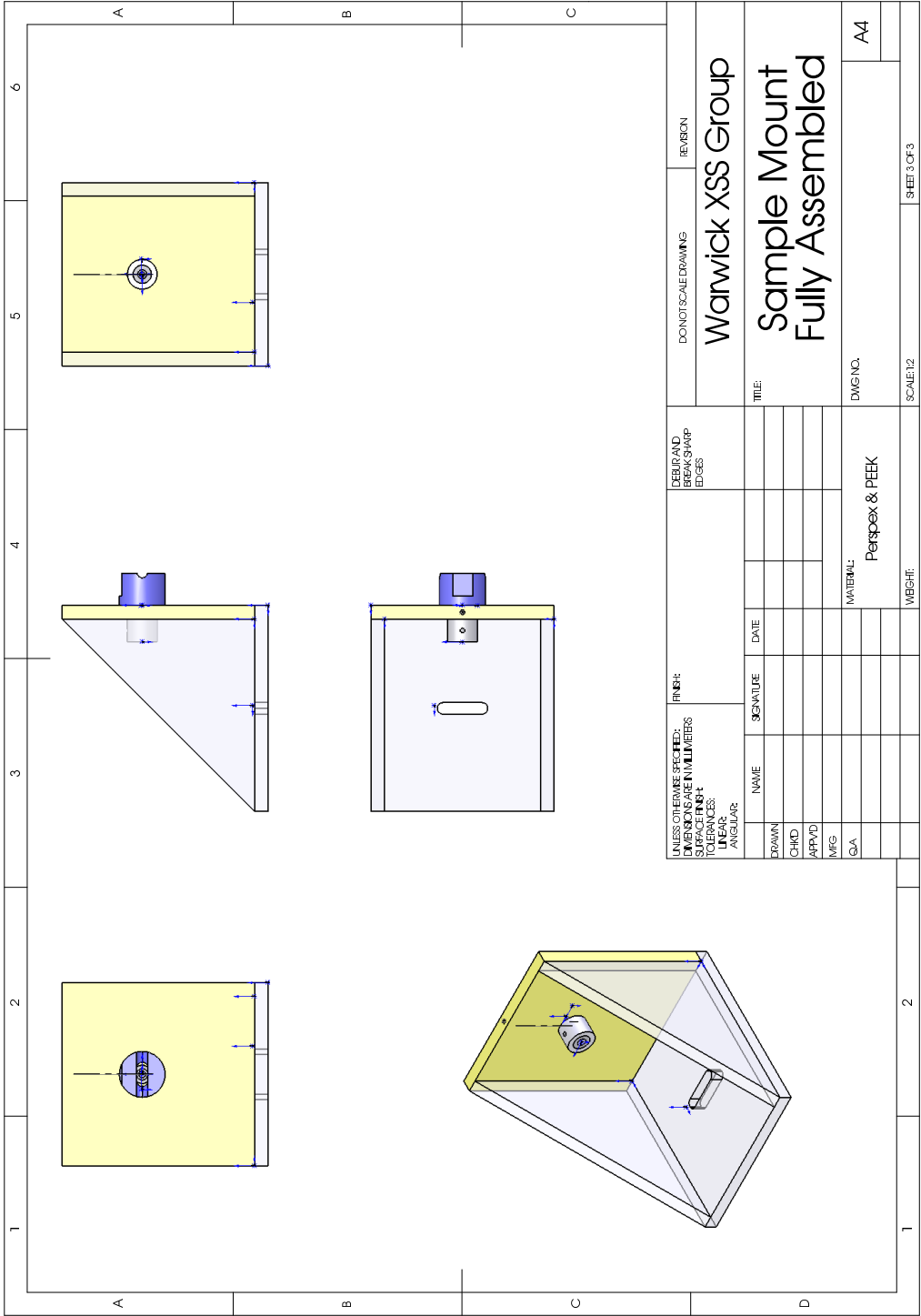


Figure A.20: The complete gas jet apparatus.

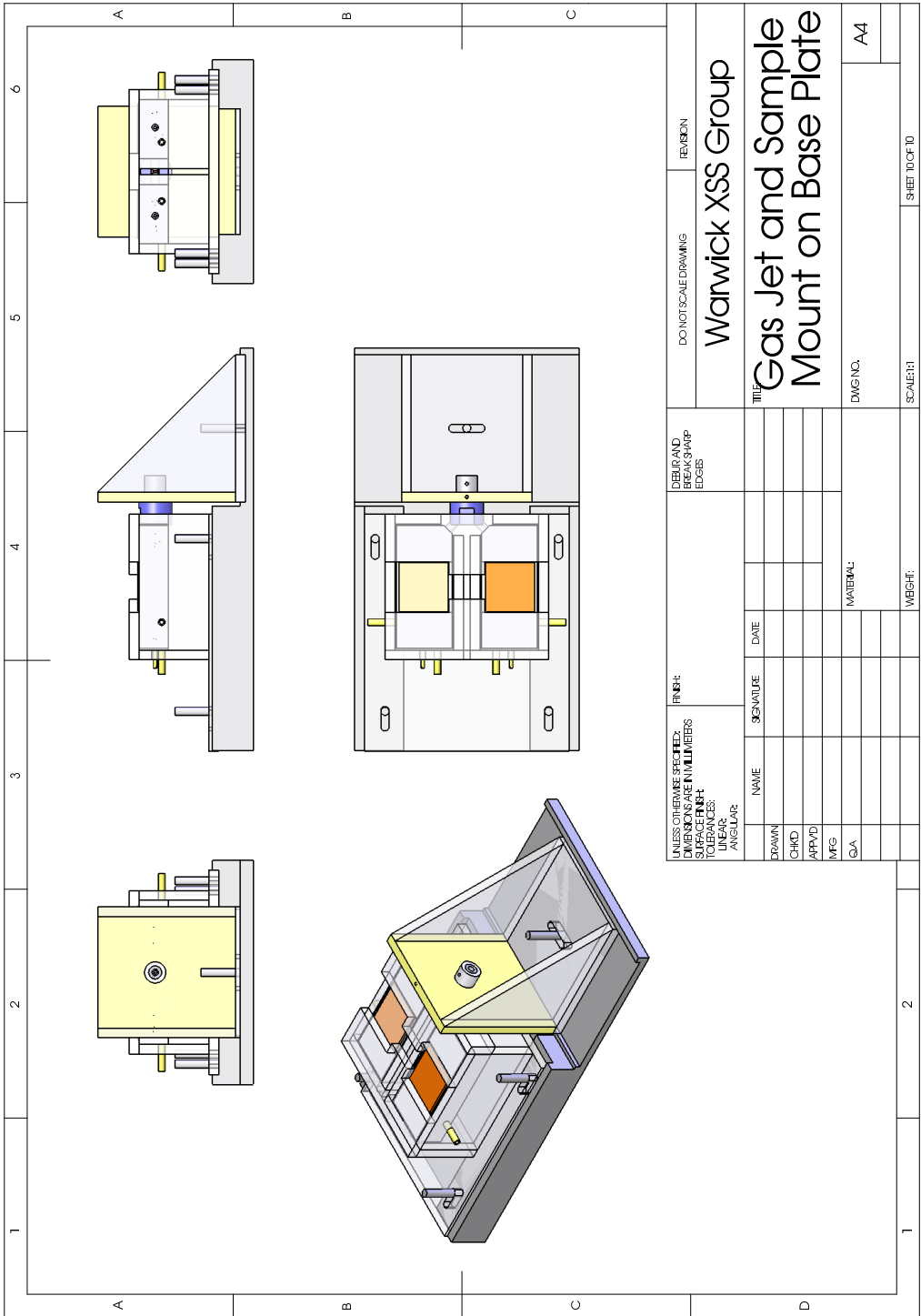
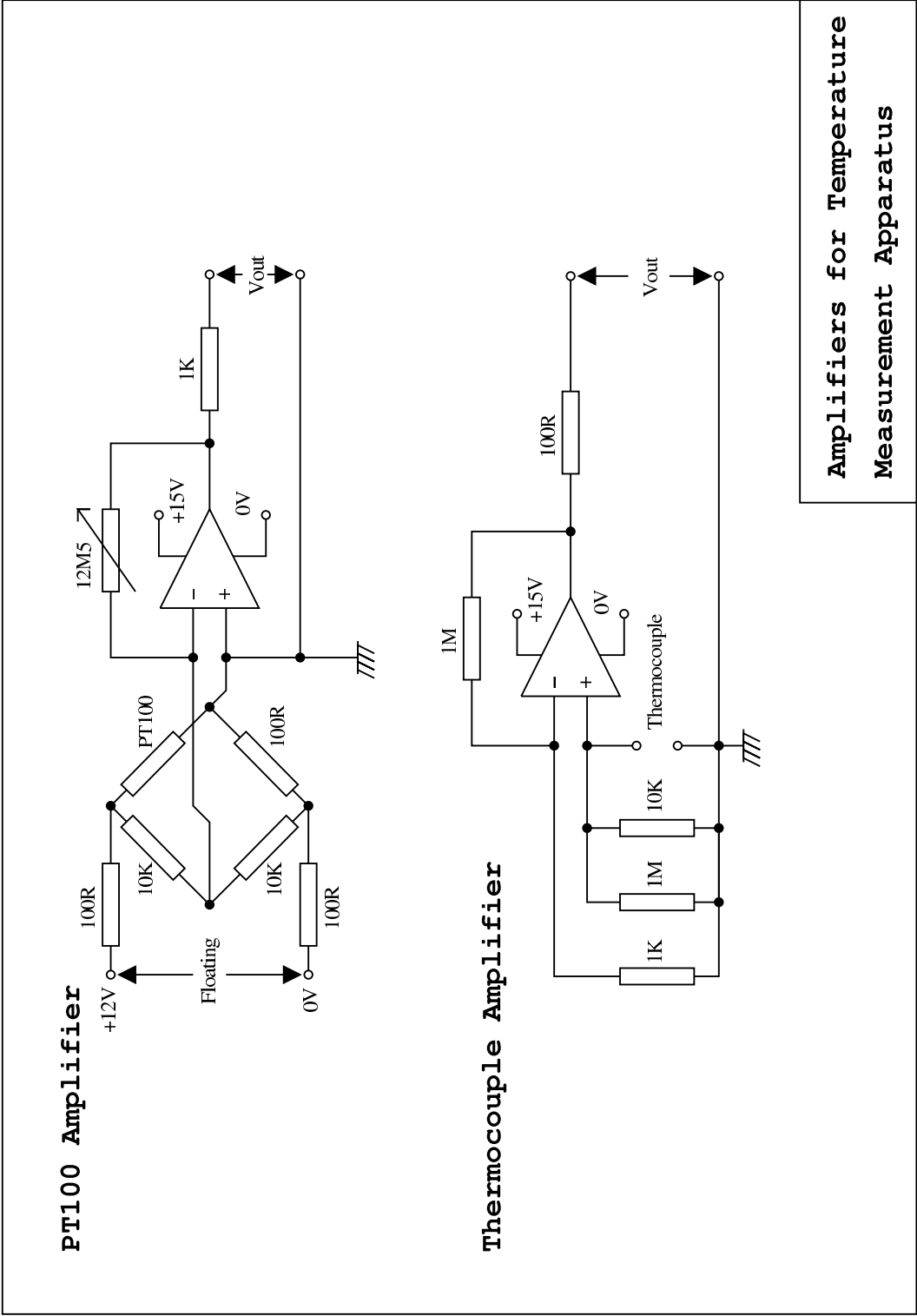


Figure A.21: Circuit schematics for the temperature measurement amplifiers. Designed by A. Lovejoy of the Warwick Physics Dept. Electronics Workshop.





Circuit schematic for Gas Jet Proportional Integral Derivative Temperature Controller

\* Screwdriver adjusted on front panel  
 \*\* Temperature setting on front panel

## **Appendix B**

# **The Ni<sub>2</sub>MnGa Crystal Structure**

Figure B.1: Crystal structure of the Body-Centred Tetragonal (BCT) Martensite in  $\text{Ni}_2\text{MnGa}$ . The structure is of space group  $I4/mmm$  with lattice parameters  $a = b = 5.90\text{\AA}$  and  $c = 5.54\text{\AA}$ . Ni atoms are shown in light blue and have crystallographic coordinates of 0.25, 0.25, 0.25; Mn atoms are red, positioned at 0.5, 0.0, 0.0; and Ga atoms are Green, positioned at 0.0, 0.0, 0.0.

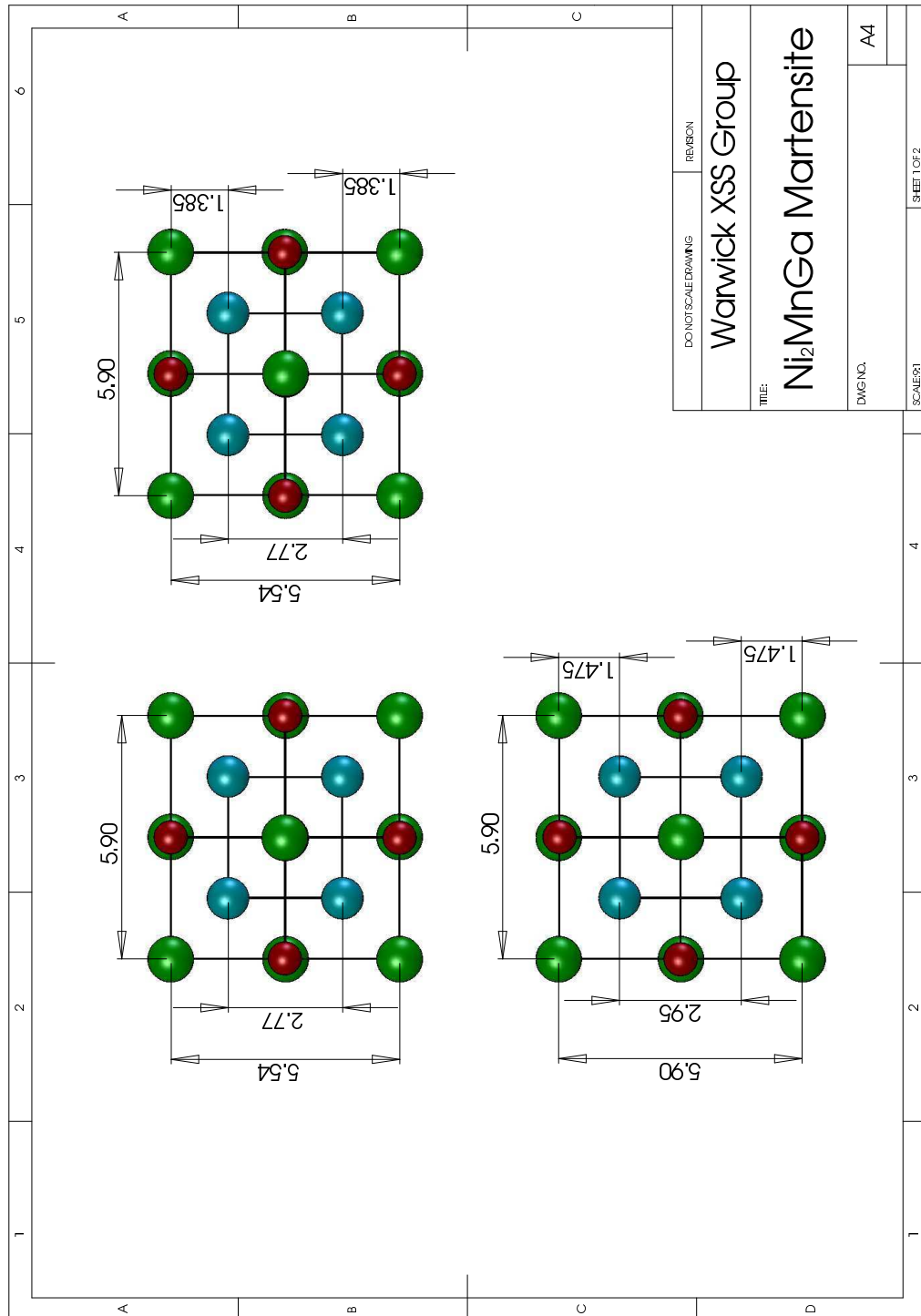


Figure B.2: Crystal structure of the L2<sub>1</sub> Face-centred Cubic (FCC) Austenite in Ni<sub>2</sub>MnGa. The structure is of space group Fm3m with lattice parameters  $a = b = c = 5.825\text{\AA}$ . Ni atoms are shown in light blue and have crystallographic coordinates of 0.25, 0.25, 0.25; Mn atoms are red, positioned at 0.5, 0.0, 0.0; and Ga atoms are Green, positioned at 0.0, 0.0, 0.0.

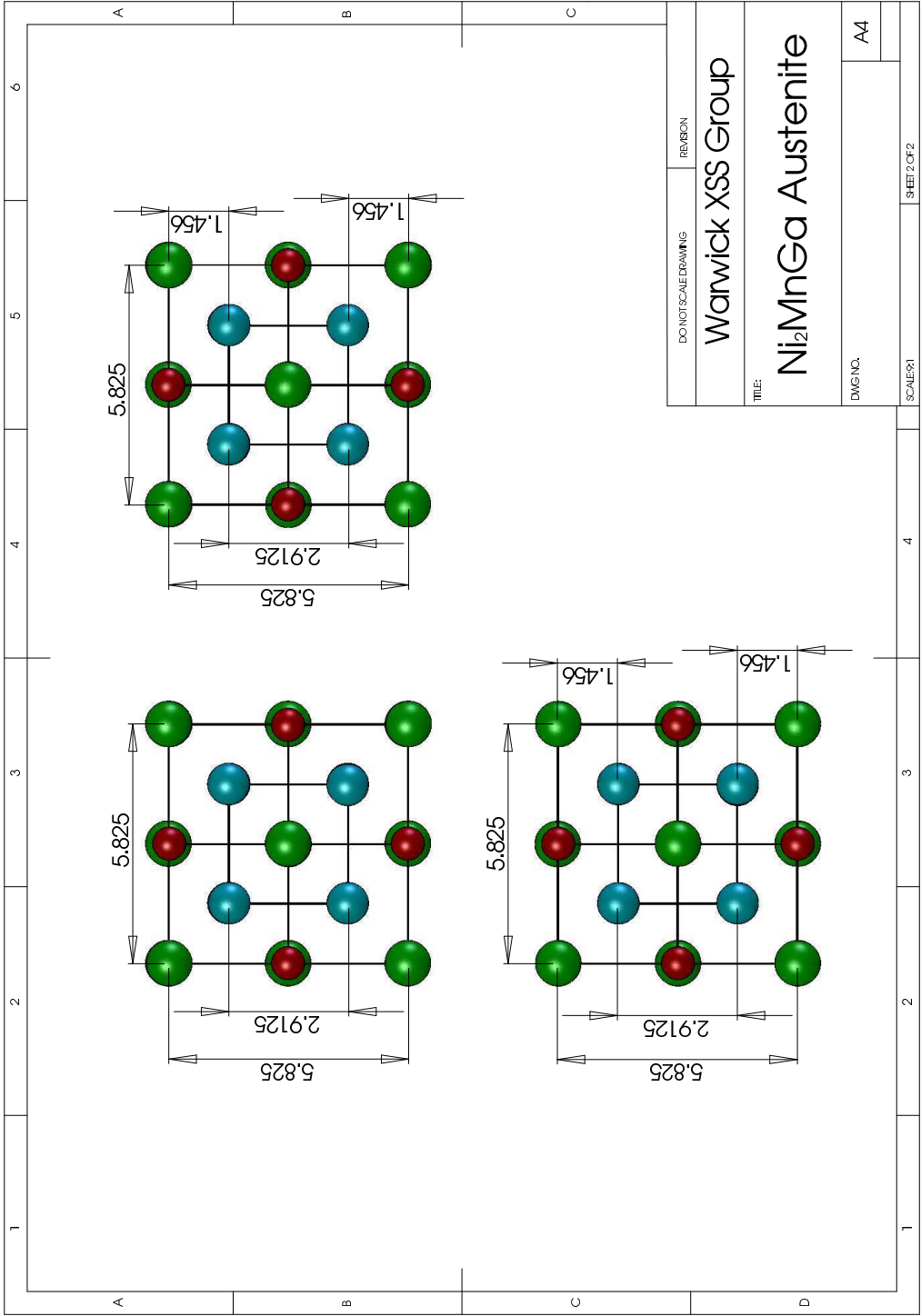
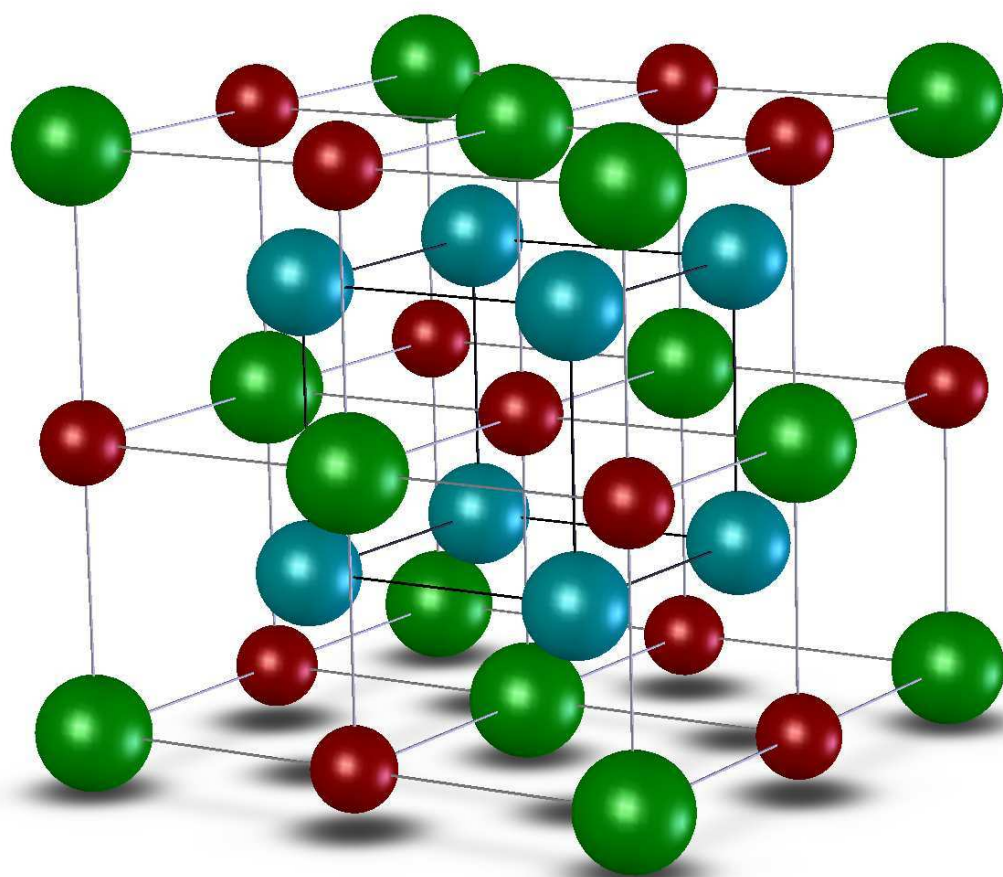


Figure B.3: A 3D view of the BCT Martensite in  $\text{Ni}_2\text{MnGa}$ . Ni atoms are shown in light blue, Mn atoms in red, and Ga atoms in Green. A similar view of the  $\text{L2}_1$  FCC Austenite could also be included here, but the differences in structure are too small to be visible by eye.



## **Appendix C**

# **Further details on DiffEXAFS analysis**

## C.1 Fe and SrF<sub>2</sub> Thermal Expansion Analysis

### C.1.1 FEFF Input Configuration Files

This section contains the FEFF input files (from 'feff.inp') that were used when calculating scattering phase and amplitude information for subsequent EXAFS and DiffEXAFS analysis as described in Chapter 4.

The first is for the iron calculation. Scattering paths were considered out to 5Å in order to match the Fourier filter window to be used in subsequent experimental EXAFS fits. This requiring a list of 58 atoms to be specified. Any scattering path contribution with amplitude less than 4% that of the largest path was rejected.

```
*      pot    xsph  fms   paths  genfmt  ff2chi
CONTROL  1      1      1      1      1      1
PRINT    1      0      0      0      1      2

CRITERIA 5.0 4.0
RPATH 5.0
EXAFS 20

POTENTIALS
*      ipot    Z  element          l_scm  l_fms  stoichiometry
      0      26  Fe              2      2      0.001
      1      26  Fe              2      2      2

ATOMS
*      x      y      z      ipot  tag      distance
0.00000  0.00000  0.00000  0      Fe      0.00000  0
1.43325  1.43325  1.43325  1      Fe      2.48246  1
-1.43325  1.43325  1.43325  1      Fe      2.48246  2
1.43325  -1.43325  1.43325  1      Fe      2.48246  3
-1.43325  -1.43325  1.43325  1      Fe      2.48246  4
1.43325  1.43325  -1.43325  1      Fe      2.48246  5
-1.43325  1.43325  -1.43325  1      Fe      2.48246  6
1.43325  -1.43325  -1.43325  1      Fe      2.48246  7
-1.43325  -1.43325  -1.43325  1      Fe      2.48246  8
2.86650  0.00000  0.00000  1      Fe      2.86650  9
-2.86650  0.00000  0.00000  1      Fe      2.86650  10
0.00000  2.86650  0.00000  1      Fe      2.86650  11
0.00000  -2.86650  0.00000  1      Fe      2.86650  12
0.00000  0.00000  2.86650  1      Fe      2.86650  13
0.00000  0.00000  -2.86650  1      Fe      2.86650  14
2.86650  2.86650  0.00000  1      Fe      4.05384  15
-2.86650  2.86650  0.00000  1      Fe      4.05384  16
2.86650  -2.86650  0.00000  1      Fe      4.05384  17
-2.86650  -2.86650  0.00000  1      Fe      4.05384  18
2.86650  0.00000  2.86650  1      Fe      4.05384  19
-2.86650  0.00000  2.86650  1      Fe      4.05384  20
0.00000  2.86650  2.86650  1      Fe      4.05384  21
0.00000  -2.86650  2.86650  1      Fe      4.05384  22
2.86650  0.00000  -2.86650  1      Fe      4.05384  23
-2.86650  0.00000  -2.86650  1      Fe      4.05384  24
0.00000  2.86650  -2.86650  1      Fe      4.05384  25
0.00000  -2.86650  -2.86650  1      Fe      4.05384  26
4.29975  1.43325  1.43325  1      Fe      4.75355  27
```

```

-4.29975    1.43325    1.43325    1    Fe    4.75355    28
 1.43325    4.29975    1.43325    1    Fe    4.75355    29
-1.43325    4.29975    1.43325    1    Fe    4.75355    30
 4.29975   -1.43325    1.43325    1    Fe    4.75355    31
-4.29975   -1.43325    1.43325    1    Fe    4.75355    32
 1.43325   -4.29975    1.43325    1    Fe    4.75355    33
-1.43325   -4.29975    1.43325    1    Fe    4.75355    34
 1.43325    1.43325    4.29975    1    Fe    4.75355    35
-1.43325    1.43325    4.29975    1    Fe    4.75355    36
 1.43325   -1.43325    4.29975    1    Fe    4.75355    37
-1.43325   -1.43325    4.29975    1    Fe    4.75355    38
 4.29975    1.43325   -1.43325    1    Fe    4.75355    39
-4.29975    1.43325   -1.43325    1    Fe    4.75355    40
 1.43325    4.29975   -1.43325    1    Fe    4.75355    41
-1.43325    4.29975   -1.43325    1    Fe    4.75355    42
 4.29975   -1.43325   -1.43325    1    Fe    4.75355    43
-4.29975   -1.43325   -1.43325    1    Fe    4.75355    44
 1.43325   -4.29975   -1.43325    1    Fe    4.75355    45
-1.43325   -4.29975   -1.43325    1    Fe    4.75355    46
 1.43325    1.43325   -4.29975    1    Fe    4.75355    47
-1.43325    1.43325   -4.29975    1    Fe    4.75355    48
 1.43325   -1.43325   -4.29975    1    Fe    4.75355    49
-1.43325   -1.43325   -4.29975    1    Fe    4.75355    50
 2.86650    2.86650    2.86650    1    Fe    4.96492    51
-2.86650    2.86650    2.86650    1    Fe    4.96492    52
 2.86650   -2.86650    2.86650    1    Fe    4.96492    53
-2.86650   -2.86650    2.86650    1    Fe    4.96492    54
 2.86650    2.86650   -2.86650    1    Fe    4.96492    55
-2.86650    2.86650   -2.86650    1    Fe    4.96492    56
 2.86650   -2.86650   -2.86650    1    Fe    4.96492    57
-2.86650   -2.86650   -2.86650    1    Fe    4.96492    58
END

```

The next 'feff.inp' file relates to SrF<sub>2</sub> calculations at the Sr-K edge. Here, the list of atoms is truncated at 4.6Å since no atoms beyond that radius contributed to the DiffEXAFS fits.

```

*      pot    xsph  fms   paths  genfmt  ff2chi
CONTROL  1      1      1      1      1      1
PRINT    1      0      0      0      1      2

CRITERIA 6.0 3.0
EXAFS    16
RPATH    9.1
NLEG     6
CORRECTIONS 0.0 0.0

POTENTIALS
*      ipot  Z  element
      0  38  Sr
      1  38  Sr
      2   9  F

ATOMS
*      x      y      z      ipot  tag      distance
0.00000  0.00000  0.00000  0      Sr      0.00000
1.44990  1.44990  1.44990  2      F_1    2.51130
-1.44990  1.44990  1.44990  2      F_1    2.51130
1.44990  -1.44990  1.44990  2      F_1    2.51130
-1.44990  -1.44990  1.44990  2      F_1    2.51130
1.44990  1.44990  -1.44990  2      F_1    2.51130
-1.44990  1.44990  -1.44990  2      F_1    2.51130

```



```

1.44990 -1.44990 -1.44990 2 F_1 2.51130
-1.44990 -1.44990 -1.44990 2 F_1 2.51130
2.89980 2.89980 0.00000 1 Sr_1 4.10094
-2.89980 2.89980 0.00000 1 Sr_1 4.10094
2.89980 -2.89980 0.00000 1 Sr_1 4.10094
-2.89980 -2.89980 0.00000 1 Sr_1 4.10094
2.89980 0.00000 2.89980 1 Sr_1 4.10094
-2.89980 0.00000 2.89980 1 Sr_1 4.10094
0.00000 2.89980 2.89980 1 Sr_1 4.10094
0.00000 -2.89980 2.89980 1 Sr_1 4.10094
2.89980 0.00000 -2.89980 1 Sr_1 4.10094
-2.89980 0.00000 -2.89980 1 Sr_1 4.10094
0.00000 2.89980 -2.89980 1 Sr_1 4.10094
0.00000 -2.89980 -2.89980 1 Sr_1 4.10094
.
.
.
END

```

## C.1.2 Scattering Paths Retained After Filtering

The following data are taken from the 'paths.dat' file output from FEFF. This file contains the properties of all the scattering paths deemed to provide a significant contribution to the observed fine-structure. Importantly, this includes the coordinates of each atom from which the photo-electron scattered, allowing the length, order and shape of each scattering path to be obtained.

The first set of data relates to the Fe calculation for which the input file was given in the previous section. Only the paths considered in the DiffEXAFS fit are shown.

```

PATH Rmax= 5.000, Keep_limit= 0.00, Heap_limit 0.00 Pwcrit= 4.00%
-----
1 2 8.000 index, nleg, degeneracy, r= 2.4825
x y z ipot label rleg beta eta
-1.433250 -1.433250 1.433250 1 'Fe ' 2.4825 180.0000 0.0000
0.000000 0.000000 0.000000 0 'Fe ' 2.4825 180.0000 0.0000
2 2 6.000 index, nleg, degeneracy, r= 2.8665
x y z ipot label rleg beta eta
0.000000 -2.866500 0.000000 1 'Fe ' 2.8665 180.0000 0.0000
0.000000 0.000000 0.000000 0 'Fe ' 2.8665 180.0000 0.0000
3 3 48.000 index, nleg, degeneracy, r= 3.9157
x y z ipot label rleg beta eta
0.000000 -2.866500 0.000000 1 'Fe ' 2.8665 125.2644 0.0000
-1.433250 -1.433250 -1.433250 1 'Fe ' 2.4825 109.4712 0.0000
0.000000 0.000000 0.000000 0 'Fe ' 2.4825 125.2644 0.0000
4 2 12.000 index, nleg, degeneracy, r= 4.0538
x y z ipot label rleg beta eta
0.000000 2.866500 -2.866500 1 'Fe ' 4.0538 180.0000 0.0000
0.000000 0.000000 0.000000 0 'Fe ' 4.0538 180.0000 0.0000
5 3 48.000 index, nleg, degeneracy, r= 4.5094
x y z ipot label rleg beta eta
-2.866500 -2.866500 0.000000 1 'Fe ' 4.0538 144.7356 0.0000
-1.433250 -1.433250 -1.433250 1 'Fe ' 2.4825 70.5288 0.0000

```

0.000000	0.000000	0.000000	0	'Fe'		2.4825	144.7356	0.0000
6	2	24.000	index,	nleg,	degeneracy,	r=	4.7536	
x	y	z	ipot	label		rleg	beta	eta
4.299750	1.433250	1.433250	1	'Fe'		4.7536	180.0000	0.0000
0.000000	0.000000	0.000000	0	'Fe'		4.7536	180.0000	0.0000
7	3	48.000	index,	nleg,	degeneracy,	r=	4.8934	
x	y	z	ipot	label		rleg	beta	eta
-2.866500	-2.866500	0.000000	1	'Fe'		4.0538	135.0000	0.0000
0.000000	-2.866500	0.000000	1	'Fe'		2.8665	90.0000	0.0000
0.000000	0.000000	0.000000	0	'Fe'		2.8665	135.0000	0.0000
8	2	8.000	index,	nleg,	degeneracy,	r=	4.9649	
x	y	z	ipot	label		rleg	beta	eta
2.866500	2.866500	2.866500	1	'Fe'		4.9649	180.0000	0.0000
0.000000	0.000000	0.000000	0	'Fe'		4.9649	180.0000	0.0000
9	3	8.000	index,	nleg,	degeneracy,	r=	4.9649	
x	y	z	ipot	label		rleg	beta	eta
-1.433250	1.433250	-1.433250	1	'Fe'		2.4825	180.0000	0.0000
1.433250	-1.433250	1.433250	1	'Fe'		4.9649	180.0000	0.0000
0.000000	0.000000	0.000000	0	'Fe'		2.4825	0.0000	0.0000
10	3	16.000	index,	nleg,	degeneracy,	r=	4.9649	
x	y	z	ipot	label		rleg	beta	eta
2.866500	-2.866500	2.866500	1	'Fe'		4.9649	180.0000	0.0000
1.433250	-1.433250	1.433250	1	'Fe'		2.4825	0.0000	0.0000
0.000000	0.000000	0.000000	0	'Fe'		2.4825	180.0000	0.0000
11	4	8.000	index,	nleg,	degeneracy,	r=	4.9649	
x	y	z	ipot	label		rleg	beta	eta
-1.433250	1.433250	1.433250	1	'Fe'		2.4825	180.0000	0.0000
0.000000	0.000000	0.000000	0	'Fe'		2.4825	0.0000	0.0000
1.433250	-1.433250	-1.433250	1	'Fe'		2.4825	180.0000	0.0000
0.000000	0.000000	0.000000	0	'Fe'		2.4825	0.0000	0.0000
13	4	8.000	index,	nleg,	degeneracy,	r=	4.9649	
x	y	z	ipot	label		rleg	beta	eta
1.433250	-1.433250	-1.433250	1	'Fe'		2.4825	0.0000	0.0000
2.866500	-2.866500	-2.866500	1	'Fe'		2.4825	180.0000	0.0000
1.433250	-1.433250	-1.433250	1	'Fe'		2.4825	0.0000	0.0000
0.000000	0.000000	0.000000	0	'Fe'		2.4825	180.0000	0.0000

The next set of data relates to the SrF<sub>2</sub> calculation. Again, only the paths considered in the DiffEXAFS fit are shown.

PATH Rmax= 9.100, Keep\_limit= 0.00, Heap\_limit 0.00 Pwcrit= 3.00%

---

1	2	8.000	index,	nleg,	degeneracy,	r=	2.5113	
x	y	z	ipot	label		rleg	beta	eta
-1.449900	1.449900	-1.449900	2	'F'		2.5113	180.0000	0.0000
0.000000	0.000000	0.000000	0	'Sr'		2.5113	180.0000	0.0000
2	3	24.000	index,	nleg,	degeneracy,	r=	3.9612	
x	y	z	ipot	label		rleg	beta	eta
1.449900	-1.449900	-1.449900	2	'F'		2.5113	125.2644	0.0000
-1.449900	-1.449900	-1.449900	2	'F'		2.8998	125.2644	0.0000
0.000000	0.000000	0.000000	0	'Sr'		2.5113	109.4712	0.0000
3	2	12.000	index,	nleg,	degeneracy,	r=	4.1009	
x	y	z	ipot	label		rleg	beta	eta
2.899800	2.899800	0.000000	1	'Sr'		4.1009	180.0000	0.0000
0.000000	0.000000	0.000000	0	'Sr'		4.1009	180.0000	0.0000
6	2	24.000	index,	nleg,	degeneracy,	r=	4.8088	
x	y	z	ipot	label		rleg	beta	eta
1.449900	-4.349700	1.449900	2	'F'		4.8088	180.0000	0.0000
0.000000	0.000000	0.000000	0	'Sr'		4.8088	180.0000	0.0000

### C.1.3 FitChi2 Input for Conventional EXAFS Fits

With the FEFF calculations complete, the phase and amplitude information was passed to FitChi2 as described in section 4.3.3 to determine the remaining fine-structure parameters. These fits were performed with the following 'fitchi.inp' configuration files. The first is for the Fe fine-structure.

```
* Input parameters for FitChi2005
EXPTSPECTRUM Fe_cal_01e_EXAFS
CHIPFILES chipfiles.dat
EDGEShift 7121
EDGEVARIABLE 0
MAXITERATIONS 500
SHAKEOFF 0.8
STARTK 4.0
ENDK 13.88
BACKGROUND 6
MAXRADIUS 5.0
```

And the second for SrF<sub>2</sub> fine-structure.

```
* Input parameters for FitChi2005
EXPTSPECTRUM Sr_cal_02.dat
CHIPFILES chipfiles.dat
EDGEShift 16105
MAXITERATIONS 5000
SHAKEOFF 0.8
ENDK 10.9
STARTK 3.24
BACKGROUND 6
```

### C.1.4 FitChi2 Input for DiffEXAFS Fits

Following the conventional EXAFS fits, the DiffEXAFS fits finally determined the structural changes resulting from thermal modulation. FitChi2 was run in its DiffEXAFS mode with the following parameters. The output from the conventional EXAFS fits are shown here since they are also the initial parameters for the DiffEXAFS fits. The Debye-Waller parameters are given in units of Å, and the edge energy in eV. Once again, the first set of parameters relates to the Fe fit.

```
* Input parameters for FitChi2005
SPECTRUMTYPE 2
EXPTSPECTRUM FefoilL_127cal
EDGEShift 7121
MAXITERATIONS 2000
STARTK 3.2
ENDK 9.6
SHAKEVARIABLE 0
```

```

EDGEVARIABLE 0
BACKGROUND 0
MINRADIUS 1.4
MAXRADIUS 5.0
FAILLIMIT 15

# Initial parameters for DiffEXAFS fit
# -----
#
# Debye Waller parameters
6.59709771E-03
5.77540594E-03
1.39169422E-02
7.23890095E-03
2.92497945E-03
6.94018517E-03
2.14862600E-02
3.37583526E-03
2.15339129E-02
#
# Edge energy
7.12100000E+03
#
# Fine structure amplitude factor
0.94400000E-01

```

And the second set of parameters to the SrF<sub>2</sub> DiffEXAFS fit.

```

* Input parameters for FitChi2005
SPECTRUMTYPE 2
INITIALDWFS InitialDwfs.dat
EXPTSPECTRUM test_56_NoBack10_Crop
CHIPFILES chipfiles.dat
EDGEShift 16105
MAXITERATIONS 2000
STARTK 3.47
ENDK 6.91
SHAKEVARIABLE 0
EDGEVARIABLE 0
BACKGROUND 4
MAXRADIUS 4.57
FAILLIMIT 8
CONVEXP 1.25
CONVLOR 1.7

# Initial parameters for DiffEXAFS fit
# -----
#
# Debye Waller parameters
9.56394278E-03
7.90237602E-03
2.08650380E-02
1.03673267E-02
#
# Edge energy
1.61038750E+04
#
# Fine structure amplitude factor
8.77501268E-01

```

### C.1.5 FitChi2 Output

The following data are taken from the 'parameters.dat' and 'Correlation.dat' files output from FitChi2 following the  $\Delta T = 3.6K$  DiffEXAFS fit described in section 4.4. The first data set is, once more, for the Fe data. It should be noted that the fit was performed on an un-normalised Difference EXAFS spectrum. Hence, these parameters differ from those in Table 5.3 by a factor of 3.6. The variance/covariance matrix components also require normalisation. The correlation matrix is unaffected. The Debye-Waller parameters are given in units of  $\text{\AA}^2\text{K}^{-1}$ , and the thermal expansion parameters in  $\text{K}^{-1}$

```
# Thermal DiffEXAFS Theory spectrum parameters
# -----
#
# Debye Waller parameters
4.80168606E-05
3.92613940E-05
1.19794330E-04
5.29250765E-05
-7.74575209E-05
4.98137251E-05
3.45342398E-09
-3.90135931E-05
1.42525721E-04
#
# Thermal Expansion parameters
4.127045E-05

# Correlation and Variance/Covariance Matrices
# i      j      Correlation [i][j]  Covariance [i][j]      i      Variance [i]
0      0      1.0000000E+00      5.2477247E-13      0      5.2477247E-13
0      1      -5.0587465E-01      -5.4330552E-13      1      2.1980186E-12
0      2      5.2090515E-01      3.8404403E-12      2      1.0357947E-10
0      3      -2.3572528E-01      -3.4072377E-13      3      3.9812689E-12
0      4      2.9880451E-02      2.0557418E-13      4      9.0196934E-11
0      5      -4.3515141E-01      -8.9457137E-13      5      8.0533793E-12
0      6      1.9955401E-01      4.3909415E-13      6      9.2262106E-12
0      7      -9.5961945E-02      -8.9448518E-13      7      1.6556829E-10
0      8      1.4129565E-01      2.2435108E-12      8      4.8042730E-10
0      9      5.8098911E-01      7.1182211E-13      9      2.8604603E-12
1      0      -5.0587465E-01      -5.4330552E-13
1      1      1.0000000E+00      2.1980186E-12
1      2      -5.3665349E-01      -8.0974166E-12
1      3      4.4633150E-01      1.3203345E-12
1      4      8.5535656E-02      1.2043668E-12
1      5      5.9798836E-01      2.5159238E-12
1      6      1.4060756E-02      6.3319289E-14
1      7      9.8272171E-02      1.8747131E-12
1      8      -1.8125407E-01      -5.8900269E-12
1      9      -7.5383974E-01      -1.8902214E-12
2      0      5.2090515E-01      3.8404403E-12
2      1      -5.3665349E-01      -8.0974166E-12
2      2      1.0000000E+00      1.0357947E-10
2      3      -4.6098074E-01      -9.3611754E-12
2      4      1.5507659E-01      1.4989218E-11
2      5      -4.1312599E-01      -1.1931868E-11
```

2	6	1.7647988E-01	5.4556151E-12
2	7	-9.4288369E-02	-1.2347628E-11
2	8	1.2199131E-01	2.7213197E-11
2	9	5.8372058E-01	1.0047541E-11
3	0	-2.3572528E-01	-3.4072377E-13
3	1	4.4633150E-01	1.3203345E-12
3	2	-4.6098074E-01	-9.3611754E-12
3	3	1.0000000E-00	3.9812689E-12
3	4	-1.3082882E-01	-2.4791914E-12
3	5	4.1502841E-01	2.3500530E-12
3	6	1.1676353E-01	7.0766815E-13
3	7	7.6971082E-02	1.9761820E-12
3	8	-9.4364767E-02	-4.1270000E-12
3	9	-4.8455428E-01	-1.6352010E-12
4	0	2.9880451E-02	2.0557418E-13
4	1	8.5535656E-02	1.2043668E-12
4	2	1.5507659E-01	1.4989218E-11
4	3	-1.3082882E-01	-2.4791914E-12
4	4	1.0000000E+00	9.0196934E-11
4	5	5.1256550E-01	1.3814474E-11
4	6	1.6338869E-01	4.7133486E-12
4	7	7.1022506E-01	8.6792154E-11
4	8	6.5186768E-01	1.3569667E-10
4	9	-1.4406832E-01	-2.3141011E-12
5	0	-4.3515141E-01	-8.9457137E-13
5	1	5.9798836E-01	2.5159238E-12
5	2	-4.1312599E-01	-1.1931868E-11
5	3	4.1502841E-01	2.3500530E-12
5	4	5.1256550E-01	1.3814474E-11
5	5	1.0000000E+00	8.0533793E-12
5	6	-1.2056761E-02	-1.0392773E-13
5	7	4.9489368E-01	1.8071307E-11
5	8	1.5016340E-01	9.3404330E-12
5	9	-7.0673549E-01	-3.3920632E-12
6	0	1.9955401E-01	4.3909415E-13
6	1	1.4060756E-02	6.3319289E-14
6	2	1.7647988E-01	5.4556151E-12
6	3	1.1676353E-01	7.0766815E-13
6	4	1.6338869E-01	4.7133486E-12
6	5	-1.2056761E-02	-1.0392773E-13
6	6	1.0000000E-00	9.2262106E-12
6	7	4.6795847E-02	1.8289742E-12
6	8	9.0402187E-02	6.0187244E-12
6	9	-1.3579538E-01	-6.9761310E-13
7	0	-9.5961945E-02	-8.9448518E-13
7	1	9.8272171E-02	1.8747131E-12
7	2	-9.4288369E-02	-1.2347628E-11
7	3	7.6971082E-02	1.9761820E-12
7	4	7.1022506E-01	8.6792154E-11
7	5	4.9489368E-01	1.8071307E-11
7	6	4.6795847E-02	1.8289742E-12
7	7	1.0000000E+00	1.6556829E-10
7	8	9.0435501E-01	2.5505942E-10
7	9	-1.2115291E-01	-2.6365766E-12
8	0	1.4129565E-01	2.2435108E-12
8	1	-1.8125407E-01	-5.8900269E-12
8	2	1.2199131E-01	2.7213197E-11
8	3	-9.4364767E-02	-4.1270000E-12
8	4	6.5186768E-01	1.3569667E-10
8	5	1.5016340E-01	9.3404330E-12
8	6	9.0402187E-02	6.0187244E-12
8	7	9.0435501E-01	2.5505942E-10
8	8	1.0000000E-00	4.8042730E-10
8	9	2.3057529E-01	8.5476071E-12

9	0	5.8098911E-01	7.1182211E-13
9	1	-7.5383974E-01	-1.8902214E-12
9	2	5.8372058E-01	1.0047541E-11
9	3	-4.8455428E-01	-1.6352010E-12
9	4	-1.4406832E-01	-2.3141011E-12
9	5	-7.0673549E-01	-3.3920632E-12
9	6	-1.3579538E-01	-6.9761310E-13
9	7	-1.2115291E-01	-2.6365766E-12
9	8	2.3057529E-01	8.5476071E-12
9	9	1.0000000E-00	2.8604603E-12

The second set of parameters are for the SrF<sub>2</sub> DiffEXAFS fit. Again this was performed on a Difference EXAFS spectrum, this time where  $\Delta T = 4.7K$ .

```
# Thermal DiffEXAFS Theory spectrum parameters
# -----
#
# Debye Waller parameters
8.67253209E-04
4.30918176E-03
9.25275659E-04
1.58996785E-03
#
# Thermal Expansion parameters
8.524332E-05

# Correlation and Variance/Covariance Matrices
# i   j   Correlation [i][j]  Covariance [i][j]
0   0   1.0000000E+00        4.7952094E-10
0   1   6.3414922E-03        8.7505267E-11
0   2   2.5864513E-01        4.6806314E-10
0   3   -2.0307984E-01       -4.2463842E-10
0   4   -6.0389700E-02       -9.0153288E-12
1   0   6.3414922E-03        8.7505267E-11
1   1   1.0000000E+00        3.9707988E-07
1   2   -2.5777118E-01       -1.3423620E-08
1   3   4.6557413E-01        2.8014087E-08
1   4   -1.5048338E-01       -6.4646107E-10
2   0   2.5864513E-01        4.6806314E-10
2   1   -2.5777118E-01       -1.3423620E-08
2   2   1.0000000E+00        6.8295598E-09
2   3   -4.9221139E-01       -3.8841564E-09
2   4   -2.3792880E-01       -1.3404736E-10
3   0   -2.0307984E-01       -4.2463842E-10
3   1   4.6557413E-01        2.8014087E-08
3   2   -4.9221139E-01       -3.8841564E-09
3   3   1.0000000E-00        9.1179536E-09
3   4   6.2656549E-01        4.0787780E-10
4   0   -6.0389700E-02       -9.0153288E-12
4   1   -1.5048338E-01       -6.4646107E-10
4   2   -2.3792880E-01       -1.3404736E-10
4   3   6.2656549E-01        4.0787780E-10
4   4   1.0000000E-00        4.6476115E-11
```

## C.2 Ni<sub>2</sub>MnGa Phase Transition Analysis

### C.2.1 FEFF Input Configuration Files

The following 'feff.inp' file was used for all Ni<sub>2</sub>MnGa conventional EXAFS analysis. As with the Fe analysis previously, the list of atoms and maximum path radius was selected such that FEFF only considered those scattering paths that would be present in the Fourier filtered experimental spectrum.

```
*          pot    xsph  fms   paths  genfmt  ff2chi
CONTROL    1      1     1     1      1      1
PRINT      1      0     0     0      1      2

CRITERIA 10.0 6.0
RPATH 3.2
EXAFS 20

POTENTIALS
*          ipot   Z   element          l_scm  l_fms  stoichiometry
          0    28   Ni          2      2      0.001
          1    28   Ni          2      2      8
          2    25   Mn          2      2      2
          3    31   Ga          2      2      4

ATOMS
*          x          y          z          ipot   tag          distance
0.00000    0.00000    0.00000    0      Ni          0.00000    0
-1.47500    1.47500    1.38500    3      Ga          2.50389    1
 1.47500   -1.47500    1.38500    3      Ga          2.50389    2
 1.47500    1.47500   -1.38500    3      Ga          2.50389    3
-1.47500   -1.47500   -1.38500    3      Ga          2.50389    4
 1.47500    1.47500    1.38500    2      Mn          2.50389    5
-1.47500   -1.47500    1.38500    2      Mn          2.50389    6
-1.47500    1.47500   -1.38500    2      Mn          2.50389    7
 1.47500   -1.47500   -1.38500    2      Mn          2.50389    8
 2.95000    0.00000    0.00000    1      Ni          2.95000    9
-2.95000    0.00000    0.00000    1      Ni          2.95000   10
 0.00000    2.95000    0.00000    1      Ni          2.95000   11
 0.00000   -2.95000    0.00000    1      Ni          2.95000   12
 0.00000    0.00000    2.77000    1      Ni          2.95000   13
 0.00000    0.00000   -2.77000    1      Ni          2.95000   14

END
```

### C.2.2 Scattering Paths Retained After Filtering

After Fourier filtering the experimental Ni<sub>2</sub>MnGa spectra. Only four paths contributed to the EXAFS and DiffEXAFS fits. These were the first four single-scattering paths as follows

```
PATH Rmax= 3.200, Keep_limit= 0.00, Heap_limit 0.00 Pwcrit= 6.00%
```



1	2	4.000	index, nleg, degeneracy, r=	2.5039					
x		y		z	ipot	label	rleg	beta	eta
1.475000		-1.475000		-1.385000	2	'Mn'	2.5039	180.0000	0.0000
0.000000		0.000000		0.000000	0	'Ni'	2.5039	180.0000	0.0000
2	2	4.000	index, nleg, degeneracy, r=	2.5039					
x		y		z	ipot	label	rleg	beta	eta
1.475000		-1.475000		1.385000	3	'Ga'	2.5039	180.0000	0.0000
0.000000		0.000000		0.000000	0	'Ni'	2.5039	180.0000	0.0000
3	2	2.000	index, nleg, degeneracy, r=	2.7700					
x		y		z	ipot	label	rleg	beta	eta
0.000000		0.000000		2.770000	1	'Ni'	2.7700	180.0000	0.0000
0.000000		0.000000		0.000000	0	'Ni'	2.7700	180.0000	0.0000
4	2	4.000	index, nleg, degeneracy, r=	2.9500					
x		y		z	ipot	label	rleg	beta	eta
0.000000		-2.950000		0.000000	1	'Ni'	2.9500	180.0000	0.0000
0.000000		0.000000		0.000000	0	'Ni'	2.9500	180.0000	0.0000

### C.2.3 FitChi2 for Conventional EXAFS Fits

The following 'fitchi.inp' was used to fit conventional Ni<sub>2</sub>MnGa EXAFS spectra in the region  $70 \leq E' \leq 550$  eV above the edge. The maximum radial component allowed through the Fourier filter was selected to limit the EXAFS to contributions from the first four single-scattering paths only. The minimum radial component removed background drift. Best results were achieved when the shake-off,  $S_0^2$ , was fixed at 0.8.

```
* Input parameters for FitChi2005
EXPTSPECTRUM B_Ni_04b_EXAFS
CHIPFILES chipfiles.dat
EDGEShift 8337.5
MAXITERATIONS 800
ENDK 12
STARTK 4.2
MINRADIUS 1.3
MAXRADIUS 2.62
BACKGROUND 0
SHAKEOFF 0.8
SHAKEVARIABLE 0
```

This lead to the following parameters for EXAFS spectra taken at a range of different temperatures well below the primary transition temperature at 51°C. It is important to note that given the first two Debye-Waller factors correspond to Ni-Mn and Ni-Ga, which have equivalent radii, and also that there is little phase contrast between these two paths, FitChi2 is unable to accurately distinguish one from the other. Therefore, it is only the average of these two parameters that is meaningful.

# Ni2MnGa EXAFS fit at 293K	# Ni2MnGa EXAFS fit at 243K
# -----	# -----
#	#

# Debye Waller parameters	# Debye Waller parameters
5.62936874E-03	7.12497167E-03
1.36715741E-02	7.65056665E-03
1.04339850E-02	7.49129026E-03
1.86782151E-02	2.87055824E-02
#	#
# Edge energy energy	# Edge energy energy
8.33777389E+03	8.33849819E+03
# Ni2MnGa EXAFS fit at 150K	# Ni2MnGa EXAFS fit at 60K
# -----	# -----
#	#
# Debye Waller parameters	# Debye Waller parameters
4.73101362E-03	6.14327250E-03
8.37937777E-03	6.18196742E-03
7.85745012E-03	4.41283626E-03
3.10884753E-02	2.31415785E-02
#	#
# Edge energy energy	# Edge energy energy
8.33736496E+03	8.33734547E+03

Fit errors were as follows

# Ni2MnGa EXAFS fit errors at 293K	# Ni2MnGa EXAFS fit errors at 243K
# -----	# -----
#	#
# Error in Debye Waller parameters	# Error in Debye Waller parameters
1.4038191E-03	3.3618546E-04
5.0354947E-03	4.3508447E-04
3.0328922E-03	5.4643975E-04
2.6116649E-03	2.1386812E-03
#	#
# Error in Edge energy energy	# Error in Edge energy energy
5.8403285E-01	1.6237932E-01
# Ni2MnGa EXAFS fit errors at 150K	# Ni2MnGa EXAFS fit errors at 60K
# -----	# -----
#	#
# Error in Debye Waller parameters	# Error in Debye Waller parameters
3.9588835E-04	7.4290572E-04
7.6356824E-04	8.9611111E-04
7.2078975E-04	9.4941881E-04
3.0138686E-03	3.9206841E-03
#	#
# Error in Edge energy energy	# Error in Edge energy energy
2.0154206E-01	3.9617785E-01

The same FitChi2 configuration was used to analyse spectra taken close to the primary transition temperature. The results were as follows

# Ni2MnGa EXAFS fit at 319K	# Ni2MnGa EXAFS fit at 318K
# -----	# -----
#	#
# Debye Waller parameters	# Debye Waller parameters
1.16150565E-02	1.11684234E-02
5.67561717E-03	5.99176956E-03
4.16647156E-03	4.18319654E-03
1.63977600E-02	1.60419229E-02
#	#
# Edge energy shift	# Edge energy shift

8.33897648E+03	8.33958883E+03
# Ni2MnGa EXAFS fit at 308K	# Ni2MnGa EXAFS fit at 302K
# -----	# -----
#	#
# Debye Waller parameters	# Debye Waller parameters
1.20860236E-02	1.28276967E-02
7.38858945E-03	1.07562375E-02
6.39718203E-03	9.61726907E-03
1.81465188E-02	1.77150060E-02
#	#
# Edge energy shift	# Edge energy shift
8.33847742E+03	8.33744509E+03

The fit errors for these spectra were

# Ni2MnGa EXAFS fit errors at 319K	# Ni2MnGa EXAFS fit errors at 318K
# -----	# -----
#	#
# Debye Waller parameters	# Debye Waller parameters
1.0590398E-03	1.1137689E-03
6.5025643E-04	7.5561905E-04
1.1874057E-03	1.2824380E-03
2.7582685E-03	2.9125775E-03
#	#
# Edge energy shift	# Edge energy shift
4.7810470E-01	5.1196055E-01
# Ni2MnGa EXAFS fit errors at 308K	# Ni2MnGa EXAFS fit errors at 302K
# -----	# -----
#	#
# Debye Waller parameters	# Debye Waller parameters
1.0754718E-03	1.2189951E-03
8.2532232E-04	1.2584772E-03
1.3974167E-03	1.9824385E-03
2.6063233E-03	2.5825199E-03
#	#
# Edge energy shift	# Edge energy shift
4.2173417E-01	4.8042362E-01

## C.2.4 FitChi2 for DiffEXAFS Fits

The following 'fitchi.inp' file was used to configure FitChi2 for processing DiffEXAFS spectra.

```
* Input parameters for FitChi2005
SPECTRUMTYPE 2
INITIALDWFS InitialDwfs.dat
CHIPFILES chipfiles.dat
EDGEShift 8337.5
STARTK 4.2
ENDK 13.0
SHAKEVARIABLE 0
EDGEVARIABLE 0
BACKGROUND 0
```

```

MINRADIUS 1.5
MAXRADIUS 3.0
EXPANSIONMODE 1
FAILLIMIT 15

```

The following parameters were produced for spectra at each of the stated temperatures.

<pre> # Ni2MnGa DiffEXAFS fit at 291K # ----- # # Thermal Expansion parameters 3.155263E-04 -3.178105E-03 -1.722270E-03 -1.268480E-04 # # Debye Waller parameters 7.37211588E-04 -1.39783678E-03 -9.68551909E-04 -1.02733499E-03  # Ni2MnGa DiffEXAFS fit at 305K # ----- # # Thermal Expansion parameters -1.328696E-03 -1.978594E-05 -2.009827E-03 -7.645151E-04 # # Debye Waller parameters 6.49393040E-04 -2.00631561E-03 -1.30093342E-03 -1.23062313E-03  # Ni2MnGa DiffEXAFS fit at 320K # ----- # # Thermal Expansion parameters 4.295717E-03 -1.275160E-02 3.302080E-03 2.891545E-03 # # Debye Waller parameters 3.90724202E-03 -4.95539087E-03 -2.41381916E-03 -4.85489321E-03  # Ni2MnGa DiffEXAFS fit at 323K # ----- # # Thermal Expansion parameters 1.859776E-02 -2.190968E-02 2.410473E-02 1.334813E-02 # # Debye Waller parameters 7.34733200E-03 -6.87410243E-03 </pre>	<pre> # Ni2MnGa DiffEXAFS fit at 299K # ----- # # Thermal Expansion parameters -4.520050E-04 -7.604286E-04 -1.000802E-03 -1.667810E-04 # # Debye Waller parameters 5.17410525E-04 -1.35695973E-03 -1.04102387E-03 -9.33427527E-04  # Ni2MnGa DiffEXAFS fit at 311K # ----- # # Thermal Expansion parameters -5.897663E-04 4.482105E-04 7.242882E-04 1.384742E-04  3.04734743E-04 -7.41509414E-04 -8.04697255E-04 -1.08014710E-03  # Ni2MnGa DiffEXAFS fit at 321K # ----- # # Thermal Expansion parameters 1.141850E-02 -1.864977E-02 1.539433E-02 7.617241E-03 # # Debye Waller parameters 4.97736848E-03 -5.78700233E-03 -1.43969806E-03 -3.15731989E-03 </pre>
--	---

-5.20084275E-03  
-7.82678449E-03

The associated fit errors were

```
# Ni2MnGa DiffEXAFS fit at 291K
# -----
#
# Thermal Expansion parameters
7.5160364E-05
1.2197837E-04
1.4051629E-04
6.8578290E-05
#
# Debye Waller parameters
3.8698917E-05
1.0630373E-04
4.0776339E-05
3.0876447E-05

# Ni2MnGa DiffEXAFS fit at 305K
# -----
#
# Thermal Expansion parameters
2.6950303E-04
1.8834314E-04
7.2660156E-04
3.3055744E-04
#
# Debye Waller parameters
1.1544393E-04
3.7033564E-04
1.2047573E-04
6.2594807E-05

# Ni2MnGa DiffEXAFS fit at 320K
# -----
#
# Thermal Expansion parameters
2.1617323E-04
2.2146092E-04
3.0769001E-04
2.0313117E-04
#
# Debye Waller parameters
9.2083730E-05
7.8468916E-05
1.1979032E-04
8.3065400E-05

# Ni2MnGa DiffEXAFS fit at 323K
# -----
#
# Thermal Expansion parameters
2.6825390E-04
1.3486364E-04
3.6547359E-04
2.5904062E-04
#
# Debye Waller parameters
8.9292663E-05
3.8755357E-05
1.0738528E-04
1.0697712E-04
```

```
# Ni2MnGa DiffEXAFS fit at 299K
# -----
#
# Thermal Expansion parameters
1.7252007E-04
2.1545208E-04
3.2323790E-04
1.6095259E-04
#
# Debye Waller parameters
6.3552318E-05
2.1361705E-04
8.0894176E-05
5.6266768E-05

# Ni2MnGa DiffEXAFS fit at 311K
# -----
#
# Thermal Expansion parameters
8.3885647E-05
1.0807270E-04
1.4819541E-04
6.0609842E-05
#
# Debye Waller parameters
3.0890565E-05
1.1819887E-04
5.5352979E-05
3.6363902E-05

# Ni2MnGa DiffEXAFS fit at 321K
# -----
#
# Thermal Expansion parameters
2.2034359E-04
1.4321002E-04
3.8374891E-04
2.7036614E-04
#
# Debye Waller parameters
4.8979898E-05
3.1563321E-05
1.1203578E-04
1.0077043E-04
```

## **Appendix D**

### **Papers submitted from work in this thesis**

## Calibration of spectra from dispersive XAS beamlines

M. P. Ruffoni\* and R. F. Pettifer

Received 26 April 2006  
Accepted 25 September 2006

Department of Physics, University of Warwick, Coventry CV4 7AL, UK. E-mail: m.p.ruffoni@warwick.ac.uk

The *DXAS Calibration* computer program provides a quantitative and automated solution to the problem of calibrating spectra from dispersive XAS beamlines. Such spectra, obtained in arbitrary energy units, are calibrated with respect to the absorption features of a supplied reference spectrum, which has been obtained under similar conditions on a calibrated beamline. In addition to basic energy coordinate transformation parameters, *DXAS Calibration* supplies instrument corrections to compensate for mismatches in instrument response functions between the dispersive and reference beamlines.

© 2006 International Union of Crystallography  
Printed in Great Britain – all rights reserved**Keywords:** dispersive XAS; calibration; instrument response functions.

## 1. Introduction

Dispersive XAS beamlines, such as ID24 of the ESRF, utilize a single Si(111) Bragg diffracting or Si(311) Laue diffracting polychromator crystal which is elliptically bent and illuminated by white X-rays, typically over an area of 10 µm vertically by 40 mm horizontally, to produce a wavelength-dispersive diffracted beam (ESRF, 2001).

This beam, spread out into a broad horizontal fan, converges to a focus, allowing a sample to be simultaneously illuminated by X-rays of wavelengths corresponding to an energy range of typically 700–1500 eV. Beyond this focal spot, each wavelength component diverges again, and is detected by a position-sensitive CCD array of 18 pixels × 1152 pixels in the case of ID24, as shown in Fig. 1.

As a result of this geometry, the energies of X-rays detected in each pixel of the CCD (which are related to X-ray wavelength given  $E = hc/\lambda$ ) are dependent on the source and optics settings, on the amount of bending in the polychromator crystal, and on the distance between the detector and the focal spot, and as such cannot be accurately determined prior to measurement. It is therefore required that calibration be carried out *a posteriori* with respect to a spectrum of known calibration.

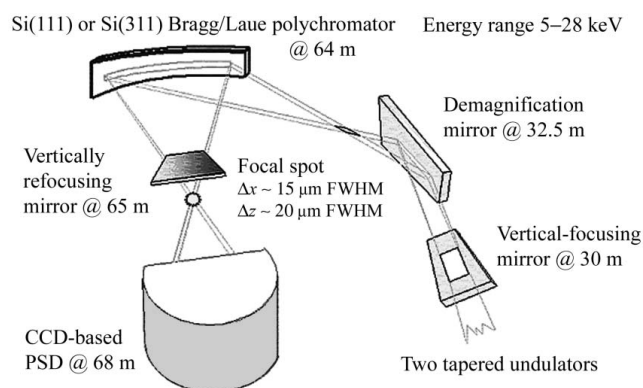


**Figure 1**  
The optics of beamline ID24 of the ESRF (ESRF, 2005).

Thus, each absorption spectrum is acquired on a relative scale and presented to the user as a function of CCD channel (pixel) number. The user is then required to manually calibrate the energy and absorption scales, converting from CCD channel number to a real energy scale and from relative to an absolute absorption scale. This is usually accomplished by comparing an acquired spectrum with a reference obtained from a standard calibrated XAS beamline such as BM29, the X-ray absorption spectroscopy beamline at the ESRF. Some tools already exist to aid the user in this task (ESRF, 2001), but none are fully automated and therefore accuracy is limited by human judgement.<sup>1</sup> Additionally, few are dedicated to the calibration requirements of dispersive-XAS beamlines and hence can often be difficult to use. *DXAS Calibration* solves these problems by providing an automated graphically driven calibration solution that is dedicated to the problems presented by dispersive-XAS beamlines.

## 2. The calibration process

## 2.1. Calibration parameters

Assuming that the dispersive and reference spectra were acquired under the same environmental conditions, from the same sample material and also, for now, that the instrument response functions of the dispersive and reference beamlines were identical, then calibration is reduced to calculating the values of a set of parameters necessary to transform the channel number 'pseudo-energy' axis to an absolute energy scale, and relative absorption to absolute absorption. Algorithmically, these parameters are the coefficients of two polynomials: one for energy calibration and one for absorption normalization, so that, for each pixel  $i$ ,

$$E'_i = a_0 + a_1 E_i + a_2 E_i^2 + \dots + a_n E_i^n, \quad (1)$$

$$\mu'_i = b_0 + b_1 \mu_i + b_2 \mu_i^2 + \dots + b_n \mu_i^n, \quad (2)$$

<sup>1</sup> Subsequent to submission, the referee has pointed out that a calibration program exists in the commercial *WinXAS* software (<http://www.winxas.de>), but this seems to be semi-automatic.

where  $E_i$  and  $\mu_i$  are the original energy (which may be just the pixel number) and absorption coefficients, respectively, and  $E'_i$  and  $\mu'_i$  are the transformed coordinates. As a result,  $a_0$  and  $b_0$  perform a simple translation of the spectrum,  $a_1$  and  $b_1$  stretch the spectrum in a linear fashion, and higher-order coefficients induce non-linear deformations in the spectrum. Setting  $a_1$  and  $b_1$  to 1 and all other parameters to 0 will return the original spectrum as it was experimentally recorded. The order  $n$  of the polynomial is specified by the user, and is typically between 2 and 4. An option also exists allowing a user to correct any absorption drift if necessary. Given that all parameters  $a_i$  and  $b_i$  are independent, they may be inserted into a single vector  $\mathbf{a}$  for use by the calibration algorithm.

Frequently, these parameters alone will suffice in generating an accurate calibration; however, it is also important to consider the case where our final assumption fails, and the instrument functions of the dispersive and reference beamlines differ. When this happens, additional instrument compensation parameters are required, which are discussed in more detail in §3.

## 2.2. Calibration algorithm

The *DXAS Calibration* code implements a Levenberg–Marquardt algorithm for general non-linear least-squares fitting of an arbitrary number of parameters (Aby & Dempster, 1974; Press *et al.*, 1992). For the purpose of creating a calibration algorithm within the assumptions given above, we must state *a priori* that it is possible to select some set of parameters,  $\mathbf{a}$ , which when applied to a dispersive spectrum,  $f(E, \mathbf{a})$ , should in theory reduce any differences in absorption structure between it and the reference spectrum,  $f_{\text{ref}}(E)$ , to a minimum. We therefore define some least-squares cost function that measures the differences in structure for any potential solution, and work to minimize it. Given also that the code is always supplied with sets of spectral data, discretely sampled at energies  $E_i$ , the differences may simply be evaluated at each data point as  $y_i(\mathbf{a}) = f(E_i, \mathbf{a}) - f_{\text{ref}}(E_i)$ .

## 3. Advanced calibration techniques

### 3.1. Matching beamline instrument functions

In some cases, especially at higher X-ray energies or with thick specimens where the absorption thickness product is greater than *e.g.* 1.5, the instrument functions of dispersive beamlines differ significantly from those of standard XAS beamlines. In these cases, the stated calibration condition that the cost function can be reduced to an acceptable minimum, simply by applying translations and deformations to the uncalibrated spectrum of the polynomial form (1) and (2), is no longer valid. It is therefore necessary to match the instrument functions of the dispersive and reference beamlines so that, idealistically, two spectra obtained from the same sample, under the same environmental conditions, are identical.

This can be achieved by convolving the reference transmission spectrum (which is of a higher resolution than the same spectrum obtained from a dispersive beamline) with instrumental weight functions that compensate for the differences in X-ray source and optics between the two beamlines, the optimal characteristics of which can again be obtained from a Levenberg–Marquardt algorithm.

Klug & Alexander (1974) describe several types of instrument corrections that are applicable to powder diffractometry, but which are adaptable to our situation, and could be applied to the reference spectrum in order to match its instrument function to that of the dispersive beamline. However, in the specific case of dispersive

spectra from ID24 and reference spectra from a standard XAS beamline such as BM29, we empirically find only two such functions to be required.

The first is a normalized Lorentzian of the form

$$L(x) = \frac{1}{\pi} \frac{\Gamma/2}{(x - x_0)^2 + (\Gamma/2)^2}, \quad (3)$$

where  $\Gamma$  is found to be 2.35 eV at the Sr *K* edge (16.105 keV). This function is applied to the transmission data (*i.e.* the data prior to taking the log to convert to absorption) and compensates for the so-called thickness effect where differences in the tails of the instrument functions between the reference monochromator and dispersive polychromator, as a function of angular deviation from the diffracting Bragg angle, induce differences in the absorption spectra. The Lorentzian form of the tails is predicted from perfect crystal theory. These Lorentzian tails to the diffracted beam reduce its monochromaticity, and hence are clearly undesirable. As a consequence, XAS beamlines commonly utilize a two-crystal Si(111) or Si(311) monochromator, arranged in the parallel configuration, so that the twice diffracted beam suppresses these tails. Dispersive beamlines, however, implement only a single Si(111) or Si(311) crystal to select X-ray wavelengths. As a result, the tails on the angular reflectivity profile are unattenuated, distorting the fine structure. For calibration purposes, convolving the reference transmission spectrum with the Lorentzian (3) will reintroduce the broadening effects eliminated by the two-crystal monochromator, matching its characteristic reflectivity profile to that of the dispersive spectrum. The second instrument weighting function is asymmetric and is a normalized exponential of the form

$$\exp(x) = \begin{cases} (1/\rho) \exp(x/\rho) & \text{for } x > 0 \\ 0 & \text{for } x \leq 0 \end{cases}, \quad (4)$$

where  $\rho$  is found to be 1.25 eV at the Sr *K* edge. This term arises due to differences in X-ray penetration into the monochromator crystals on the two beamlines. For a perfect crystal of Si(111), diffracting in the dynamical regime, X-ray penetration into the crystal is calculated from the extinction length to be of the order of 1  $\mu\text{m}$ . However, a dispersive beamline has a bent crystal polychromator, which in turn has bent lattice planes that break the conditions necessary for purely dynamical diffraction. Equally, the crystal is not deformed sufficiently for purely kinematical diffraction to occur. Therefore, the X-ray penetration depth lies somewhere between the extinction and absorption lengths, the values predicted for each regime, respectively. This penetration can be increased further in the presence of damage to the surface of the crystal that may have resulted from its preparation process.

The result is that, on the dispersive beamline, X-rays of a given energy diffract from many more lattice planes of greater depth, which in turn spatially smears the diffracted beam perpendicular to the planes. These X-rays are therefore detected in several pixels along the length of the CCD, broadening the spectrum. Given also that the beam intensity decays exponentially as it penetrates the crystal, with a sharp discontinuity at the crystal surface, the smeared intensity of a single wavelength component of the diffracted radiation will decay exponentially in space as shown in equation (4). This introduces an erroneous asymmetrical energy shift in the observed structure. On ID24, the geometry dictates that this shift is towards higher energies. The observed penetration depth as a function of the radius of curvature of the polychromator,  $p(R)$ , may be calculated from

$$p(R) = \frac{\rho}{\Delta E(R)} P_x, \quad (5)$$



where  $\Delta E(R)$  is the CCD energy resolution and  $P_x$  is the horizontal size of each CCD pixel. On ID24,  $P_x = 25.0 \mu\text{m}$ , and, at the Sr  $K$  edge,  $\Delta E(R) = 1.26 \text{ eV}$ , giving  $p(R) = 24.6 \mu\text{m}$ .

Other effects, such as from samples themselves, may also degrade dispersive measurements with respect to those from reference beamlines. One such example is a reduction in resolution and white-line intensity owing to small-angle scatter by BN-based powder samples (Hagelstein *et al.*, 1998). However, these effects are neglected here for two reasons. Firstly, they generally represent only a small change in the XAFS spectrum as a whole, and are found not to affect the overall quality of calibration fits; and, secondly, such effects may be avoided by selecting suitable samples for calibration measurements; for instance, by making such measurements through reference foils rather than powder specimens.

### 3.2. Implementation of convolutions

Convolution theorem dictates that the convolution of two functions, *e.g.*  $f$  and  $g$ , is given by

$$f'(E) = \int_{-\infty}^{\infty} f(E')g(E - E')dE'. \quad (6)$$

This may be evaluated by taking the Fourier transforms of  $f$  and  $g$ , multiplying them together, and back-transforming the resulting function. Therefore, computational problems involving convolutions are commonly tackled using a fast Fourier transform code. The result is very rapid evaluation of the convolution, which is ideal for iterative applications as implemented here, but comes at the expense of potentially introducing transform artefacts to the spectrum.

It is also possible, however, to take the discretely sampled spectrum data,  $f$ , and perform the convolution numerically at each data point as long as the function with which it is being convolved,  $g$ , goes to zero as  $E'$  goes to infinity. Fortunately, this is the case with equations (3) and (4). Evaluating the convolution this way will guarantee the absence of any Fourier transform artefacts, but at the expense of speed. Given the importance of an accurately calibrated spectrum, *DXAS Calibration* evaluates any required convolutions using this latter numerical technique.

The speed penalty resulting from this choice of algorithm is not too severe in practice. Given that a typical sampling interval for an XAS beamline is between 0.1 and 1.0 eV, and that the characteristic widths of both the Lorentzian and exponential convolution functions are of the order of a few eV, the convolution may be accurately evaluated by summing contributions from only a few tens of data points. As a result, evaluating the convolution, and Marquardt difference and derivative matrices of a spectrum spanning 1000 eV (sampled every 0.5 eV) with a Lorentzian of  $\Gamma = 3.40 \text{ eV}$  and an exponential of  $\rho = 1.25 \text{ eV}$ , takes approximately 2 s on a Pentium IV 3.0 GHz processor.

### 3.3. Instrument parameter integration

Without instrument function compensation, the output parameters from the coordinate transformation algorithm may be considered optimal after just one execution. However, if the instrument functions between dispersive and reference beamlines differ enough to require additional instrument function calibration, the optimal parameters for coordinate transformation are dependent on the convolution functions that have been applied to the reference spectrum. The instrument parameters must therefore be optimized first. Unfortunately the reverse is also true. In order to optimize the instrument parameters on the reference spectrum, a dispersive spectrum with calibrated axes is required. This circular argument means that neither the coordinate transforms nor instrument corrections may be opti-

**Table 1**

Estimated and optimized parameter values for calibration at the Fe  $K$  edge.

Parameter	Estimate	Calibrated value
$a_0$	$7.027 \times 10^3$	$7.032 \times 10^3$
$a_1$	$3.038 \times 10^{-1}$	$2.951 \times 10^{-1}$
$a_2$	0	$-7.356 \times 10^{-6}$
$a_3$	0	$1.178 \times 10^{-8}$
$b_0$	$7.929 \times 10^{-1}$	$7.185 \times 10^{-1}$
$b_1$	$5.854 \times 10^{-1}$	$9.324 \times 10^{-1}$

Background	Parameter value
$x^0$	$9.120 \times 10^{-2}$
$x^1$	$6.384 \times 10^{-2}$
$x^2$	$1.599 \times 10^{-2}$
$x^3$	$-6.710 \times 10^{-3}$
$x^4$	$6.368 \times 10^{-3}$
$x^5$	$8.137 \times 10^{-3}$

mized with just one execution of their respective fitting algorithms. The solution must therefore be obtained by executing each algorithm in turn, allowing it to improve its solution with respect to the other, and iterating until self-consistency is reached; that is, when neither algorithm is capable of reducing the differences in absorption structure any further.

## 4. Calibration of XAS spectra from Fe and Sr $K$ edges

### 4.1. Calibration at the Fe $K$ edge

*DXAS Calibration* has been successfully tested on data obtained from ID24 at the Fe  $K$  edge (7.112 keV) of a polycrystalline Fe foil. At this energy the instrument function mismatch between ID24 and BM29, the chosen reference beamline, was minimal, and therefore calibration could be achieved without the implementation of any instrument corrections. The fit parameters are therefore only represented by coordinate transformations and background corrections. A cubic polynomial (four parameters) was fitted to the energy axis, and a linear polynomial (two parameters) was fitted to the absorption axis. Background correction was performed by fitting a six-coefficient Chebyshev polynomial to the residual differences between the two spectra and subtracting it.

The reference spectrum used in this calibration was obtained from a similar Fe foil, but from one of a thickness such that the jump at the edge,  $\Delta\mu x$ , was approximately 1.0.

An initial estimate of the parameter values was passed to the calibration algorithm, along with an initial Marquardt scale factor of  $1.0 \times 10^{-3}$ . Calibration then optimized the parameters, aborting after seven failed attempts to reduce the spectral differences, and resulted in a solution with residual differences at each point of less than 0.4% of the average absorption. These final parameter values, and also the initial estimate values, are given in Table 1. The calibration solution is shown in Fig. 2.

### 4.2. Calibration at the Sr $K$ edge

At the Sr  $K$  edge (16.105 keV), best results are obtained from a Laue diffracting crystal, since many distortions become present at such high energies in Bragg geometry (Hagelstein *et al.*, 1995). However, for the purpose of testing this code, measurements were made using Bragg geometry, where the instrument functions of ID24 and BM29 differ significantly. As such, successful energy-scale calibration required use of instrument correction parameters. Both the Lorentzian correction for diffraction monochromaticity, and exponential correction for polychromator transparency, were utilized.

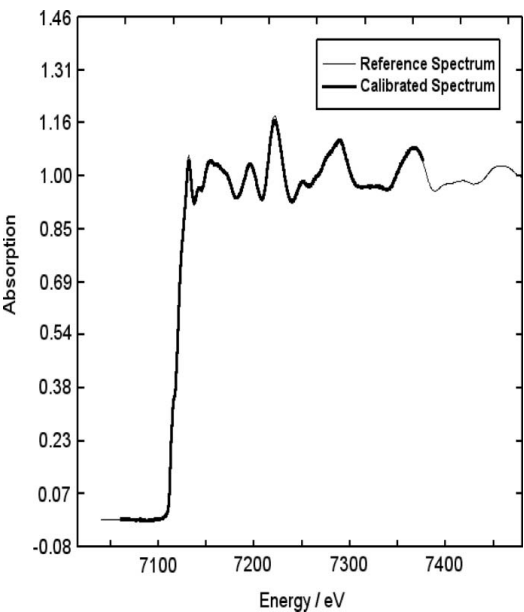


**Figure 2**  
Calibration of an ID24 Fe *K*-edge spectrum with respect to a similar one obtained from BM29. Both spectra were obtained from samples of polycrystalline iron foil. At the Fe *K* edge, the mismatch in instrument functions between ID24 and BM29 is negligible, and so this calibration consists only of polynomial-based coordinate transformations and a background correction.

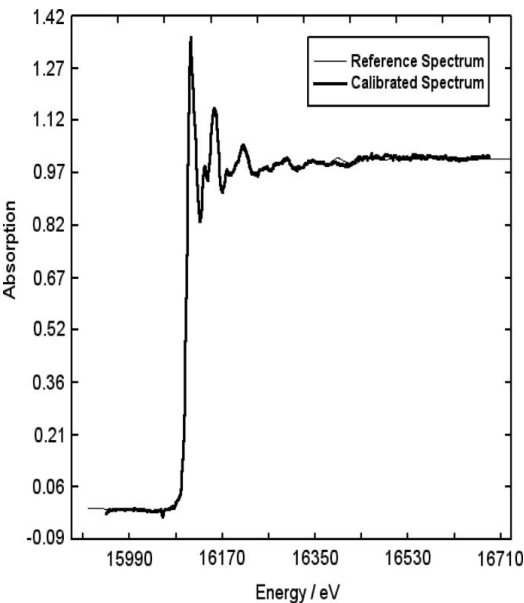


**Figure 3**  
Calibration of an ID24 Sr *K*-edge spectrum with respect to a similar one obtained from BM29. Both spectra were obtained from BN-based pellets of powdered SrF<sub>2</sub>. At the Sr *K* edge, there is significant deviation in instrument functions between ID24 and BM29, so, in addition to coordinate calibration and background correction, convolution-based instrument corrections have also been applied to the BM29 reference spectrum in order that its instrument function matches that of ID24.

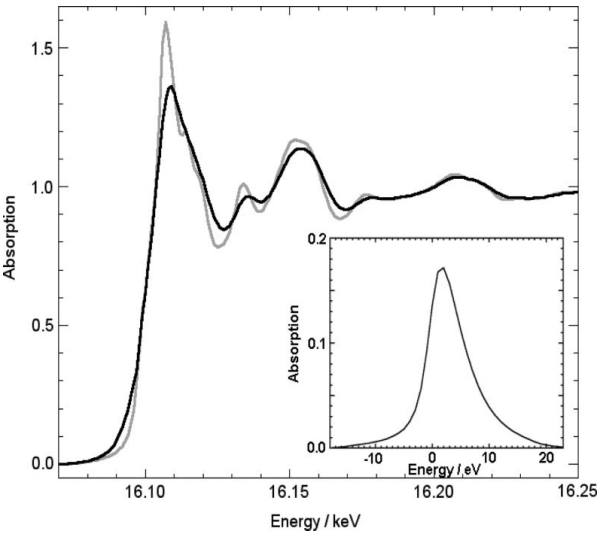
Polynomial coordinate transformations again consisted of a cubic polynomial for energy calibration, and a linear polynomial for absorption normalization. Background correction again consisted of a six-coefficient Chebyshev polynomial. The BM29 reference spectrum was obtained from a similar SrF<sub>2</sub> pellet as that used on ID24, which again had an edge jump of approximately 1.0.

**Table 2**  
Estimated and optimized parameter values for calibration at the Sr *K* edge.

Parameter	Estimate	Calibrated value
$a_0$	$1.571 \times 10^4$	$1.569 \times 10^4$
$a_1$	$1.228 \times 10^0$	$1.220 \times 10^0$
$a_2$	0	$3.147 \times 10^{-4}$
$a_3$	0	$-4.3507 \times 10^{-7}$
$b_0$	$6.190 \times 10^{-1}$	$7.185 \times 10^{-1}$
$b_1$	$9.205 \times 10^{-1}$	$9.324 \times 10^{-1}$
$\Gamma$	1.00 eV	2.35 eV
$\sigma$	1.00 eV	1.25 eV

Background	Parameter value
$x^0$	$-1.092 \times 10^{-2}$
$x^1$	$1.231 \times 10^{-1}$
$x^2$	$5.224 \times 10^{-2}$
$x^3$	$-4.072 \times 10^{-3}$
$x^4$	$-1.915 \times 10^{-3}$
$x^5$	$8.419 \times 10^{-3}$



**Figure 4**  
The Sr *K* edge acquired from BM29, shown before (grey) and after (black) the application of instrument corrections necessary to match its overall instrument function to that of ID24. The product of the two correction functions, Lorentzian and exponential, is shown as an insert.

The initial estimate and calibrated parameter values are shown in Table 2, with the calibrated solution shown in Fig. 3. The BM29 reference spectrum is shown in Fig. 4 before and after the application of the instrument correction functions. The overall product of the two correction functions is shown as an insert. Some systematic differences between the ID24 and BM29 spectra persist after calibration, which most likely originate from inhomogeneities in the powdered pellets. Despite these, residual spectral differences at each point are approximately 0.7% of the average absorption, with fine-structure oscillations in calibrated and reference spectra coincident.

5. Conclusions

*DXAS Calibration* provides a quantitative and automated approach to the problem of calibration of dispersive XAS spectra. While providing a solution to the primary problem of coordinate transformation, it also moves beyond current techniques to consider calibration of spectra against references obtained from beamlines with significantly different instrument response functions. This not only

allows for calibration of spectra within a more general framework, but also provides quantitative information on how dispersive beamlines perform with respect to others.

The core of *DXAS Calibration* is coded in cross-platform compatible C++ with a *Visual Basic* graphical user interface for Windows users. The source code, a windows executable file, the examples given here and comprehensive instructions are included in the package. All components of the code are freeware, and are released under the conditions of the GNU General Public License.

The authors would like to thank the beamline staff of ID24 and BM29, particularly S. Pascarelli, O. Mathon and A. Trapananti, for their ongoing help and support for this project.

## References

- Adby, P. & Dempster, M. (1974). *Introduction to Optimization Methods*, pp. 64–69; 103–106. London: Chapman and Hall.
- ESRF (2001) *XAID: software tools for visualization and analysis of XAFS spectra*, [www.esrf.fr/computing/scientific/xop/xaid/doc/](http://www.esrf.fr/computing/scientific/xop/xaid/doc/).
- ESRF (2005) *ID24 beamline optics*, <http://www.esrf.fr/UsersAndScience/Experiments/XASMS/ID24/BeamlineDescription/BeamlineOptics/>.
- Hagelstein, M., Ferrero, C., Hatje, U., Ressler, T. & Metz, W. (1995). *J. Synchrotron Rad.* **2**, 174–180.
- Hagelstein, M., Lienert, U., Ressler, T., San Miguel, A., Freund, A., Cunis, S., Schulze, C., Fontaine, A. & Hodeau, J.-L. (1998). *J. Synchrotron Rad.* **5**, 753–755.
- Klug, H. & Alexander, L. (1974). *X-ray Diffraction Procedures*, pp. 290–297. New York: Wiley.
- Press, W. H., Flannery, B. P., Teukolsky, S. A. & Vetterling, W. T. (1992). *Numerical Recipes in Fortran*, 2nd ed., pp. 675–680. Cambridge University Press.

# An Introduction to Differential EXAFS

M. P. Ruffoni\*, R. F. Pettifer\*, S. Pascarelli†, A. Trapananti† and O. Mathon†

\**Department of Physics, University of Warwick, Coventry, CV4 7AL, UK*

†*European Synchrotron Radiation Facility, 6 Rue Jules Horowitz, BP 220, 38043, Grenoble Cedex, France*

**Abstract.** Differential EXAFS (DiffEXAFS) is a novel technique for measuring atomic perturbations on a local scale that result from the modulation of a given sample property. Experiments conducted to date have revealed a sensitivity to such perturbations of the order of femtometres [1], two orders of magnitude more sensitive than is considered possible by conventional EXAFS techniques [2]. Here, the concept behind DiffEXAFS is described, and experimental factors required to detect such a signal discussed.

**Keywords:** Differential EXAFS, DiffEXAFS, Atomic Perturbations

**PACS:** 61.10.Ht

## CONCEPT

Differential EXAFS (DiffEXAFS) is a novel technique for the study of small atomic perturbations, which was developed by Pettifer et al. over a period of years leading up to publication in May 2005 [1]. The technique employs the subtle changes in EXAFS signals induced by the modulation of a given sample property to measure changes in photoelectron scattering path length, and thus deduce any atomic displacements in the local area of the absorbing atom.

A Differential EXAFS spectrum is the difference between two conventional EXAFS spectra (designated + and -), taken with all sample properties kept constant, except for the unit modulation of some property of interest<sup>1</sup>. This is very similar in principle to XMCD, except that instead of only studying magnetic effects in the near-edge region, DiffEXAFS examines the extended x-ray absorption structure for perturbations of the sample. For instance, dichroic signals can be produced by altering the angle between the linear polarisation vector and the sample magnetisation to give information about magnetostriction, or changes of temperature to give thermal effects. Given that strains contributing to these signals are small, it is possible to express them in terms of a first order Taylor expansion of the x-ray fine-structure function,  $\chi$ , with respect to the modulated parameter.

$$\chi(k) = \sum_j A_j(k) \sin(ks_j + \phi_j(k)) \quad (1)$$

$$\Delta\chi = \sum_j A_j(k) k \cos(ks_j + \phi_j(k)) \Delta s_j \quad (2)$$

<sup>1</sup> If non-unit modulation is employed, the spectrum is referred to as a Difference EXAFS spectrum, which must be normalised to unit modulation in order to extract information on structural changes.

Strictly speaking,  $A_j(k)$  and  $\phi_j(k)$  are also path length,  $s_j$ , dependent, but changes in these parameters are negligible compared to  $\Delta s_j$ . In some situations though, additional factors are significantly dependent on the modulated parameter, such as the Debye-Waller factor when samples undergo temperature modulation. In this case, the differential fine-structure function becomes

$$\Delta\chi = \sum_j A_j(k) \left( k \cos(ks_j + \phi_j(k)) \Delta s_j - 2k^2 \sin(ks_j + \phi_j(k)) \Delta\sigma_j^2 \right) \quad (3)$$

This difference can be seen in Figure 1, where a typical Joule magnetostriction DiffEXAFS signal is plotted for a 90° rotation in sample magnetisation, and a typical thermal DiffEXAFS signal plotted for a 1K change in sample temperature; both at the Fe-K edge. The former spectrum is described by equation (2), and the latter by (3). Indeed, the Debye-Waller contributions to the thermal signal dominate, producing DiffEXAFS that is almost in phase with the original fine-structure, with thermal expansion only being detectable as a slight phase shift. Since the structure present in a DiffEXAFS spectrum is intimately linked to atomic perturbations, a different signal can be expected from the same absorption edge depending on which property is modulated, and how that affects the sample structure.

## IMPLEMENTATION

The concept of DiffEXAFS is quite trivial. The reason it has not been demonstrated in practice until recently comes down to experimental limitations. Most structurally perturbative phenomena induce atomic displacements of the order of a few femtometres for unit modu-

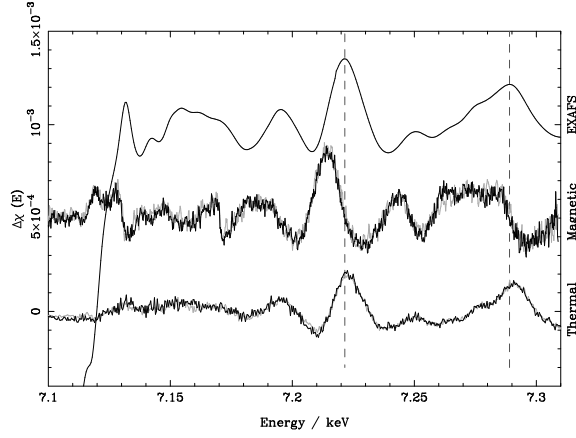


**FIGURE 1.** DiffEXAFS signals at the Fe-K edge for magnetisation modulation of FeCo and thermal modulation of Fe foil. EXAFS for the pure Fe sample is shown, which is virtually identical to the FeCo structure. As can be seen, the modulation of different sample properties results in very different signals. The magnetisation signal only contains one component through magnetostrictive strain, whereas the thermal signal contains components from expansion of the crystal lattice and changes to atomic vibrational amplitudes.

lation of a sample property, giving strains of the order of  $10^{-5}$ .

Conventional EXAFS typically only has sensitivity to strains of the order of  $10^{-3}$  depending on circumstances [2], so in order to resolve a difference signal, sample modulation must be a hundred times larger, inducing displacements of the order of 0.1pm. DiffEXAFS however, offers direct sensitivity to displacements of the order of femtometres.

Such sensitivity is achieved due to the method by which DiffEXAFS spectra are acquired, and the beam conditions over that time. Three main problems must be overcome. Firstly, statistical noise in  $\Delta\chi$  in each spectrum must be low - no more than about  $10^{-5}$  for femtometre resolution, which suggests the use of a high-intensity 3<sup>rd</sup> generation synchrotron source such as an undulator beam.

The next problem is that of beam energy stability. If the energy of photons passing through the sample changes between the + and - measurements, spurious signals can be generated from the resulting shift in fine-structure. Assuming the noise limit in  $\Delta\chi$  is  $10^{-5}$ , the edge energy would need to be stable to at least 0.1meV for any drift signal be indistinguishable from the noise.

The third and final problem is that of spatial beam stability. Unless the sample material under study is perfectly homogenous, subtle changes in thickness could generate a difference in x-ray absorption if the beam were to move between the + and - measurements. Beam drift must therefore be minimised, or the beam spot size in-

creased such that any drift changes the illuminated section of sample by only a tiny fraction.

Given that both energy and spatial stability of a beam are time-dependent, measurements of the sample at the + and - modulation states must be made in as short a space of time as possible; with both complete spectra acquired in a period of a couple of seconds or less. The solution therefore, is to use a Dispersive XAS (D-XAS) beamline. To date, all DiffEXAFS experiments have been conducted on ID24 of the ESRF [3], which has the added advantage of being mounted on a twin undulator source, providing x-ray intensities of the order of  $10^{13}$  photons/sec to minimise statistical noise.

A complete spectrum can be acquired and output in about 200ms, which ideally, with rapid sample modulation apparatus, allows two spectra to be obtained under different sample conditions in less than a second; the limiting factor being how quickly the sample responds to the modulation stimulus. However, whilst such quick measurements minimise time-dependent beam drifts, exposure times of the order of 100ms are not capable of providing statistical noise in  $\Delta\chi$  of  $10^{-5}$  as required in one pair of +/- measurements.

It is therefore necessary to average the DiffEXAFS signal over many pairs of measurements - typically around a thousand, giving a total acquisition time for a single DiffEXAFS spectrum of anything from thirty minutes to two hours depending on the speed of sample modulation. Averaging over such a period requires the consideration of additional factors, most notably the decay of beam intensity as electrons are lost from the storage ring. This, and other linear and exponential drift effects, may be accounted for by taking XAS transmission measurements in the following sequence as described by Mathon et al. for XMCD signals [4]

$$I^{0+}, I^{1-}, I^{2+}, I^{3-}, \dots, I^{2n-2+}, I^{2n-1-}, I^{2n+} \quad (4)$$

and then calculating the DiffEXAFS signal from the following algorithm.

$$\Delta\chi = \frac{1}{2n} \ln \left( \frac{I^{0+} (I^{2+})^2 \dots (I^{2n-2+})^2 I^{2n+}}{(I^{1-})^2 (I^{3-})^2 \dots (I^{2n-1-})^2} \right) \quad (5)$$

## DIFFEXAFS VS. CONVENTIONAL EXAFS

DiffEXAFS can be compared to conventional EXAFS by taking the example of, say, thermal expansion, where typical strains are of the order of  $10^{-5} \text{K}^{-1}$ . Conventional EXAFS would require sample modulation of around 100K between measurements for any variation in fine-structure to be measurable. DiffEXAFS however, could resolve changes with a modulation of just 1K, allowing

structural changes in the same 100K region to be probed in considerably greater resolution. The resulting measurement then yields not just the net structural change over the whole region, but precise incremental perturbations as a function of temperature.

It is true that such parameter resolution may not be required in all situations, particularly where phenomena inducing structural changes are either linear or vary only weakly as a function of the modulated sample property. However, many phenomena do not conform to these restraints; most notably non-linear phenomena such as phase transitions. In these situations the ability to detect atomic displacements over small changes in sample parameters is an absolute necessity. Indeed, this is where we believe the full power of DiffEXAFS is exploited.

Whilst conventional EXAFS will be able to detect net perturbations across some such discontinuity, and describe the sample structure in the stable region either side, it is generally not possible to look at how the sample responds approaching and receding from the transition - to say whether there are any onset features, or whether any particular structural instabilities become evident close to the primary transition itself. Even if a given transition were to induce perturbations large enough to be probed in a number of individual steps with conventional EXAFS, DiffEXAFS will always still offer around two orders of magnitude greater sensitivity and thus potentially a hundred times more sampling points across the transition region. No other XAFS technique offers this potential.

## FUTURE APPLICATIONS

DiffEXAFS is not limited to the study of any particular set of materials or to the study of any given type of phenomenon. In principle it may be used to examine *any* situation where the modulation of a sample property results in some small degree of atomic perturbation on a local scale.

Initial data from [1] demonstrated the measurement of magnetostriction by DiffEXAFS, which should be of great interest to those wishing to examine the atomic origins of this and other -striction type phenomena. Work is also currently being undertaken to study the more complicated case of samples undergoing temperature modulation.

However, the real interest will be in one of two areas. Firstly, in the study of non-linear phenomena as already described. Then in the examination of disordered or amorphous systems, where techniques such as diffraction fail, and where macroscopic measurements of sample properties may not necessarily scale down to the locally observed atomic perturbations due to the presence of intermediate scale deformations, such as the relief of

microscopic strain by sample defects.

At present, factors limiting the resolution of atomic perturbations are all experimental in origin, and relate to the stability or otherwise of beam components, noise in measured spectra, and to the accuracy and precision with which the sample can be modulated.

CCD detectors used in experiments to date have achieved statistical noise in  $\Delta\chi$  of about  $10^{-5}$ , determined by a 14-bit quantisation limit on read-out. A more sensitive detector (i.e. one with a greater number of bits) should be capable of  $10^{-6}$  based on the flux available from a typical 3rd generation undulator, enabling investigation of displacements on a 0.1fm scale. This would further test beam stability. To prevent corruption of a signal on this scale, energy stability would be required to 0.01meV between +/- measurements; suggesting improvements to beamline components, a reduction in time between +/- measurements, or a combination of the two. The effects of spatial drift must also be reduced, which is most easily achieved by increasing the beam spot size, currently about  $(10 \times 10)\mu m$ , to about  $(30 \times 30)\mu m$ .

However, the area where the greatest advances can be made, is in the modulation of the sample. Apparatus constructed to date has only focused on sample magnetisation and temperature. New designs will allow the study of different phenomena via the modulation of different sample properties. Developments to these and existing designs, capable of modulating the sample at, say, extremes of temperature or pressure, would further expand the technique. And improvements to the stability of the sample at measurement, and the reproducibility of modulation between + and - states, will allow signals to be detected from ever smaller changes to the sample; particularly useful where large atomic displacements occur from tiny changes in sample parameters, as is the case at phase-transitions.

## ACKNOWLEDGMENTS

The authors would like to thank D. Sutherland, A. Lovejoy, and A. Sheffield for their work in constructing apparatus for DiffEXAFS experiments, and S. Pasternak and F. Perrin for help during experiments on ID24.

## REFERENCES

1. R. F. Pettifer, O. Mathon, S. Pascarelli, M. D. Cooke, and M. R. J. Gibbs, *Nature* **435**, 78–81 (2005).
2. G. Dalba, P. Fornasini, R. Grisenti, and J. Purans, *Phys. Rev. Lett.* **82**, 4240–4243 (1999).
3. S. Pascarelli, O. Mathon, M. Muñoz, T. Mairs, and J. Susni, *J. Synchrotron Rad.* **Accepted** (2006).
4. O. Mathon, F. Baudalet, I. J.-P., S. Pasternak, A. Polian, and S. Pascarelli, *J. Synchrotron Rad.* **11**, 423–427 (2004).

# Verifying DiffEXAFS measurements with Differential X-ray Diffraction

M. P. RUFFONI,<sup>a\*</sup> R. F. PETTIFER,<sup>a</sup> S. PASCARELLI<sup>b</sup> AND O. MATHON<sup>b</sup>

<sup>a</sup>*Department of Physics, University of Warwick, Coventry, CV4 7AL, UK, and*

<sup>b</sup>*European Synchrotron Radiation Facility, 6 Rue Jules Horowitz, BP220, 38043,*

*Grenoble Cedex, France. E-mail: m.p.ruffoni@warwick.ac.uk*

*(Received 0 XXXXXXXX 0000; accepted 0 XXXXXXXX 0000)*

## Abstract

Differential EXAFS (DiffEXAFS) is a novel technique for measuring atomic perturbations on a local scale (Pettifer *et al.*, 2005). Here we present a complimentary technique for such studies: Differential X-ray Diffraction (DiffXRD), which may be used to independently verify DiffEXAFS results whilst using exactly the same experimental apparatus and measurement technique. A test experiment has been conducted to show that DiffXRD can be used to successfully determine the thermal expansion coefficient of SrF<sub>2</sub>.

## 1. Introduction

Since the development of Differential EXAFS (DiffEXAFS) (Pettifer *et al.*, 2005), the study of small atomic perturbations has attracted much interest. Here we present a complimentary technique for such studies: Differential X-ray Diffraction (DiffXRD).

This technique uses the same experimental apparatus and measurement technique as its EXAFS counterpart, such as that described by Pettifer *et al.* for magnetostriction measurements. The difference however, is that the sample through which transmission absorption measurements are taken (i.e. polycrystalline, amorphous, etc.) is replaced with its single crystal counterpart.

In kinematic diffraction theory, this introduces Laue diffraction features to the measured transmission intensity, where x-rays at certain energies are scattered out of the main line of the beam. These scattered photons do not enter the detector at the end of the beamline, causing an anomalous drop in transmitted intensity; seen as an apparent increase in x-ray absorption, which is observed as a discrete peak, independent of any true absorption fine-structure.

Clearly such features render the XAFS itself useless. However, being from diffraction in origin, they contain information on the structure of the sample material, and hence are sensitive to atomic perturbations in the same way as DiffEXAFS, albeit on a structurally averaged scale rather than a local atomic scale.

From Bragg's law and  $E = hc/\lambda$  it is easy to show that for a given diffraction peak

$$\left(\frac{\Delta E}{E}\right)_{hkl} = -\left(\frac{\Delta d}{d}\right)_{hkl} \quad (1)$$

Where  $\Delta E/E$  is the observed fractional change in peak position due to a relative change in inter-planer spacing,  $\Delta d/d$ , corresponding to the Miller indices  $hkl$ . In the case of, say, thermal expansion, this change is in turn

$$\left(\frac{\Delta E}{E}\right)_{hkl} = -\alpha_{ij}\Delta T \quad (2)$$



where  $\alpha_{ij}$  are the coefficients of the second-rank thermal expansion tensor, each of which can be obtained by the analysis of an appropriate diffraction peak. In the case of cubic crystals, von Neumann's Principle dictates that properties such as thermal expansion are isotropic (Nye, 1985). The corresponding tensor therefore contains only one independent parameter;  $\alpha_{ij}$  is reduced to  $\alpha$ , and  $\Delta E/E$  is the same for all diffraction peaks.

In order to accurately determine  $\Delta E$  using conventional XRD techniques, it is typically necessary to vary the temperature of the sample by many tens of Kelvin between measurements such that a clear peak shift can be observed and thus measured. However, by utilising the same measurement technique as DiffEXAFS - namely taking the difference between two spectra acquired in a short space of time in high stability, low noise conditions, where the only change between measurements is the modulation of a given sample property - then it is possible to detect extremely subtle shifts, and so obtain  $\Delta E$  over temperature changes of the order of 1K or less.

Thus, simply by substituting a DiffEXAFS sample with its single crystal counterpart, it is possible to obtain an independent measure of crystal perturbations without having to change any other part of the experimental setup.

Interestingly, the resolution of DiffXRD features is limited by different factors than DiffEXAFS measurements. Pettifer et al. showed that DiffEXAFS is sensitive to atomic displacements of the order of femtometres, being limited by the achievable statistical noise in the spectrum. If the same noise were limiting a DiffXRD spectrum, it would theoretically be possible to detect signals from displacements of the order of  $10^{-2}\text{fm}$ . However, such a feature would be produced from  $\Delta E \sim 10^{-7}$  eV, about two or three orders of magnitude smaller than the energy stability typically achievable between two absorption measurements taken a second or so apart. Thus, it is energy stability and energy resolution of the beamline that defines the smallest signal

measurable by DiffXRD.

## 2. Experiment

DiffEXAFS experiments are conducted on ID24, the Dispersive XAS beamline of the ESRF, as shown in Figure 1 (Pascarelli *et al.*, 2006b).

A single crystal of  $\text{SrF}_2$  (FCC fluorite structure with  $a = 5.7996\text{\AA}$ ) was cleaved along its 111 lattice planes, producing a section about  $5 \times 5$  mm big and  $70\mu\text{m}$  thick, and mounted at the focal spot of the beamline, producing an absorption jump of 1.9 at the Sr-K edge. This spectrum has been normalised to a unit jump and plotted on Figure 2. Laue diffraction peaks are clearly present in the observed signal. Also plotted on Figure 2 is the DiffXRD signal, generated by subtracting the absorption signal shown from another taken with the sample heated by 1K relative to it.

Such a change in sample temperature increases the size of the crystal unit cell according to thermal expansion. Given  $\text{SrF}_2$  has a cubic crystal structure, the thermal expansion is described by just one coefficient. All the observed diffraction peaks are equivalent, such that each will exhibit the same thermally induced change in position irrespective of the type of reflection.

The absence of any difference features at the same energy as the Sr-K edge in Figure 2 is testament to energy stability of the beam between the two absorption measurements used to construct the DiffXRD signal. The observed differences are therefore from a genuine change in observed x-ray absorption rather than from drifts in the beam between measurements.

The diffraction peak at 16.35keV, corresponding to the largest feature in the DiffXRD signal, was extracted and transformed back to transmission space using  $I_1/I_0 = \exp(-\mu x)$ . A normalised Gaussian was then fitted to the transmission spectrum to determine its centroid energy, width at half-maximum, and height. This fit is shown

in Figure 3, with the parameters listed in Table 1.

It should be noted that whilst diffraction peaks are Lorentzian in form, the energy resolution of ID24 at energies in excess of 15keV causes some broadening, transforming them to Gaussians. Previous work has shown an additional asymmetric component is also present (Ruffoni & Pettifer, 2006), caused by x-ray penetration depth effects. However, we find that this does not make a significant contribution here.

Although the convolution of an instrument function with the diffraction signal clearly alters the peak's observed width and height and thus any fitted parameters, this is not a problem from the point of view of DiffXRD. As shown in equation (1), structural changes in the sample material are derived from a change in the measured energy of a given peak. Therefore, the only requirement for DiffXRD is that the peak retains its shape between the two measurements under different sample conditions, allowing this shift to be determined.

The DiffXRD signal, shown in Figure 4, was obtained for a temperature change in the sample of 6K rather than 1K; increasing the degree of peak movement between measurements, and thus making the difference feature larger and easier to define. Given the degree of movement is linearly related to the change in temperature by (2) (for small temperature changes), the energy shift per Kelvin may be restored by dividing the observed shift by the temperature difference. Using the Gaussian width and height parameters from Table 1 to fix the shape of the diffraction peak to that seen in Figure 3, the DiffXRD feature was characterised by calculating the difference in observed absorption between two such peaks, slightly offset in energy relative to one another, giving the separation shown at the bottom of Table 1. The centroid of the difference feature is defined as half way between the two constituent peak centroids, and thus is not the same as that of the initial Gaussian fit.

Using equation (2), the thermal expansion coefficient of  $\text{SrF}_2$  was found to be (18.7

$\pm 0.8) \times 10^{-6} \text{K}^{-1}$ ; in agreement with the published value of  $18.1 \times 10^{-6}$  at 300K (Roberts & White, 1986).

### 3. Conclusions

It has therefore been shown that DiffXRD is a viable technique for the study of *average* crystal perturbations, using an identical experimental arrangement as would be used for DiffEXAFS measurements.

Clearly, one advantage of DiffXRD over DiffEXAFS is the sheer simplicity of the technique; equation (1) being considerably more straightforward to extract structural changes from than, say, equation 2 from Pettifer et al. for DiffEXAFS.

Also, if the current trend of reducing focal spot sizes on beamlines continues (Pascarelli *et al.*, 2006a), then in the future it will become easier to introduce diffraction phenomena into absorption spectra, making DiffXRD measurements simpler to perform. Additionally, if spot sizes decrease below about  $(1 \times 1) \mu\text{m}$ , it will become possible to perform DiffXRD measurements on single crystallites in typical polycrystalline samples.

However, DiffXRD cannot be considered a replacement for DiffEXAFS, in spite of this, since it is hindered by the same limitations that affect standard XRD measurements. Firstly, the technique cannot be applied to disordered or amorphous systems unlike EXAFS, but most importantly, structural information derived from DiffXRD is based on mean atomic perturbations over a periodic crystal structure. It does not yield information on *local* atomic perturbations - one of the real strengths of DiffEXAFS.

DiffXRD should therefore be considered complementary to DiffEXAFS. Simply by substituting a DiffEXAFS sample with its single crystal counterpart (where available) and taking the same difference measurements with the same experimental apparatus, it is possible to obtain an independent measure of perturbations to the crystal

structure to verify those from DiffEXAFS. Conversely, it could also be used to identify and quantify any discrepancies between local atomic perturbations and average (macroscopic) perturbations via a common experimental arrangement.

#### Acknowledgements

The authors would like to thank D. Sutherland, A. Lovejoy, and A. Sheffield for their work in constructing apparatus for DiffEXAFS experiments, and S. Pasternak and F. Perrin for technical help whilst working on ID24.

#### References

- Nye, J. F. (1985). *Physical Properties of Crystals: Their Representation by Tensors and Matrices*, pp. 20–24. Oxford: Oxford University Press.
- Pascarelli, S., Aquilanti, G., Dubrovinsky, L., Guilera, G., Mathon, O., Muñoz, M., Newton, M. A., Pasquale, M. & Trapananti, A. (2006*a*). In *Proceedings of the 13th International Conference on X-ray Absorption Fine-Structure*, vol. Submitted.
- Pascarelli, S., Mathon, O., Muñoz, M., Mairs, T. & Susni, J. (2006*b*). *J. Synchrotron Rad.* **Accepted**.
- Pettifer, R. F., Mathon, O., Pascarelli, S., Cooke, M. D. & Gibbs, M. R. J. (2005). *Nature*, **435**, 78–81.
- Roberts, R. B. & White, G. K. (1986). *J. Phys C: Solid State Phys.* **19**, 7167–7172.
- Ruffoni, M. P. & Pettifer, R. F. (2006). *J. Synchrotron Rad.* .

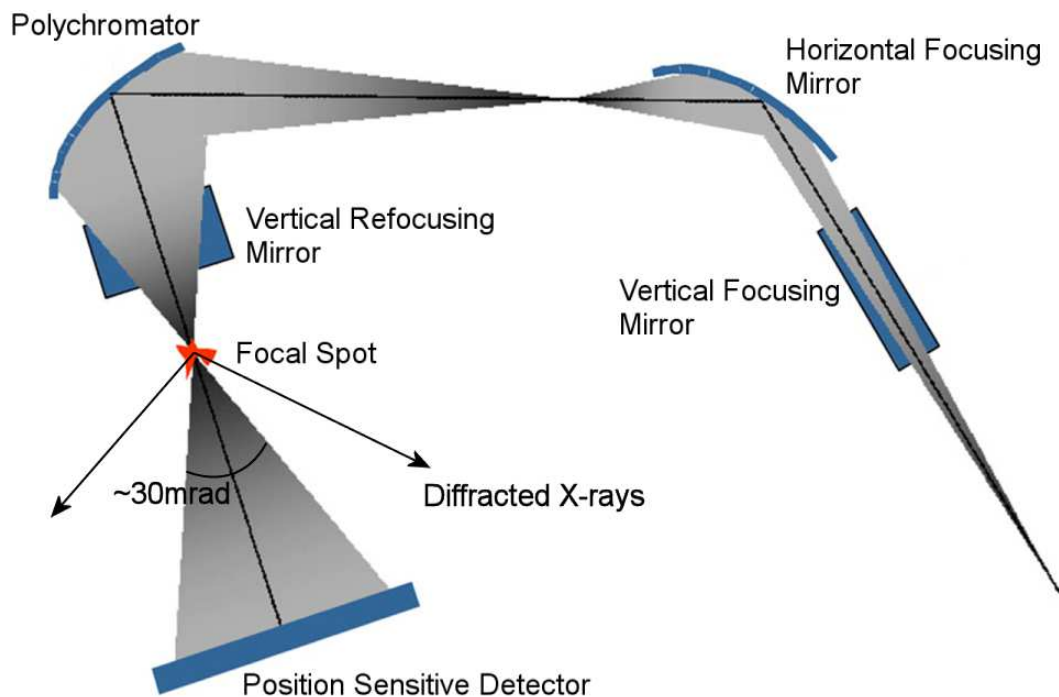


Fig. 1. A schematic representation of the optics on ID24 of the ESRF. A white beam from an undulator source illuminates a bent Si(111) polychromator crystal, creating a wavelength dispersive fan of x-rays covering an equivalent energy range of several hundred eV. Diffraction by planes in the sample cause x-rays of certain wavelengths to scatter out of the main beam, which do not then enter the detector. This causes an apparent drop in transmitted x-ray intensity at those energies, and thus a diffraction glitch.

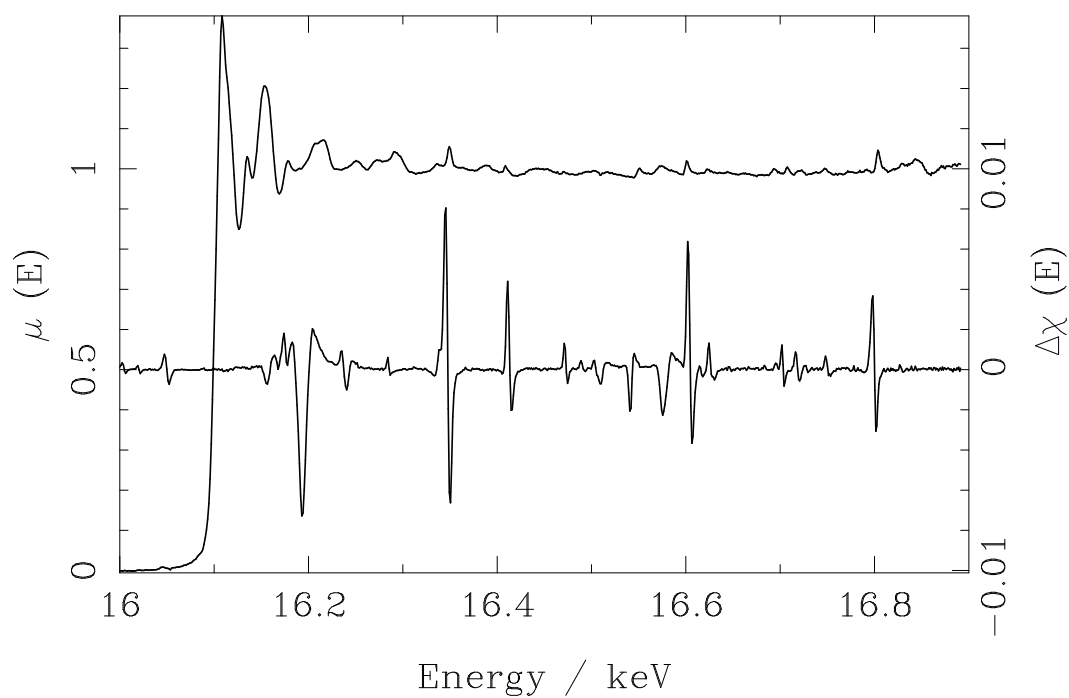


Fig. 2. The Sr-K edge measured in transmission through a single crystal of  $\text{SrF}_2$  (top plot with left scale). Diffraction glitches are clearly present on the absorption fine-structure. As the temperature of the specimen is changed by 1K at room temperature, these glitches shift in energy due to thermal expansion in the crystal, producing the DiffXRD signal shown below (right scale).

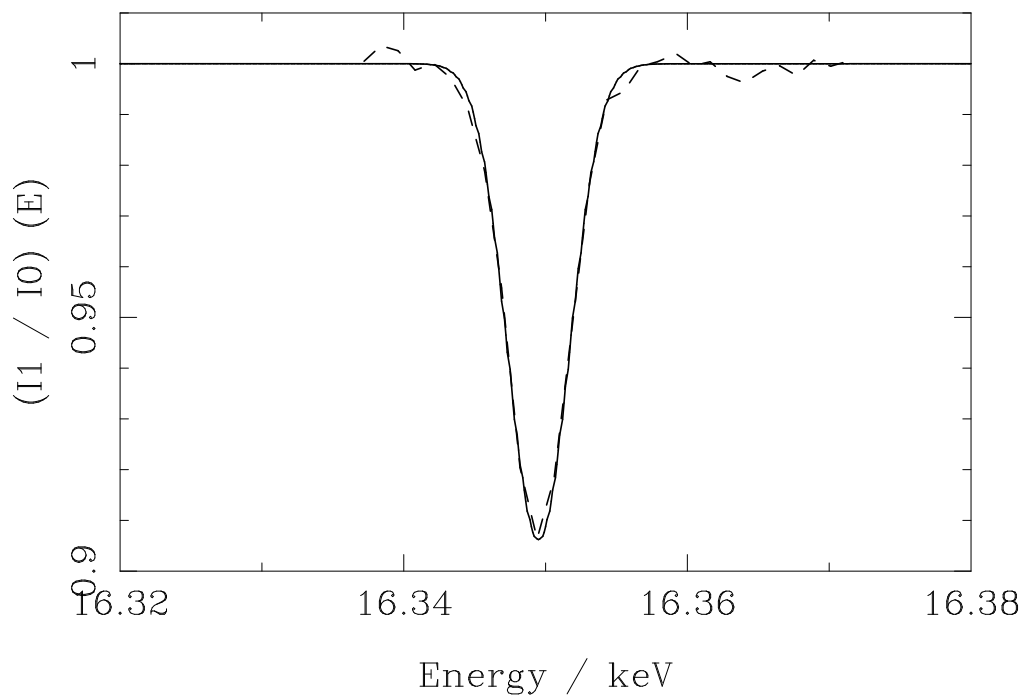


Fig. 3. The diffraction glitch (dashed line) at about 16.35keV is extracted from the x-ray *transmission* spectrum, and the background subtracted. A Gaussian is fitted to the glitch (solid line) to determine its centroid energy, width at half maximum, and relative height.



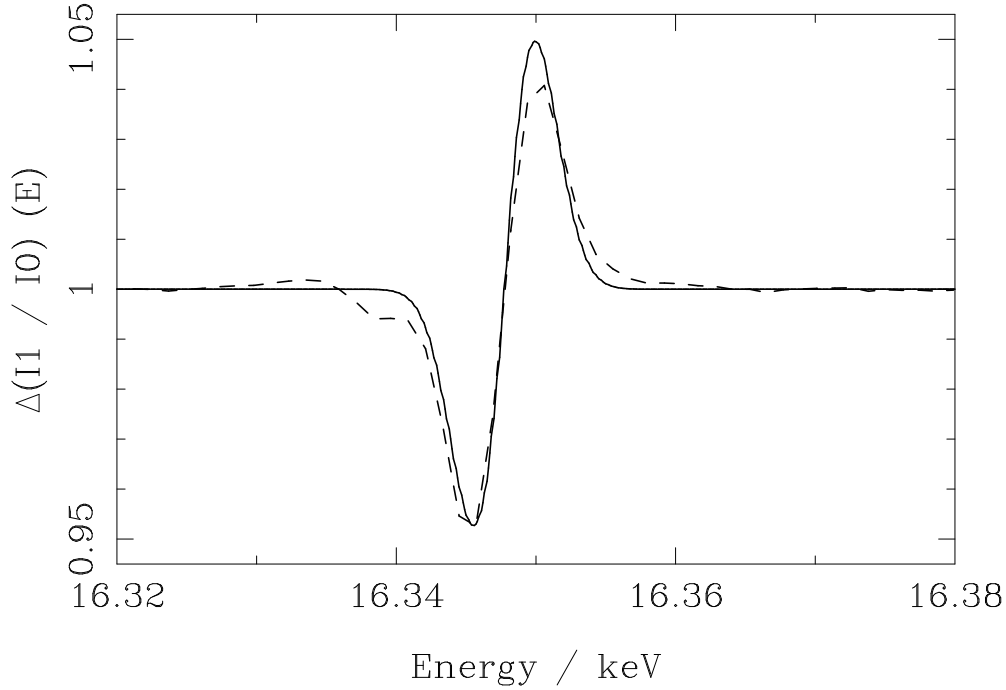


Fig. 4. The DiffXRD transmission signal obtained for  $\Delta T = 6K$  in the energy region of the glitch shown in Fig 3 (dashed line). The difference between a pair of Gaussians of width and height determined by the fit in Fig 3, and offset in energy relative to 100one another, are fitted to the feature (solid line); the energy offset being related to the fractional change in lattice spacing.

Table 1. *Fitted parameters for the diffraction peak shown in Figure 3 and for the corresponding DiffXRD feature shown in Figure 4. The thermal expansion coefficient has been derived using equation (2). Energies shown are not absolute energies, but based on a calibration with respect to another spectrum of known calibration. The errors shown are for the Gaussian and DiffXRD fits only and do not incorporate errors in calibration.*

Conventional Gaussian Fit	
Parameter	Value
Centroid / eV	$16349.505 \pm 0.002$
FWHM / eV	$2.137 \pm 0.002$
Relative height	$(-9.3782 \pm 0.0003) \times 10^{-2}$
DiffXRD Fit	
Parameter	Value
Centroid / eV	$16347.74 \pm 0.07$
Gaussian Separation / eV <sup>†</sup>	$1.84 \pm 0.08$
Thermal Expansion / $\times 10^{-6}K^{-1}$	$18.7 \pm 0.8$

<sup>†</sup> For a temperature modulation of 6.0K.

# Bibliography

- [1] P. Aaby and M. Dempster. *Introduction to Optimisation Methods*, pages 64–69 and 103–106. Chapman and Hall, London, 1974. ISBN 0-412-11040-7.
- [2] V. L. Aksenov, A. Yu. Kuzmin, J. Purans, and S. I. Tyutyunnikov. EXAFS spectroscopy at synchrotron radiation beams. *Phys. Particles Nuclei*, 32:1–33, 2001.
- [3] F. Albertini, S. Besseghini, A. Paoluzi, Pareti L., M. Pasquale, F. Passaretti, C. P. Sasso, A. Stantero, and E. Villa. Structural, magnetic and anisotropic properties of Ni<sub>2</sub>MnGa melt-spun ribbons. *J. Magn. Magn. Mater.*, 242-245:1421–1424, 2002.
- [4] P. A. Algarabel, C. Magen, L. Morellon, M. R. Ibarra, F. Albertini, N. Magnani, A. Paoluzi, L. Pareti, M. Pasquale, and S. Besseghini. Magnetic-field-induced strain in Ni<sub>2</sub>MnGa melt-spun ribbons. *J. Magn. Magn. Mater.*, 272-276:2047–2048, 2004.
- [5] J. Als-Nielsen and D. McMorrow. *Elements of Modern X-ray Physics*, pages 40–53. Wiley, New York, 2001. ISBN 0-471-49858-0.
- [6] A. Ankudinov, B. Ravel, and J. J. Rehr. *FEFF 8 version 8.20*, page 1. University of Washington, 2002.
- [7] A. Ankudinov, B. Ravel, and J. J. Rehr. *FEFF 8 version 8.20*. University of Washington, 2002.
- [8] C. A. Ashley and S. Doniach. Theory of extended x-ray absorption edge fine structure (EXAFS) in crystalline solids. *Phys. Rev. B*, 11:1279–1288, 1975.

- [9] E. C. Bain. *Trans AIME*, 70:25, 1924.
- [10] M. de Broglie. Sur une nouveau procédé permettant d'obtenir la photographie des spectres de raies des rayons Röntgen. *Comptes Rendus*, 157:924–926, 1913.
- [11] Ch. Brouder, G. Krill, M. Benfatto, and C. R. Natoli. Multiple-scattering v.s. intermediate valence in samarium sulfide. In J. Mustre de León, Stern E. A., D. E. Sayers, Y. J. Ma, and J. J. Rehr, editors, *Proceedings of the Fifth Conference on X-ray Absorption Fine Structure (1988)*, *Physica B*, volume 158, pages 495–497. Seattle (USA), 1989.
- [12] P. J. Brown, B. Dennis, J. Crangle, T. Kanomata, M. Matsumoto, U.-U. Neumann, L. M. Justham, and K. R. A. Ziebeck. Stability of martensitic domains in the ferromagnetic alloy  $\text{Ni}_2\text{MnGa}$ : a mechanism for shape memory behaviour. *J. Phys C: Solid State Phys.*, 16:65–75, 2004.
- [13] G. Bunker. Application of the ratio method of EXAFS analysis to disordered systems. *Nucl. Instr. and Meth.*, 207:437–444, 1983.
- [14] V. A. Chernenko, E. Cesari, V. V. Kokorin, and I. N. Vitenko. The Development of New Ferromagnetic Shape Memory Alloys In Ni-Mn-Ga System. *Scripta Metall. Mater.*, 33:1239–1244, 1995.
- [15] L. S. Ching, J. P. Day, and A. L. Ruoff. Pressure and temperature dependence of the elastic constants of LiBr and LiCl. *J. Appl. Phys.*, 44:1017–1020, 1973.
- [16] G. Dalba, P. Fornasini, R. Grisenti, and J. Purans. Sensitivity of Extended X-Ray-Absorption Fine Structure to Thermal Expansion. *Phys. Rev. Lett.*, 82:4240–4243, 1999.
- [17] Kronig R. de L. Zur Theorie der Feinstruktur in den Röntgenabsorptionsspektren. *Z. Physik*, 70:317, 1931.
- [18] Kronig R. de L. Zur Theorie der Feinstruktur in den Röntgenabsorptionsspektren. II. *Z. Physik*, 75:191–210, 1932.

- [19] Kronig R. de L. Zur Theorie der Feinstruktur in den Röntgenabsorptionsspektren. III. *Z. Physik*, 75:468–475, 1932.
- [20] J. W. M. DuMond. Theory of the use of more than two successive x-ray crystal reflections to obtain increased resolving power. *Phys. Rev.*, 52:872–883, 1937.
- [21] P. J. Durham, J. B. Pendry, and C. H. Hodges. Calculation of X-ray absorption near-edge structure, XANES. *Comput. Phys. Commun.*, 25:193–205, 1982.
- [22] M. M. Elcombe. The lattice dynamics of strontium fluoride. *J. Phys C: Solid State Phys.*, 5:2702–2710, 1972.
- [23] D. L. Foulis, R. F. Pettifer, and P. Sherwood. The removal of the muffin-tin approximation and use of self-consistent-field electron-densities for calculating the k-edge x-ray-absorption near-edge structure of chlorine. *Europhysics Letters*, 29:647–652, 1995.
- [24] S. J. Gurman. The small-atom approximation in EXAFS and surface EXAFS. *J. Phys C: Solid State Phys.*, 21:3699–3717, 1988.
- [25] S. J. Gurman, N. Binstead, and I. Ross. *J. Phys C: Solid State Phys.*, 17:143, 1984.
- [26] M. Hagelstein, C. Ferrero, U. Hatje, T. Ressler, and W. Metz. Curved Crystal Transmission Optics for Energy-Dispersive X-ray Absorption Spectroscopy. *J. Synchrotron Rad.*, 2:174–180, 1995.
- [27] M. Hagelstein, A. Fontaine, and J. Goulon. High Brilliance Beamline for Time Resolved X-ray Absorption Spectroscopy at ESRF. In H. Kuroda, T. Ohta, T. Murata, Y. Udagawa, and M. Nomura, editors, *Proceedings of the 7th International Conference on X-ray Absorption Fine Structure*, pages 240–242. Jpn. J. Appl. Phys., Tokyo, 1993.
- [28] L. Hedin. *X-ray Spectroscopy*, page 230. McGraw Hill Inc., 1974. ISBN 0-07-002674-2.

- [29] L. Hedin and S. Lundqvist. Effects of Electron-Electron and Electron-Phonon Interactions on the One-Electron States of Solids. *Solid State Phys.*, 23:1, 1969.
- [30] F. Heusler, Starck W., and E. Haupt. *Verh. Dtsch. Phys. Ges.*, 5:219, 1903.
- [31] Princeton Instruments. Data sheet: CCD Cameras based on EEV 1152 x 1242 CCD.
- [32] I.-K. Jeong, R. H. Heffner, M. J. Graf, and Billinge S. J. L. Lattice dynamics and correlated atomic motion from the atomic pair distribution function. *Phys. Rev. B*, 67:104301, 2003.
- [33] G. W. C. Kaye and T. H. Laby. *Tables of physical and chemical constants*, page 73. Longman, Harlow, 16th edition, 1995. ISBN 0-582-22629-5.
- [34] C. Kittel. *Introduction to solid state physics*, page 126. Wiley, New York, 7th edition, 1996. ISBN 0-471-11181-3.
- [35] H. Klug and L. Alexander. *X-ray Diffraction Procedures*, pages 290–297. Wiley, New York, 2nd edition, 1974. ISBN 0-471-49369-4.
- [36] E.-E. Koch, D. E. Eastman, and Y. Farge. Synchrotron radiation - a powerful tool in science. In E.-E. Koch, editor, *Handbook on Synchrotron Radiation, Vol 1a*, pages 1–63. North-Holland, Amsterdam, 1983. ISBN 0-444-86709-0.
- [37] D. C. Koningsberger and Prins R., editors. *X-Ray Absorption: Principles, Applications, Techniques of EXAFS, SEXAFS, and XANES*. Wiley, New York, 1988. ISBN 0-471-87547-3.
- [38] S. Krinsky. Fundamentals of Hard X-ray Synchrotron Radiation Sources. In D. M. Mills, editor, *Third Generation Hard X-ray Synchrotron Radiation Sources*, pages 1–40. Wiley, New York, 2002. ISBN 0-471-31433-1.
- [39] S. Krinsky, M. L. Perlman, and R. E. Watson. Characteristics of synchrotron radiation and of its sources. In E.-E. Koch, editor, *Handbook on Synchrotron Radiation, Vol 1a*, pages 65–171. North-Holland, Amsterdam, 1983. ISBN 0-444-86709-0.

- [40] P. A. Lee, P. H. Citrin, P. Eisenberger, and B. M. Kincaid. Extended x-ray absorption fine structure - its strengths and limitations as a structural tool. *Rev. Mod. Phys.*, 53:769–806, 1981.
- [41] P. A. Lee and J. B. Pendry. Theory of the extended x-ray absorption fine structure. *Phys. Rev. B*, 11:2795–2811, 1975.
- [42] G. Leibfried and W. Ludwig. Theory of anharmonic effects in crystals. *Solid State Phys.*, 12:275, 1961.
- [43] K. Levenberg. A Method for the Solution of Certain Non-linear Problems in Least Squares. *Quart. Appl. Math*, 2:164–168, 1944.
- [44] F. W. Lytle. The EXAFS family tree: a personal history of the development of X-ray absorption fine structure. *J. Synchrotron Rad.*, 6:123–134, 1999.
- [45] D. Marquardt. An Algorithm for Least-squares Estimation of Nonlinear Parameters. *J. Soc. Indust. Appl. Math.*, 11:431–441, 1963.
- [46] V. V. Martynov and V. V. Kokorin. The crystal structure of thermally- and stress-induced Martensites in  $\text{Ni}_2\text{MnGa}$  single crystals. *J. Phys III (France)*, 2:739–749, 1992.
- [47] O. Mathon, F. Baudelet, Itie J.-P., S. Pasternak, A. Polian, and Pascarelli S. XMCD under pressure at the Fe K edge on the energy dispersive beamline of the ESRF. *J. Synchrotron Rad.*, 11:423–427, 2004.
- [48] L. F. Mattheiss. Energy Bands for Solid Argon. *Phys. Rev.*, 133:A1399–A1403, 1964.
- [49] Z. Nishiyama. *Martensitic Transformation*, pages 9–10. Academic Press, New York, 1978.
- [50] Z. Nishiyama. *Martensitic Transformation*, pages 11–13. Academic Press, New York, 1978.

- [51] Z. Nishiyama. *Martensitic Transformation*, pages 345–347. Academic Press, New York, 1978.
- [52] F. C. Nix and D. MacNair. The Thermal Expansion of Pure Metals: Copper, Gold, Aluminium, Nickel, and Iron. *Phys. Rev.*, 60:597–605, 1941.
- [53] J. F. Nye. *Physical Properties of Crystals: Their Representation by Tensors and Matrices*, pages 20–24. Oxford University Press, Oxford, 1985. ISBN 0-198-51165-5.
- [54] S. Pascarelli, O. Mathon, and G. Aquilanti. New opportunities for high pressure X-ray absorption spectroscopy using dispersive optics. *J. of Alloys and Compounds*, 362:33–40, 2004.
- [55] S. Pascarelli, O. Mathon, M. Muñoz, T. Mairs, and J. Susini. Energy dispersive absorption spectroscopy for micro-XAS applications. *J. Synchrotron Rad.*, 13:351–358, 2006.
- [56] M. Pasquale, C. P. Sasso, L. H. Lewis, L. Giudici, T. Lograsso, and D. Schlager. Magnetostructural transition and magnetocaloric effect in  $\text{Ni}_{55}\text{Mn}_{20}\text{Ga}_{25}$  single crystals. *Phys. Rev. B*, 72:094435, 2005.
- [57] W. B. Pearson. *A Handbook of Lattice Spacings and Structures of Metals and Alloys*. Pergamon Press, New York, 1958.
- [58] R. F. Pettifer. Unpublished.
- [59] R. F. Pettifer. *The determination of the structure of some chalcogenide glasses by extended X-ray absorption fine structure*. Ph.D. thesis, University of Warwick, 1978.
- [60] R. F. Pettifer, M. Borowski, and P. W. Loeffen. The physics of ionization chambers - or how to improve your signal-to-noise ratio for transmission EXAFS measurements. *J. Synchrotron Rad.*, 6:217–219, 1999.

- [61] R. F. Pettifer and A. D. Cox. The Reliability of ab initio Calculations in Extracting Structural Information from EXAFS. In A. Bianconi, L. Incoccia, and S. Stipcich, editors, *EXAFS and Near Edge Structure*, pages 66–72. Springer-Verlag, Berlin, 1983.
- [62] R. F. Pettifer, D. L. Foulis, and C. Hermes. Multiple scattering calculations for biological catalysts. *Journal de Physique*, 47:545, 1986.
- [63] R. F. Pettifer and C. Hermes. Absolute Energy Calibration of X-ray Radiation from Synchrotron Sources. *J. Appl. Cryst.*, 18:404–412, 1985.
- [64] R. F. Pettifer, O. Mathon, S. Pascarelli, M. D. Cooke, and M. R. J. Gibbs. Measurement of femtometre-scale atomic displacements by X-ray absorption spectroscopy. *Nature*, 435:78–81, 2005.
- [65] A. V. Poiarkova and J. J. Rehr. Multiple-scattering x-ray-absorption fine-structure Debye-Waller factor calculations. *Phys. Rev. B*, 59:948–957, 1999.
- [66] A. V. Poiarkova and J. J. Rehr. Recursion Method for Multiple Scattering XAFS Debye-Waller Factors. *J. Synchrotron Rad.*, 6:313–314, 1999.
- [67] W. H. Press, S. A. Teukolsky, W. T. Vetterling, and B. P. Flannery. *Numerical Recipes in Fortran*, pages 675–680. Cambridge University Press, Cambridge, 2nd edition, 1992. ISBN 0-521-43064-X.
- [68] J. E. Rapp and H. D. Merchant. Thermal expansion of alkali halides from 70 to 570K. *J. Appl. Phys.*, 44:3919–3923, 1973.
- [69] G. Raunio and S. Rolandson. Lattice Dynamics of NaCl, KCl, RbCl, and RbF. *Phys. Rev. B*, 2:2098–2103, 1970.
- [70] J. J. Rehr. Private communication.
- [71] J. J. Rehr and R. C. Albers. Scattering-matrix formulation of curved-wave multiple-scattering theory: Application to x-ray-absorption fine structure. *Phys. Rev. B*, 41:8139, 1990.



- [72] J. J. Rehr and R. C. Albers. Modern Theory of XAFS. *Rev. Mod. Phys.*, 72:621, 2000.
- [73] J. J. Rehr, R. C. Albers, C. R. Natoli, and Stern E. A. New high-energy approximation for x-ray absorption near-edge structure. *Phys. Rev. B*, 34:4350–4353, 1986.
- [74] R. B. Roberts and G. K. White. Thermal expansion of fluorites at high temperatures. *J. Phys C: Solid State Phys.*, 19:7167–7172, 1986.
- [75] M. P. Ruffoni and R. F. Pettifer. Calibration of Spectra from Dispersive XAS Beamlines. *J. Synchrotron Rad.*, 13:489–493, 2006.
- [76] M. P. Ruffoni, R. F. Pettifer, S. Pascarelli, and O. Mathon. Thermal Expansion as determined by Differential EXAFS, 2005. Submitted to ESRF.
- [77] M. P. Ruffoni, R. F. Pettifer, S. Pascarelli, and O. Mathon. Verifying DiffEXAFS measurements with Differential X-ray Diffraction, 2006. Submitted.
- [78] M. P. Ruffoni, R. F. Pettifer, S. Pascarelli, A. Trapananti, and O. Mathon. The atomic origins of Thermal Expansion as determined by Differential EXAFS, 2006. Submitted to ESRF.
- [79] M. P. Ruffoni, R. F. Pettifer, S. Pascarelli, A. Trapananti, and O. Mathon. An introduction to Differential EXAFS, 2006. Accepted.
- [80] M. P. Ruffoni, R. F. Pettifer, S. Pascarelli, A. Trapananti, O. Mathon, and M. Pasquale. The study of phase changes in  $\text{HoBaFe}_2\text{O}_5$  and in  $\text{Ni}_2\text{MnGa}$  using Differential EXAFS, 2006. Submitted to ESRF.
- [81] D. E. Sayers, F. W. Lytle, and E. A. Stern. New Technique for Investigating Noncrystalline Structures: Fourier Analysis of the Extended X-Ray-Absorption Fine Structure. *Phys. Rev. Lett.*, 27:1204–1207, 1971.
- [82] W. L. Schaich. Comment on the theory of extended x-ray absorption fine structure. *Phys. Rev. B*, 8:4028–4032, 1973.

- [83] E. Sevilano, H. Meuth, and J. J. Rehr. Extended x-ray absorption fine structure Debye-Waller factors. I. Monatomic crystals. *Phys. Rev. B*, 20:4908–4911, 1979.
- [84] V. V. Shmidt. Contribution to the theory of the temperature dependence of the fine structure of x-ray absorption spectra. *Bull. Acad. Sci. USSR. Phys. Ser.*, 25:988–993, 1961.
- [85] V. V. Shmidt. Contribution to the theory of the temperature dependence of the fine structure of x-ray absorption spectra. II. Case of high temperatures. *Bull. Acad. Sci. USSR. Phys. Ser.*, 27:392–397, 1961.
- [86] International XAFS Society. Error Reporting Recommendations: A Report of the Standards and Criteria Committee, 2000.
- [87] Stenstrom. *Ann. der. Phys.*, 57:347, 1918.
- [88] U. Stuhr, P. Vorderwisch, V. V. Kokorin, and Lindgård. Premartensitic phenomena in the ferro- and paramagnetic phases of  $\text{Ni}_2\text{MnGa}$ . *Phys. Rev. B*, 56:14360–14365, 1997.
- [89] R. Stumm von Bordwehr. A History of X-ray Absorption Fine-structure. *Ann. Phys. Fr.*, 14:377–466, 1989.
- [90] H. E. Swanson, N. T. Gilfrich, and G. M. Ugrinic. *Standard X-ray Diffraction Powder Patterns No. 539*, volume 5. 1955.
- [91] C. Q. Tran, C. T. Chantler, Z. Barnea, D. Paterson, and D. J. Cookson. Measurement of the x-ray mass attenuation coefficient and the imaginary part of the form factor of silicon using synchrotron radiation. *Phys. Rev. A*, 67:042716, 2003.
- [92] K. Ullakko, J. K. Huang, V. V. Kokorin, and R. C. O’Handley. Magnetically controlled shape memory effect in  $\text{Ni}_2\text{MnGa}$  intermetallics. *Scripta Mater.*, 36:1133–1138, 1997.
- [93] A. N. Vasil’ev, A. D. Bozhko, V. V. Khovailo, I. E. Dikshtein, V. G. Shavrov, V. D. Buchelnikov, M. Matsumoto, S. Suzuki, T. Takagi, and J. Tani. Structural

- and magnetic phase transitions in shape-memory alloys  $\text{Ni}_{2+x}\text{Mn}_{1-x}\text{Ga}$ . *Phys. Rev. B*, 59:1113–1120, 1999.
- [94] W. H. Wang, Z. H. Liu, J. Zhang, J. L. Chen, Wu G. H., W. S. han, T. S. Chin, G. H. Wen, and X. X. Zhang. Thermoelastic intermartensitic transformation and its internal stress dependency in  $\text{Ni}_{52}\text{Mn}_{24}\text{Ga}_{24}$  single crystals. *Phys. Rev. B*, 66:052411, 2002.
- [95] C. M. Wayman. *Introduction to the Crystallography of Martensitic Transformations*, page 77. Macmillan, New York, 1964.
- [96] C. M. Wayman. *Introduction to the Crystallography of Martensitic Transformations*, pages 78–80. Macmillan, New York, 1964.
- [97] P. J. Webster. Ph.D. thesis, University of Sheffield, 1968.
- [98] P. J. Webster, K. R. A. Ziebeck, S. L. Town, and M. S. Peak. Magnetic order and phase transformation in  $\text{Ni}_2\text{MnGa}$ . *Philosophical Magazine B*, 49:295–310, 1984.
- [99] [www.esrf.fr/UsersAndScience/Experiments/XASMS/BM29/](http://www.esrf.fr/UsersAndScience/Experiments/XASMS/BM29/).
- [100] [www.esrf.fr/UsersAndScience/Experiments/XASMS/ID24/](http://www.esrf.fr/UsersAndScience/Experiments/XASMS/ID24/).
- [101] A. Zheludev, S. M. Shapiro, P. Wochner, and L. E. Tanner. Precursor effects and premartensitic transformation in  $\text{Ni}_2\text{MnGa}$ . *Phys. Rev. B*, 54:15045–15050, 1996.